Durham E-Theses

Cosmological Simulations with Dark Matter from beyond the Standard Model

SCHEWTSCHENKO, JASCHA,ALEXANDER

How to cite:

Use policy

Abstract

We study the non-linear structure formation in cosmologies where the collision-less cold dark matter (CDM) is either replaced by interacting dark matter or (partly) replaced by a free-streaming non-cold dark matter component. We focus in the first case on models with a non-vanishing interaction cross-section between dark matter and radiation in the early Universe, i.e. photons (γCDM) and neutrinos (νCDM). We study the properties of the dark matter structures that form in the presence of the collisional damping using N-Body simulations. For their halo shapes, we find similar effects as for standard thermalized fermionic Warm Dark Matter (WDM). However, for the abundance of these structures, the interacting DM models are clearly distinguishable from WDM below the characteristic damping scale. We also have a closer look at dark matter halos that resemble those hosting the two main galaxies in our Local Group, the Milky Way (MW) and Andromeda (M31). By using a high-resolution zoom-simulation of Local Group-like environments, we reveal how the DM-radiation interactions help to ease certain CDM "small scale problems". Furthermore, the combination of these Local Group simulations with our previous cosmological simulations allows us to constrain the cross-section in our model by comparing the abundance of satellite galaxies in our Milky Way with the predictions for subhaloes. Thanks to the sensitivity of the subhalo abundance to the suppression of the primordial perturbations, even our most conservative constraints are orders of magnitude tighter than those previously obtained from CMB data.

In the case of neutrinos or other non-cold dark matter, we study ways to predict numerically the evolution of this free-streaming component correctly. We identify shortcomings in all the previously proposed techniques we encountered in our studies of various models with massive neutrinos and come up with a new, adaptive Eulerian technique to treat the neutrino fluid accurately. In particular, we introduce our implementation called SEPARA. First test results for the code are presented while full cosmological simulations will be performed in the near future.

Cosmological Simulations with Dark Matter from beyond the Standard Model

Jascha Alexander Schewtschenko

Durham University
Physics Department
Institute for Computational Cosmology / Institute for Particle Physics
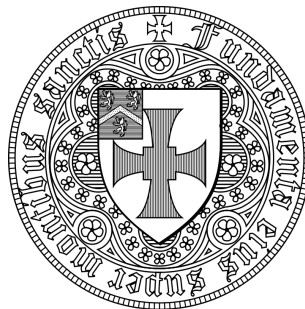Phenomenology

Supervisors:

Prof. Carlton Baugh
Prof. Silvia Pascoli

DISSERTATION

submitted to the University of Durham
in accordance with the regulations for
admittance to the Degree of

DOCTOR OF PHILOSOPHY

2016

Contents

List of Figures

Declaration

The work described in this thesis was developed between the years 2011 and 2015.

During this time, the author was a postgraduate research student under the supervision of Prof. Carlton M. Baugh in the Institute for Computational Cosmology (ICC) and Prof. Silvia Pascoli in the Institute for Particle Physics Phenomenology (IPPP) at the Department of Physics at the University of Durham.

This work has not been submitted for any other degree at the university of Durham or any other University. All research results and figures presented here that are not explicitly marked with external references have been produced by this author. Furthermore, the following content is either already published, submitted or in preparation to be published:

- The contents of Chapter 4 are based on Schewtschenko et al. (2015b).

- Chapter 3 and 5 contain work by this author that was published in Boehm et al. (2014) and Schewtschenko et al. (2015a).

- One of the applications given in Chapter 7 originates from work that was co-authored by this author and was published in Shanks et al. (2014).

- Additionally, both Chapter 5 and 7 contain work that is in preparation to be published in Schewtschenko (2016) and Schewtschenko et al. (2016).

The copyright of this thesis rests with the author. No quotation from it should be published without the author's prior written consent and information derived from it should be acknowledged.
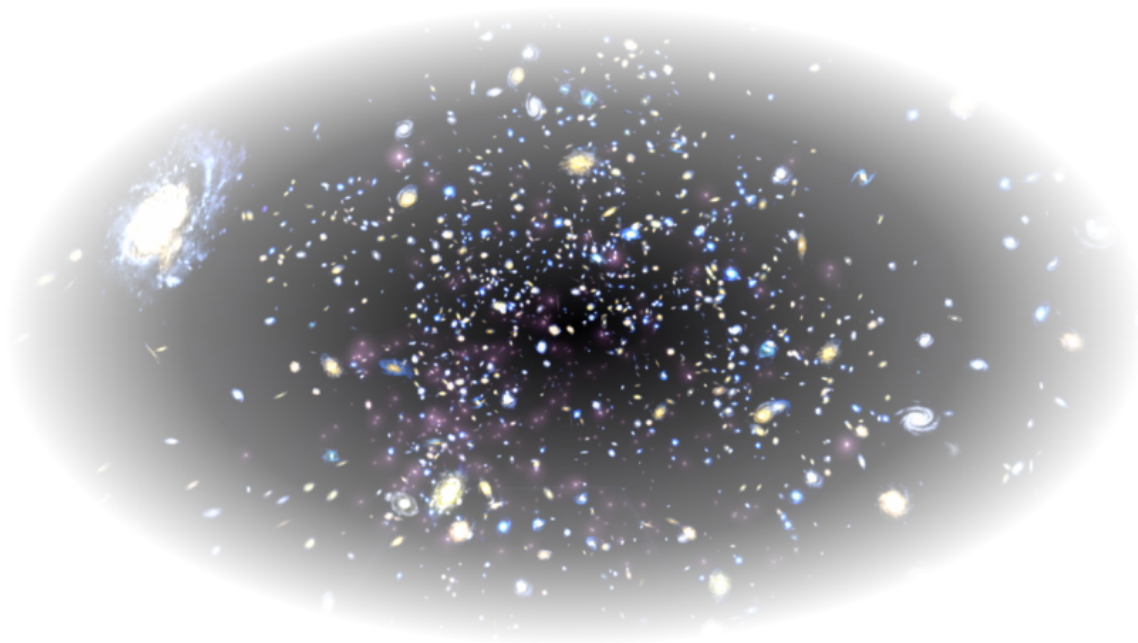
真正的知识是知道无知的程度。

— 孔子 (Confucius)

Augmented Content

This thesis features additional multimedia and inter-
active content. It is embedded in an augmented real-
ity using the open DARO framework for mobile devices.
In order to access the data, a DARO-compatible browser
(`http://icc.dur.ac.uk/~daro`) is needed to scan the
DARO QR access code printed here.

---

quote translation: "Genuine knowledge is to know the extent of one's ignorance."
credits for background image: NASA

Acknowledgements

First and foremost, my thanks go to Carlton, Silvia and Celine. Your guidance as well as patience and expertise helped me so often to stay on track, especially in those times when results were earned harder than anticipated. I could not have asked for a better supervision.

I also have to thank to all my colleagues and collaborators for all their assistance they provided for my work, in particular to Ryan Wilkinson who besides his great scientific skills has proven to be a master of polishing the words of our publications, to John Helly whose great programs and scripts are valued throughout the department, to Sabine Schindler and Lindsay Borrero whose administrative skills had been invaluable for organizing everything from seminar room for small meetings to travel arrangements for conferences, and last but not least to our formidable ICC IT Team, i.e. Lydia Heck, Allan Lotts and Peter Draper, who seemingly never slept to keep our workstations and super computer running for our studies and always had an open door for any questions and problems (even if it was about yet another raise for my already bloated disk quota).

I would also like to thank my fellow PhD students and especially my office mates over the years, Michelle, Tamsyn, Alex (I+II), Claudia, Matthieu, Jun, Bruno, Sergio and Flora for making even the longest work days in our crowded office enjoyable. My time as a PhD student in Durham would have also not been so much joy without all the friends at Ustinov College, in particular, Jane & Joonas, Gan, Polina, Sarah, Tom, Sep, Eric and Yuexian, many of whom are now scattered over the whole globe. Thank you for all the great times we shared. Thanks to my good old friends Leena, Zoe, Hans-Christian, Thomas and Annegret back "abroad" who have been always there for me, even if the physical distance between us definitely took its toll on the frequency we were able to see each other in the last couple of years. At this occasion, I also want to thank to my (not yet so old) local friends here in England, Kieran, Rich, Cat($\times$ 2) & family. Thanks to you, I did not only have the chance to learn so much more about the nature of dark matter, but also so much about the friendliness and hospitality of the people here in the North-East as well as the beauty of this region which we explored on our countless trips together. These are all cherished memories that I will take with me to wherever my life will

take me next.

One person, who so far tried to avoid any public acknowledgement of his great support out of modesty, but definitely deserves every bit of it, is David Creed. Not only made your generous donation the scholarship for this PhD possible, but our personal meetings and discussions were always an inspiration for me. So I cannot get around to express my deepest gratitude to you and your wife Anne for everything you have done for me.

And finally, VERY special thanks to my family, in particular to my Mum and Dad. Any attempt to express how much your support over all the years means to me would only end in a blatant understatement. You have always been there for me and without you, none of this would have been possible.

PART I
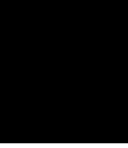
PREAMBLE

CHAPTER 1

Motivation

The study of dark matter (DM) is certainly one of our biggest challenges. It was proposed as a possible explanation for the anomalies in the dynamics of visible galaxies and galaxy clusters, where the circular velocities of visible substructures and stars by far exceed the velocities supported by the gravitational centripetal forces of a system with the observed matter distribution (Zwicky, 1937; Babcock, 1939; Rubin and Ford, 1970) (cf. Fig.1.1(left)).
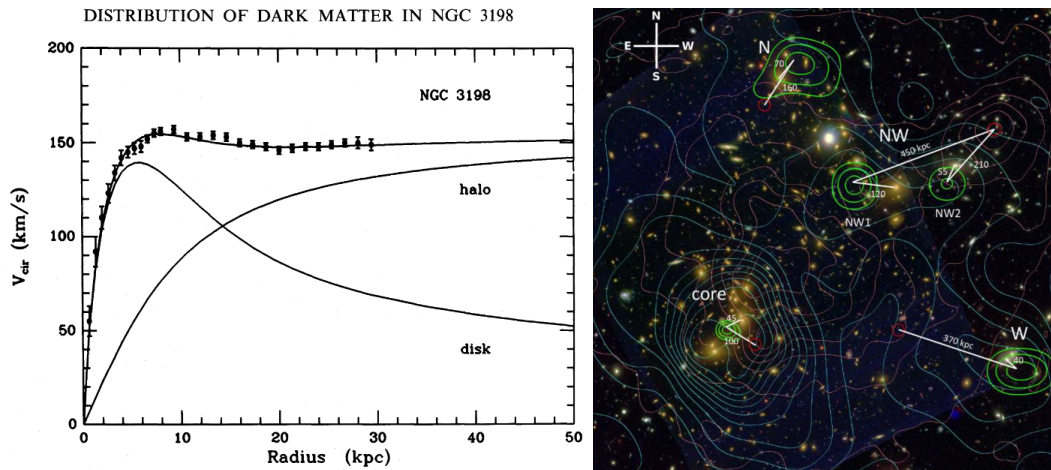
FIGURE 1.1: Evidence for Dark Matter: (left) Observed (dots with error bars) rotation curves for galaxy cluster NGC 3198 and fit (solid lines) based on a two component model with thin exponential disk and a spherical halo(van Albada et al., 1985); (right) mass reconstruction of galaxy cluster Abell 2744: total mass distribution obtained from gravitational lensing shown by cyan and gas distribution by magenta equidensity contours with green contours and red circles marking the centres of mass respectively(Hoekstra et al., 2013).

In modern surveys similar gravitational anomalies were observed when gravitational lensing was used to "weigh" galaxies (Hoekstra et al. (2013),Fig.1.1(right)). In both cases, it was found that a two component model with the visible matter embedded in an invisible "dark" matter halo of about the 4 times the visible mass matches the observations (van Albada et al., 1985). The accurate prediction of other observables such as the Cosmic Microwave Background (CMB) (Bennett

et al., 2003; Tauber, 2005) supported the validity of the current Standard Model of Cosmology, ΛCDM, which predicts that the composition of the Universe is dominated by both dark energy (DE) as the driving force of the accelerated expansion at low redshift and dark matter, leaving the known, visible matter accounting for less than 5% of the total energy density (cf. Sec. 2.2.5).

There have been attempts to explain the observed mass difference between the visible and the dynamical/gravitational mass with alternative models to General Relativity (GR) such as modified Newtonian dynamics (MoND) (Milgrom, 1983) that agree with GR on the well tested smaller scales, but account for additional gravitational acceleration on galactic scales and above. But recent observations such as the offset between the gravitational centre and the centre of visible mass in certain halo clusters (Clowe et al., 2006) favours the idea that DM is indeed made up of one or more types of unknown particles in addition to the known 'particle zoo' of the otherwise very successful standard model of particle physics rather than requiring a change to the laws of gravity.
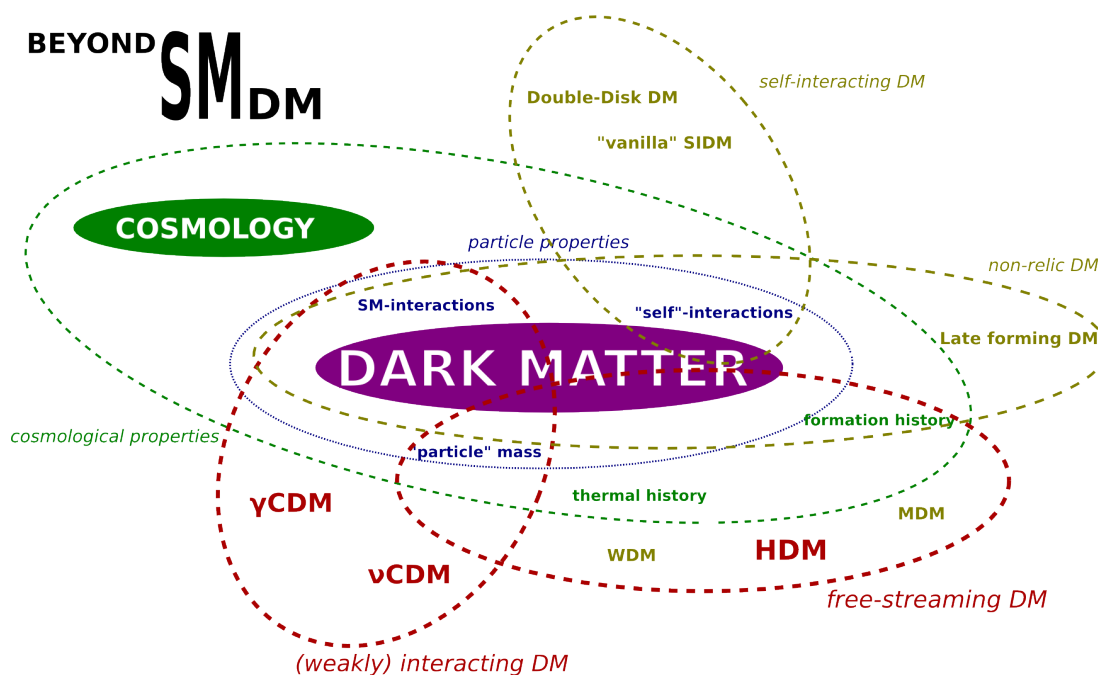
FIGURE 1.2: DM beyond the SM: DM properties and associated Beyond SM (BSM) models

The search for these particles and the determination of their properties involves physicists studying both extreme ends of the scales known to mankind. Particle physicists search at the smallest length and time scales in their direct and indirect detection experiments (Cirelli, 2012; Akerib et al., 2014a). The DM candi-

dates such as axions or neutrinos are among the lightest (predicted) massive particles. On the other hand, we have the cosmologists and astrophysicists, whose "experiment" is the observable Universe itself and the dynamical scales involved are naturally the largest ever observed. These also allow for a very sensitive probe for the properties of DM, which may have a significant, impact on the observable matter distribution of the Universe and astrophysical processes therein. As the scales involved do not permit us to physically redo this cosmological experiment or to control or alter the conditions therein to test different hypotheses about DM, and even analytical approaches only allow for predictions on the largest scales while breaking down in the presence of non-linear structure growth, numerical simulations of the Universe and the dark matter are our most powerful tool today. Fig.1.2 shows various properties of DM that go beyond the collision-less, cold fluid, that DM is assumed to be in the standard model. This thesis focuses on the two big groups marked in red.

After a summary of the most important theoretical background in part II, I present in part III my work on using computational cosmology to study potential effective interaction with photons and neutrinos which affects its distribution very early in the history of the Universe and the subsequent formation of small-scale structures we observe in the late Universe. In Chapter 3, the theoretical background for such *interacting dark matter* (IDM) is reviewed, whereas Ch. 4 and 5 contain our predictions for the structures formed in the observable Universe as well as significantly improved constraints on the interaction cross-section.

In part IV, I discuss how to use simulations to study neutrinos, the only, yet sub-dominant HDM component, we already identified by confirming that they are massive. After an introduction to the Cosmic Neutrino Background (CνB) and the perturbation approach to study its evolution in Chapter 6, I review the various techniques previously used for simulating their evolving distribution in Chapter 7 and compare results I obtained with them. In Chapter 8, I finally present `SEPARA`, a completely new innovative approach to treat neutrinos fully non-linear by tracking their advection on a grid.

PART II
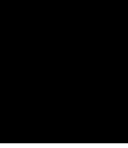
BACKGROUND

CHAPTER 2

Standard Models - What we (believe to) know

Here, we briefly introduce aspects of the standard models (SM) of particle physics and cosmology. For the former we outline the particle zoo and the properties of neutrinos within the standard model before turning to the results of oscillation experiments and the implied nature of neutrinos beyond the standard model (BSM). For the SMoC, we briefly derive the metric of the Universe from the cosmological principles and discuss the cosmic evolution with its various epochs of radiation, matter and dark energy domination. We also identify the contributions of the particles in the SMoPP to the content of the Universe and their role in both the linear evolution early Universe as well as non-linear structure formation in the late Universe.

2.1 Particle Physics

The standard model of Particle physics has proven to be very successful at predicting the properties not only of known particles correctly, but even of particles previously unknown such as the top quark, tau neutrino and the Higgs boson (Aad et al., 2012). It consists of the 48 fermions (6 leptons and 18 "coloured" quarks plus their anti-particles), 12 gauge bosons mediating the electro-weak (W^+,W^-,Z,photon) and strong interactions (8 "coloured" gluons) and one scalar Higgs bosons as shown in Fig. 2.1.

In this model neutrinos are massless and all other known particles (and their composite particles such as hadrons) are charged or unstable or at least interact strongly enough through either the electro-weak or the strong force to disqualify them as a candidate for the elusive, dark matter. Thus, the inclusion of dark matter as well as massive neutrinos require certain extensions or alternatives to this standard model such as SUSY (Martin, 1998) or νMSM (Asaka et al., 2005).
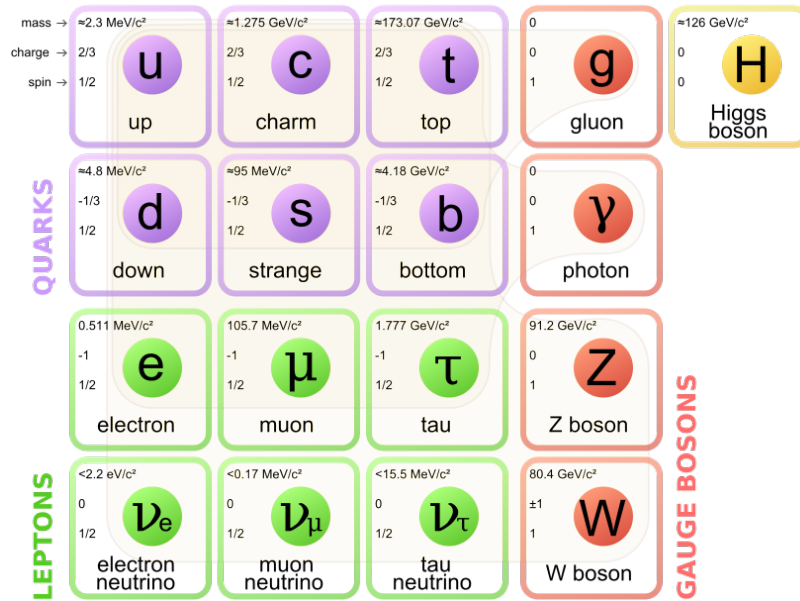
FIGURE 2.1: Illustration of the Standard Model of Particle Physics (pic)

2.1.1 Neutrinos

Neutrinos are among the most elusive and lightest particles in the whole standard model. As with their charged lepton partners (electron, muon and tau), they come in three different flavours. They were first proposed by Pauli (Pauli, 1930) as an explanation for the missing energy and momentum in the observed products of a β-decay. But their very weak interactions with other particles (cf. Sec. 2.1.1) made the first direct detections from reactor sources (Reines and Cowan, 1956) or later from atmospheric interactions (Achar et al., 1965) a challenge for particle physicists of those times. While the successful detection of the atmospheric and reactor neutrinos supported the predictions of their existence, the significant detections of solar neutrinos (Davis et al., 1968) revealed first discrepancies in form of the "Solar neutrino problem". A deficit of up to 66% in the detected flux of electron neutrinos produced as by-products of the fusion processes in the Sun compared to predicted flux from the solar models was observed. This dogged neutrino physics until the oscillation of electron neutrinos into the other flavours was confirmed by two independent groups (Kajita, 1999; McDonald and SNO Collaboration, 1999). This explanation, however, requires that the neutrinos must have massive eigenstates in contradiction to the standard model. In the following subsections, this and further properties of neutrinos will be discussed in more detail.

Neutrino Oscillation / Mass

In the Standard Model of Particle Physics (SMoPP), the three active neutrinos are massless as they have no right-handed counterparts for a Dirac mass term. On the other hand, recent neutrino experiments have revealed that the neutrino flavour states are actually a non-trivial superposition of the neutrino massive states. This relation is described by a unitary mixing matrix U:

$$\nu_L := \begin{pmatrix} \nu_{eL} \\ \nu_{\mu L} \\ \nu_{\tau L} \end{pmatrix} = U \begin{pmatrix} \nu_{1L} \\ \nu_{2L} \\ \nu_{3L} \end{pmatrix} =: U n_L \tag{2.1}$$

The time evolution of an arbitrary flavour state ν_a is given by the following solution of the Schroedinger equation

$$|\nu(t)\rangle = \exp(-iHt)|\nu_a(0)\rangle = \sum_i \exp(-iE_i t) U_{ai}^* |\nu_i\rangle \tag{2.2}$$

with $H = \text{diag}(E_1, E_2, \cdots)$ and E_i being the energies of the massive states. Since the flavour states do not correspond to the eigenstates of the Hamiltonian, i.e. the massive states, they oscillate. In the simplest case of a 2-ν oscillation with a mixing matrix

$$U = \begin{pmatrix} \cos\Theta & \sin\Theta \\ -\sin\Theta & \cos\Theta \end{pmatrix} \tag{2.3}$$

where Θ is the mixing angle, and neutrinos being ultra-relativistic, this results in a transition probability between two flavour states a and b given by

$$P(\nu_a \to \nu_b) = |\sum_i U_{bi} U_{ai}^* \exp(-i\frac{\Delta m_{i1}^2}{2E}t)|^2 = \sin^2 2\Theta \sin^2 \frac{\Delta m_{21}^2}{4E}t \tag{2.4}$$

with Δm_{21} being the mass difference between the massive states and E the energy of the neutrino involved. Such oscillations were observed in numerous experiments (e.g. Inoue (2004); An et al. (2012)), that allowed determination of the mass differences Δm_{ij} as well as the mixing angles between the three massive eigenstates. The latest global results for the parameters of a three-neutrino mixing are listed in Tab. 2.1.

With the non-vanishing mass differences, at least two neutrino eigenstates have to be massive. The actual mass depends on the hierarchy of states as the oscillation experiments only reveal the relative mass differences between them and do

parameter	best fit	$\pm 1\sigma$
$\Delta m^2_{21}[10^{-5}\text{eV}^2]$	7.5	0.19
$\Delta m^2_{31}[10^{-3}\text{eV}^2]$	2.45	0.05
$\sin^2\Theta_{12}$	0.304	0.013
$\sin^2\Theta_{23}$ (NO)	0.452	0.05
$\sin^2\Theta_{23}$ (IO)	0.579	0.06
$\sin^2\Theta_{13}$	0.0218	0.0010

TABLE 2.1: Latest global best-fit values for the neutrino oscillation parameters (Bergström et al., 2015). For $\sin^2\Theta_{23}$, values for normal (NO) and inverted ordering (IO) of the neutrino mass hierarchy are given. For all other parameters, the values are (almost) identical for the different mass orderings results and well within the given 1σ confindence interval.

not allow us to determine whether they are in the *Normal Ordering*(NO) or *Inverted Ordering*(IO) (see Fig. 2.2).
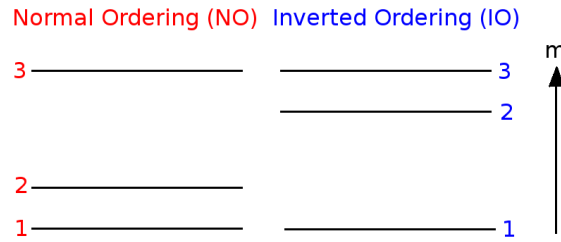
FIGURE 2.2: Illustration of mass hierarchies of massive neutrino states

This implies that at least two mass eigenstates have to be massive even in the case where the lowest mass eigenstate has a vanishing mass expectation value and a lower bound of the sum of these masses is ~ 0.05 eV for the normal and ~ 0.1 eV for the inverted mass hierarchy. At the same time β-decay experiments Fogli et al. (2008) have determined an upper mass bound for the sum of ~ 2.2 eV.

The fact, that we observe a neutrino mass at all, is not covered by the Standard Model. But it is possible to extend the model to allow Dirac and/or Majorana mass term for the neutrinos:

Dirac mass One way to give neutrinos mass is to introduce right-handed, sterile neutrinos, ν_R, similar to the partners of the other fermions in the SM. This allows us to write down a Higgs-Yukawa interaction term for the flavour neutrino states $\nu_L = (\nu_{eL}, \nu_{\mu L}, \nu_{\tau L})$ that is consistent with the gauge symmetries in the SM:

$$\mathcal{L}_{\text{Dirac}} = -\frac{(v+H)}{\sqrt{2}}Y\bar{\nu}_L\nu_R + h.c. \tag{2.5}$$

with H being the physical Higgs boson, v the vacuum expectation value (vev) of the Higgs doublet Φ and Y is a matrix of the coupling constants for the new Yukawa couplings. The Dirac mass m_D for each massive state is thus given by the product of the components of the diagonalized Yukawa coupling matrix Y_{ii} and the Higgs vev. This is actually the weak point of this theory as the coupling has to be very small ($Y \sim 10^{-13}$) to obtain eV-scale neutrino masses.

Majorana mass Another way to obtain a mass term for neutrinos is to assume that they are Majorana particles, i.e. their own anti-particles. This allows to write down a mass term of the form

$$\mathcal{L}_{\text{Majorana}} = -\frac{1}{2} v_L^T C^+ M^M v_L + h.c. \tag{2.6}$$

with C being the charge conjugation matrix and M_M the Majorana mass and $h.c.$ denotes the hermitian conjugate of the first term. Such a Majorana term for the doublet v_L fields is ruled out in the SM framework by symmetry as it leads to a SU(2) scalar triplet. However, the Majorana mass m_R^M can contribute to the sterile, singlet neutrinos.

Writing down the mass matrix of the combined mechanisms, i.e. for an extended SM with sterile right-handed neutrinos that furthermore obtain a Majorana mass, yields

$$\begin{pmatrix} 0 & m_D \\ m_D & m_R^M \end{pmatrix}. \tag{2.7}$$

In the limit of very large Majorana masses (i.e. much heavier sterile neutrinos), diagonalizing this matrix leads to the following masses for the massive eigenstates:

$$m_1 = -\frac{m_D^2}{m_R^M}, \tag{2.8}$$

$$m_2 \sim m_R^M. \tag{2.9}$$

This so-called *see-saw mechanism* hereby suppresses the Dirac mass and allows larger, more natural Yukawa couplings even for very light neutrinos.

While the actual mechanism that gives neutrinos mass is of lesser importance for the work presented in this thesis, it is noteworthy that models like the νMSM which introduces right-handed sterile neutrinos are able to provide valid candidates for Warm dark matter (WDM).

Neutrino interactions

Possible interactions of the active neutrinos with other (left-handed) fermions are so far very accurately described in the Standard Model of Particle Physics by the weak interaction Lagrangian

$$\mathcal{L}_{\text{int}}^{(CC)} = \frac{g}{\sqrt{2}} \left(\bar{q}_L^U V \gamma^\sigma q_L^D W_\sigma^+ + \bar{\nu}_L \gamma^\sigma l_L W_\sigma^+ \right) + \text{h.c.} \tag{2.10}$$

for the *charged weak current* and

$$\mathcal{L}_{\text{int}}^{(NC)} = \frac{1}{cos\Theta_w} \left(\sum_{\alpha=L,R} \sum_{\beta=U,D} g_\alpha^\beta \bar{q}_\alpha^\beta \gamma^\sigma q_\alpha^\beta Z_\sigma + g_L^\nu \bar{\nu}_L \gamma^\sigma \nu_L Z_\sigma + \sum_{\alpha=L,R} g_\alpha^l \bar{l}_\alpha \gamma^\sigma l_\alpha Z_\sigma \right) + \text{h.c.} \tag{2.11}$$

for the *neutral weak current* where

$$q_\alpha^U = \begin{pmatrix} u_\alpha \\ c_\alpha \\ t_\alpha \end{pmatrix} \qquad q_\alpha^D = \begin{pmatrix} d_\alpha \\ s_\alpha \\ b_\alpha \end{pmatrix} \qquad l_\alpha = \begin{pmatrix} e_\alpha \\ \mu_\alpha \\ \tau_\alpha \end{pmatrix} \qquad \nu_\alpha = \begin{pmatrix} \nu_{e\alpha} \\ \nu_{\mu\alpha} \\ \nu_{\tau\alpha} \end{pmatrix} \tag{2.12}$$

are the quarks/charged lepton mass fields and neutrino flavour fields, g is the EW-coupling constant of the Standard Model and g_α^β are coefficients for the coupling between the Z bosons and the fermion fields. All trilinear couplings can be combined to obtain the interactions of the neutrinos with the environment as well as the decay modes for the muons and tauons. Since a comprehensive discussion of all interactions would exceed the limits of this thesis, I focus here on specific ones that are of importance for my work and restrict the discussion (mostly) to the tree-level only:

Elastic Neutrino-charged lepton scattering: Using the weak interaction via the Z- and the W-boson, (anti)neutrinos can scatter with charged leptons elastically and exchange momenta. Fig. 2.3 shows the respective tree-level Feynman diagrams for this process for neutrinos (in case of anti-neutrinos the charged t-channel diagram has simply to be replaced by a corresponding s-channel).

In the case of charged current interactions as seen in Fig. 2.3 (left), neutrinos can only scatter with the charged lepton of the same flavour, while for neutral currents such restrictions do not exist and neutrinos and anti-neutrinos are able to interact with any fermion f, i.e. including quarks bound in nuclei.

Quasi-elastic Neutrino-charged lepton scattering: The charged weak current in-
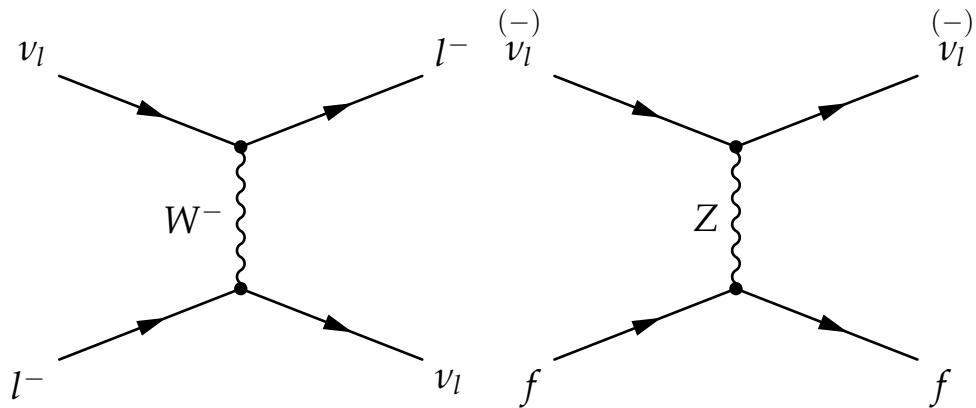
FIGURE 2.3: The two tree-level Feynman diagrams for the elastic scattering process of charged leptons (l)/ fermions (f) and neutrinos for (left) charged and (right) neutral current

teraction also offers decay modes for charged-leptons, allowing them and the neutrinos to "change" from one flavour to another as shown in the Feynman diagram in the example in Fig. 2.4.
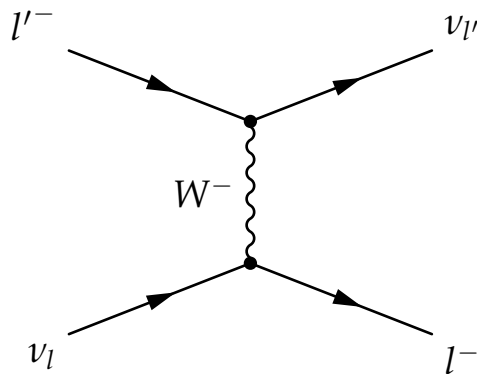
FIGURE 2.4: The tree-level Feynman diagrams for the charged-current Quasi-elastic elastic scattering process between the charged leptons l, l' and the corresponding neutrinos.

In the case that the scattering product is more massive than the particles before the scattering, these processes are constrained by an energy threshold. Assuming a scattering process of type

$$\nu_A + B \rightarrow \nu_B + A \tag{2.13}$$

and assuming B is at rest, that the neutrino masses are negligible and that $m_A > m_B$, the incoming neutrino has to have an energy of at least

$$E_{\nu_A}^{\text{th}} = \frac{m_A^2}{2m_B} - \frac{m_B}{2} . \tag{2.14}$$

For example, in case of an *inverse muon decay* defined by

$$\nu_\mu + e^- \rightarrow \nu_e + \mu^- \, , \tag{2.15}$$

the incoming muon-neutrino has to have a "temperature" of at least $T_e^{\text{th}} = 10.92\,\text{GeV}$.

$\nu + \bar{\nu} \leftrightarrow f + \bar{f}$**:** Neutrinos can also decay into other fermions and vice versa. This is done by an exchange of a Z-boson at tree-level (or e.g. photons at 1-loop level). It should be noted, that the annihilation of neutrinos into other fermions is severely constrained by the high energy threshold for the production of the fermion-anti-fermion pairs.

Neutrino-nucleon scattering: Similar to the interaction with charged leptons, neutrinos can also interact with quarks (bound in hadrons) via weak interactions. While elastic scattering allows a momentum transfer, charged-current reactions lead to neutron decay $n \rightarrow p + e^- + \bar{\nu}_e$ observed at *Big Bang Nucleosythesis* (BBN), pion decay used in accelerator experiments for the muon-neutrino production or *inverse neutron decay* $\bar{\nu}_l + p \rightarrow n + l^+$ used in neutrino detectors among others.

2.2 Cosmology

Cosmology as a branch of physics differs in one significant aspect from most other fields of science. While other fields provide the possibility to study the subject under laboratory conditions with controlled parameters and from different points of view and take place on time and length scales that allow us to repeat the experiments multiple times in a feasible amount of time and space, the cosmologists are stuck in just one position as an observer within the only available realization of a cosmos. Furthermore, the time scales of current cosmological dynamics of gigayears restrict every observation to study the same snapshot in time of this "experiment". Thus, the standard scientific approach of getting several realizations of the same experiment in order to distinguish significant observed effects from statistical ones do not work in this field. In fact, without any further assumptions, any attempt to gain knowledge about the universe would just be in vain, since even the most obscure hypothesis that matches the observed snapshot (e.g. one that explains every observed inhomogeneity as a result of different local laws of physics

or unique primordial structures) cannot be ruled out and is thus as valid as any other. Therefore, it has been assured that a "reasonable" modern cosmology has to rest on some set of fundamental principles:

2.2.1 Fundamental principles

Copernican Principle: We are not at a preferred position in the Universe, i.e. on sufficiently large scales, the observable properties of the Universe are the same for all observers no matter where they are.

Isotropy: If averaged over sufficiently large scales, the observed properties of the Universe are independent of direction.

The first assumption is important because it states that the observable part of the Universe is a fair sample of the whole one, while the second one says that the observable properties are not only independent of the position but also of the direction of the observation. Thus, the universe is assumed to be beyond its large scale structures *homogeneous* and *isotropic*, which is often called the *Cosmological principle*. This allows us to get after all a sample set of realizations of specific processes in the Universe by studying similar objects like galaxies which lie in different directions and at different distances (and therefore different redshifts) and determine their statistical properties.

Besides these main principles, another sensible assumption which is widely accepted and used is that the main force relevant for cosmology is gravity. This is due to the fact that both strong and weak interactions basically happen on length scales of elementary particles and the range of electromagnetism is limited by the shielding of electrically charged particles, even if magnetism can bridge larger scales than the other forces. The gravitation, on the other hand, is described by the *General Theory of Relativity* and thus by Einstein's famous field equations

$$G_{\alpha\beta} = \frac{8\pi G}{c^2} T_{\alpha\beta} + \Lambda g_{\alpha\beta} \, , \tag{2.16}$$

where Λ is the cosmological constant. Since the structure of space-time $g_{\alpha\beta}$ & $G_{\alpha\beta}$ determines the motion of matter and energy $T_{\alpha\beta}$ and vice versa, this theory is obviously non-linear and hard to handle. On large space and time scales we will therefore often fall back to Newtonian theory for e.g. calculating specific dynamics.

2.2.2 Metric

The two fundamental assumptions listed in Sec. 2.2.1 help us furthermore to derive a quite simple metric for this homogeneous, isotropic Universe. In general, a metric is given by a (symmetric) 4×4 tensor $g_{\alpha\beta}$ which we have already seen above in the field equations. For example, isotropy requires that space-time-components $g_{0i} = g_{i0}$ vanish in order not to single out a preferred direction in space. Additionally, if we use the the so-called *comoving coordinates*, which are spatial coordinates attached to ideal observers following the mean motion of matter and energy in the universe[1] such that $dx^i = 0$, it requires that the eigen time of these observers equal the coordinate time dt and the eigen time element $ds^2 = g_{\alpha\beta} x^\alpha x^\beta$ becomes

$$ds^2 = c^2 dt^2 = c^2 (dx^0)^2 \Rightarrow g_{00} = c^2 \ . \tag{2.17}$$

Incorporating this into the metric tensor, we see that it is now reducible and hence allows us to decompose space-time into a family of three-dimensional spatial slices. Introducing a time-dependent spatial scale parameter and considering that isotropy requires that the spatial subspaces have spherical symmetry, we finally get

$$ds^2 = c^2 dt^2 - a^2(t) \left[dr^2 + f_k^2(r) d\omega^2 \right] \ , \tag{2.18}$$

which is called Robertson–Walker metric. r is the radial coordinate, ω the solid-angle element with $d\omega^2 = d\Theta^2 + \sin^2\Theta d\phi^2$ and $f_k(r)$ is a radial function defining the curvature of the three-dimensional space. While isotropy is fulfilled by construction for any such function, homogeneity now requires that $f_k(r)$ has to be either trigonometric, hyperbolic or linear defining a spherical, hyperbolic or Euclidean space:

$$f_k(r) = \begin{cases} K^{-\frac{1}{2}} \sin(K^{\frac{1}{2}} r) & (K > 0) \\ r & (K = 0) \\ |K|^{-\frac{1}{2}} \sinh(|K|^{\frac{1}{2}} r) & (K < 0) \end{cases} \tag{2.19}$$

As we can see, the curvature of space has been directly parametrized by a parameter K. The latest constraints show that this *curvature parameter K* and Ω_K respec-

---

[1]In fact, only "free-falling" observers that follow this so-called *Hubble flow* caused by the expansion/contraction of the Universe perceive the universe to be isotropic. Any motion of the observer relative to this flow would, for example, result in the light emitted by the "flowing" matter of the universe to be seen more redshifted in some directions than in the corresponding opposite one due to the relativistic Doppler effect.

tively[2] are in fact very very close to zero, i.e. $-0.005 < \Omega_K < 0.005$ at a confidence level of 95% (Planck Collaboration et al., 2015d).

2.2.3 Cosmological Stress-Energy-Momentum Tensor

Before we can derive the dynamics of the system by solving the Einstein field equation, we have to specify the Stress-Energy Tensor for such a cosmological environment. We therefore assume that the matter and radiation of the universe on certain scales can be considered to be distributed homogeneously and isotropically as in a perfect fluid. This cosmic fluid is thus characterized by the following (covariant) stress-energy tensor[3]

$$T_{\alpha\beta} = (\rho + \frac{p}{c^2})u^\alpha u^\beta - g^{\alpha\beta}p \, , \tag{2.20}$$

where ρ and p are the energy density and (isotropic) pressure as measured by an observer in the rest frame of the fluid and u^α is the corresponding fluid 4-velocity. The density is composed of the contributions of the radiation ρ_r, the non-relativistic matter ρ_m and the vacuum energy ρ_λ. Since we assumed that we are dealing with a homogeneous and isotropic fluid, the pressure and the density are simply related by an equation of state

$$p = w\rho \, , \tag{2.21}$$

with $w = 1/3$ for the radiation / photon fluid, 0 for the collision-less non-relativistic dust and -1 for the vacuum energy contribution if it is a cosmological constant.

2.2.4 Dynamics

The scale factor $a(t)$ above has been introduced to take the expansion of the Universe into account when modelling the metric. Observations have shown that the Universe is in fact expanding and the Einstein equations offer solutions for a Universe of that form. Using the derived Robertson-Walker metric (Eq. 2.18) and the stress-energy tensor for the cosmic fluid (Eq. 2.20) to determine the Einstein tensor $G_{\alpha\beta}$, we obtain *Friedman's equations*, which describe the dynamics of the scale

---

[2]In the literature, $\Omega_K = -\frac{Kc^2}{H_0^2}$ is called the curvature density, but since Ω_K and K differ only by a constant factor, we will use the same name for both parameters.

[3]The full derivation of this tensor can be found e.g. in (Peebles, 1993, Ch.10).

factor:

$$\left(\frac{\dot{a}}{a}\right)^2 = \frac{8\pi G}{3}\rho(t) + \frac{Kc^2}{a^2} + \frac{\Lambda}{3} =: H^2(t) \tag{2.22}$$

$$\frac{\ddot{a}}{a} = -\frac{4\pi G}{3}\left(\rho + \frac{3p}{c^2}\right) + \frac{\Lambda}{3}, \tag{2.23}$$

where Λ is the cosmological constant seen in Eq. 2.16 and $H(t) = \dot{a}/a$ is the so-called *Hubble parameter*, i.e. the relative expansion rate at time t. The value of H today is called *Hubble constant*. By introducing the *critical density*

$$\rho_{\text{crit}}(t) := \frac{3H^2(t)}{8\pi G}, \tag{2.24}$$

which is the density of a spatially flat universe (i.e. K = 0). Normalizing the densities of both the relativistic, "hot" matter/radiation $\rho_r(t)$ and the non-relativistic, "cold' matter $\rho_m(t)$ yields

$$\Omega_r(t) = \frac{\rho_r(t)}{\rho_{\text{crit}}(t)}, \qquad \Omega_m(t) = \frac{\rho_m(t)}{\rho_{\text{crit}}(t)}. \tag{2.25}$$

The cosmological constant can be treated in a similar way and is often replaced by

$$\Omega_\Lambda(t) = \frac{\Lambda}{3H(t)}.$$

While the density $\rho_m(t)$ of non-relativistic matter evolves as a^{-3} since the gas is naturally thinned out by the expansion, radiation dilutes faster as a^{-4} since its particles additionally lose energy by being redshifted due to the cosmological expansion. Inserting these relations into Eq. 2.22, the first Friedman equation finally becomes

$$H^2(t) = H_0^2\left[\Omega_{r0}a^{-4} + \Omega_{m0}a^{-3} + \Omega_{\Lambda 0} + \Omega_K a^{-2}\right] =: H_0^2 E^2(a). \tag{2.26}$$

This defines a first-order differential equation in a, which determines the evolution of the cosmological expansion in general. Usually, $a(t_0) = 1$ is chosen as the initial condition where t_0 marks the time today. If we use a scale factor a that satisfies the ordinary differential equation (ODE) above, the metric in Eq. 2.18 obtained in this way is called the *Friedman-Lemaître-Robertson-Walker* (FLRW) metric.

2.2.5   Composition

So far, we have shown how the space-time of the Universe evolves in the presence of generic matter, radiation and a cosmological constant. The amount and composition of the visible content of the Universe can be determined by the radiation (visible light, IR, UV) observed by our telescopes and the specific absorption of emission spectra imprinted on it and shown in the right pie chart in Fig. 2.5. From observations, we learn that most of the visible mass of the Universe exists in the form of interstellar gas consisting of hydrogen and helium with traces of heavier elements (Gnacinski and Krogulec, 2006). A small fraction of that gas has managed to cool enough over time to collapse into stars. Heavier elements that make up all the solid matter and could only be created as products of stellar fusion processes or related supernovae finally account for the smallest part of the baryonic content of the Universe. That leaves two further components that are known in the standard model of particle physics, photons and neutrinos. Photons make up the radiation in the Universe and while there are many sources of photons in the Universe today (e.g. black body radiation of stars and gas), by far the largest amount originates as emission from the early stages of the then much hotter Universe dominated by radiation (Lacasa, 2014). After the Universe cooled enough for the Hydrogen atoms to recombine, the decoupled photons were able to travel (mostly) unscattered and form the *cosmic microwave background* (CMB). This is also true for neutrinos, where the CνB (cf. Chapter. 6) is expected to dominate all other neutrino sources today. The difference from photons is that we are not able to observe these low-energy neutrinos and merely deduce their quantity from assumption made about the thermal history of the early Universe. Additionally, depending on their particle mass and thus the time when they become non-relativistic, they may contribute to the radiation as well as to the matter content.

As I have already briefly mentioned in the motivation, there is strong evidence that the visible matter may not be all there is in the Universe. The standard model of cosmology introduces two additional components, dark energy (DE) and dark matter (DM) to account for the gravitational anomalies observed on the largest scales, i.e. the accelerated expansion expressed by the cosmological constant and the observed stronger gravitational potential inside galaxies and galaxy clusters. Both these components are not accounted for in the current standard model of particle physics[4], yet are a vital part of the current standard model of Cosmology,

---

[4]Quantum field theory predicts the existence of such a *vacuum energy*, but such predictions are in disagreement by over 100 orders of magnitude compared to the measured cosmological constant.
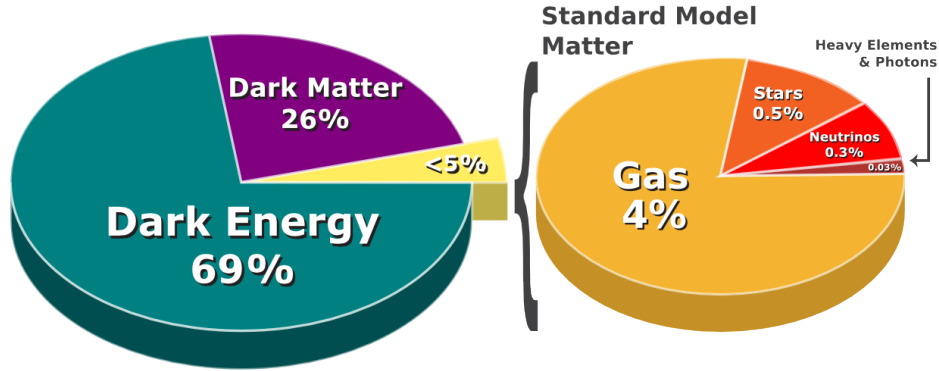
FIGURE 2.5: Composition of the Universe in ΛCDM with minimal neutrino mass

ΛCDM. In the absence of any direct evidence for interactions between DM and known particles beyond gravitation and lack of knowledge about its particle mass, DM is generally assumed to exist as a collision-less, cold fluid in the Universe.

2.2.6 Evolution of the matter/radiation distribution

With dark energy serving as a global background, the evolution of the distribution of the other remaining components (DM, baryonic matter, neutrinos and photons) needs to be determined. From the small Gaussian-like perturbation imprinted on the CMB, we know how the distribution of then coupled baryons and photons looked like at a very high redshift ($z = 1100$) (Planck Collaboration et al., 2015a). According to our current understanding these *primordial* perturbations originate from quantum fluctuations present at the very first moments of the Universe (Straumann, 2006). Using this information, we can then follow the evolution of the components of the Universe by solving the Boltzmann equations known from statistical mechanics:

$$\underbrace{\frac{\partial f}{\partial x^\mu} \frac{\mathrm{d} x^\mu}{\mathrm{d} t} + \frac{\partial f}{\partial P^\nu} \frac{\mathrm{d} P^\nu}{\mathrm{d} t}}_{\frac{\mathrm{d} f}{\mathrm{d} t}} = C[f; \{f_i\}] \,, \tag{2.27}$$

This is often dubbed the "vacuum catastrophe" of Cosmology.

where f and f_i are the phase-space distribution functions of specific particle types, X^μ and P^ν are the 4-position and 4-momentum respectively. The LHS is the Liouville term, while the RHS is the collisional integral accounting for particle destruction and creation. If the RHS vanishes, this equation simply states that the number of particles in a given (potentially moving) element of phase space does not change with time.

I will VERY briefly describe the significant importance of this equation in two different cases[5].

Abundance

In the first, simpler case, we are interested in the global evolution of the abundance of a specific particle in an unperturbed FLRW metric (cf. Section 2.2.2). Here, f only depends on time and physical momentum p, which is related to the conjugate momentum by the scale factor a in this unperturbed metric. Using the geodesic equation, Eq. 2.27 simplifies into:

$$\frac{\partial f(t,p)}{\partial t} - Hp\frac{\partial f(t,p)}{\partial p} = C[f; f_i] \, . \tag{2.28}$$

By integrating the momentum out, we now obtain a first-order partial differential equation describing the evolution of the global number density $n = \int \frac{d^3p}{(2\pi)^3} f(t,p)$ of each particle species:

$$\frac{\partial n}{\partial t} - 3Hn = \int \frac{d^3p}{(2\pi)^3} C[f; f_i] \Rightarrow \frac{1}{a^3}\frac{d(na^3)}{dt} = \tilde{C}[n; \{n_i\}] \, . \tag{2.29}$$

Let us assume, that we are interested in a particle species 1 that interacts either with itself or another particle 2 and results in a pair of particles of type 3 and 4. In this case, the net particle production and destruction described by the collisional integral can be simply written as

$$\tilde{C}[n_1; \{n_i\}] = -\alpha n_1 n_2 + \beta n_3 n_4 \, , \tag{2.30}$$

where the coefficient $\alpha = \langle \sigma v \rangle$ is the *thermally averaged interaction cross-section*, while β relates to α as $\tilde{C}[n_1; \{n_i\}]$ has to vanish in chemical equilibrium for this process.

---

[5]A more detailed version of the outlined derivation, can be found in e.g. Dodelson (2003); Ma and Bertschinger (1994a).

Thus, we get:

$$\frac{1}{a^3}\frac{\mathrm{d}(n_1 a^3)}{\mathrm{d}t} = -\langle\sigma v\rangle\left[n_1 n_2 - \left(\frac{n_1 n_2}{n_3 n_4}\right)_{\mathrm{eq}} n_3 n_4\right] \tag{2.31}$$

We now we divide the number densities n_i by their entropy density $s \sim a^{-3}$ to obtain the comoving densities instead. Time in the derivation is substituted by the expansion factor and we introduce the interaction rate for particle 1 given by $\Gamma_1 = n_2\langle\sigma v\rangle$. Thus, Eq. 2.31 transforms into

$$\frac{1}{N_1}\frac{\mathrm{d}N_1}{\mathrm{d}a} = -\frac{\Gamma_1}{H}\left[1 - \left(\frac{N_1 N_2}{N_3 N_4}\right)_{\mathrm{eq}}\left(\frac{N_1 N_2}{N_3 N_4}\right)^{-1}\right], \tag{2.32}$$

which shows that this interaction of particle species 1 with the other particles freezes out, when H becomes larger than Γ_1. We define the point of freeze-out at $H \sim \Gamma$.

This result can now be used to derive the relic density of weakly interacting massive particles such as neutrinos or other dark matter candidates once their interactions with the other components have frozen out as the densities of the matter and radiation in the expanding Universe is diluted and velocities are redshifted. Let us assume for example a interaction of the form

$$\chi + \bar{\chi} \rightleftharpoons l + \bar{l}, \tag{2.33}$$

where a massive dark matter particle χ and its antiparticle can annihilate to produce to essentially massless particles $l + \bar{l}$. Let us further assume that l and its antiparticle are still tightly coupled to the cosmic plasma in the early Universe, which keeps their equilibrium densities fixed ($N_l = (N_l)_{\mathrm{eq}}$) and that there is no initial asymmetry between the particles and their antiparticles ($N_\chi = N_{\bar{\chi}}$). We also define the ratio $x \equiv M_\chi/T$ between DM particle mass M_χ and the temperature of the involved components T to replace t as a measure of time. On this scale the dark matter particles become non-relativistic at $x_{\mathrm{nl}} \sim 1$ from where on the back reaction in Eq. 2.33 is kinematically disfavoured and $(N_\chi)_{\mathrm{eq}} \sim x^{3/2}\exp(-x)$ drops exponentially until freeze-out takes place at about $x_f \approx 10$. Finally, by assuming that all this takes place well within the radiation dominated era ($H(a) \sim T^2 \Rightarrow H(a) = H(M_\chi)x^{-2}$) and within a small enough time interval such that the *effective number of degrees of freedom in entropy* $g_{\star S}(T) \sim s/T^3$ remains constant, Eq. 2.31 becomes the following *Riccati equation*, i.e. a first-order ordinary differential equation that is

quadratic in the unknown function $N_\chi(x)$

$$\frac{\mathrm{d}N_\chi}{\mathrm{d}x} = -\frac{\lambda}{x^2} \left[N_\chi^2 - (N_\chi^2)_{\mathrm{eq}} \right] , \qquad (2.34)$$

with

$$\lambda = \frac{2\pi^2}{45} g_{\star s} \frac{M_\chi^3 \langle \sigma v \rangle}{H(M_\chi)} . \qquad (2.35)$$

For a velocity-independent cross-section (s-wave), λ can also to be considered constant in the time frame of interest, but in general that is not the case. A way to obtain an x-independence, we define $\lambda_0 \sim \lambda/x^{p/2}$ where p is the degree of the leading order term of the expanded cross-section, i.e. $\langle \sigma v \rangle \sim v^p$. Fig. 2.6 shows a numerical solution of that equation, i.e. the evolution of the abundance of a dark matter candidate. Different effective values of λ_0 as well as different degrees p of velocity-dependencies of the interaction result in significantly different relic abundances. While $N_\chi \approx (N_\chi)_{\mathrm{eq}}$ for very high temperatures $x \ll 1$, the final abundance
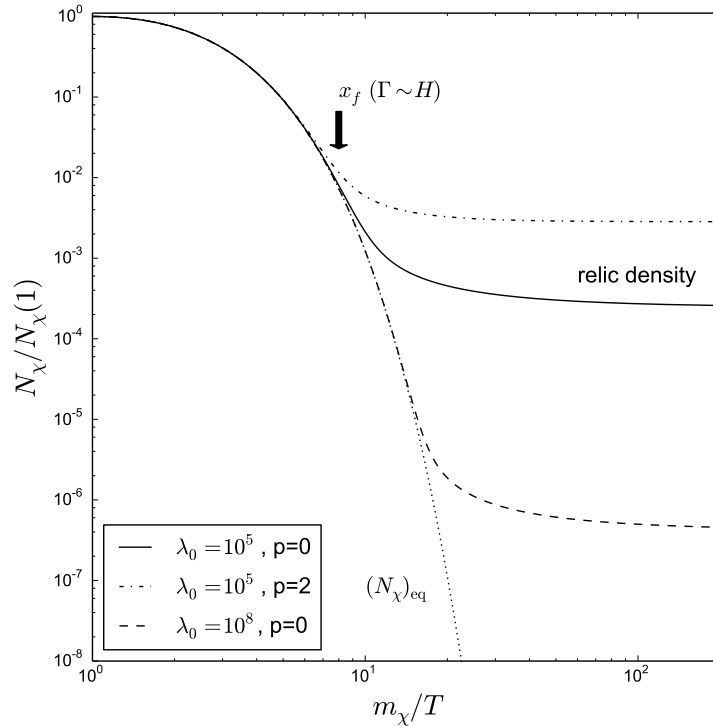
FIGURE 2.6: Evolution of the normalized comoving number density around freeze-out x_f for various choices of λ. The dotted line marks the equilibrium number density, that drops exponentially as the production of DM is strongly suppressed for $m/T > 1$. The point of freeze-out for the model with the solid line is also marked by the arrow.

can be approximated by

$$N_\chi^{\text{final}} \approx \frac{x_f}{\lambda} \,. \tag{2.36}$$

where x_f can be determined from the freeze-out condition $H(x_f) \sim \Gamma(x_f)$.

Evolution of local perturbations

Additionally, we are also interested in how small primordial fluctuations in the matter distribution and therefore in the space-time metric itself are evolving over time. For that study, we first introduce such minor perturbations in the FLRW metric (Eq. 2.18) where the components up to first-order are given by[6]:

$$g_{00} = [1 + 2\psi(x,t)] \,, \tag{2.37}$$
$$g_{ij} = a^2\delta_{ij}[1 + 2\phi(x,t)] \,, \tag{2.38}$$

where ψ and ϕ are functions corresponding to the Newtonian potential and a perturbation in the spatial curvature respectively.

For cold fluids such as dark matter or baryons before shell-crossing, we can use the single-stream approximation, where non vanishing velocity dispersions can be neglected. Considering small perturbations $\delta\rho$ and δp in the local density and pressure respectively, the energy-momentum tensor for a perfect fluid (Eq. 2.20) is then to linear order given by

$$T_{00} = -(\bar{\rho} + \delta\rho) \,, \tag{2.39}$$
$$T_{0i} = (\bar{\rho} + \bar{p})v_i \,, \tag{2.40}$$
$$T_{ij} = (\bar{p} + \delta p)\delta_{ij} + \Sigma_{ij} \,, \tag{2.41}$$

where $\Sigma_i j$ is an anisotropic shear perturbation ($\Sigma_{ii} = 0$) for contributions from free-streaming particles like neutrinos. We define the overdensity $\delta \equiv \delta\rho/\bar{\rho}$ and the velocity divergence $\theta \equiv ik^j v_j$ in k-space. Applying the energy-momentum conservation ($T^{\mu\nu}_{;\mu} = 0$) assuming that the initial perturbations are isentropic, i.e. satisfy the same equation of state as in Eq. 2.21, we obtain for the evolution of δ and θ for a single, uncoupled fluid in the perturbed metric given in k-space by

$$\dot{\delta} = -(1 + w)(\theta - 3\dot{\phi}) \,, \tag{2.42}$$
$$\dot{\theta} = -H(1 - 3w)\theta - \frac{\dot{w}}{1 + w}\theta + \frac{w}{1 + w}k^2\delta - k^2\Theta + k^2\psi \,, \tag{2.43}$$

---

[6]Henceforth, we define $c = 1$ for simplicity and use w.l.o.g. the conformal Newtonian gauge.

where $\Theta \equiv -(k_i k_j/k^2 - 1/3\delta_{ij})(T^i_j - \delta^i_j T^k_k/3)$.

For a pressure-less, cold perfect fluid ($w = \Theta = 0$) such as CDM, the fluid equations simply become

$$\dot{\delta}_c = -\theta_c + 3\dot{\phi}, \quad \dot{\theta}_c = -H\theta_c + k^2\psi , \tag{2.44}$$

since all other terms vanish.

In the case of interactions between two fluids as in the case of baryons with photons before decoupling or dark matter with photons and neutrinos (cf. part III), momentum is transferred between both fluids which thus affects the evolution of θ fro each component by adding an additional "source term" (cf. photon distribution below). For baryons, we thus obtain:

$$\dot{\delta}_b = -\theta_b + 3\dot{\phi}, \quad \dot{\theta}_b = -H\theta_b + c_s^2 k^2 \delta_b + k^2\psi + \dot{\kappa}(\theta_\gamma - \theta_b) . \tag{2.45}$$

For components such as neutrinos or photons, the phase-space distribution $f(x^i, P_j, t)$ is not longer simply approximated by a discrete peak around the averaged local velocity, but is represented by a wide-spread continuum. In this perturbed metric, the 4-momentum becomes up to first order in the perturbations:

$$P^\mu = \left(E(1 - \psi), \vec{p}\,\frac{1 - \phi}{a} \right) , \tag{2.46}$$

where $\vec{q}$ is the physical 3-momentum, $E = \sqrt{m^2 + p^2}$ and where we exploited the constraint that $P^2 = -m^2$. The energy-momentum tensor in this more general case is given by

$$T_{\mu\nu} = \int dP_1 dP_2 dP_3 (-g)^{-\frac{1}{2}} \frac{P_\mu P_\nu}{P^0} f(x^i, P_j, t) . \tag{2.47}$$

Using Eq. 2.46 to expand the total derivative in Eq. 2.27 up to the first order while switching to comoving coordinates $x^i = r^i/a$, comoving momenta $q^i = ap^i$ and conformal time $d\tau = dt/a$, we get

$$\frac{\partial f}{\partial \tau} + \frac{\partial f}{\partial x^i}\frac{dx^i}{d\tau} + \frac{\partial f}{\partial q}\frac{dq}{d\tau} = C[f; \{f_i\}] . \tag{2.48}$$

The term with dependence on the direction of the momentum $\hat{p}^i = p^i/p$ is missing here as it is a second order term in the perturbation.

Using the geodesic equation to expand the time derivative of the momentum

$\partial q / \partial \tau$, Eq. 2.48 yields

$$\frac{\partial f}{\partial \tau} + \frac{q^i}{\varepsilon} \frac{\partial f}{\partial x^i} + q \left(\dot{\phi} - \varepsilon n_i \frac{\partial \psi}{\partial x_i} \right) \frac{\partial f}{\partial q} = C[f; \{f_i\}] , \qquad (2.49)$$

where $\varepsilon \equiv E / a$ is the comoving energy. It is convenient to write the phase-space density in terms of the unperturbed (zero-th order) distribution $f_0(q)$ and a perturbation term $\Psi(x^i, q^i, \tau)$ such that

$$f(x^i, q^i, \tau) = f_0(q) \left[1 + \Psi(x^i, q^i, \tau) \right] . \qquad (2.50)$$

Rewriting Eq. 2.49 this way and Fourier-transforming it to get rid of spatial derivatives, we obtain the following Boltzmann equations in k-space:

$$\frac{\partial \Psi}{\partial \tau} + i \frac{q^i}{\varepsilon} + q \left(\dot{\phi} - \varepsilon (\vec{k} \cdot \vec{n}) \psi \right) \frac{d \ln f_0}{d \ln q} = \frac{1}{f_0} C[f; \{f_i\}] . \qquad (2.51)$$

Take notice that this equation depends on the (normalized) direction of the momentum $\vec{n} = \frac{\vec{q}}{q}$ only through its angle with $\vec{k}$. Thus, assuming that Ψ is initially axially symmetric, this will not change according to Eq. 2.51. Expanding this angular dependence of Ψ in a Legendre series, i.e.

$$\Psi(\vec{k}, \vec{n}, q, \tau) = \sum_{l=0}^{\infty} (2l + 1)(-i)^l \Psi_l(\vec{k}, q, \tau) P_l(\vec{k} \cdot \vec{n}) , \qquad (2.52)$$

Eq. 2.51 yields the following infinite series of coupled first-order differential equations, the so-called *Boltzmann hierarchy*, for the evolution of the coefficients Ψ_l of this expansion:

$$\dot{\Psi}_0 = -\frac{qk}{3\epsilon} \Psi_1 + \dot{\phi} \frac{d \ln f_0}{d \ln q} + \left(\frac{f}{f_0} \right)_{C,0} , \qquad (2.53)$$

$$\dot{\Psi}_1 = \frac{qk}{3\epsilon} \left(\Psi_0 - \frac{2}{5} \Psi_2 \right) - \frac{\epsilon k}{q} \psi \frac{d \ln f_0}{d \ln q} + \left(\frac{f}{f_0} \right)_{C,1} , \qquad (2.54)$$

$$\dot{\Psi}_l = \frac{qk}{3\epsilon} \left(\frac{l}{2l-1} \Psi_{l-1} - \frac{l+1}{2l+3} \Psi_{l+1} \right) + \left(\frac{f}{f_0} \right)_{C,l} , \quad l \geq 2 , \qquad (2.55)$$

where $(\frac{f}{f_0})_{C,l}$ are the coefficients of the expansion of the interaction term on the RHS of Eq. 2.51.

The perturbed energy density, $\delta \rho$, pressure, p, velocity dispersion, θ, and shear stress, Θ can be written in this expansion. Due to the symmetry of the terms in the

Legendre series, this yields

$$\delta\rho = 4\pi a^{-4} \int q^2 dq \epsilon f_0(q)\Psi_0 , \tag{2.56}$$

$$\delta p = \frac{4\pi}{3} a^{-4} \int q^2 dq \frac{q^2}{\epsilon} f_0(q)\Psi_0 , \tag{2.57}$$

$$\delta\theta = \frac{4\pi}{3(\bar{\rho}+\bar{p})} k a^{-4} \int q^2 dq q f_0(q)\Psi_1 , \tag{2.58}$$

$$\delta\Theta = \frac{8\pi}{15(\bar{\rho}+\bar{p})} a^{-4} \int q^2 dq \frac{q^2}{\epsilon} f_0(q)\Psi_2 , \tag{2.59}$$

$$\tag{2.60}$$

In the massless limit as for e.g. photons with $\epsilon = q$, we can then derive the conservation equations for δ_γ and θ_γ by taking the time derivative of Eqs. 2.56-2.59 and combining the results with Eqs. 2.53-2.55:

$$\dot{\delta}_\gamma = -\frac{4}{3}\theta_\gamma + 4\dot{\phi} , \tag{2.61}$$

$$\dot{\theta}_\gamma = k^2\left(\frac{1}{4}\delta_\gamma - \Theta_\gamma\right) + k^2\psi + \dot{\theta}(b \leftrightarrow \gamma) , \tag{2.62}$$

$$\tag{2.63}$$

where $\dot{\theta}(b \leftrightarrow \gamma) = \dot{\kappa}(\theta_b - \theta_\gamma)$ is the momentum transfer between photons and baryons due to Thomson scattering. The direction-independent zero-th momentum of the interaction term vanishes here and $\dot{\kappa} \sim n_e\sigma_{Th}$ is the interaction rate between photons and baryons.

2.2.7 Observations / Tests for γCDM

There are multiple windows into the past to test the validity of ΛCDM.

Cosmic Background While there is no direct observation of the postulated singularity i.e. the hot "Big Bang" at the beginning of the Universe, the existence of the CMB with its black body spectrum is evidence that the universe started in such a hot, dense state. The analysis of the primordial perturbation imprinted in the CMB as shown in the angular temperature power spectrum in the top panel of Fig. 2.7 are very accurately predicted by the ΛCDM model once the free parameters are fitted to the observations. The observed relative amplitude and position of the peaks in the spectrum tell us about the composition of the Universe (e.g. CDM/baryon

ratio), expansion rate and curvature of the Universe at around the time of recombination (Ade et al., 2014) among other parameters in the model.

Element abundance The measurement of the abundance of the light "elements" deuterium, helium-3, helium-4, and lithium-7, regions of the Universe where stellar nucleosynthesis, i.e. production of these elements in the fusion process in stars, is limited not only provides another evidence of a very early hot state of an expanding Universe where BBN could take place, but also gives us for each element a measurement of the baryon-to-photon ratio at that time. The results for ^3He and ^4He seem to be in good agreement with an independent measurement of that ratio using the CMB, while there is a discrepancy for the lithium-7 results, which has yet to be explained if the standard model is correct (Coc et al., 2004).

Structure formation Finally, the observable structures that formed in the late Universe provide us with very powerful tests of ΛCDM and its parameters. First of all, galaxies serve us as (biased) tracers of the large-scale structures in the Universe, i.e. the linear perturbations described in Sec. 2.2.6 and the weakly non-linear regime where the smaller perturbations have "condensed" into the filaments, walls and galaxy cluster halos that form the "so-called" cosmic web. The lower panel in Fig. 2.7 shows a comparison between the matter power spectrum of the LSS as obtained by the 2dF galaxy survey and the predictions for ΛCDM. The observed redshift position of the galaxies in such surveys does not only contain the information about the spatial distribution, but as well about the dynamics, i.e. local gravitational flows and the Hubble flow. Thus, it is very sensitive not only to the composition of the Universe, but also to the evolution thereof to test whether dark energy is more complex than just a cosmological constant. Additionally, the *baryonic acoustic oscillations* (BAO) that have been imprinted into the matter distribution from the time before decoupling can be observed on the largest scales of the galaxy distribution in surveys (Cole et al., 2005) and serve as a ruler to measure the expansion of the Universe, i.e. the Hubble parameter in the ΛCDM framework, as well as to test alternative models for dark energy (Shi et al., 2011). On the smaller galactic and sub-galactic scales, we have the observations of the abundance, distribution and properties of nearby galaxies such as the Milky Way and Andromeda and their satellite galaxies as well as the distribution of interstellar gas, that leaves an absorption spectrum imprinted on the emitted light of distant quasars dubbed the "Lyman-α forest (Gunn and Peterson, 1965; Lynds, 1971). These are the scales that
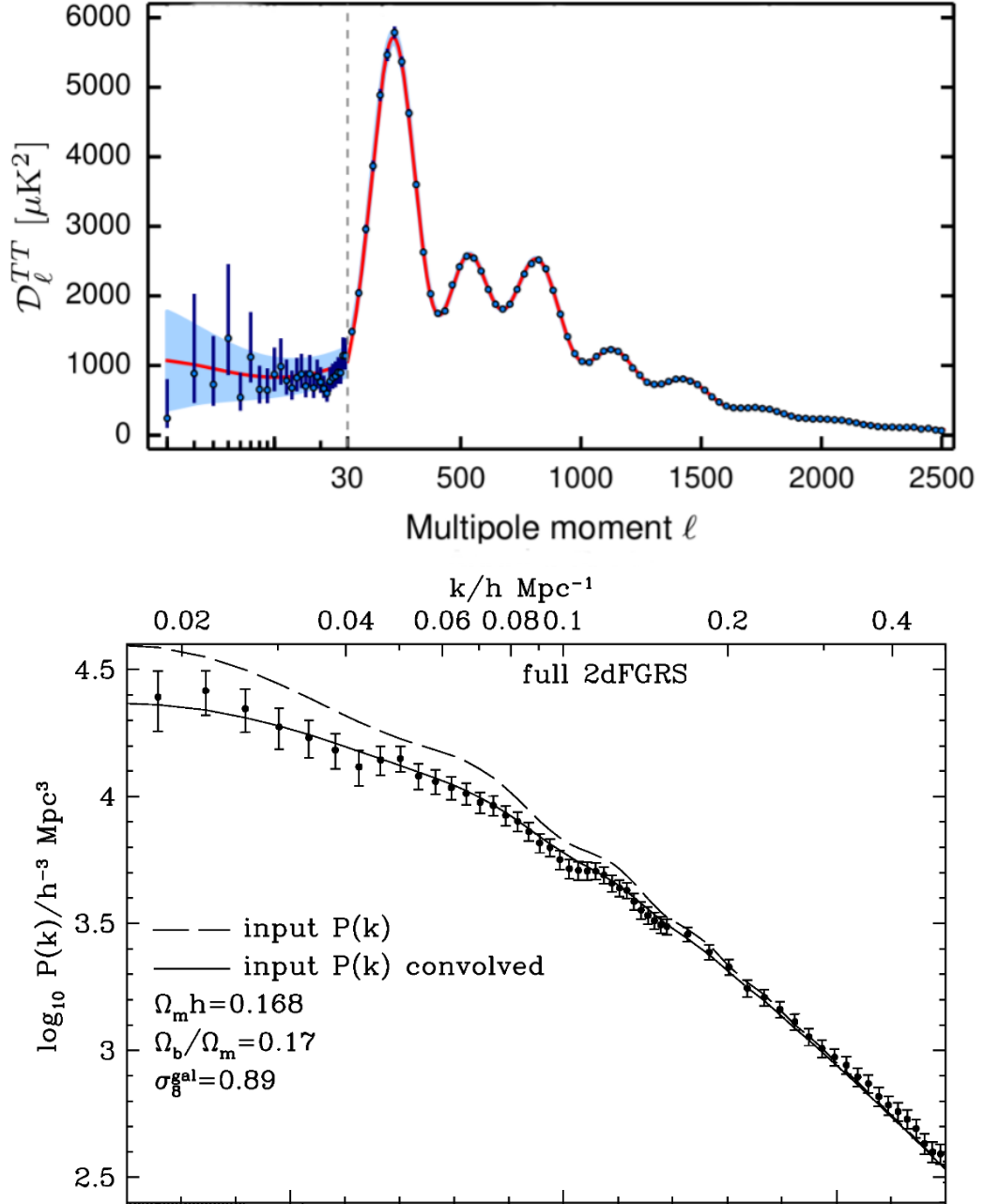
FIGURE 2.7: Tests of ΛCDM: (Top) CMB TT angular power spectrum as observed by Planck and predicted by ΛCDM with fitted parameters (Planck Collaboration et al., 2015b). The blue dots correspond to measurements made with Planck and their error bars account for measurement errors as well as for an estimate of the uncertainty due to cosmic variance. The red solid line represents the best fit of the SMoC while the blue-shaded area around it shows the predictions of all the variations of the standard model that best agree with the data; (Bottom) Redshift-space) galaxy power spectrum from the completed 2dF redshift survey (Cole et al., 2005). The dashed line refers to the input power spectrum for a dark matter model with the listed parameters while the solid line refers to the same prediction convolved with the window function of the survey catalogue.

are most affected by the nature of neutrinos and DM and not only enable us to determine parameters such as the neutrino mass (cf. Part IV), but also provide us with potential evidence that the assumption in ΛCDM that DM is a cold collision-less fluid may be flawed (cf. Part III).
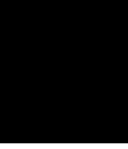
DARK MATTER

INTERACTIONS

CHAPTER 3

Linear Theory / Background

Dark matter (DM) is the most dominant and yet most elusive component of matter in the Universe. Exploring its nature is therefore one of the greatest challenges in both cosmology and particle physics today. The usual treatment of DM in structure formation calculations neglects possible interactions between DM and other species. Yet if DM is a (thermal) weakly interacting massive particle (WIMP), interactions (and more precisely, annihilations) are essential to obtain the correct relic density. It is therefore important to study the impact of DM interactions on other cosmological observables.

3.1 Motivation - WIMP miracle & candidates

One important motivation to consider DM interaction with other particles in the SM is to explain the observed relic abundance $\Omega_{\mathrm{dm}}h^2 = 0.1199$ (Planck Collaboration et al., 2015d) today. Assuming such interactions, dark matter was in full thermal equilibrium with SM particles at sufficiently high temperature T. Thus, the number density of the still relativistic DM particles would be equal to the other relativistic components. Once the temperature fell below the DM particle mass, DM particles became non-relativistic and their number density started dropping exponentially $n_{\mathrm{dm}} \sim \exp(-m_{\mathrm{dm}}/T)$ as they annihilate. Within the standard model of Cosmology, this second stage continued until the increasing Hubble expansion rate $H = \dot{a}/a \sim T^2/M_{\mathrm{Planck}}$ during the radiation-dominated Universe surpassed the two-body interaction rate Γ_{dm} between DM particles that is responsible for their annihilation at temperature T_F

$$\Gamma_{\mathrm{dm}} = \frac{\mathrm{d}n_{\mathrm{dm}}}{\mathrm{d}t} = n_{\mathrm{dm}}\langle\sigma_{\mathrm{dm}\to\mathrm{SM}}v_{dm}\rangle\,, \qquad (3.1)$$

where n_{dm} is the number density of DM particles, $\sigma_{\mathrm{dm}\to\mathrm{SM}}$ is the DM-SM interaction cross-section and v_{dm} the velocity dispersion within the DM particles in their

rest frame. At this point in time, DM decoupled thermally from the SM particles and the annihilation stopped. After that, the decrease in the DM density was only driven by the expansion of the Universe that dilutes all the content and scales for any non-relativistic component as T^{-3}. Assuming that the interaction cross-section is velocity-independent, i.e. $\langle \sigma_{dm \to SM} v_{dm} \rangle$ is constant, and that dark matter decoupled while already being non-relativistic, we can determine this freeze-out temperature T_F and with it the cross-section needed to obtain the observed DM energy density. Using the relations stated above, this is given in good approximation by:

$$\langle \sigma_{dm \to SM} v_{dm} \rangle \simeq \frac{10^{-37} cm^2 \cdot c}{\Omega_{dm} h^2} \simeq 2.5 \cdot 10^{-26} \frac{cm^3}{s} \ . \tag{3.2}$$

This is surprisingly close to interaction cross-section expected from interaction via the weak force in the SM, thus coining the name "WIMP miracle". In this sense, if speaking of "weak interactions" or "weakly-interacting" from here-on in this thesis, we do not refer exclusively to weak-force interactions, but interactions that are somewhat similar in strength to the weak force and far below stronger scales such that of the EM force.

It should be noticed that there are various ways beyond the SM to influence the abundance of DM such as an altered expansion rate around freeze-out or additional non-thermal production after decoupling . Thus, the measurement of the cross-section by other, independent means such as by direct (Marrodán Undagoitia and Rauch, 2016) or indirect detection (Conrad, 2014) experiments would allow to probe the very early Universe for such BSM physics.

Common BSM theories provide a variety of "weakly-interacting" candidates:

Supersymmetry (SUSY) - In the minimal SUSY SM (MSSM), the conservation of *R-parity* implies, that the lightest supersymmetric particle has to be stable and thus qualifies as a candidate for dark matter. Considering that the DM particles also have to be electrically neutral to be "dark", possible MSSM candidates are e.g. the neutralino and sneutrino, which both have electroweak scale interactions (Chung et al., 2005).

Kaluza-Klein (KK) - The compactified extra-dimension(s) in the 5D *minimal Universal extra dimension* (mUED) model of the KK theory, a massless 5D scalar leads to a "tower" of massive vector fields ("modes") in the effective 4D space-time we observe. The first excitation mode of the gauge field that is equivalent to the photon is the lightest KK-particle (LKP). It is stable under

KK − parity and serves as a DM candidate (Servant and Tait, 2003).

Little Higgs - In the *Little Higgs* models, the SM is extended by two additional symmetries - a global one that is broken at the TeV scale, for which the Higgs plays the role as a pseudo-Goldstone boson, and a second, discrete $\mathbb{Z}^2$ symmetry known as *T-parity*, which results in the context of the *littlest Higgs Model with T-parity* (Hubisz and Meade, 2005) in four additional gauge bosons , of which the "heavy photon" B_H is stable, neutral and considered a DM candidate.

In our work, we do not pick a specific model, but simply work within an effective theory. Hence, we assume the existence of an effective interaction term between some unspecified, otherwise sterile DM particles and our SM particle of choice, photons and neutrinos in the Lagrangian. Depending on the actual type-/mass of the mediator in our "black-box", this can lead to a momentum/velocity-dependence of our effective cross-sections, but as in the discussion about the WIMP miracle, we mainly focus in the following on velocity-independent scenarios.

3.2   Modified Boltzmann equations

In order to study the evolution of the different components that make up the content of the Universe, one has to solve the Boltzmann equations for each of those phase-space fluids. When switching from Lagrangian framework which follows the fluids on their characteristics to the Eulerian fixed in space, we integrate out the velocity space after multiplying with the momentum, expand to the linear order in the density perturbations δ, ignore the diffusive terms and thus obtain the following linearised Euler equations in Fourier space (cf. Sec. 2.2.6):

$$\dot{\theta}_b = k^2\psi - \mathcal{H}\theta_b + c_s^2 k^2 \delta_b - R^{-1}\dot{\kappa}\left(\theta_b - \theta_\gamma\right) , \tag{3.3}$$

$$\dot{\theta}_\gamma = k^2\psi + \left(\frac{1}{4}\delta_\gamma - \sigma_\gamma\right)k^2\delta_b - \dot{\kappa}\left(\theta_\gamma - \theta_b\right) - C_{\gamma-\mathrm{dm}} , \tag{3.4}$$

$$\dot{\theta}_{\mathrm{dm}} = k^2\psi - \mathcal{H}\theta_{\mathrm{dm}} - C_{\mathrm{dm}-\gamma} , \tag{3.5}$$

where ψ is the gravitational potential, $\mathcal{H}$ is the conformal Hubble rate and θ and σ are the velocity divergence and anisotropic stress potential associated with the respective baryon, photon and DM fluid. For the EM interactions in the SM, the first two equations include the terms with $\dot{\kappa} \equiv a\sigma_{\mathrm{Th}}cn_e$ being the Thomson scattering

rate with respect to conformal time and $R \equiv (3/4)(\rho_b/\rho_\gamma)$ is a pre-factor to ensure momentum conservation. $C_{\mathrm{dm}-\gamma}$ and $C_{\gamma-\mathrm{dm}} = -S^{-1}C_{\mathrm{dm}-\gamma}$ are the new interactions term that have to be added to include interactions between dark matter and the cosmic photon background. Analogous to the EM interaction,

$$C_{\mathrm{dm}-\gamma} = \dot{\mu}\left(\theta_{\mathrm{dm}} - \theta_\gamma\right) \tag{3.6}$$

depends on the new interaction rate $\dot{\mu} \equiv a\sigma_{\mathrm{dm}-\gamma}cn_{\mathrm{dm}}$, where $\sigma_{\mathrm{dm}-\gamma}$ is the elastic scattering cross-section between dark matter and photons, and $S \equiv (3/4)(\rho_{\mathrm{dm}}/\rho_\gamma)$ as the scaling of the counter term in the momentum transfer. For the DM-neutrino interactions that are discussed in this thesis as well, similar modifications can be added to the Euler equations to include these interactions as well.

These kind of interaction models have been previously extensively studied by Boehm et al. (2001a) and subsequent papers. Recently, Wilkinson et al. (2014a) presented an implementation of these modified Euler equation for the CLASS Boltzmann solver, which was then used to constrain the allowed cross-sections in such models using the most recent CMB measurements (cf. Sec. 3.3.1).

3.3 Linear solutions for γ/νCDM

Among all the possible contributions to the collisional damping of DM fluctuations, the largest occurs when DM interacts with photons (γCDM) or neutrinos (νCDM). There are two reasons for this: (i) photons and neutrinos have the largest energy density of any standard model particle until matter-radiation equality, (ii) they are relativistic and therefore tend to drag DM particles out of small mass overdensities if they are coupled to DM. The damping scale becomes in that case even for smallest cross-sections significantly large (cf. Eq.3.11).

Photons and neutrinos do not have exactly the same effect on DM fluctuations due to their different thermal histories, with photons staying coupled to the thermal bath for much longer due to Thomson scattering. Additionally, for large cross-section we may encounter the effect of mixed damping when neutrinos have been already decoupled from the rest of the SM sector and stream freely, while DM remains still coupled to them (Boehm et al., 2001a). Hence, their effect on the matter power spectrum is also different, as illustrated in Fig. 3.1, where we show the linear theory matter power spectra for collision- less CDM, γCDM, νCDM and for the alternative (collision-less) WDM model, which we will include in this discussion

for comparison.
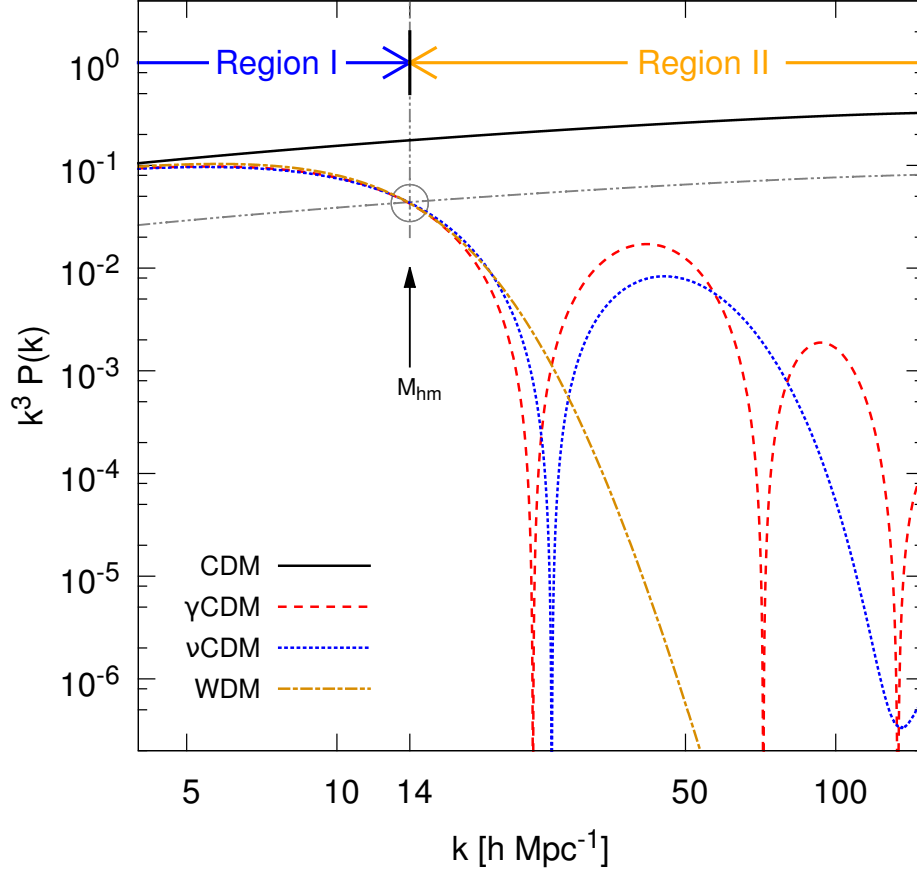
FIGURE 3.1: The linear matter power spectra for collision-less CDM (solid, black), γCDM (dashed, red), νCDM (dotted, blue) and WDM (dashed-dotted, orange) at redshift $z = 49$. The interaction cross-sections for γCDM and νCDM and the particle mass for WDM have been selected such that the initial suppression with respect to CDM is identical (see Table 4.1). The characteristic length scale, at which the power spectra of all the alternative DM models drop below 1/4 of the CDM spectrum (represented by horizontal dash-dotted line), is called the *half-mode* mass, M_{hm}, is marked by an arrow and separates regions I and II, which are discussed with reference to Fig. 3.2.

In the case of a thermalized, non-interacting, fermionic WDM particle, the suppression in the matter power spectrum is typically approximated by the transfer function (Bode et al. 2001)

$$T(k) = \left[1 + (\alpha k)^{2\mu}\right]^{-5/\mu} , \qquad (3.7)$$

where

$$\alpha = 0.048 \left[\frac{m_{DM}}{keV}\right]^{-1.15} \left[\frac{\Omega_{DM}}{0.4}\right]^{0.15} \left[\frac{h}{0.65}\right]^{1.3} \frac{Mpc}{h} . \qquad (3.8)$$

Here, Ω_{DM} is the DM energy density, h is the reduced Hubble parameter and $\mu \simeq$ 1.2 is a fitting parameter[7]. The scale α in Eq. 3.8 encapsulates the effect of free-streaming, which erases primordial fluctuations below a wavelength given by

$$\lambda_{\mathrm{fs}} = \int_{t_{\mathrm{dec}}}^{t_0} \frac{v(t)}{a(t)} \mathrm{d}t \; \approx \; r_{\mathrm{H}}(t_{\mathrm{NR}}) \left[1 + \frac{1}{2} \log\left(\frac{t_{\mathrm{EQ}}}{t_{\mathrm{NR}}} \right) \right] , \qquad (3.9)$$

where $v(t)$ is the thermal velocity of the WDM particle. In this expression, t_{dec} is the DM decoupling time, t_0 is the time today, $a(t)$ is the cosmological scale factor, $r_{\mathrm{H}}(t_{\mathrm{NR}})$ is the comoving size of the horizon when DM becomes non-relativistic (at time t_{NR}) and t_{EQ} is the epoch of matter-radiation equality.

A similar transfer function can be used to model the cut-off in the matter power spectra in γCDM and νCDM (Boehm et al. 2002) with

$$\tilde{\alpha} = \beta_X \left[\frac{\sigma_{\mathrm{DM}-X}}{\sigma_{\mathrm{Th}}} \frac{m_{\mathrm{DM}}}{\mathrm{GeV}} \right]^{0.48} \left[\frac{\Omega_{\mathrm{DM}}}{0.4} \right]^{0.15} \left[\frac{h}{0.65} \right]^{1.3} \frac{\mathrm{Mpc}}{h} , \qquad (3.10)$$

where X is γ or ν, $\beta_\gamma \approx 1.25 \times 10^4$, $\beta_\nu \approx 1.04 \times 10^4$, $\sigma_{\mathrm{DM}-X}$ is the DM–radiation cross-section and σ_{Th} is the Thomson cross-section. This transfer function fixes the half-mode scale for γCDM and νCDM, thus providing a means to compare the impact of the interactions with respect to WDM, but does not encapsulate the full suppression of the power spectrum.

Eq. 3.10 corresponds to an analytical calculation of the collisional damping scale given by[8]

$$\lambda_{\mathrm{cd}}^2 = \frac{2\pi^2}{3} \int_0^{t_{\mathrm{dec}}} \frac{\rho_X}{\wp} \frac{v_X^2 \, (1+\Theta_X)}{a^2 \, \Gamma_X} \, \mathrm{d}t . \qquad (3.11)$$

In this equation, $\wp = \rho_X + p_X$, where ρ_X is the energy density, p_X the pressure, v_X is the velocity dispersion and Γ_X is the total interaction rate of the DM interaction partner and Θ_X contains the contribution from heat conduction.

As the integral in Eq. (3.11) is dominated by the contribution at late times, the collisional damping scale can be approximated by

$$\lambda_{\mathrm{cd}}^2 \approx \frac{2\pi^2}{3} \left[\frac{\rho_X}{\wp} \frac{v_X^2 \, (1+\Theta_X)}{a^2} \frac{t^2}{\alpha_X} \right] \Bigg|_{t_{\mathrm{dec}}} , \qquad (3.12)$$

---

[7]There is an alternative fit for α and μ that is often used in the literature (e.g. Viel et al. 2005), but the difference is marginal for our analysis.

[8]We neglect the possible contributions from self-interactions and *mixed* damping and simplify the calculation to a single DM interaction partner.

using $\Gamma_X = H = \alpha_X/t$ at $t = t_{\text{dec}}$, where H is the Hubble rate, $\alpha_X = 1/2$ if $t_{\text{dec}} < t_{\text{EQ}}$ and $\alpha_X = 2/3$ otherwise. On scales smaller than λ_{cd}, primordial fluctuations are erased.

We summarise the impact of the damping scales λ_{fs} and λ_{cd} in linear theory in Fig. 3.2. To distinguish these quantities from the half-mode mass scale, M_{hm}, we present the mass corresponding to the relevant damping scale as a function of the DM mass (for WDM) and interaction cross-section (for γCDM and νCDM).
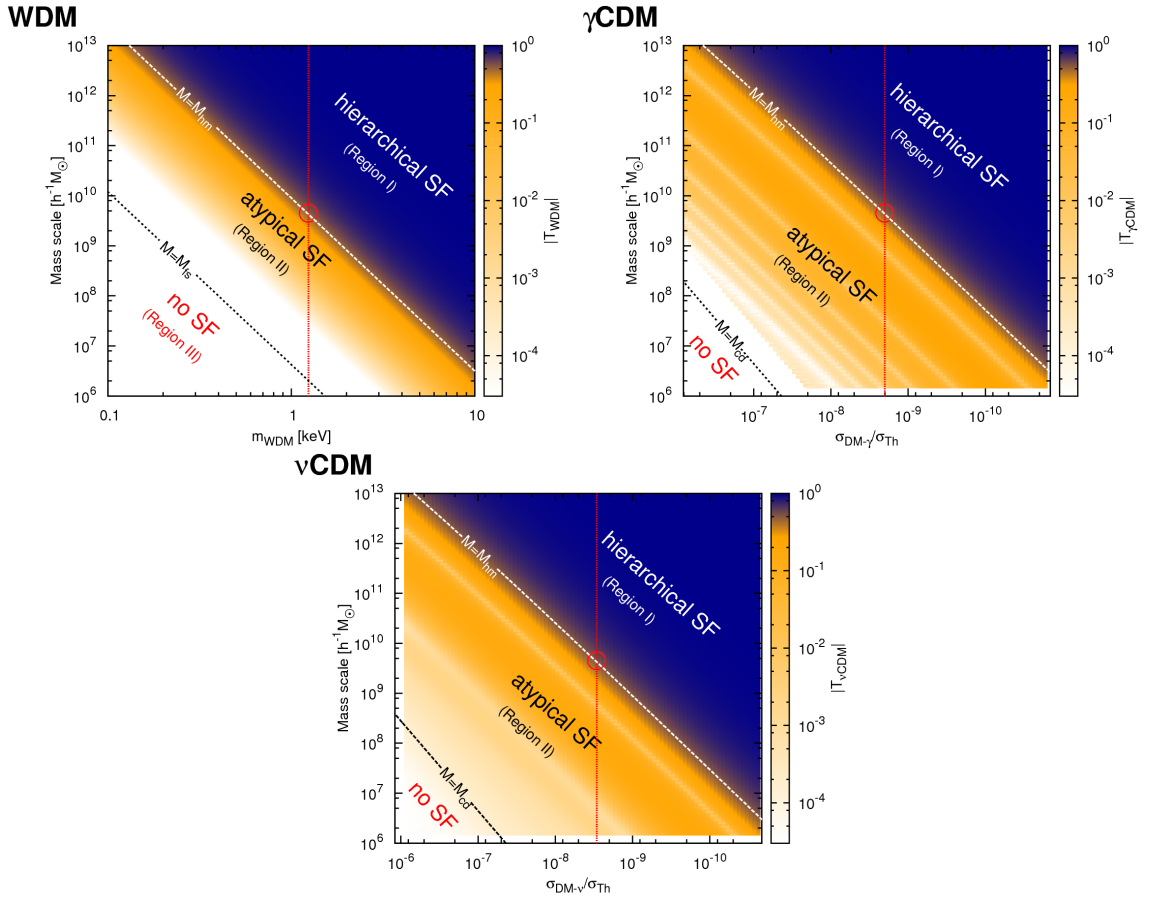
FIGURE 3.2: Characteristic mass scales for the suppression of primordial fluctuations by free-streaming (WDM, top), photon collisional damping (γCDM, middle) and neutrino collisional damping (νCDM, bottom). The half-mode mass scale, M_{hm}, is defined by the initial cut-off in the transfer function and marks the upper boundary of region II, where hierarchical structure formation (SF) may no longer occur due to a reduced number of low-mass progenitors. M_{fs} and M_{cd} are the masses corresponding to the free-streaming and collisional damping scales respectively and define the boundary of region III, where structures no longer form. The colour scale shows the absolute value of the transfer function, $T(k)$, and the vertical red lines correspond to the DM parameters listed in Table 4.1.

We identify three regions in Fig. 3.2. Regions I and II are already labelled in Fig. 3.1 and there is now an additional region (III) occurring at much higher wavenum-

bers than are plotted in this figure. In region I, haloes form hierarchically, while in region III, all primordial perturbations have been erased. In between lies a transition region (region II), where some primordial density fluctuations may survive to form structure, but these are already sufficiently suppressed to disfavour a typical hierarchical structure formation. Region II extends down to much smaller scales for γCDM and νCDM compared to WDM due to the prominent oscillations in the matter power spectrum[9]. The separation between regions I and II is determined by the half-mode mass scale (as in Fig. 3.1), while the transition between regions II and III is governed by the free-streaming scale (for WDM) or collisional damping scale (for γCDM and νCDM).

3.3.1   Constraints from CMB

For large values of the DM–radiation scattering cross-section, the suppression is prominent in both the CMB temperature and polarization power spectra. A comparison between the predicted spectra and the first-year data from *Planck* (Ade et al. 2014) using a *Monte Carlo-Markov Chain* (MCMC) technique gives upper bounds of 8×10^{-31} (m_{DM}/GeV) cm^2 and 2×10^{-28} (m_{DM}/GeV) cm^2 on the γCDM and νCDM cross-sections respectively, where m_{DM} is the DM particle mass (at 68% CL, assuming a constant cross-section) (Wilkinson et al. 2014a,b). As mentioned in the previous section, the linear prediction for the matter distribution slightly differ for neutrinos and photons interactions. In addition, γCDM has a direct impact on the CMB, while νCDM only affects the CMB indirectly, and the parameter space for νCDM suffers from significant degeneracies (see Wilkinson et al. 2014b). This is the reason why the constraints differ for γCDM and νCDM.

3.3.2   Cosmological parameters

A final topic to discuss in this chapter is the choice of the cosmological parameters for these extended models. Recent studies hinted that γ/νDM favour slightly higher values for H_0 for cross-section that are still allowed by the CMB constraints (Wilkinson et al., 2014b). This may ease the tension between the Planck measurements and other results from other probes (Ade et al., 2014), but would

---

[9]We note that oscillations are also expected in the transfer functions for certain WDM models at small scales (see e.g. Boyanovsky and Wu 2011). However, at these scales, the transfer function is already strongly suppressed by free-streaming so the regeneration of power from these oscillations is expected to be much weaker than in γCDM and νCDM.

also potentially force us to adapt our cosmological parameters to the interaction cross-section we want to study. As we have shown in Boehm et al. (2014) (cf. Ch. 5), these cross-sections are orders of magnitude smaller than those considered in Wilkinson et al. (2014b). In order to check whether the choice of the cross-section
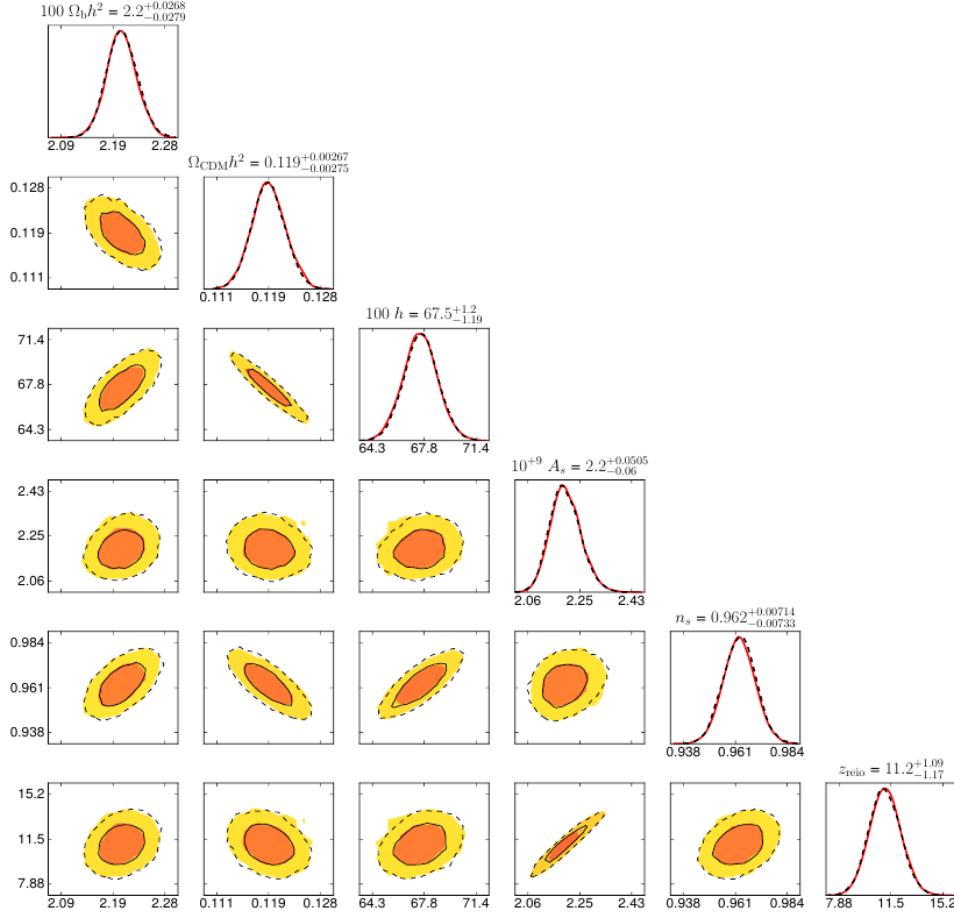
FIGURE 3.3: Triangle plot for a fit of the free cosmological parameters in the γCDM model with fixed interaction cross-section $\sigma_{DM-fl} = 2 \times 10^{-9} \, \sigma_{Th} \, (m_{DM}/GeV)$ against the 1-year Planck CMB data. The coloured regions are the 68% and 95% confidence regions for the fit while the dashed line mark the equivalent regions for a similar fit for the vanilla CDM model.

affects the choice of the cosmological parameters to be consistent with the CMB, we performed MCMC runs for our γCDM model with the interaction cross-section fixed to $\sigma_{DM-fl} = 2 \times 10^{-9} \, \sigma_{Th} \, (m_{DM}/GeV)$ against the 1-year Planck data. The triangle plot in Fig. 3.3 shows the resulting coloured 1σ and 2σ confidence regions for the remaining free parameters. The dashed lines represent the same regions for a vanilla CDM model. So, while there may exists a degeneracy between the interaction cross-section and H_0 that becomes significant for larger cross-sections, the best-fits for all the cosmological parameters of our underlying ΛCDM model are

not significantly affected for the cross-sections used in our studies. This allows us to keep them fixed to their SM best-fit values throughout our work.

DM–ν/γ interactions & Large-scale structures

This chapter follows closely Schewtschenko et al. (2015b) and deals with interactions of photons and neutrinos with a WIMP-like DM candidate and explores the implications on the formation of non-linear cosmic structures studying the DM distribution and galaxy halo properties. We also show that semi-analytical descriptions of the matter distribution in the non-linear regime fail to reproduce our numerical results, emphasizing the challenge of predicting structure formation in models with physics beyond collision-less DM.

Unless explicitly stated otherwise, the values we use throughout this chapter for the γCDM and νCDM cross-sections and the WDM mass are given in Table 4.1. These parameters are motivated by the constraints we will obtain in the following chapter following our previous work (Boehm et al. 2014) and have been selected such that the scale at which the transfer function is suppressed by a factor of two with respect to CDM (hence giving a factor of four reduction in power) is identical. This scale defines the *half-mode* mass, M_{hm}, and marks the threshold between regions I and II in Fig. 3.1. It is in region II, where the power spectra for γCDM, νCDM and WDM differ significantly from each other which effects we discuss in this chapters.

4.1 Simulations

To calculate the non-linear evolution of the matter distribution, we run a suite of high-resolution N-body simulations using the parallel Tree-Particle Mesh code, `GADGET-3` (Springel 2005). To model a wide dynamical range, we perform simulations in large boxes (of side lengths 100 h^{-1} Mpc and 300 h^{-1} Mpc) and a small box (of side length 30 h^{-1} Mpc), all containing 1024^3 particles.

The simulations begin at a redshift of $z = 49$ (the DM–radiation interaction rate is negligible for $z < 49$) and use a gravitational softening of 5% of the mean particle separation. The initial conditions are created with an adapted version of a

	$(m_{\mathrm{DM}}/\mathrm{GeV})$ $\times \sigma_{\mathrm{Th}}$	$(m_{\mathrm{DM}}/\mathrm{GeV})$ $\times \mathrm{cm}^2$	$(m_{\mathrm{DM}}/\mathrm{g})$ $\times \mathrm{cm}^2$
γCDM	2.0×10^{-9}	1.3×10^{-33}	7.5×10^{-10}
νCDM	2.9×10^{-9}	1.9×10^{-33}	1.1×10^{-9}

	m_{DM} [keV]	α $[h^{-1}\,\mathrm{Mpc}]$
WDM	1.2	0.037

TABLE 4.1: The (constant) elastic scattering cross-sections for γCDM and νCDM and the particle mass for WDM, expressed in various units. σ_{Th} is the Thomson cross-section, m_{DM} is the DM mass and α is defined in Eq. (3.8). Note that the mass of the WDM particle is motivated by the reproduction of the half-mode mass in the γCDM and νCDM models, as explained in the text.

second-order LPT code (Crocce et al. 2012), using input matter power spectra from a modified version of the Boltzmann code, CLASS (Lesgourgues 2011).

We use the best-fitting values of the cosmological parameters obtained by the *Planck* collaboration in the "*Planck* + WP" dataset (Ade et al. 2014), assuming a flat ΛCDM cosmology. In principle, a consistent treatment of an interacting DM model would require one to study each cross-section within its own best-fitting cosmology. However, we find that the parameters for ΛCDM lie within one standard deviation of such best fits. Therefore, we keep the cosmological parameters fixed for all the models studied here.

Lovell et al. (2014) showed that in the case of WDM, one can safely ignore thermal velocities, without introducing a significant error on the scales of interest, if the DM particle is heavier than ~ 1 keV. We confirmed this by performing simulations with and without a thermal velocity dispersion and obtaining convergence on the scales of interest. Hence, we only consider models in which late-time free-streaming can be neglected.

Fig. 4.1 shows the projected DM distribution in the 30 h^{-1} Mpc box for (i) collision-less CDM and (ii) an extreme γCDM model that is allowed by *Planck* CMB data (Wilkinson et al. 2014a). Fewer small structures are present in γCDM as an immediate result of the suppression of small-scale power shown in Fig. 3.1. The only exception is found along the filaments, where spurious structures contaminate the otherwise smooth environment (Wang and White 2007). Similar results are obtained for νCDM and WDM. For abundance measurements (Sec. 4.2), DM haloes are identified using a *friends-of-friends* group finder (Davis et al. 1985) with a linking length of 20% of the mean particle separation. For the halo properties (Sec.
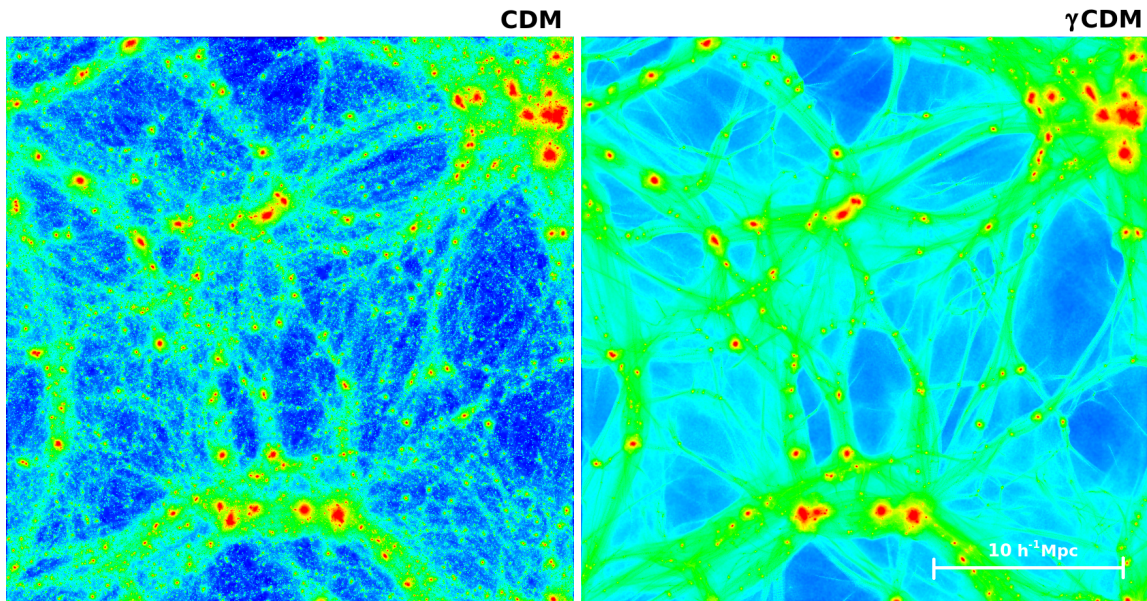
FIGURE 4.1: The simulated distribution of DM at redshift $z = 0$ in a box of side length 30 h^{-1} Mpc for two models: collision-less CDM (left) and γCDM with $\sigma_{\mathrm{DM}-\gamma} = 10^{-7}\,\sigma_{\mathrm{Th}}\,(m_{\mathrm{DM}}/\mathrm{GeV})$ (right), which is allowed by *Planck* CMB data (Wilkinson et al. 2014a). The colours indicate the DM density on a scale increasing from blue to red. Due to collisional damping, we obtain fewer small-scale structures in γCDM than are seen in CDM.

4.3), we instead use the *AMIGA halo finder* (Knollmann and Knebe 2009), where collapsed structures are defined as spherically overdense regions of radius r_{vir} with a mean density given by

$$\frac{3M_{\mathrm{vir}}}{4\pi r_{\mathrm{vir}}^3} = \Delta_{\mathrm{th}}\rho_{\mathrm{crit}} \,. \tag{4.1}$$

In this expression, M_{vir} is the virial mass, ρ_{crit} is the critical density and Δ_{th} is the mean overdensity of a virialized halo with respect to the critical density, according to the spherical top-hat collapse model.

4.2 Halo Abundance

The suppression of small-scale density fluctuations in the early Universe (cf. Sec. 3) has a significant effect on the subsequent structure formation. This has been studied in detail for WDM (e.g. Lovell et al. 2014), where the halo mass function (HMF) was compared to semi-analytical predictions. In this section, we perform a similar analysis for γCDM and νCDM by comparing the simulated HMFs with the *Press-Schechter* formalism (Press and Schechter 1974) and modifications thereof. In

addition, we study the spatial distribution of DM haloes on large scales.

4.2.1 Semi-Analytical Halo Mass Functions

The *Press-Schechter* formalism uses the known primordial perturbations and their linear growth to calculate the fractional volume of space occupied by virialized objects of a given mass, assuming a spherical collapse model (Press and Schechter 1974). The halo mass function (HMF) can be written as

$$\frac{\mathrm{d}n(M)}{\mathrm{d}M} = -\frac{1}{2} f^{(\mathrm{HMF})}(\sigma^2) \frac{\bar{\rho}}{M^2} \frac{\mathrm{d}\ln\sigma^2(M)}{\mathrm{d}\ln M} , \qquad (4.2)$$

where $n(M)$ is the number density of DM haloes of mass $M \to M + \mathrm{d}M$, $\bar{\rho}$ is the average matter density of the Universe and $\sigma^2(M)$ is the variance of the linear density field given by

$$\sigma^2(M) = \frac{1}{2\pi^2} \int_0^\infty k^2 P(k) \hat{W}^2(k, R) \, \mathrm{d}k . \qquad (4.3)$$

The variance is smoothed on a mass-dependent scale $R(M)$, using a suitable window function $W(r, R)$, which has a Fourier transform $\hat{W}(k, R)$ (Jenkins et al. 2001).

The *Sheth-Tormen* (ST) formalism (Sheth et al. 2001) combines the Press-Schechter formalism with an ellipsoidal collapse model. In this model, the function $f^{(\mathrm{HMF})}(\sigma^2)$ in Eq. 4.2 represents the fraction of collapsed haloes and is defined by

$$f_{\mathrm{ST}}^{(\mathrm{HMF})}(\sigma^2) = A\sqrt{\frac{2}{\pi}} \left[1 + x^{-2p}\right] x \exp\left[-x^2/2\right] . \qquad (4.4)$$

In this expression, $x \equiv \sqrt{a}\delta_c/\sigma$, where δ_c is the cosmology-dependent linear over-density at the time of collapse. The parameters $A \approx 0.3222$, $p \approx 0.3$ and $a \approx 0.707$ were obtained by fitting to simulation results (Sheth et al., 2001).

The window function, $W(r, R)$, is in general, arbitrary. However, certain choices of window function are advantageous as they allow for both a sensible definition of the smoothed density field and an semi-analytical solution for the Fourier transform. A real-space top-hat, $W(r, R) = \Theta(1 - |r/R|)$, has the advantage of a well-defined smoothing scale, R, defined in terms of the halo mass, $M(R)$, as

$$R = \left(\frac{3M}{4\pi\bar{\rho}}\right)^{1/3} . \qquad (4.5)$$

However, recent papers (Schneider et al. 2013; Benson et al. 2013) have shown that this choice does not reproduce the HMF for cosmologies with a cut-off in the matter power spectrum at small scales. Instead, the predicted HMF continues to increase with decreasing M, while the suppression of primordial matter perturbations demands the opposite. The reason for this behaviour is illustrated in Fig. 4.2, where the Fourier-transformed real-space top-hat and (intermediate) steps of the HMF calculations are shown by red/dashed lines. For this type of window function, one obtains significant contributions from a wide range of unsuppressed larger scales, which dominate the resulting variance and thus, the predicted HMF.

A k-space top-hat window function is only sensitive to local changes in the matter distribution in k-space and thus reproduces the expected suppression in the halo abundance for damped power spectra (see Fig. 4.2, blue/solid lines). However, the mass-smoothing scale relation (M–R) must now be defined without the simple geometrical justification of Eq. (4.5), which was used in the real-space case.

Here we use the definition of Lacey and Cole (1993), which defines the cut-off wavenumber, k_s, in relation to the mass, M, based on the normalization choice

$$k_s = \left(\frac{M}{6\pi^2 \bar{\rho}} \right)^{-1/3} . \qquad (4.6)$$

This corresponds to a correction factor of $c \equiv Rk_s \approx 2.42$ with respect to Eq. 4.5, so that the semi-analytical HMF matches numerical simulations at large scales[10].

Alternatively, Schneider et al. (2012) found that while the r-space top-hat did not match the results of their N-body simulations, an additional mass-dependent correction factor,

$$\frac{n(M)}{n^{\mathrm{ST}}(M)} = \left(1 + \frac{M_{\mathrm{hm}}}{\beta M} \right)^{-\alpha} , \qquad (4.7)$$

could correct for this, where α and β are free parameters. Schneider et al. (2012) set $\beta = 1/2$ and found a best-fitting value of $\alpha = 0.6$. As discussed in the next section, we find better agreement with our simulation results by setting $\beta = 2$; we will refer to this version of Eq. 4.7 as the *modified* Schneider et al. correction.

4.2.2 Simulated Halo Mass Function

We plot the differential HMFs measured in the collision-less CDM, γCDM, νCDM and WDM simulations in Fig. 4.3. We also show the predictions obtained

---

[10]Note that Schneider et al. (2013) and Benson et al. (2013) follow a very similar approach, but with slightly different values for c.
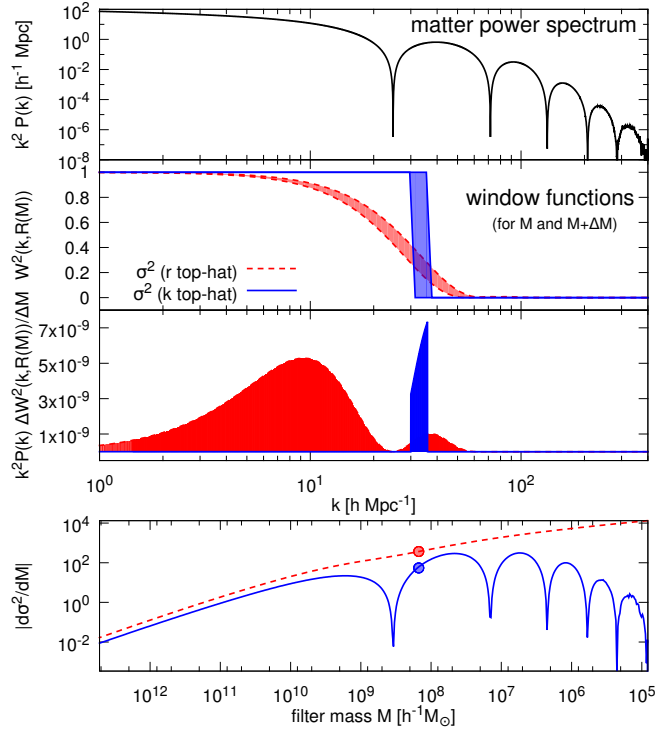
FIGURE 4.2: Real-space and *k*-space top-hat window functions in Press-Schechter HMF predictions for γCDM. The upper panel shows the matter power spectrum, while the second panel shows the Fourier transform of the two window functions (*r* top-hat and *k* top-hat). Each window function is evaluated for two filter masses, *M* and $M + \Delta M$. The difference between the two filter masses is highlighted by the shaded region in each case. The third panel shows the result of applying this differential filter to the matter distribution. Finally, the lower panel shows the integrated result for both window functions. The red and blue points are the results for the specific filter mass *M* used in the middle two panels.

using the semi-analytical approximations described in Sec. 4.2.1.

The mass function proposed by Schneider et al. (2012) predicts fewer haloes than are seen in collision-less CDM but nevertheless overestimates the abundance of haloes less massive than $\sim 10^{10.5} \ h^{-1} \ M_\odot$. Using a modified version of the Schneider et al. correction, with $\beta = 12/$ instead of $\beta = 1$ extends the reproduction of the simulation results down to a halo mass of $\sim 10^{8.6} \ h^{-1} \ M_\odot$ for WDM. However, it does not reproduce the abundance of haloes seen in the simulations of γCDM and νCDM, underestimating the measured abundance of haloes at $10^{8.6} \ h^{-1} \ M_\odot$ by a factor of two. The clear upturn observed in the HMF at low masses in Fig. 4.3 (i.e. below $M_{\mathrm{vir}} \lesssim 10^9 \ h^{-1} \ M_\odot$) is due to non-physical, spurious structures (Wang and White 2007). We try to avoid contamination from such artificial structures by only considering the mass function and halo properties for objects with masses far above this value.
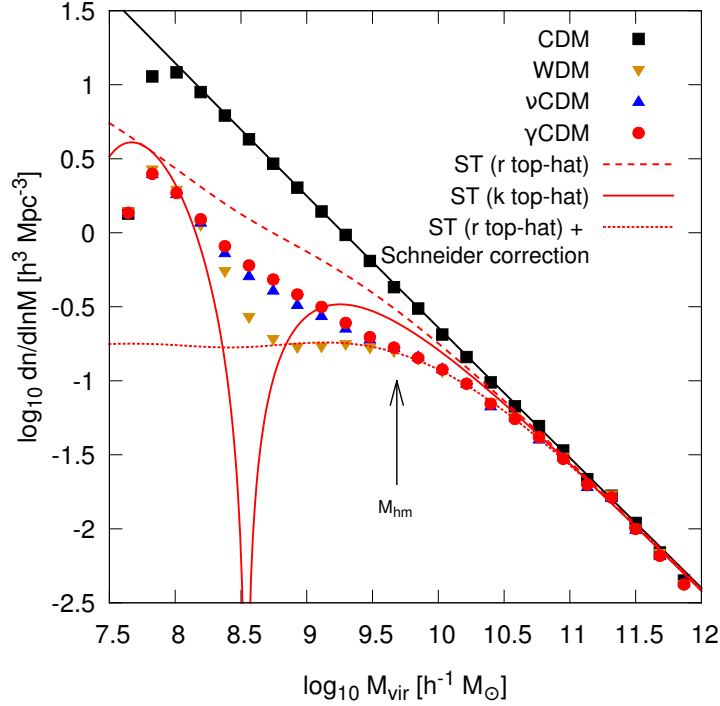
FIGURE 4.3: The HMFs for collision-less CDM, WDM, νCDM and γCDM at redshift $z = 0$. The HMF measured in models with damped power spectra contains contributions from spurious haloes, which dominate at the smallest masses and result in the upturn seen at $M_{\rm vir} \sim 10^9\, h^{-1}\, M_\odot$. Above this scale and below the half-mode mass, $M_{\rm hm}$ (marked by the arrow), the abundance of haloes in γCDM and νCDM exceeds that seen in WDM. Predictions using the Sheth-Tormen (ST) formalism with a real-space (dashed) or k-space (solid) top-hat window function, as well as the modified Schneider et al. correction (dotted), are also shown. All the semi-analytical predictions fail to predict the HMFs for γCDM and νCDM.

A comparison between the simulated abundance of haloes in the four models and the semi-analytical predictions reveals significant differences. The main feature, the reduced number of haloes in γCDM, νCDM and WDM, with respect to CDM, is a consequence of the damping of primordial fluctuations on small-scales. There is also a larger number of low-mass structures in γCDM and νCDM, relative to WDM, due to the prominent oscillations in the power spectra of the former models, at wavenumbers larger than the scales on which fluctuations are suppressed.

A direct comparison between the γCDM and WDM models (see Fig. 4.4) reveals that in both cases, the suppression of the HMF follows a universal profile, if the halo mass is plotted normalized by the half-mode mass, $M_{\rm hm}$. An excess of haloes in γCDM with respect to WDM occurs at $M_{\rm hm}$ for all the cross-sections studied in this work. A similar result is found for νCDM.

The higher halo abundance seen in the γCDM and νCDM simulations com-
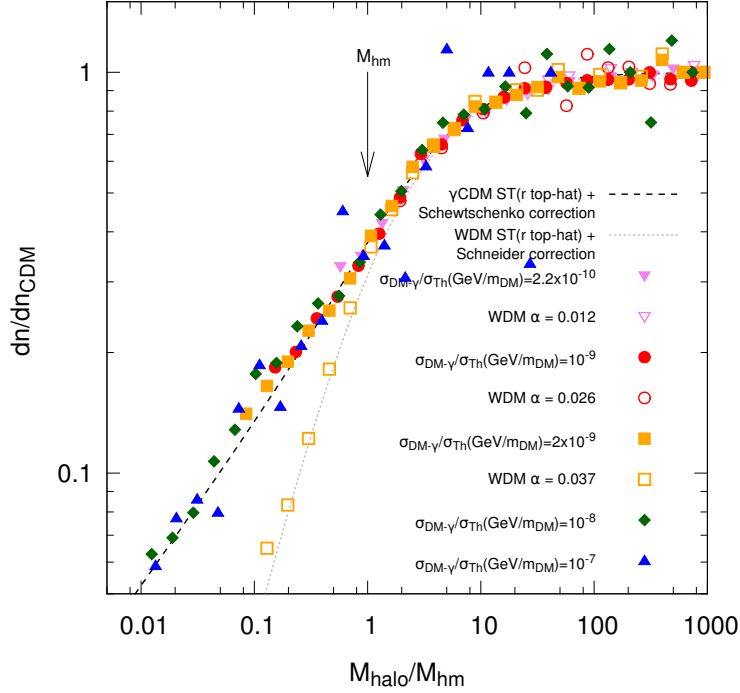
FIGURE 4.4: The relative halo abundance expressed in units of the half-mode mass, M_{hm}, for γCDM (filled symbols) and WDM (unfilled symbols), with respect to CDM, at redshift $z = 0$. The suppression in the HMF is universal with respect to the values of the γCDM cross-section and WDM particle mass. The result for WDM matches the semi-analytical prediction of a r-space top-hat with the Schneider et al. correction (dotted line). However, we obtain more haloes in γCDM than in WDM as a result of the significant oscillations in the matter power spectrum. Hence, the modified Sheth-Tormen HMF does not provide a good fit to our simulation results. The dashed lines shows a new correction/fit used e.g. in Moliné et al. (2016) that predicts the HMF for γCDM over the shown (normalized) mass range much more accurately.

pared to that found in WDM is difficult to explain since the primordial matter power spectra shown in Fig. 3.1 are very similar down to the wavenumber corresponding to the half-mode mass, M_{hm}. There is a much stronger suppression in the γCDM and νCDM spectra than in WDM immediately below M_{hm}. The scales where the power in γCDM and νCDM exceeds that in WDM correspond to halo masses that are an order of magnitude smaller than M_{hm}, marked by the location of the first oscillation in the halo abundance for γCDM and νCDM, according to the Sheth-Tormen formalism. Instead of showing a strong reduction in halo abundance below M_{hm}, the simulated HMFs for γCDM and νCDM seem to bridge the gap between the primary power cut-off scale and the subsequent increase in the halo abundance resulting from the oscillating matter power spectra.

Given that the simulations for WDM, γCDM and νCDM use similar initial

conditions (e.g. identical box size, phases, number of particles), numerical errors can most likely be excluded as a possible explanation for this deviation. Therefore, this is a strong hint that the understanding of structure formation in the Sheth-Tormen formalism, which works so well in the strictly hierarchical case, appears to fail when there is oscillating power in the initial matter distribution.

4.2.3 Halo Bias

We determine the linear clustering bias of DM haloes, $b_{\mathrm{lin}}(M)$, using the ratio between the halo-density cross-correlation and the density-density auto-correlation on large scales (i.e. at small wavenumbers):

$$b_{\mathrm{lin}}(M) = \lim_{k \to 0} \frac{P_{\mathrm{hm}}(M)}{P_{\mathrm{mm}}} \; .$$ (4.8)

Using the cross-correlation of haloes and mass rather than the autocorrelation of
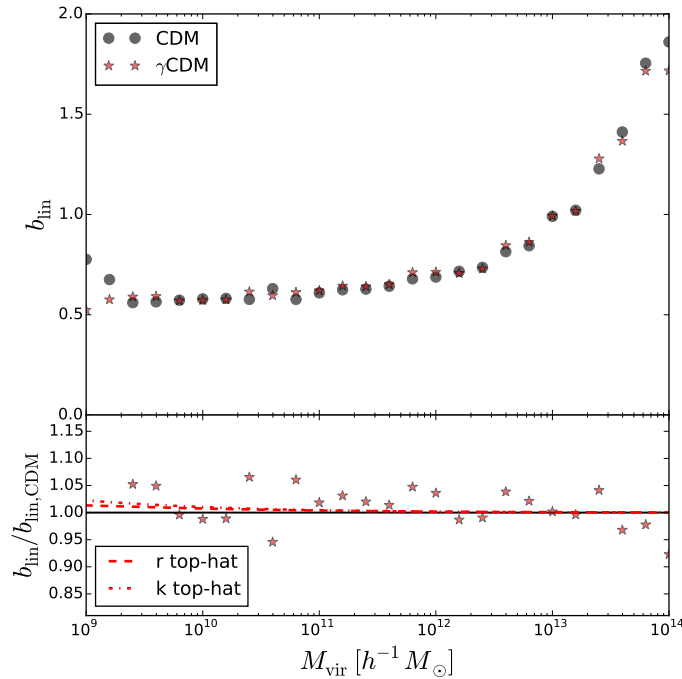
FIGURE 4.5: Linear halo bias: (top) absolute halo bias for CDM (circles) and γCDM with $\sigma_{\mathrm{DM}-\gamma} = 2 \times 10^{-7} \, \sigma_{\mathrm{Th}} \, (m_{\mathrm{DM}}/\mathrm{GeV})$ (stars); (bottom) relative halo bias compared to CDM with analytical predictions using ST theory with a r top-hat (dashed) and k top-hat (dot-dashed) for comparison.

haloes reduces the impact of shot noise (see Angulo et al. 2008). To ensure that we

recover the asymptotic value of $b_{\text{lin}}(M)$, we use the largest simulation box of side length $300\,h^{-1}$ Mpc. For large scales ($k \lesssim 0.1\,h^{-1}$ Mpc), convergence is reached as the halo bias becomes constant. Therefore, we can replace the limit in Eq. 4.8 with the average over all scales larger than $k = 0.1\,h^{-1}$ Mpc to reduce the impact of statistical fluctuations arising from the small number of high-mass haloes and low-wavenumber modes in the simulation box. This wavenumber scale corresponds to the largest mode in the $100\,h^{-1}$ Mpc box and, as the shot noise fluctuations are less important for the more abundant low-mass DM haloes, we use the smaller box to measure the halo bias for masses below $10^{11}\,h^{-1}\,M_{\odot}$.

We do not find a significant deviation from the bias expected in collision-less CDM for WDM, γCDM or νCDM, which agrees with the expectations from the semi-analytical models of halo bias. We therefore conclude that the suppression of small-scale structure in the matter power spectra in γCDM and νCDM takes place independently of the linear background in both overdense and underdense regions. Thus, the clustering properties do not change on the mass scales probed here ($M \gtrsim 10^9\,h^{-1}\,M_{\odot}$).

4.3 Results: Halo Properties

As seen in Sec. 4.2, DM–radiation interactions lead to a reduced abundance of low-mass DM haloes. In this section, we focus on three key properties of these haloes: their shape, density profile and spin.

For this analysis, it is important to only consider DM haloes that are dynamically relaxed. We apply the selection criteria presented in Maccio' et al. (2007) and Neto et al. (2007). The DM haloes must satisfy the following conditions[11]:

- *Centre-of-mass displacement*: The offset, s, between the halo centre-of-mass, r_{cm}, and the potential centre, r_{cp}, normalized by the virial radius, r_{vir}, satisfies

$$s = \|r_{\text{cp}} - r_{\text{cp}}\| < 0.07 \,. \tag{4.9}$$

- *Virial ratio*: The total kinetic energy of the halo particles within r_{vir} in the halo rest frame, T, and their gravitational potential energy, U, satisfies

$$2T/\|U\| < 1.35 \,. \tag{4.10}$$

---

[11]We omit the substructure mass fraction criterion as this is strongly correlated with the centre-of-mass displacement criterion listed (Neto et al. 2007).

These criteria reduce the number of haloes in our sample by a factor of two, but also significantly decrease the scatter as major mergers and their unrelaxed descendants are removed.

In addition to applying these conditions, our mass-averaged results are restricted to: (i) the subset of haloes with a virial mass smaller than $10^{11} \, h^{-1} \, M_\odot$, i.e. the mass range that shows a suppression in the halo abundance, and (ii) in order to avoid resolution problems, larger than 1000 particles, i.e. mass bins larger than $\sim 10^{9.3} \, h^{-1} \, M_\odot$. The latter criterion ensures that the estimates for our observables have converged (Power et al. 2003). This lower limit also minimizes the possibility of contamination by spurious structures as they form and mainly affect haloes on small mass scales ($M \lesssim 10^9 \, h^{-1} \, M_\odot$); this can be checked by studying their contribution to the HMF plotted in Fig. 4.3.

4.3.1 Halo Shape

To characterize the shape of DM haloes, we study the following quantities derived from the three eigenvalues ($a \geq b \geq c$) of the inertia tensor, as calculated by the *AMIGA halo finder*:

- sphericity: c/a

- elongation: b/a

- triaxiality: $\left(a^2 - b^2\right) / \left(a^2 - c^2\right)$.

In Fig. 4.6, we plot the sphericity measured from the sample set of relaxed haloes. We observe no significant deviation from CDM for WDM, γCDM or νCDM. The same is true for the elongation and triaxiality, and for different redshifts and interaction cross-sections. Thus, we cannot distinguish these models by the shape of their DM haloes.

4.3.2 Density Profile and Concentration

To analyse the density profiles of DM haloes, we first average the density in shells around the centre-of-mass for all haloes in a given mass bin. A comparison of the results with a fitted NFW profile (Navarro et al. 1997) reveals a sufficiently good agreement to justify parametrising the halo profiles in this way[12]. The NFW

---

[12]The fit starts at a minimum radius from the halo centre as defined by Power et al. (2003) to ensure convergence of the density profile.
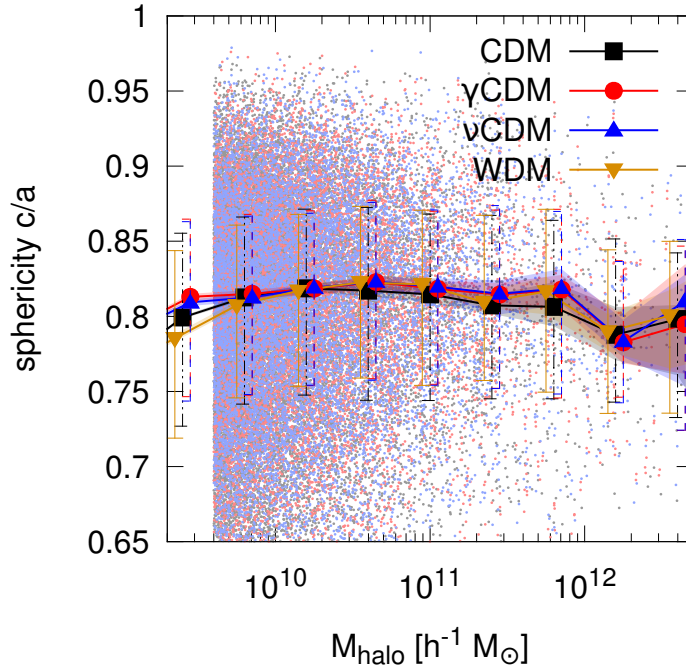
FIGURE 4.6: Sphericity of relaxed DM haloes for CDM, γCDM, νCDM and WDM at redshift $z = 0$. The symbols show the sphericity in mass bins ranging from 4×10^9 h^{-1} $M_\odot$ to 10^{11} h^{-1} $M_\odot$ for the different models as labelled. The shaded areas indicate the 95% CL on the median, given the underlying scatter in the halo sample set (small dots), while the error bars mark the 20% to 80% interval for this distribution. The sphericity of DM haloes measured in WDM, γCDM and νCDM shows no significant deviation from CDM.

profile is completely characterized by the concentration parameter, c_{NFW}, which is determined by the halo finder using the approximation presented in Prada et al. (2012). In Fig. 4.7, we plot the concentration versus mass, cross-section and redshift relations. We observe a significantly lower median value of c_{NFW} in the mass bins below the half-mode mass for γCDM and νCDM compared to CDM. This reduction in concentration with increasing interaction cross-section is similar to the effect seen in WDM simulations with reducing particle mass, which has been explained as being due to the delayed formation time of low-mass haloes (Lovell et al., 2012). At these late times, the interacting DM models become (effectively) non-collisional for the cross-sections studied here, in the same way that free-streaming in WDM models becomes negligible at low redshifts. Therefore, it is valid to assume that this lower concentration also originates from the later collapse of the DM haloes in these models.

As we increase the interaction cross-section, the deviation from CDM becomes larger due to an increase in the mass scale of the suppression. Since we have fixed

FIGURE 4.7: The concentration–mass relation (top) shows a strong mass-dependence for γCDM, νCDM and WDM, which develops at scales below $\sim 10^{11}\,h^{-1}\,M_\odot$. These models are indistinguishable from CDM for more massive haloes. This deviation in the concentration depends strongly on the interaction cross-section (middle) and becomes slightly smaller at higher redshifts (bottom). The data points are the median values for the mass bins ranging from $4 \times 10^9\,h^{-1}\,M_\odot$ to $10^{11}\,h^{-1}\,M_\odot$, while the shaded regions mark the 95% CL on the median, given the underlying scatter in the halo sample set (small dots in the top plot). The error bars mark the 20% to 80% interval for this distribution.

the mass interval, the median concentration decreases as a larger number of high-mass haloes become affected.

4.3.3 Halo Spin

We quantify the spin of DM haloes using the "classical" definition of Peebles (1969):

$$\lambda = \frac{J|E|^{1/2}}{GM_{\mathrm{vir}}^{5/2}} \,,$$

(4.11)

where J and E are, respectively, the total angular momentum and total energy of the material within the virial mass, M_{vir}, of a halo.

In the linear and quasi-linear regime, the halo spin is described reasonably well using *tidal torque theory* (hereafter TTT; White 1984) and originates from tidal interactions between collapsing haloes. In this framework, the angular momentum of a (proto-)galaxy depends on the mass, but also weakly on the formation time. However, it should be noted that comparisons with numerical simulations have revealed that TTT becomes less applicable as haloes approach turn-around and virialization (Porciani et al. 2002). It is still an open question whether haloes acquire significant angular momentum due to mergers with other haloes, as well as from tidal torques (Maller et al. 2002; D'Onghia and Navarro 2007).

In Fig. 4.8, we plot the median halo spin against virial mass for the different models. We find a similar reduction and evolution of halo spin for γCDM, νCDM and WDM, compared to CDM. There are various explanations for the difference in halo spin with respect to CDM. As this effect is seen for haloes consisting of more than a few thousand particles, we can rule out a numerical convergence problem. If it originates solely from tidal torques, then the weak dependence of angular momentum on formation time would yield a smaller spin for the earlier formation time found. If mergers are responsible for spinning up haloes, then the lack of smaller progenitors of low-mass haloes and consequently, smoother accretion on to these haloes in γCDM, νCDM and WDM, would also result in a lower net spin. The fact that the difference remains constant over time while the absolute value grows, seems to support the idea that not only the initial tidal torque on the collapsing structure, but also the environment at late times, influences the spin.

4.4 Conclusion

We have shown that even relatively weak DM–radiation interactions can alter structure formation on small cosmic scales. In Boehm et al. (2014) (cf. Ch. 5), we showed that the number of Milky Way satellites is reduced when DM has
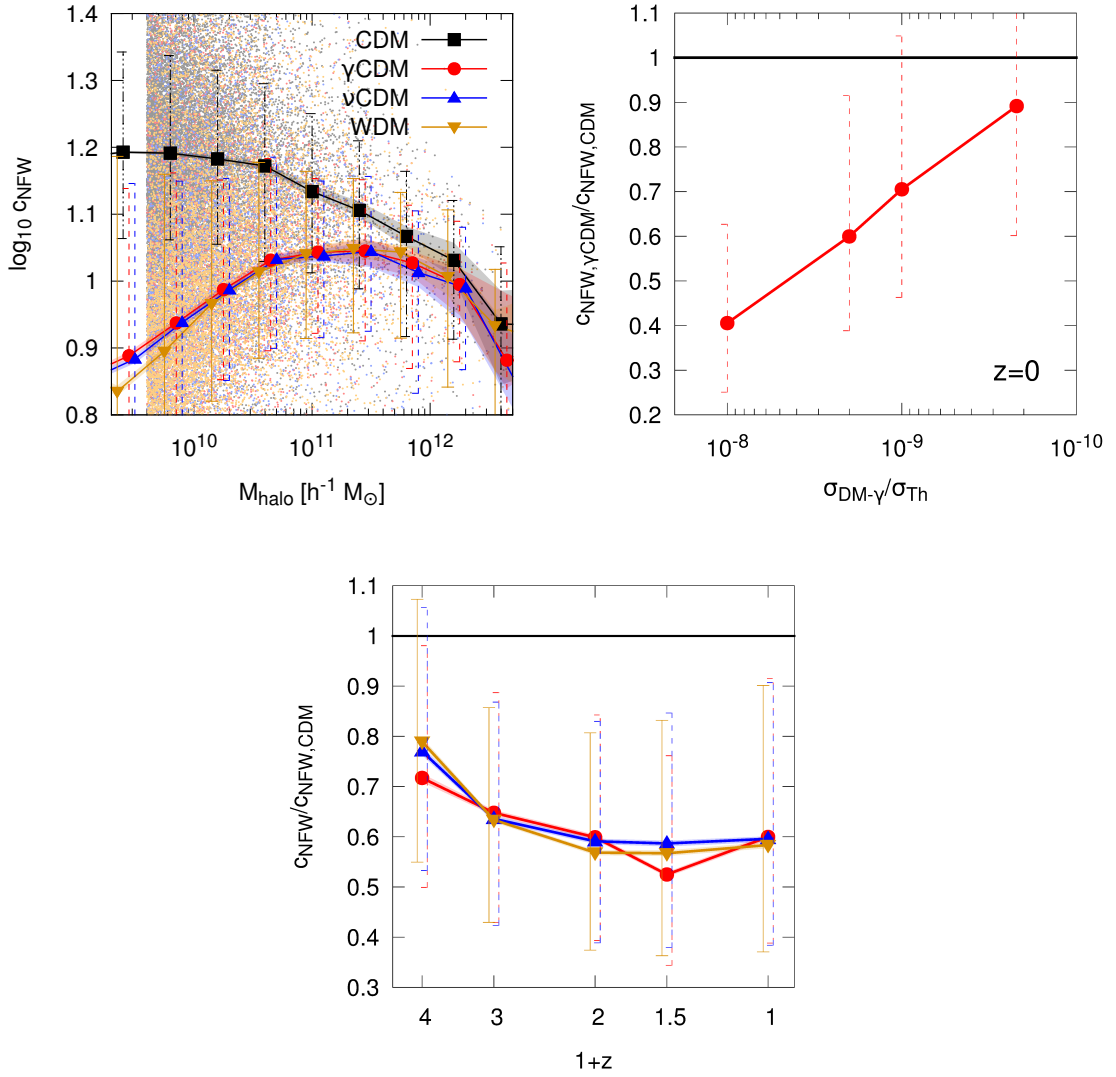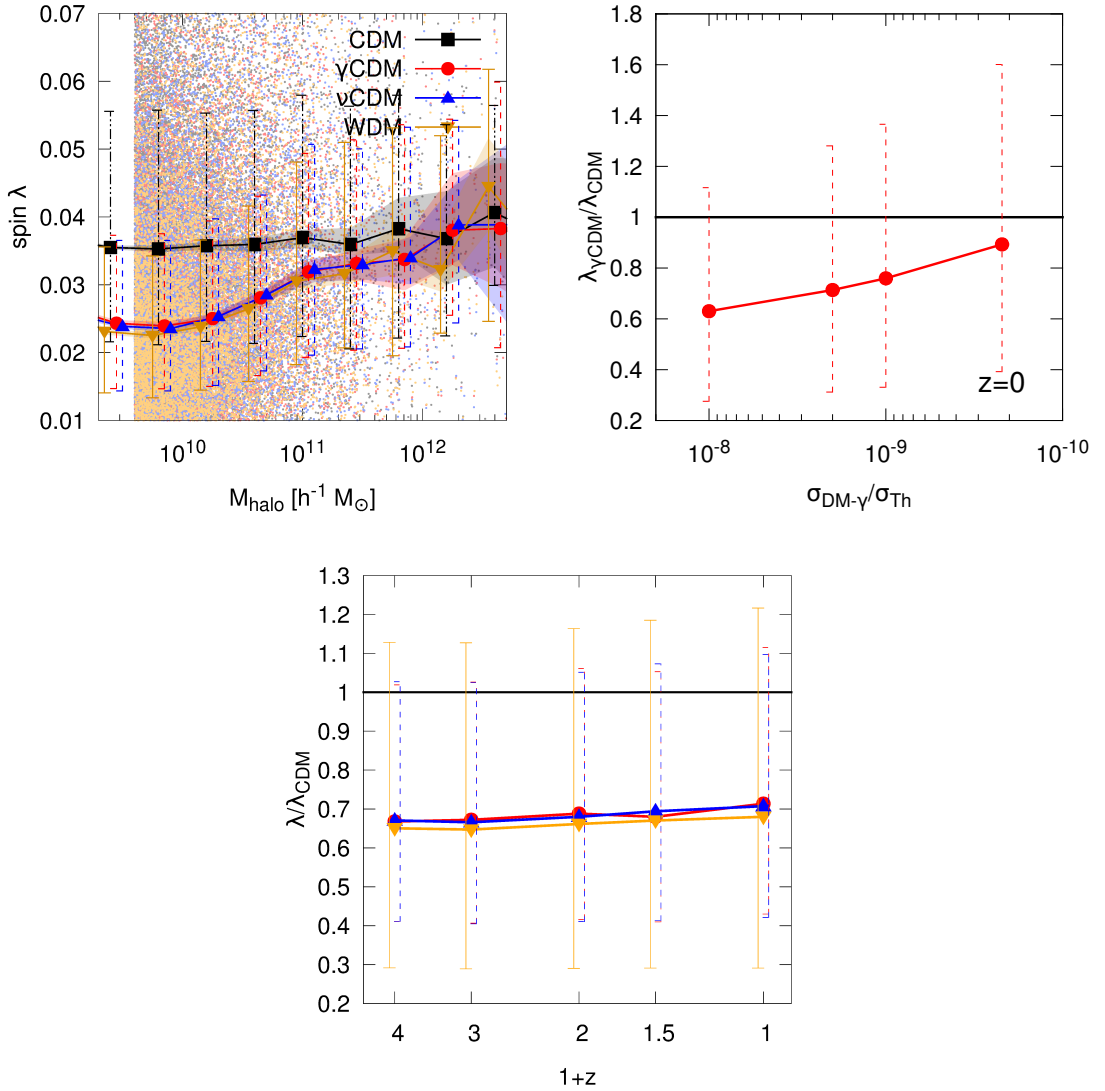
FIGURE 4.8: The spin–mass relation (top) shows a mass-dependence for γCDM, νCDM and WDM, which develops at scales below $\sim 10^{11}\ h^{-1}\ M_\odot$. These models are indistinguishable from CDM for more massive haloes. This spin reduction on small scales depends on the interaction cross-section (middle) while the relative deviation from collision-less CDM remains constant over time (bottom). The data points are the median values for the mass bins ranging from $4 \times 10^9\ h^{-1}\ M_\odot$ to $10^{11}\ h^{-1}\ M_\odot$, while the shaded regions mark the 95% CL on the median, given the underlying scatter in the halo sample set (small dots in the top plot). The error bars mark the 20% to 80% interval for this distribution.

primordial interactions with photons (γCDM) or neutrinos (νCDM) and that the resulting number of satellites can be used to place constraints on the interaction cross-section. In this chapter, we have extended our previous analysis to study the abundance of DM haloes and their internal properties, namely their shape, density profile and spin. We have also compared different models (γCDM, νCDM and WDM) in which the power spectrum of density fluctuations is suppressed on small

scales.

The halo mass functions measured in our simulations show that the γCDM and νCDM models contain more haloes than WDM around a mass of $10^9\,h^{-1}\,M_\odot$ for the parameters considered here. This behaviour is not reproduced by various semi-analytical descriptions of the halo mass function. We note that these mass scales are an order of magnitude larger than the scale on which spurious haloes are expected to make a significant contribution (Wang and White, 2007). The source of this over-abundance of haloes with respect to WDM needs to be addressed but could be due to the choice of models for the initial conditions in WDM.

Both the NFW concentration parameter in the density profile and the spin show departures from CDM for low-mass haloes. The halo shape, on the other hand, is independent of the DM model. The lower halo concentration and angular momentum may be due to the delayed formation time of low-mass haloes in γCDM and νCDM and are similar to the trends seen in WDM. However, it should be noted that these halo properties do not provide a means to distinguish between γCDM, νCDM and WDM.

Ideally, the next step in this study would be to include baryonic physics in our simulations, which may have an impact on some of the results reported in our DM-only simulations. Bryan et al. (2013) have shown that efficient gas cooling results in an increased halo spin, while AGN feedback counters this trend. The mass-concentration relation of the haloes is very similar when baryons are included (Schaller et al., 2015) and the baryons only affect the radial density profile of the inner core within 5% of the virial radius, producing a contraction. Recent studies also include a possible coupling of DM with dark radiation (Buckley et al., 2014), which leads to a similar suppression of initial fluctuations as seen in our models and, depending on the cross-section, should give rise to similar results as those discussed in this thesis.

CHAPTER 5

CDM Small-scale problems and constraints in interacting γ/νCDM models

In the previous chapter we discussed the implications of early-time interactions between DM and photons or neutrinos for the formation and the properties of DM halos in the Universe. While these results may be potentially testable with future cosmological observations, in this chapter we turn our focus to our cosmic neighbourhood, in particular the Milky Way (MW) and Andromeda (M31) DM halos which make up the Local Group (LG) together with a few other smaller galaxies. While the rather low mass scales and close proximity of structures within the Local Group and, in particular, within the MW and M31 host halos, render techniques used for studies of big galaxies and galaxy clusters such as strong gravitational lensing (Giocoli et al., 2014) much more challenging, the fact that substructures and even individual halo stars can be resolved and their kinematics be measured allows us to learn more about the properties of their host halo (Bonaca et al., 2014). Studies of these small (sub)structures provide us valuable insights since the properties of the satellite galaxies are much more sensitive to changes in the properties of dark matter particles which we will demonstrate in this chapter. Indeed, tensions between LG observations and the predictions from N-Body simulations of CDM, dubbed the "small scale problems" of CDM, sparked the interest of cosmologists into alternative dark matter models such as WDM, SIDM or the IDM model we are working with here[13].

This chapter is structured as follows. First, we discuss two of the challenges to vanilla CDM in Sec.5.1. Then, in Sec.5.2 we introduce the zoom simulations of the Local Group used to study these small structures before showing in Sec. 5.3 how IDM eases (and potentially even solves) the tensions of these "small scale problems". Finally, we use these observables in Sec. 5.4 to constrain the parameter space for the interacting DM model.

---

[13]For a review of the problems of CDM on small scales, see e.g. Weinberg et al. (2013)

5.1 Small-Scale "Challenges" of CDM

With its hierarchical "bottom-up" structure formation, the standard ΛCDM model successfully predicts the evolution of the cosmic matter distribution from the initial smooth state with only small perturbations to the lumpy state we observe in galaxies and galactic clusters today, while e.g. the "top-down" fragmentation-driven HDM model (Melott, 1982) fails to do so. But despite this success, simulations based on the standard ΛCDM model seem to diverge from observations in several potentially problematic ways. In the following subsection we will explore two of these "challenges" to the standard model and show how the predictions and observations can be reconciled by using interacting DM instead.

5.1.1 Missing Satellite Problem

In CDM models, galaxies are orbited by smaller satellite galaxies within their DM halo, upon which they were accreted on. Each of them is sitting in a dark matter halo of their own. Given the very small intrinsic cut-off scale of CDM for primordial fluctuations , halos today are expected to be filled with enormous numbers of subhalos down to earth mass size (Diemand et al., 2005; Springel et al., 2008)) that were seeded by the primordial perturbations, collapsed and survived their infall into larger host halos over sufficiently long time without becoming extensively tidally disrupted.

Numerical simulations of the CDM model predict a large number of substructures that by far exceeds the amount of observed satellite galaxies in the two host galaxies, the Milky Way (MW) and Andromeda (M31), that we are able to study in detail (Klypin et al., 1999; Moore et al., 1999). Prior to the 21st century, only the nine "classical" dwarf galaxies were known within the virial radius of the Milky Way halo besides the Magellanic Clouds and another eleven were found in the neighbouring Andromeda galaxy halo. In contrast, CDM predicts several few orders of magnitude more dwarf galaxies than are observed under the assumption that many of the predicted DM subhalos host visible galaxies. This led to naming this first challenge to the standard model the "Missing Satellite Problem" (MSP). Even with the discoveries of additional fainter dwarf galaxies inside both the Milky Way and M31 halos over the last two decades and a better insight into their properties (e.g. Alam et al. (2015),Kalirai et al. (2010)), this tension between predictions and observations has only eased slightly, as we will confirm in our analysis for CDM in Sec. 5.3, but has not vanished altogether.

5.1.2 Too Big To Fail Problem

Another challenge that comes with the vanilla CDM model is, that we not only observe fewer of the smaller satellites than predicted, but also that the largest, brightest ones, i.e. the "classical" MW satellites seem to be less massive and less concentrated than their simulated counterparts from N-Body DM-only simulations (Boylan-Kolchin et al., 2011). This tension was dubbed the "Too Big To Fail" (TBTF) problem. The stellar kinematics observed in the satellite galaxies do not match those of the most massive predicted subhalos within a Milky Way-sized halo. The $V_{\mathrm{max}} - R_{\mathrm{max}}$ plot of the original publication as shown in Fig. 5.1 and the rotation curve plots often used in recent literature (e.g. Garrison-Kimmel et al. (2014)) illustrate this problem in two different, yet similar ways. In the rotation curve plots, the
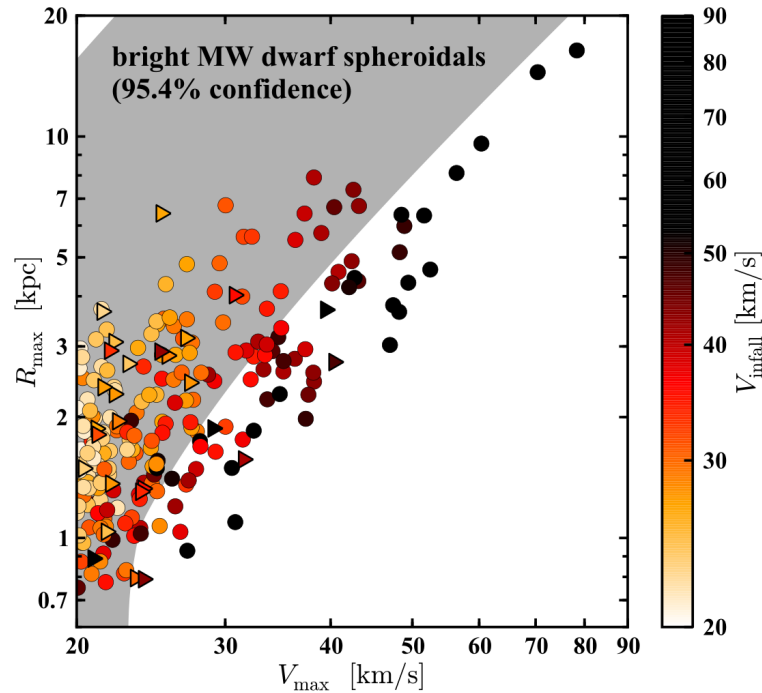
FIGURE 5.1: Subhaloes from all six Aquarius simulations (circles) and Via Lactea II (triangles), color-coded according to V_{infall}. The shaded gray region shows the 2σ confidence interval for possible hosts of the bright MW dwarf spheroidals (Boylan-Kolchin et al., 2011, Fig.2)

stellar circular velocity at the half-light radius $V_{\mathrm{circ}}(r_{1/2})$ for the "classical" dwarf spheroidal (dSph) galaxies in the MW and overplot the rotation curves for the most massive substructures found in a simulated Milky Way-like DM halo. Even if the three predicted halos are ignored that deviate the most and associate these with the Magellanic Clouds and Sagittarius which are outliers in the satellite galaxy population, there are still too many rotation curves that are not matched by the

observational data. Hence, the theoretical rotation curves tend to predict too high a circular velocity at given radius.

An alternative way to visualize this problem (Fig. 5.1) is to use the measured line-of-sight velocity dispersion, $\sigma_\star$, in order to extrapolate V_{max} for the observed satellites and compare these results to those obtained from the simulations. This, again, shows that the simulated satellites are having central densities that are too high to host the bright MW dwarf spheroidals, i.e. we find far too many massive and concentrated halos in our CDM predictions to match the few observed MW satellites.

5.2   Simulations

As the source of our first sample set of MW-like halos, we chose to filter the results of the simulation suite presented in Ch. 4 using two criteria to identify MW candidates from the identified halos:

mass Motivated by calculations that attempt to reconstruct the MW mass distribution based on the measured kinematics of the observed satellites and stars (Xue et al., 2008; Boylan-Kolchin et al., 2013; Piffl et al., 2014), we consider DM haloes to be MW-like if their mass is in the range $(0.8 - 2.7) \times 10^{12} \mathrm{M}_\odot$.

environment The MW appears to be located in an unremarkable region away from larger structures such as the Virgo Cluster and the major filaments feeding the Centaurus Cluster (Courtois et al., 2013). We therefore reject candidates with larger-mass DM haloes within a radius of 2 Mpc.

Applying these criteria upon our single-resolution simulation suite provides us with a sample set of 126 halos, that can be used to obtain statistically significant measurements of the observables we are interested in.

But in our studies of satellites in Milky Way-sized halos, we reach the limits of what it is currently feasible to resolve with such N-body simulations in a cosmologically representative box. We have to keep the box size as large as possible, so that we do not miss the contribution from the large-scale perturbation modes, but at the same time we need to resolve the structures of interest with enough particles to calculate their properties reliably. While the estimate of the virial mass uses all the particle tracers within a halo and can be considered to be accurate at the single-digit percentage level for structures containing a few hundred particles, radial profiles, such as the circular velocity, bin the particles into much smaller

distance-dependent subsets and thus converge much more slowly (Power et al., 2003).

A solution to this is to use an alternative technique instead. We first identify Local Group (LG) candidates in an *N*-body simulation of a large cosmological volume such as those in Ch. 4 and then re-simulate the region containing these haloes at much higher mass resolution. Thus, this allows for a much higher local resolution to be attained while still keeping the larger lower-resolution box as background.

The Lagrangian regions of higher resolution in the cosmological volume are chosen by identifying and flagging the structures of interest at the final redshift and then picking a convex hull around the region they are spread over in the initial conditions. In this way, we ensure that these structures evolve exclusively in a high-resolution environment. Additionally, a padding around this region resolved at intermediate resolutions that become outwards step-wise coarser smooths the transition between the regions of lowest and highest resolution and provides a more accurate local background around the region of interest.

For the re-simulations, we chose a subset of the selection of Local Group candidates used in the `APOSTLE` project (Fattahi et al., 2016; Sawala et al., 2016b). These candidates shown in Fig.5.2 and listed in Tab. 5.1 were picked from a $(100\text{Mpc})^3$ CDM N-Body simulation from the `DOVE` simulation suite using a slightly different set of following criteria than those listed above:

mass There should be a pair of MW and Andromeda mass host haloes, with masses in the range $(0.5 - 2.5) \times 10^{12} \ M_\odot$.

dynamics The separation between the two haloes should be 800 ± 200 kpc, with relative radial and tangential velocities below 250 km s^{-1} and 100 km s^{-1} respectively.

environment There should be no other large structures nearby, i.e. an environment with an unperturbed Hubble flow out to 4 Mpc.

These criteria are more restrictive than those employed in our earlier work on the structure of haloes (Schewtschenko et al., 2015b) since they also take into account the internal kinematics of the LG. We obtain four LG candidates and therefore, eight MW-like haloes. If we assume that the gravitational interaction between the LG haloes is limited, the mass, environment and dynamics[14] of the haloes would

---

[14]The formation process of structures is slightly delayed by the presence of DM interactions. Therefore, both the separation and the relative velocities may actually lie outside the bound set by

not be significantly different if we had run a γCDM or νCDM version of the DOVE simulation.

We perform the re-simulations with the GADGET-3 N-body simulation code (Springel, 2005) assuming the γCDM model, while bearing in mind that the results for νCDM would be very similar (cf. Ch. 4). We use the same cosmology (WMAP7)[15], random phases and second-order LPT method (Jenkins, 2010) as Sawala et al. (2016b). We re-simulate the four LG candidates with a particle mass $m_{\mathrm{part}} = 7.2 \times 10^5 \, M_\odot$ and a comoving softening length $l_{\mathrm{soft}} = 216$ pc. This corresponds to a mass resolution that is intermediate between levels 4 and 5 in the Aquarius simulations of Springel et al. (2008) (level 1 being the highest resolution). We also re-simulate the two host haloes in one of our LG Candidates (AP-7/AP-8) at an even higher resolution ($m_{\mathrm{part}} = 6 \times 10^4 \, M_\odot$, $l_{\mathrm{soft}} = 94$ pc; which is comparable to Aquarius level 3). These simulations (denoted with the suffix -HR) are used to confirm that our results have converged and allow us to obtain more reliable predictions for the innermost parts of the halo.

Fig.5.2 shows the projected matter density of the uniform-resolution DOVE simulation box for CDM and renderings of all four Local Group candidates selected from it which have been re-simulated at higher resolution for both CDM and γCDM. Since we have two MW/M31-like halos per re-simulated group, this results in the sample set of 8 MW-like halos that are listed in Tab.5.1 with their respective properties. These complement the lower-resolution, but much larger sample set obtained from the simulation suite outlined in the previous chapter.

Substructures within the host halos are identified using the AMIGA halo finder (Knollmann and Knebe, 2009). We also performed halo matching between the vanilla CDM and our γCDM predictions in both the full cosmological box and our "zoom" simulation. To do this, we identified particles located at the same position of the perturbed grid used as the initial conditions and tracked their membership to structures predicted in the simulation runs at the redshift of interest. If two (sub)halos share at least half of the most bound particles, we consider this as a match.

---

the "Dynamics" criterion as the haloes are at a different point in their orbit around each other for γCDM. However, as long as this delay between CDM and γCDM is not too large, we essentially have the same dynamical system in both cases and the substructures within the host haloes will be unaffected.

[15]The fact that we are using the older WMAP7 cosmology instead of the most recent data is not a concern since we are only interested in the effects of DM interactions on a selected local environment.
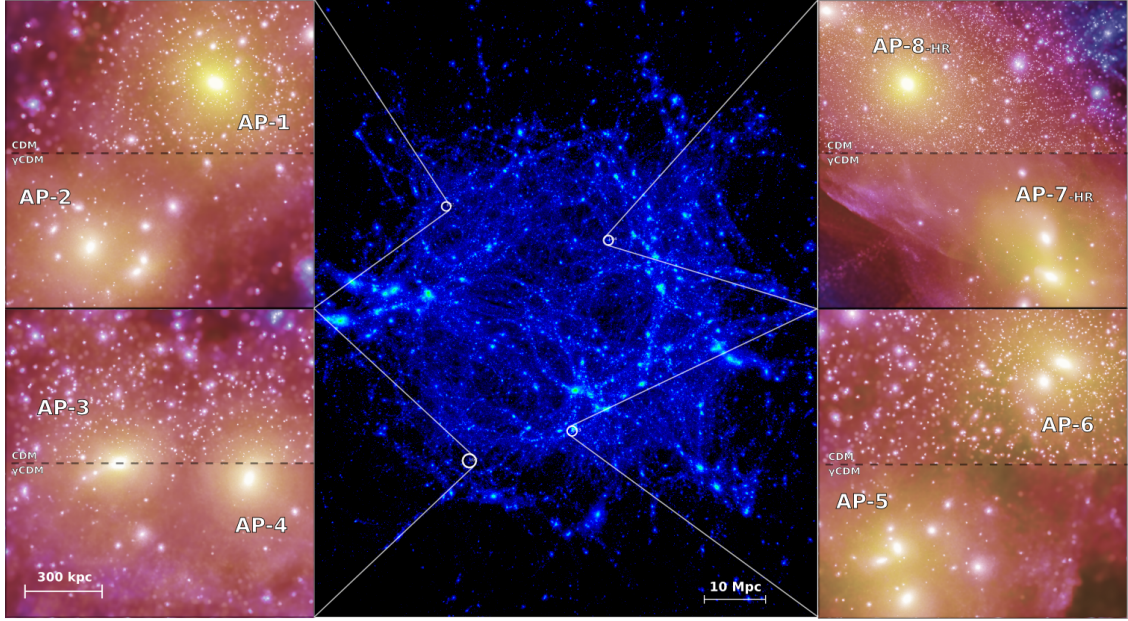
FIGURE 5.2: The centre panel shows a projection of the DM distribution in the full $(100 \text{ Mpc})^3$ DOVE simulation box, where the circles denote the four regions (with radii $1\,h^{-1}$ Mpc) that are used for the "zoom" re-simulations. To the left and right, each of the four Local Group candidates is rendered with the projected density encoded as brightness, where the colour scheme represents the local velocity dispersion from low (violet) to high (yellow/white). Each of these four panels is split in half with the upper and lower halves corresponding to CDM and γCDM with $\sigma_{\text{DM}-\gamma} = 2 \times 10^{-9}\,\sigma_{\text{Th}}\,(m_{\text{DM}}/\text{GeV})$ respectively. The MW-like host haloes are labelled with the identifiers listed in Tab. 5.1.

ID	M_{vir} $[10^{12}\,M_\odot]$	V_{max} $[\text{km s}^{-1}]$	$\sigma_{\text{DM}-\gamma}$ $[\sigma_{\text{Th}}\,(m_{\text{DM}}/\text{GeV})]$
AP-1	1.916	200.3	$0,\ 2 \times 10^{-9}$
AP-2	1.273	151.5	
AP-3	0.987	157.9	$0,\ 2 \times 10^{-9}$
AP-4	0.991	163.0	
AP-5	2.010	167.5	$0,\ 2 \times 10^{-9}$
AP-6	1.934	165.1	
AP-7	1.716	163.7	$0,\ 10^{-10},\ 10^{-9},$
AP-8	1.558	193.3	$2 \times 10^{-9},\ 10^{-8}$

TABLE 5.1: Properties of "zoomed" MW-like host halos (in CDM simulation runs). Halo properties for γCDM runs vary slightly within a few percent for interaction cross-sections listed here used in this study. The first column specifies the ids for each MW-like halo in our sample set, while the second and third contain their virial mass and maximal circular velocity respectively. The fourth column lists the interaction cross-sections covered by our "zoom" simulations for each Local Group candidate.

5.3 Results

Coming back to the small-scale problems, we first have a look, how we observe it in our simulations. While the projected density plot of our simulated MW candidate AP-7 in the left panel in Fig. 5.3 visualizes the problematicly high abundance of smaller structures in the vincinity of the shown MW-like halo, Fig. 5.4 quantifies this discrepancy between the predictions for CDM (blue) and observations with a subhalo-velocity-function (SHVF) for the Milky Way[16]. As we do not know the mass of the Milky Way (and M31) exactly, the left panel in Fig. 5.4 shows the predictions for the high mass end of the likely mass range. The right panel does the same for the low mass end, where the tensions are less prominent, but yet existent. In the case of the numerical predictions, the maximum circular velocities of substructures used are determined directly from the dynamics of the N-Body tracers in the simulations. The marked 2σ uncertainty region around the averaged SHVF is calculated from the spread within the sample of MW-like halos.

For observed satellites, it is not so straightforward to determine their V_{max} as their visible stellar tracers are often not only sparse and lack information about their tangential velocities, but cannot be found out to the radius R_{max} at which the circular velocity of the halo peaks. For example, for the well-studied Milky Way dwarf spheroidal satellites listed in Wolf et al. (2010b) and McConnachie (2012), the median half-light radius of $r_{1/2} \simeq 300$ pc is around a full order of magnitude smaller than the respective (extrapolated) $R_{max} \sim 1000 - 6000$ pc. Thus, as the stellar velocity dispersion data only probes the gravitational potential within the stellar extent, even under the assumption that the stars trace the underlying DM distribution perfectly, the extrapolation of the measured circular velocity V_{circ} to estimate the maximum, V_{max}, depends sensitively on the actual density profile of the halo.

If at least the line-of-sight stellar velocity dispersion anisotropy $\sigma_\star$ is known, Wolf et al. (2010b) have shown that under the assumption of a dispersion-supported profile for the stellar mass distribution, the mass lying within the half-light radius, $r_{1/2}$, depends only on the total velocity dispersion $\sigma_{tot}(r_{1/2})$ at that radius, which in turn can be approximated by its radius-averaged quantity $\langle \sigma_{tot}^2 \rangle$ which is equal

---

[16]In Sec. 5.4, we show how to obtain a similar SHVF for Andromeda. But as we used reconstructed data that potentially underestimates the true SHFV and thus overestimates the tension between the observations and CDM, we limit our discussion here to Milky Way. Nonetheless, given the similar stellar mass function found for both host halos, we do not expect the true M31 SHFV to be in significantly less tension with the numerical predictions than is case for the Milky Way.
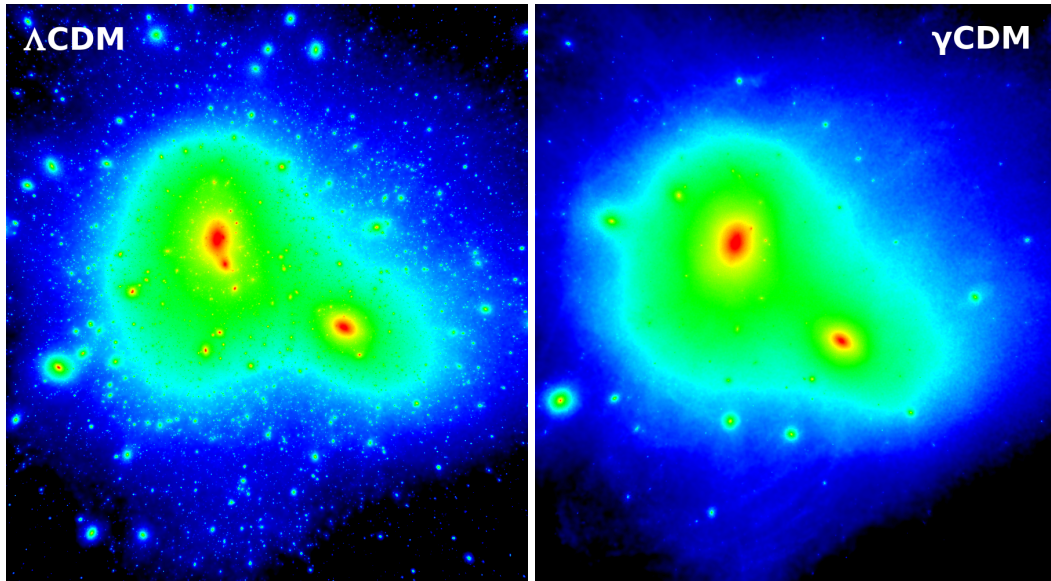
FIGURE 5.3: The simulated distribution of DM in a MW-like halo. The shading represents the projected DM density, with colours from black to red from lower to higher densities. The panels show the AP-7-HR MW-like halo in 'zoom' simulations of different cosmological models: CDM (left) and γCDM with $\sigma_{DM-\gamma} = 2 \times 10^{-9}\, \sigma_{Th}\, (m_{DM}/\text{GeV})$ (right). The large number of subhaloes observed in the left panel illustrates the MW satellite problem. By replacing CDM with γCDM, the number of subhaloes is reduced dramatically to the point where it matches observations for a particular value of the interaction cross-section.

to the known line-of-sight stellar velocity dispersion $\sigma_\star = \frac{V_{circ}(r_{1/2})}{\sqrt{3}}$. By definition, this yields

$$V_{\max} \geq \sqrt{3}\sigma_\star\,. \tag{5.1}$$

A common assumption in the literature is that both sides of Eq. 5.1 are equal (Klypin et al., 1999), which is only true if R_{max} is of the same size as $r_{1/2}$. This is obviously not the case for the smaller satellites found in the Milky Way. For our discussion here, this approximation suffices, but for the determination of the cross-section limit in Sec. 5.4, we keep in mind that we most likely tend to underestimate $V_{\max}$ this way.

We also have to take certain limitations of the surveys used to obtain the observed abundance of satellite galaxies into account. As the most massive satellites in the MW are expected not to fail to form stars efficiently (Boylan-Kolchin et al., 2011) which results in them being expected to have a high brightness and thus an easy detectability, we can assume that our observations are complete for the mass/velocity ranges they lie in. On the other hand, most of the smaller MW subhalos ($V_{\max} \leq 10$ km/s) were only detectable by modern, sensitive sky surveys, in particular, the *Sloan Digital Sky Survey* (SDSS) (Alam et al., 2015). Since SDSS (DR12)
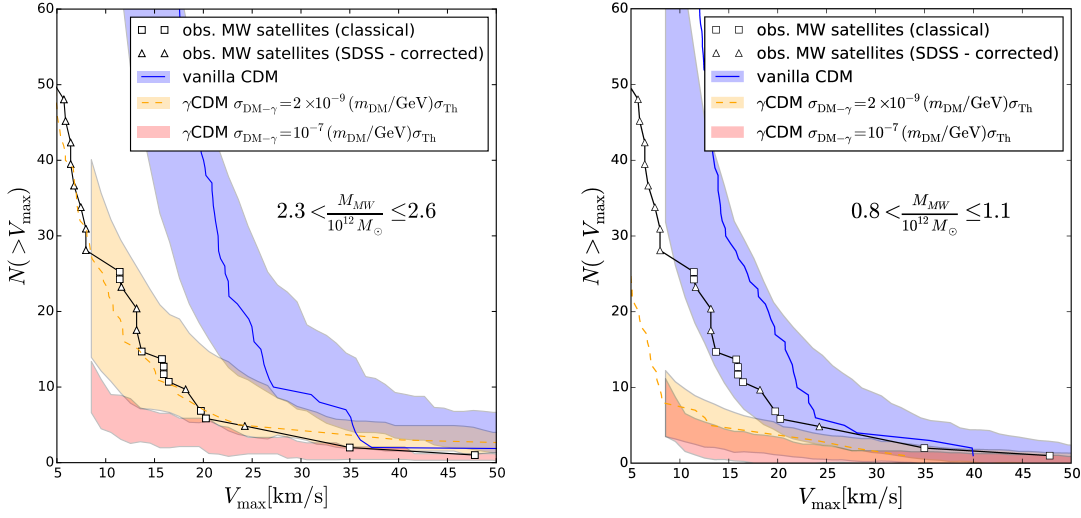
FIGURE 5.4: The number of satellite galaxies in a MW-like DM halo as a function of their maximum circular velocity: simulation results are shown for CDM and γCDM with $\sigma_{DM-\gamma} = 2 \times 10^{-9} \sigma_{Th} (m_{DM}/GeV)$ (yellow) and $\sigma_{DM-\gamma} = 10^{-8} \sigma_{Th} (m_{DM}/GeV)$ (red). The lines and shading show the mean cumulative number counts of MW satellites for a simulated DM halo in the lowest mass bin $M_{MW} = (0.8 - 1.1) \times 10^{12} M_\odot$ (right panel) and highest $M_{MW} = (2.3 - 2.7) \times 10^{12} M_\odot$ (left panel) respectively with the 1σ uncertainty showing the spread in the sample set. The lines in the left and right panel refer to the SHVF of the heaviest and lightest MW-like halos in our LG candidates, AP-3 and AP-4, respectively. Also plotted are the observational results (Willman 2010, solid black lines), which are corrected for the completeness of the Sloan Digital Sky Survey coverage. The maximum circular velocity, V_{max}, is selected as a measure for the mass and is determined directly from the simulations (for the observations it is derived from the observed stellar line-of-sight velocity dispersions using the assumption that $V_{max} = \sqrt{3}\sigma_\star$; Klypin et al. 1999).

does not cover the whole sky, but only 14,555 square degrees, i.e. about a third, of it, we have to correct the observed number counts accordingly. There is an ongoing discussion about the anisotropy of the distribution of satellite galaxies within halos (Ibata et al., 2013; Cautun et al., 2015), but we assume for simplicity that the number density of substructures in the unobserved areas is about the same as in the observed ones, thus resulting in a weight of 2.85 for all SDSS satellites. This can be justified using the results of cosmological N-body simulations that have shown that preferentially flattened satellite distributions are indeed restricted to the brightest satellites, and that as fainter and fainter populations are considered, their distributions become increasingly isotropic (Wang et al., 2013). There are further limitations to the detectability of satellites in the SDSS survey, mainly resulting from the depth of the survey. The SDSS survey can only be considered to be complete for satellites within the virial radius of the MW halo and with an absolute magnitude of $M_V \geq -6$ (Koposov and Belokurov, 2008). This not only limits the minimal dy-

namical mass for which we can assume completeness, but may also lead to missing massive satellites in the survey if their brightness is lower due to a lower star formation efficiency. Similarly, the surveys of Andromeda satellites are only complete for halos containing stellar masses of about $10^5 M_\odot$ (Sawala et al., 2015). Here, we ignore such corrections, but keep in mind that the observed satellite counts potentially underestimate the abundance of MW and M31 substructures.

Now let us see, how the included interactions affect the number of substructures predicted to be found in Milky Way-like halos. As seen in the "global" abundance studies of small halos (cf. Ch. 4)), the presence of early-time interactions between DM and neutrinos or photons and the reduction in the power spectrum below a characteristic scale, (partially) erases the seeds of the substructures lying below this cut-off and thus reduces the abundance within the host halos. We have also already shown in Sec. 4.2.3 that this suppression is independent of the environment, so it is not surprising that we observe a similar reduction in the subhalo abundance within the MW-like host halos as well. This can be seen qualitatively by comparing the two projected density plots for AP-7 (Fig.5.3) and qualitatively by comparing the SHVF plots for the IDM models (red, yellow) in Fig.5.4 with the observations.

Having found a way to reduce the abundance of the smaller substructures to fix the MSP, we now turn to the largest satellites that are troubled by the TBTF problem. In Chapter 4, we discussed how the concentration of DM halos is affected by early interactions of DM with photons and neutrinos, which delay the halo formation time. So we have to confirm if this holds for MW/M31 substructures as well. For that purpose, we reproduced in Fig. 5.5 the $V_{\max} - R_{\max}$ scatter plot of Boylan-Kolchin et al. (2011) with our own simulation data. To obtain the confidence bands for the observed MW satellites, we used the measured stellar line-of-sight velocity dispersion $\sigma_\star$ in order to obtain a lower bound on $V_{\max}$. Assuming a NFW profile for the satellites, both sides in Eq. 5.1 are equal if and only if the radius $R_{\max}$ of the maximum velocity dispersion coincides with the de-projected half-light radius $r_{1/2}$. Otherwise we get a branch in the $V_{\max} - R_{\max}$ plane for each of the other two possible cases of a lower and higher $R_{\max}$ where $V_{\max}$ exceeds this lower bound. Fig.5.5 includes the extrapolated $V_{\max}$ 1σ confidence region of the brightest dwarf galaxies in the MW (left panel) as well as M31 (right panel) using observational data from McConnachie (2012)[17]. For the MW, the Magellanic Clouds and Sagit-

---

[17]For the half-light radius of Ursa Minor, we replace the value in McConnachie (2012) with a fit found in Wolf et al. (2010b).
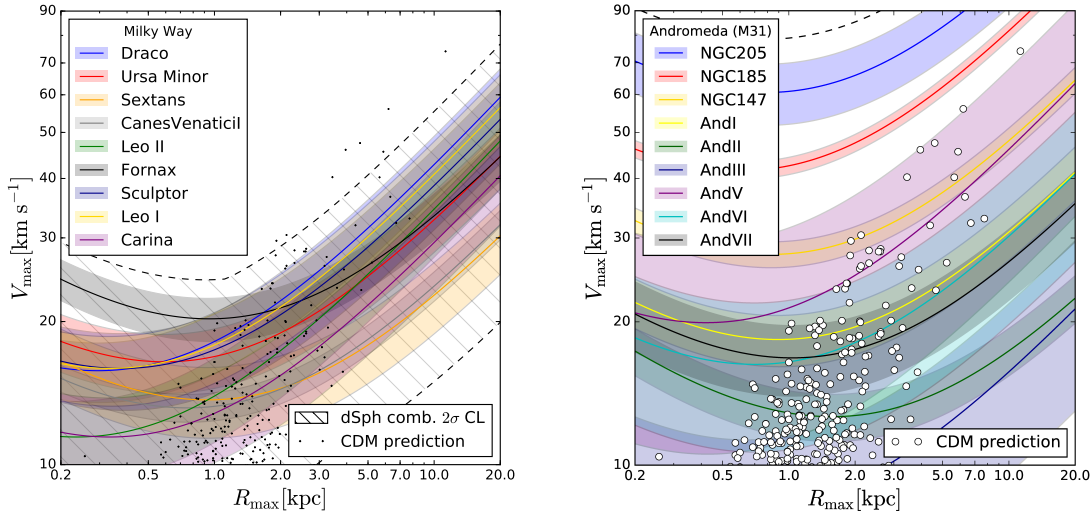
FIGURE 5.5: The "Too big to fail problem" in vanilla CDM: V_{max}-R_{max} plot with 1σ confidence interval for the 9 brightest dwarf galaxies of the Milky Way (left panel) and Andromeda (right panel) derived from the observational data and its uncertainties found in McConnachie (2012). For comparison, the numerical predictions for our MW-like host halo AP-1 in a vanilla CDM model are marked with circles while the 2σ confidence interval for all MW dwarfs combined has been marked by the hatched area.

tarius have been omitted while for Andromeda, M33 is not shown due to its exceptionally large size. For the MW, we also marked the 2σ combined confidence region for all these satellites defined by these bands Wolf et al. (2010b). We then included the predictions for a MW/M31-like host halo in the standard CDM model for comparison. For the Milky Way, we can clearly see that a significant fraction of our simulated subhalos display a peak in circular velocity (V_{max}) that is too high and/or too close to the centre and that in general, we obtain far too many massive, concentrated subhalos to be populated by the satellites found in the Galaxy. Even for M31, where there are more massive dwarf spheroidals than in the Milky Way, we still predict far too many massive subhalos to match them with observed satellites at such high V_{max}.

Reducing now the concentration and mass with IDM as seen in Ch. 4 would drive R_{max} up and thus ease the tension seen in Fig.5.5. In order to study this effect on single halos and their subhalos more closely, we identify matched halos pairs in the vanilla CDM and interacting DM simulations and compare their mass parameter. We show the results of this comparison in Fig.5.6, where we plot the respective properties for the halo pairs found in the full 30 Mpc/h cosmological box run as well as in the Local Group 'zoom' re-simulation. While there is a significant scat-
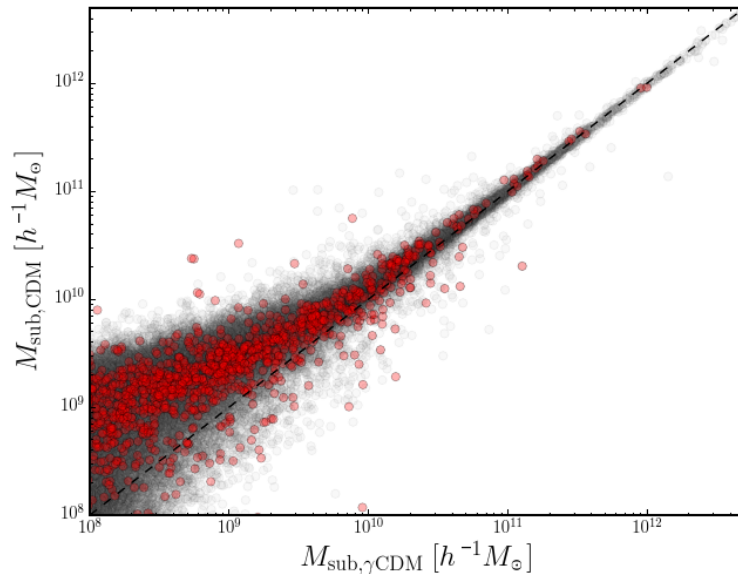
FIGURE 5.6: Comparison of properties for matched halo pairs in CDM and γCDM ($\sigma_{\mathrm{DM}-\gamma}$ = $10^{-9}\,\sigma_{\mathrm{Th}}\,(m_{\mathrm{DM}}/\mathrm{GeV})$): We show the (sub)halo mass for all halo matches in our 30 Mpc/h "un-zoomed" box runs (unfilled circles), the matches for subhalos inside MW-like host halos thereof (red, filled circles) and the matches for the substructures found in our four "zoom" Local Group re-simulations.

ter, most γCDM sub(halos) within the MW subhalo mass range are lighter (and less concentrated) than their vanilla CDM counterparts. This is exactly the result needed to solve the second small scale challenge faced by CDM. The reduced mass lowers the rotation curves, while the lower concentration moves R_{max} out to higher values, thus lowering the circular velocities for all radii below R_{max}. As a result, the γCDM rotation curves shown in red in Fig. 5.7 (left panel) are now in significantly better agreement with the observed data compared to the vanilla CDM predictions.

We obtain the same results if we use the $V_{\mathrm{max}} - R_{\mathrm{max}}$ values which are directly measured for our predicted halos instead of their rotation curves. The right panel in Fig.5.7 shows the results for all 8 "zoom" MW/M31 candidates in the γCDM re-simulations at a cross-section of $\sigma_{\mathrm{DM}-\gamma} = 10^{-9}\,\sigma_{\mathrm{Th}}\,(m_{\mathrm{DM}}/\mathrm{GeV})$ on top of the same 2σ confidence interval as seen in Fig.5.5. Significantly fewer simulated subhalos lie outside the confidence region of the observed "classical" MW dSph satellites. If we increase the cross-section as shown in Fig.5.8 for AP-7 and AP-8, we can see how these subhalo properties change. At the same time, we also notice how we actually run out of candidates to match the observed satellites as the abundance of satellites is significantly reduced for the most extreme cross-sections studied (cf. 5.1.1).
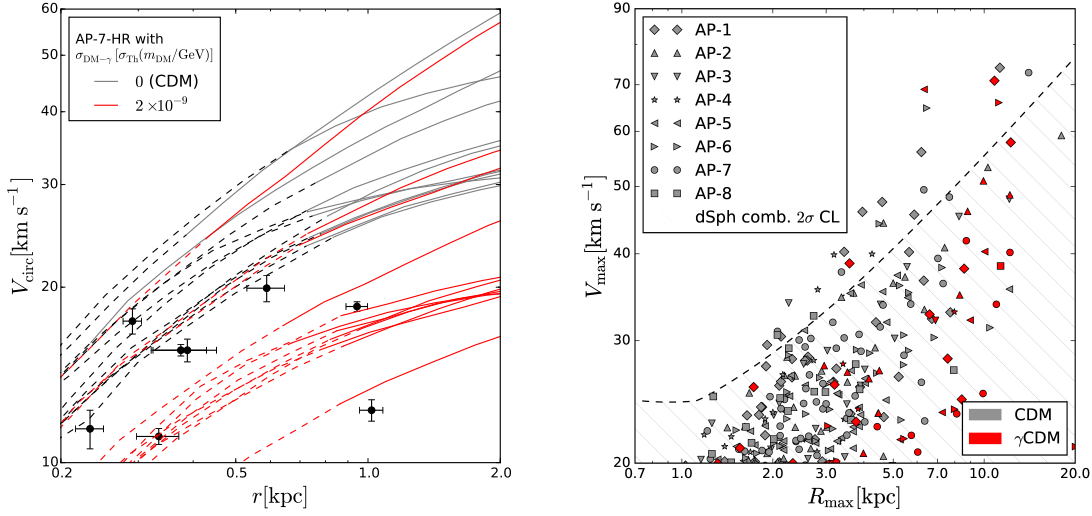
FIGURE 5.7: "Too big to fail problem" solved by γ CDM: (left panel) rotation curves and observed half-light radius/stellar velocity dispersion of the 11 most massive subhalos in AP-7-HR for CDM (black lines) and γCDM ($\sigma_{\mathrm{DM}-\gamma} = 10^{-9}\,\sigma_{\mathrm{Th}}$ ($m_{\mathrm{DM}}/$GeV, red lines) combined with a scatter plot of the half-light radii and circular velocities of the "classical" MW dwarfs (circles) and M31 dwarfs (squares). The dotted extensions of the rotation curves mark the regions where the circular velocity can still be measured in the simulation, but convergence cannot be guaranteed (cf. Power et al. (2003)). For the same models, the $V_{\mathrm{max}} - R_{\mathrm{max}}$ plot for all halos in the "zoom" LG candidates also shows significant less tension as fewer predicted halos can be found outside the 2σ confidence interval for the MW dwarf galaxies (hatched region).

5.4 Constraints on the DM interaction cross section

We have shown in the previous section, how the small-scale challenges to standard CDM may be "solved" by including interactions between the dark matter and standard model particles such as photons or neutrinos. Unfortunately, we cannot use these results as a proof for the presence of such interaction since other alternative DM models like SIDM, WDM or feedback in hydro simulations (cf. Sec. 5.5) have all similar effects on the predicted observables studied here and breaking this degeneracy is beyond the scope of this thesis. But we can nonetheless learn something about the nature of dark matter by turning the question around and asking ourselves instead, whether we can rule out certain areas in the parameter space for such extended DM models and IDM in particular.

In the case of the satellite abundance, the changes to DM by any of the alternative models either reduce the number of predicted DM subhalos (WDM, IDM) or their efficiency to form stars, thus rendering them too faint to be detectable by today's surveys. Thus, while ignoring the effects contributed by those alternative
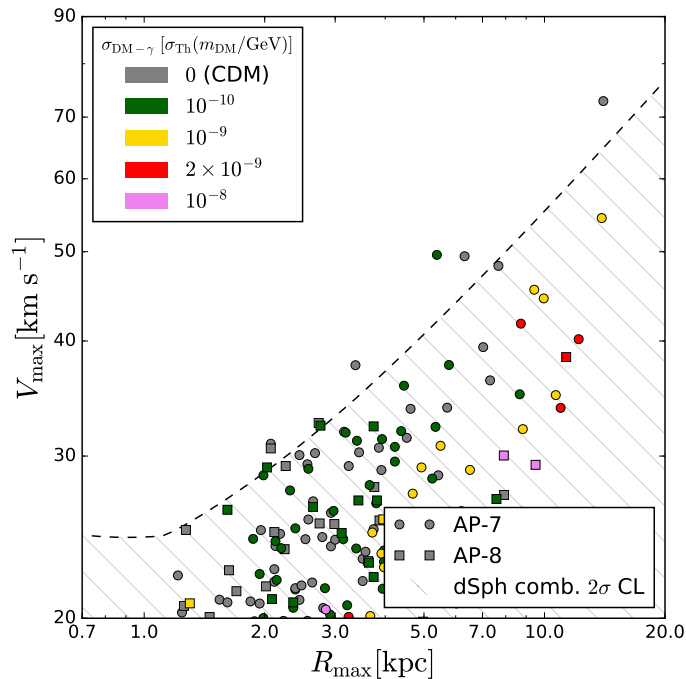
FIGURE 5.8: The "Too big to fail problem" solved by γ CDM: V_{max}-R_{max} plot for AP-7 and AP-8 for various cross-sections, as labelled, with the hatched region marking the 2σ confidence interval for the observed MW satellites as introduced in Fig. 5.5

models in our predictions, it is still valid to ask what the maximum cross-section is that is still allowed to obtain at least the observed satellite galaxies within the MW host halo.

Tidal Dwarf Galaxies aside, which originate from the fragmentation of gas-rich tidal streams within the host galaxy (e.g. Bournaud (2010)), the only way for the observed MW satellite galaxies to form is inside a DM halo of their own. Thus, the number of (invisible) DM subhalos naturally limits the number of visible, observable galaxies. Before we use this argument to determine the maximal suppression of the number of substructures allowed before running out of predicted hosts for observed satellites, we want to extend the observational data set, we already discussed in Sec. 5.1.1, using the data obtained from our second large host halo with the Andromeda Galaxy (M31) in its centre.

Unfortunately, for 14 out of the known 33 satellites of M31, a measurement of the stellar velocity dispersion $\sigma_\star$ is not yet available. As we need this information to compose the complete SHFV, we try to exploit the relation between the dynamical mass and the measured absolute visual magnitudes M_v of the satellite galaxies

that can been observed in both the Milky Way and M31 (McConnachie, 2012); the result for this exercise is plotted in Fig. 5.9(left) combined with a log-linear fit of the available data for M31.

It has been previously found in studies with semi-analytical models (Font et al., 2011) as well as hydrodynamical simulations (Sawala et al., 2014), that the star formation efficiency is mass-dependent with smaller halos being less efficient. This also affects the log-linear relation between the brightness and dynamical mass as it reduces the absolute magnitude M_v associated with substructures at smaller masses. This effect is observable as an asymmetric scatter with data points spread out further above the fit. For constraints on the cross-section, we only have to worry about not overestimating the substructure abundance above a certain velocity/mass threshold. Thus, we simply assume that the M31 satellites, for which we have to reconstruct the dynamical mass, satisfy in the worst-case this relation within at most a 2σ confidence region around it. Knowing their available half-light radii, we can then determine a lower bound on their stellar velocity dispersion. By using Eq.5.1, we finally obtain a lower estimate on $V_{\max}$. The cumulative subhalo-velocity function (SHVF) including the reconstructed satellite data for Andromeda as well as sky coverage corrections for the Milky Way is shown in the bottom panel in Fig.5.9. In that figure, we also plot the stellar mass function for comparison, which can be obtained from the absolute magnitude measurements in McConnachie (2012) by assuming a mass-to-light ratio of 1. According to recent studies, the Andromeda halo mass (e.g.Sofue (2015)) seems to be at least equal to the Milky Way mass if not significantly larger. The stellar mass function shown seems to support this as the cumulative abundance for M31 exceeds the one for the Milky Way if the latter is corrected for SDSS sky coverage. In order to obtain a SHVF of at least that magnitude, we would have to push our reconstructed data points for the dynamical mass in Fig.5.9 (left) well above our measured log-linear relation. While this potentially underestimated SHVF is still usable for the purpose we need it for, i.e. a conservative constraint on the interaction cross-section, it is worth to briefly discuss possible explanation for its occurrence.

- The M31 satellites with measured dynamics already reveal a much larger spread for even larger dynamical masses compared to those found in the Milky Way. This could be evidence that at least some subhalos have a significantly lower star formation efficiency than the known MW satellites, which would result in a much higher actual dynamical mass for their measured brightness.
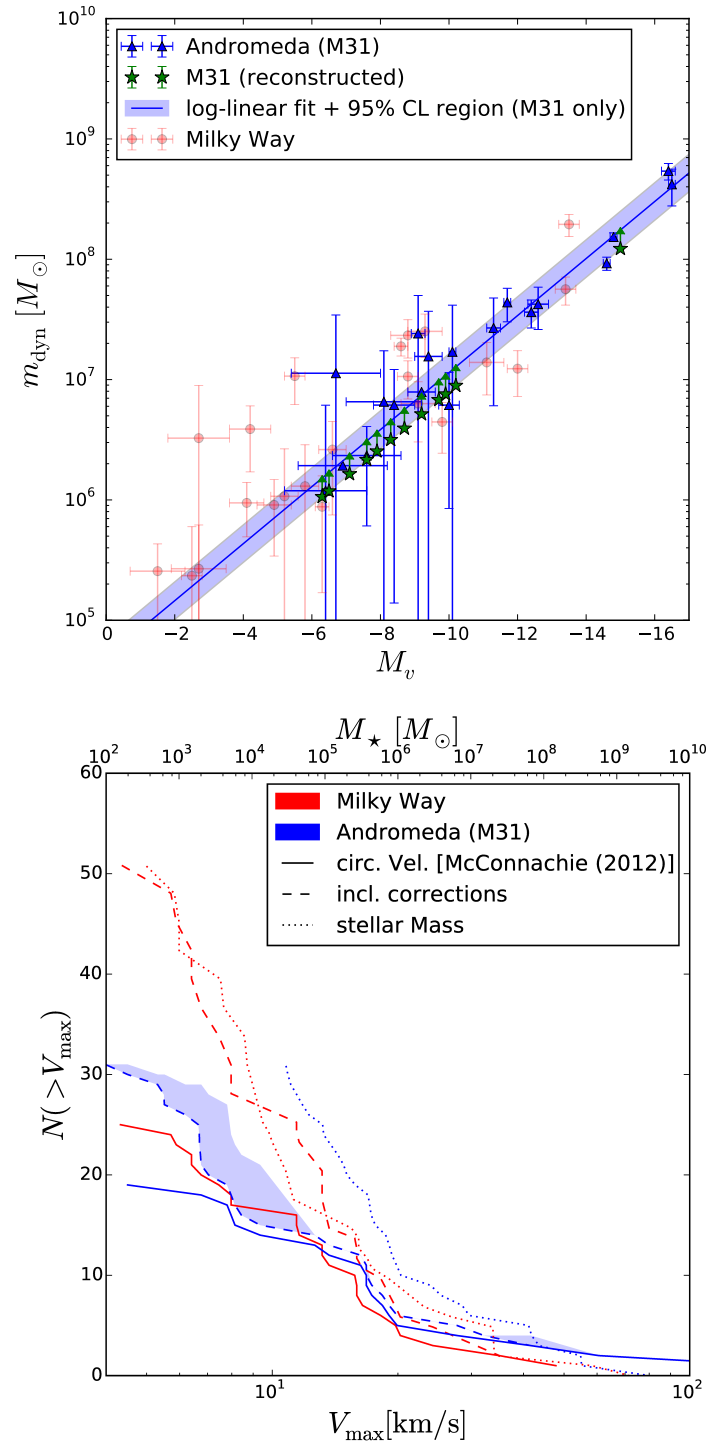
FIGURE 5.9: Reconstruction of the Subhalo-Velocity Function for M31: (top panel) Absolute Magnitude-Dynamical Mass relation. All satellites with dynamical information are plotted and are used in the log-linear fit. Lower bounds for the M31 satellites without measured dynamical mass are added at the 2σ confidence level of the fit. For comparison, we also plot the data points for MW satellites (red circles). (bottom panel) Cumulative Subhalo-Velocity function for the observed Milky Way and M31 satellites as well as with correction for sky coverage and the estimated dynamical mass for MW and M31 respectively. The blue, shaded area marks the region of uncertainty that corresponds to the confidence region in the log-linear fit. Additionally the figure contains the cumulative subhalo-solar mass function.

- Alternatively, there could be a bias in the measurement of the half-light radius $r_{1/2}$ for M31 satellites as the extend of satellites in M31 is more difficult to determine due to the much higher distance they are observed at and could lead to to smaller $r_{1/2}$ as contributions of stars at the edges of the satellite galaxies are missed. This would affect the calculation of $\sigma_\star$ and, consequently, of V_{max}. As the expected dynamical mass is about twice as large as the one derived from our reconstruction method, this systematic inaccuracy would have to be significant.

- As discussed, Eq.5.1 only provides a lower estimate for V_{max}, only being an equality if r_{max} coincides with the measured $r_{1/2}$. Since we use this approximation both for the smaller MW satellites as well as for those of M31, those two sets would have to have significantly different mass profiles to account for this discrepancy.

- Another possible explanation for the tension between the corrected MW and M31 SHVF is that the distribution of MW satellites is not isotropic as assumed for the sky coverage applied here and the regions of the sky not covered by SDSS contain much fewer satellites than the observed regions. This would result in a lower corrected cumulative abundance for MW satellite.

While the second explanation can be blamed on systematic measurement errors, the other two would require an explanation for the fact that their satellites, despite lying is such similar host halos, would show such different properties.

With our lower bounds for the SHVF, we can now constrain the interaction cross section by comparing the observed and predicted numbers of substructures. The uncertainties in the simulation results are derived from the spread in the sample sets (for each host halo mass bin), while for the observations, the Poisson error of the counting process is given by the square-root of the total number counts in both host halos. A model is ruled out if the number of predicted subhaloes is smaller than the observed number within a combined 2σ uncertainty region of these observables (see Fig.5.10(left)). We also included our "zoomed" MW candidates as data points within the according mass bins, but we only consider them for the constraints in the two mass bins where the two MW candidates AP-7 and AP-8 belong to as those are the only one, for which we have a full set of re-simulations with varying cross-sections.

As we are potentially underestimating V_{max} for observed satellites as well as their abundance due to some ignored corrections (cf. Sec.5.1.1), these bounds may
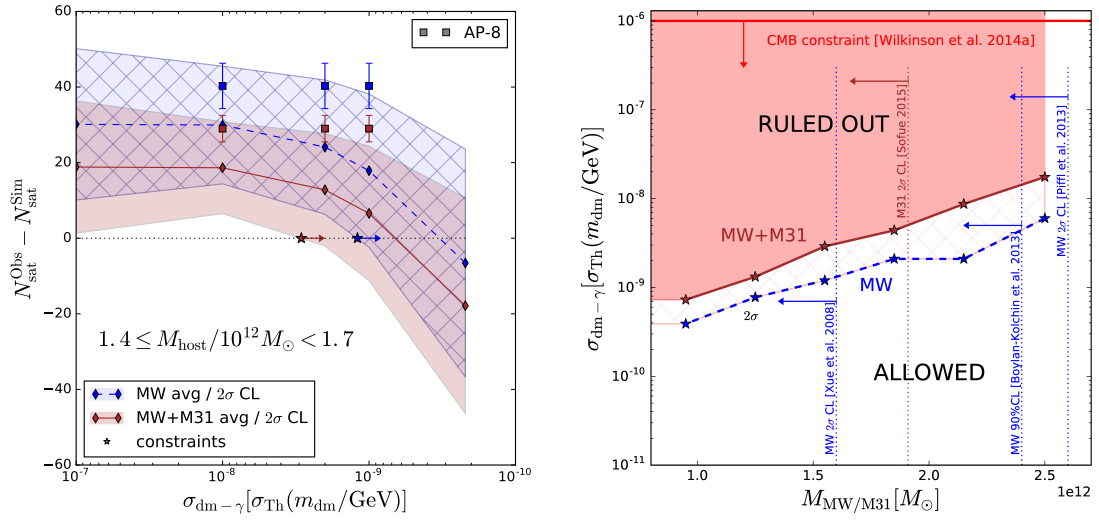
FIGURE 5.10: Constraints on the γCDM cross section. Left panel: the over-abundance of satellites predicted in the simulations for the Milky Way (dashed line) and combined MW/M31 (solid line) versus the cross section for the MW/M31 halo mass bin $(1.4. - 1.7) \times 10^{12} \mathrm{M}_\odot$, where the blue hatched and brown shaded bands represent the 2σ uncertainties for the two data sets. The results for AP-8, which lies in this mass bin, are also shown as well for comparison. Right panel: constraints on the cross section are plotted with respect to the MW/31 halo mass for the Milky Way alone (dashed line) and for the combined MW/M31 data set (solid line). For the combined MW/M31 data set, we assume an identical mass for both halos. The most recent CMB constraint (Wilkinson et al., 2014a) and selected upper mass bounds for the MW and M31 halo are shown for comparison.

be even tighter, but definitely not weaker. From this, we conclude that based on the MW data alone the cross section does not exceed

$$\sigma_{\text{DM}-\gamma}^{\text{MW}} \leq 6.0 \times 10^{-9} \, \sigma_{\text{Th}} \, (m_{\text{DM}}/\text{GeV}) \tag{5.2}$$

at a 2σ confidence level[18], which constitutes an improvement of about 2-3 orders of magnitude compared to recent CMB constraints (Wilkinson et al., 2014a). If the Milky Way halo turns out to be lighter than the 'worst-case' scenario considered for this result, then the constraints may tighten by a whole order of magnitude as shown in the compilation of the constraints for all considered halo mass bins in the right panel of Fig. 5.10.

For the combined Milky Way/Andromeda analysis, we assume that the Andromeda halo is of the same mass as the MW halo. This is a valid approach for obtaining conservative constraints as it simply fixes the maximum mass of the two host halos and any lower mass for one or the other will reduce the abundance of predicted subhalos and thus tighten the constraints obtained. We also consider the same allowed mass range for M31 that we used for the Milky Way before. This is done account for those mass constraints published in the recent past beyond those shown in the plot that still allow for such high masses for both halos (e.g. Fardal et al. (2013)). This gives us an upper bound on the constant DM-photon interaction cross-section of

$$\sigma_{\text{DM}-\gamma}^{\text{MW+M31}} \leq 1.75 \times 10^{-8} \, \sigma_{\text{Th}} \, (m_{\text{DM}}/\text{GeV}) \, . \tag{5.3}$$

It should be noted though that the most recent analysis on the M31 mass constraints shown in Fig.5.10 (Sofue, 2015) limits Andromeda's total mass to $M_{\text{tot,200}} \leq 19.1 \times 10^{12} M_\odot$ at a 2σ CL and that of the Milky Way to even lower values ($\leq 17.2 \times 10^{12} M_\odot$). Using this as an upper mass would bring the maximally allowed cross-section down to about the cross-section obtained for the Milky Way alone if the full mass range is considered.

While all of our results are obtained under the assumption of a constant cross-section between DM and photons, we can use them to obtain constraints for similar models such as neutrino interactions (νCDM) by identifying "identical" models by their identical half-mode scale. While Fig.3.1 reveals that the primordial perturbations for those models differ on very small scales, our studies in Ch.4 have shown that both γCDM and νCDM produce very similar halo abundances if the

---

[18]This constraint is slightly weaker than that published in Boehm et al. (2014). This deviation from our previous results mainly arises from the smaller correction factor for SDSS sky coverage used in this analysis, which takes the newer data releases into account.

corresponding cross-sections are matched according to their characteristic damping scale M_h (cf. Ch.3). This relation between the constant interaction cross-section is fitted by

$$\sigma_{DM-\nu} = (3.21/2.74)^{1/0.421} \sigma_{DM-\gamma} \, , \tag{5.4}$$

which translates into an upper bound for the constant DM-neutrino interaction cross-section of

$$\sigma_{DM-\nu}^{MW+M31} \leq 2.55 \times 10^{-8} \, \sigma_{Th} \, (m_{DM}/GeV) \, . \tag{5.5}$$

It is noteworthy that studies including a treatment of baryonic physics and thus the brightness of the satellites in their predictions may still reduce these bounds significantly. They will not have to rely on the reconstruction techniques applied here. Furthermore, they can enforce additional cuts on the predicted subhalo samples to account for limitations to the completeness in the surveys.

5.5 Conclusion

We have shown that the interacting DM model has the ability to ease tensions between the properties of the small structures observed in the Milky Way and M31 and those predicted by N-body simulation of CDM. The ability of the IDM model to erase primordial perturbations below a cross-section-dependent mass scale and thus the seeds of the excess subhalos that riddle the CDM predictions allows us to solve the MSP. The delayed formation time of the surviving halos, helps to reduce both their concentration as well as their halo mass, which both contributes to easing the tensions found for the most massive satellites in the Milky Way in the TBTF problem.

Nonetheless, this success should not be interpreted as direct evidence for the presence of such dark matter-SM interactions at early times since alternative models provide similar solutions. We have to acknowledge that the observations of the satellite population in the Milky Way as well as in M31 are limited for the reasons stated above and that the actual abundance may be highly underestimated, as the satellite galaxies used to identify the DM subhalos are either too faint or even may fail to produce stars and thus lack visible tracers. Recent numerical studies (cf. e.g. Sawala et al. (2015)) have confirmed that the velocity threshold at which the subhalo observations diverge from the predictions is close to the value at which heating of intergalactic gas by the UV photo-ionizing background should suppress gas accretion onto halos and may explain why the subhalos remain dark and thus in-

visible in current surveys. It should be noted, that all theoretical predictions, which include baryonic physics apply subgrid physics to follow processes which operate below the resolution scale such as star formation and have to use tuned parameters within these models. Additionally, the huge uncertainties about the mass of the Milky Way halo, allow us to consider a lighter host halo for our observed satellites as done in Fig. 5.4(right panel). While this is not enough to make the tension to go away, it may contribute to a solution. Thus, it would be unrealistic to claim that the MSP supports a DM model beyond the standard, collision-less CDM such as WDM, SIDM or our IDM. However, better understanding is needed of the physical constraints of those parameters in hydro simulations and semi-analytical models and of the halo mass of our Galaxy to rule out the possibility of IDM.

As with the MSP, DM interactions are not the only possible "solution" of the TBTF in CDM. A lower halo mass for our MW candidates also eases the tension. This can be seen in Fig. 5.8 by comparing the results for the two halos AP-3 and AP-4, which are among the lightest of our 8 candidates, with those of the other halos. And again, recent studies with hydro simulations have shown that also the TBTF problem can be solved in CDM by including baryonic physics in the predictions, with the gas flattening the density profile in the inner core region (Sawala et al., 2014). Alternative dark matter models such as SIDM (Vogelsberger et al., 2014) or WDM (Lovell et al., 2014) also have the potential to solve this problem. WDM faces a possible "catch-22" dilemma as the particle masses required to solve TBTF in the thermalized scenario lie below those ruled out by constraints based on the subhalo abundance (Schneider et al., 2014). So, as for the MSP we cannot consider the existence of the TBTF problem and its possible solution by interacting DM as evidence for the existence of such interactions, but we have shown how this alternative DM model may at least contribute to the necessary corrections.

Finally, we have exploited the fact, that as all those alternative DM / physics models tend to ease these problems in a similar fashion, we can use the observables in question, in particular, the abundance of satellite galaxies/substructures in the Milky Way and Andromeda to place upper bounds on the (constant) interaction cross-section in our γCDM model ($\sigma_{DM-\gamma} \leq 2.66 \times 10^{-33} \, (m_{DM}/GeV) \, cm^2$) by applying the latest upper mass bounds on MW and M31 (Sofue, 2015). We also derive constraints for νCDM ($\sigma_{DM-\nu} \leq 3.86 \times 10^{-33} \, (m_{DM}/GeV) \, cm^2$) by exploiting the relation found between the characteristic cut-off scales of both interaction models. In both cases, it is interesting to note that our upper bounds on the interaction cross-section for high-MeV particle masses happen to be of the same order

of magnitude as the weak interaction cross-section. This agrees with premise of the WIMP miracle (cf. Ch. 3 and results in the correct relic abundance for the DM after the interaction has frozen out.
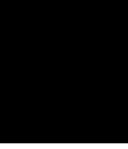
NEUTRINOS - THE KNOWN DARK MATTER

CHAPTER 6

CνB - relic neutrinos in the Universe

This chapter is dedicated to discussing the properties and role of neutrinos in the cosmic evolution in detail. This includes a description of their decoupling, abundance and free-streaming as well as the implications of them being massive. We present results by solving the linearised Boltzmann equations as an illustration of how neutrinos affect the evolution of the Universe before the collapse of non-linear structures.

6.1 Thermal History

6.1.1 Neutrinos in Cosmology

Relic neutrinos, which are an important product of the standard hot Big Bang, play a significant role in the evolution of the Universe. Fig. 6.1 lists certain "historical" events that are important for neutrinos in the context of cosmology and are discussed in the following sections in detail.
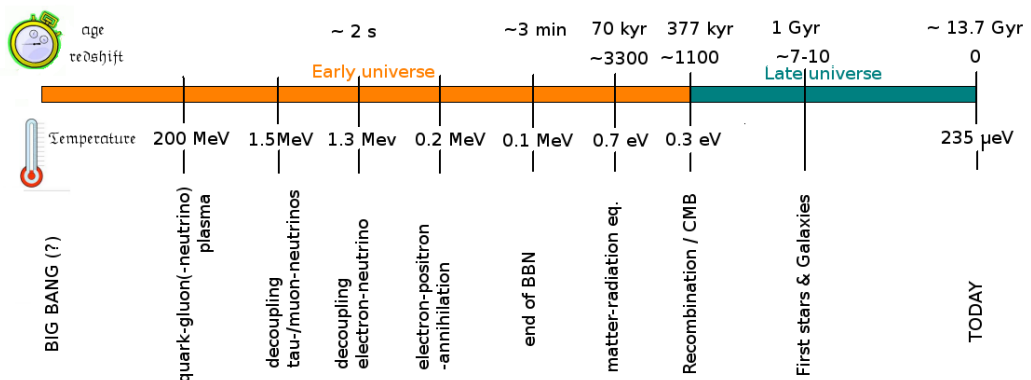
FIGURE 6.1: Timeline of the Standard model of the Universe.

Early Universe / Thermal history

In the first second of the history of the Universe, at temperatures T_γ of the primordial plasma of above 1 MeV, neutrinos were in thermal equilibrium through weak interactions with other particles (see Sec. 2.1.1). Because of the small number density of nuclei with respect to leptons, interactions with quarks bound in the nucleons were negligible. Among the leptons, the interactions with electrons and positrons dominated the interactions of neutrinos with the charged leptons as many muons and tauons had already decayed through the charged-current channel of the weak interaction into either charged leptons plus the corresponding (anti-)neutrinos or, in the case of the heavier tauon, also into hadrons. Thus, of all the possible interactions, the only ones of interest for the coupling of neutrinos with the rest of the Universe at that time are the neutral-current annihilation/production

$$\nu_f + \nu_f \leftrightarrows e^+ + e^- \, , \tag{6.1}$$

with $f \in \{e, \nu, \tau\}$, the neutral-current elastic scattering

$$\overset{(-)}{\nu_f} + e^\pm \leftrightarrows \overset{(-)}{\nu_f} + e^\pm \, , \tag{6.2}$$

and the charged-current weak elastic scattering

$$\overset{(-)}{\nu_e} + e^\pm \leftrightarrows \overset{(-)}{\nu_e} + e^\pm. \tag{6.3}$$

Neutrinos come out of thermal equilibrium with their cosmic environment when the rate of change of the temperature of the Universe $|\dot{T}_\gamma|/T_\gamma$ exceeded their interaction rate Γ with the environment, i.e. in this case with the thermalized electrons and positrons. Since $T_\gamma \propto a^{-1}$, this leads to the *freeze-out condition* given by (cf. Sec. 2.2.6)

$$\Gamma \sim H \Rightarrow n\langle \sigma v \rangle \propto G_F^2 T_\gamma^5 \sim H \, , \tag{6.4}$$

with $n \propto T_\gamma^3$ being the relativistic number density, $\sigma \propto G_F^2 T_\gamma^2$ the combined cross-section of the scattering and annihilation interaction modes in Eq. 6.1, Eq. 6.2 and Eq. 6.3, G_F the Fermi constant and $v \sim 1$ is the relativistic neutrino velocity in units of c. Expressing the expansion rate H at this still radiation-dominated era in terms of the Planck mass m_{pl}

$$H \propto \frac{T_\gamma^2}{m_{pl}} \, , \tag{6.5}$$

yields an approximate decoupling temperature of

$$T_\gamma^{\nu,\text{decoupling}} \propto (m_{pl}G_F^2)^{-\frac{1}{3}} \sim 1\,\text{MeV}\,. \tag{6.6}$$

While this is a rough approximation, more precise calculations considering the different interactions for electron-neutrinos and the other two flavours (Dolgov, 2002) lead to

$$T_\gamma^{\nu_e,\text{decoupling}} \sim 1.34\,\text{MeV} \qquad T_\gamma^{\nu_{\{\tau,\mu\}},\text{decoupling}} \sim 1.5\,\text{MeV}, \tag{6.7}$$

i.e. a slightly earlier decoupling time for the muon- and tauon-neutrinos as they do not participate in all the weak interactions.

Once neutrinos are out of thermal equilibrium, they are not reheated at the point of electron-positron annihilation and therefore end up with a lower temperature than the CMB photons given by

$$T_\nu = \left(\frac{4}{11}\right)^{1/3} T_\gamma\,. \tag{6.8}$$

This relation between photon and neutrino temperature also allows us to quantify the neutrino content in the Universe. For any light neutrino (that decouples while still being relativistic), the present-day number density of neutrinos and anti-neutrinos is related to the present cosmic background photon density n_γ by

$$n_\nu + n_{\bar{\nu}} = \frac{3}{2}\frac{\zeta(3)}{\pi^2}(T_\nu)^3 = \frac{6}{11}\frac{\zeta(3)}{\pi^2}(T_\gamma)^3 = \frac{3}{11}n_\gamma \sim 112\,\text{cm}^{-3}\,, \tag{6.9}$$

with $\zeta(\cdot)$ being Riemann's Zeta function. Thus, assuming a mass m_i for each massive neutrino state, the present energy density of light massive neutrinos is given by

$$\Omega_\nu^0 h^2 = \frac{\sum_i m_i (n_\nu + n_{\bar{\nu}})}{\rho_{\text{crit}}^0}h^2 \sim \frac{\sum_i m_i}{94.14\,\text{eV}}\,, \tag{6.10}$$

where ρ_{crit} is the critical density of the Universe today and h is the reduced Hubble constant.

It should be noted, that neutrinos in the early Universe, while still being relativistic, contribute as an additional radiation component. This has consequences not only for the time, t_{eq}, of *matter-radiation equality*, which affects the growth of density fluctuations and leaves an imprint on the CMB and in structure formation in the late Universe, but also influences BBN by altering the expansion rate around

neutron freeze-out. The latter effect is measurable in the neutron-proton-ratio of the Universe and allows us to make a prediction about the number of neutrino species N_ν (or other additional relativistic components at BBN).

Late Universe / Free-streaming

After decoupling, neutrinos remain relativistic for some time before they are adiabatically red-shifted to a temperature below the relativistic regime at $T_\nu \approx \frac{M_\nu}{3}$. Their velocity distribution at the decoupling obeys the Fermi-Dirac (FD) distribution $f(p)$

$$f(q) = \frac{1}{e^{q/T_\nu} + 1} \, , \tag{6.11}$$

where q is the momentum and T_ν the temperature of the neutrinos. This not only causes many neutrinos to remain in the relativistic regime longer than others, but also gives rise to slow neutrinos that are available for clustering. Fig. 6.2 shows the velocity distribution of neutrinos and Cold Dark matter (CDM) obtained from a simulation at an early and later redshift. It can be seen that the neutrino velocities
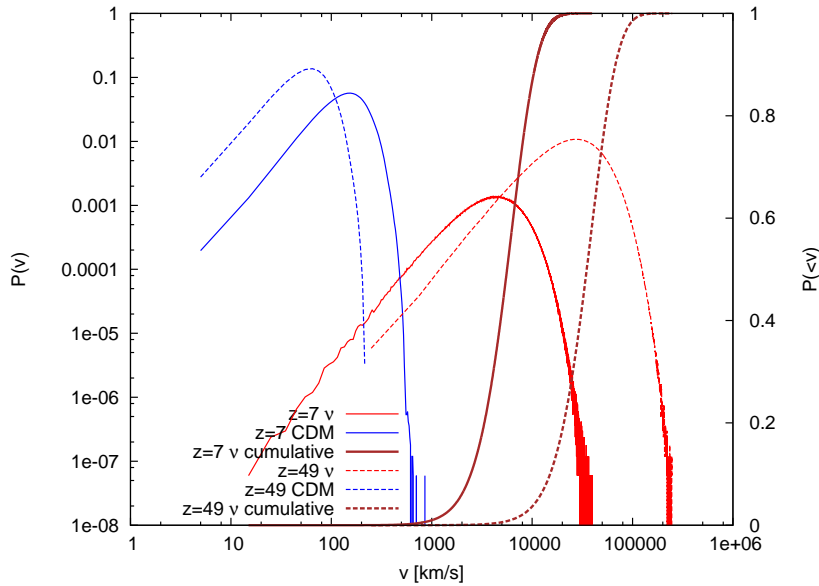
FIGURE 6.2: Differential ($P(v)dV$) and cumulative ($P(< v)$) velocity distribution at redshifts $z = 49$ (solid) and $z = 7$ (dashed) for neutrinos (red,violet) and CDM (blue) respectively.

exceed by far the velocities of the CDM which are induced by gravitational interactions.

The most important feature of neutrinos is their large streaming scale due to a

lack of any thing other than a gravitational interaction with their environment and their high average velocities. The corresponding comoving redshift-dependent free-streaming wave number is given by

$$k_{fs} = \sqrt{\frac{3}{2}} \frac{H(z)}{v_{th}(1+z)} \begin{cases} H(z), & \text{relativistic, high z} \\ (1+z)^{-1/2}, & \text{non} - \text{relativistic} \end{cases} \quad (6.12)$$

Fig. 6.3 shows the evolution of the free-streaming length. It can be seen that there
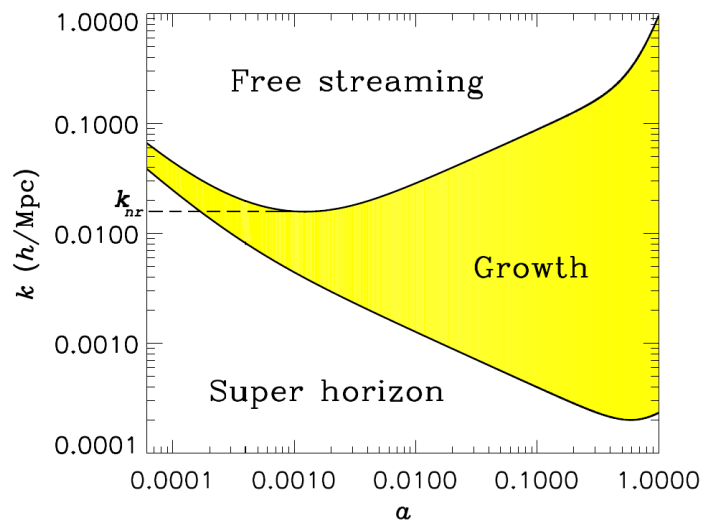
FIGURE 6.3: Free-streaming scale of cosmic neutrinos: The upper black line is the comoving neutrino free-streaming scale k_{fs}, above which structure formation is suppressed while the lower line is the comoving Hubble scale, aH. The maximal free-streaming scale k_{nr} has been thereby marked (Hannestad, 2010).

is a minimal free-streaming wave vector k_{nr} located at approximately the redshift where neutrinos become non-relativistic. On scales smaller than k_{fs} neutrinos cannot cluster due to the free-streaming (except for a smaller number in the low velocity tail of the FD distribution). While on scales larger than k_{nr} neutrino perturbations are not affected by the free-streaming and grow like their CDM counterparts. This is observable e.g. in the matter power spectrum as it leads to a loss of power on small scales that depends on the mass of the neutrinos (see Sec. 6.3.2). Taking our upper (lower) mass bound into account, this gives us a scale range for this effect of $k = 0.002 - 0.04 \ (0.013 - 0.57)h/\text{Mpc}$ where the lower bound is given by k_{nr} and the upper bound by present day k_{fs}.

6.2 Linear Theory

To study the evolution of the linearised phase-space distribution for massive neutrinos of mass m, we use the results derived in Sec. 2.2.6. These particles are governed by the linearised collision-less Boltzmann equation given by Eq. 2.51, where the RHS vanishes for collisionless particles. The unperturbed neutrino distribution f_0 of the particle momenta for the neutrinos is given by the relativistic form of the Fermi-Dirac distribution as they decouple while being highly relativistic:

$$f_0(q) \sim \frac{1}{\exp(q/aT(a)) + 1} \tag{6.13}$$

where $T(a)$ is the temperature of the neutrino fluid at expansion factor a. By substituting the distribution function with $\tilde{\Psi}(\cdot) \equiv \Psi(\cdot) \left(\frac{d \ln f_0(q)}{d \ln q} \right)^{-1}$, we get the simplified Boltzmann equation

$$\tilde{\Psi}'(\vec{k}, \vec{q}, x) = -i \frac{q}{\epsilon(q,x)} \mu \tilde{\Psi}(\vec{k}, \vec{q}, x) - \phi'(k, x) + i \frac{\epsilon(q,x)}{q} \mu \psi(k, x) , \tag{6.14}$$

where $\mu \equiv \vec{k} \cdot \vec{q}/q$ is given by the cosine of the angle between the wavenumber $\vec{k}$ and momentum $\vec{q}$, $x \equiv k\tau$ and the prime denotes the derivative $\partial/\partial x$ thereof. By expanding Eq. 6.14 using Legendre polynomials, we obtain the Boltzmann hierarchy for $\tilde{\Psi}$ given by

$$\tilde{\Psi}'_0(k, q, x) = -\frac{q}{\epsilon(q,x)} \tilde{\Psi}_1(k, q, x) - \phi'(k, x) , \tag{6.15}$$

$$\tilde{\Psi}'_1(k, q, x) = \frac{q}{3\epsilon(q,x)} \left[\tilde{\Psi}_0(k, q, x) - 2\Psi_2(k, q, x) \right] - \frac{\epsilon(q,x)}{3q} \psi(k, x) , \tag{6.16}$$

$$\tilde{\Psi}'_l(k, q, x) = \frac{q}{(2l+1)\epsilon(q,x)} \left[l\tilde{\Psi}_{l-1}(k, q, x) - (l+1)\Psi_{l+1}(k, q, x) \right] \ (l \geq 2) . \tag{6.17}$$

The observable quantities such as the neutrino density and the velocity dispersion are given by the integrals of the respective equations in this series (cf. Eqs.2.56 & 2.58). While formal analytical solutions to this problem exist, numerical approximations can be very expensive as they have to deal with the infinite nature of the sums involved. To overcome this problem, methods like the *Fluid Approximation* were proposed (Shoji and Komatsu, 2010), that exploit the fact that for late times with redshifted momenta and high neutrino masses, the evolution of the $l = 0$ and $l = 1$ modes in the Boltzmann hierarchy (Eq.6.17) effectively decouple from the higher modes. The $\tilde{\Psi}_2$ contribution in the evolution of Ψ_1 is by far dominated

by the gravitational potential term as the latter grows rapidly due to the factor $(\epsilon/q)^2$ with respect to the other terms, once the particles become non-relativistic. This renders any contributions from higher modes irrelevant for the evolution of the first two modes and thus allows for a cut-off in the hierarchy at $l_{max} = 1$, if we are only interested in the observables listed above. Shoji and Komatsu (2010) tested the validity of this approach and confirmed that this method can predict the linear evolution of the neutrino density at the sub-percent error level for redshifts close to zero, high particle masses ($m_\nu = 1.0eV$) and up to cluster scales ($k \sim 0.05$ h/Mpc), especially if the cut-off mode is increased to $l_{max} = 2$ instead as also is done in Boltzmann solvers such as CAMB (Lewis and Challinor, 2011) or CLASS(Lesgourgues, 2011) for low-momentum neutrinos. Any predictions of the neutrino power spectrum at higher redshift or for lower particle masses that are more in agreement with the newest bounds are not very reliable in predicting the correct neutrino distribution[19]. However, recent studies (Archidiacono and Hannestad, 2015) considered even higher cut-offs ($l_{max} = 3$), and were able to improve the accuracy for predictions based on the linearised Boltzmann equations and such an approximation.

6.2.1 Going beyond linear growth

While it is rather straightforward to extend a linear theory for a non-free-streaming component such as CDM or baryons to higher orders of perturbation theory, such an attempt is much more complicated if neutrinos are included as their free-streaming violates the single-stream approximation (i.e. $v \equiv v(x)$) used in the linear theory. For (almost) cold fluids such as CDM, stellar matter and even gas, this is valid up to the point of shell-crossing, when the now spatially overlapping phase-space sheets of matter collapse into the non-linear structures we observe today. Works such as (Wong, 2008) and (Saito et al., 2009) extended the calculation of the evolution of the CDM and baryon distribution (and in some cases the contributions from the neutrinos coupling to that matter) to a more accurate higher-order perturbation theory, while leaving the neutrinos at linear order. A similar approach has been implemented recently in Archidiacono and Hannestad (2015), where the gravitational background for the still "linear" neutrinos has been calculated based

---

[19]It should be noted that the larger deviation of the neutrino density predictions for lower masses are countered by the smaller contribution that these play in the total matter distribution. Thus, such predictions can be still sufficiently good for LSS surveys as these are used to probe the overall matter distribution.

on semi-analytical models of the non-linear growth of the dark matter and baryon perturbations, which seems to reproduce the neutrino densities found in N-Body simulations (cf. Ch. 7) very well.

One approximation to overcome the violation of the single-stream approximation by free-streaming components such like neutrinos was presented by Dupuy and Bernardeau (2014). There the neutrino phase-space fluid is split up into multiple "streams". Each of these streams can then be solved in a similar way as a cold fluid like DM, but require us to deal with a large number of components that may even be coupled at high redshift or the presence of an interaction with the dark sector.

6.3 Measurements/Detection

Considering all the assumptions that were used to obtain the current standard model for the relic neutrinos of the cosmic neutrino background (CνB) described in the previous sections of this chapter, an experimental confirmation of the predicted observables such as their relic energy density Ω_ν or their temperature T_ν would provide valuable evidence for the correctness of our understanding of the processes in the early Universe and the very nature of neutrinos themselves.

6.3.1 Particle Experiments

The detection of neutrinos and measurement of their properties has been one of the major challenges in modern particle physics. Nowadays a growing number of particle experiments have managed to detect solar and atmospheric neutrinos more and more reliably (e.g. Inoue (2004); IceCube Collaboration et al. (2006)) and allow us to study the nature of their oscillations and thus to determine a lower bound on their particle mass among other properties. But the much lower energy of the relic neutrinos (cf. Fig.6.4) eludes direct direction in these experiments as the natural energy threshold for the inverse β-decay in the radiochemical (e.g. Hampel (1997)) or liquid scintillator techniques (e.g. Inoue (2004)) for the target materials used is still in the low MeV/high keV range and thus many orders above the expected energy range of the CνB today. In the case of neutral-current (and in 'same-flavoured' partners charged-current) elastic charged lepton-neutrino scattering, there is no such minimum energy required in the process, but the sensitivity of the experiments is limited by minimum energy of the scattered charged target

particle that can be then detected e.g. by emission of *Cherenkov radiation* while travelling through the detector medium and such events can be distinguished from background noise. A method to specifically detect the low-energy relic neutrinos
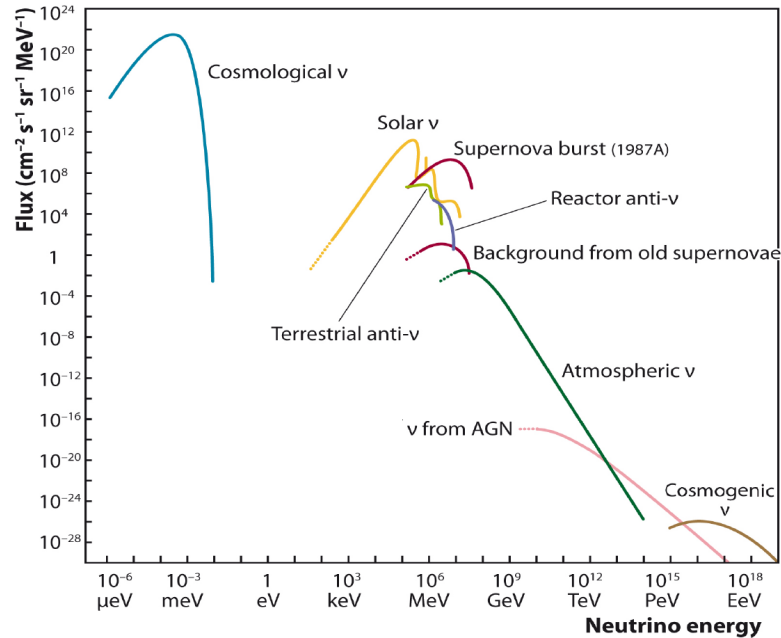
FIGURE 6.4: Measured and expected fluxes of natural and reactor neutrinos [source: IceCube]

that overcomes these problems is to use the so-called *neutrino-induced β-decay*. This was first proposed by Weinberg (1962) and recently picked up as the proposal for the *PTOLEMY* experiment (Betts et al., 2013). Here, a tritium target undergoing β-decay is studied and the energy of the emitted electron is measured with an energy resolution finer than the neutrino mass. In case of a "normal" β-decay ($^3H \rightarrow {}^3He + e^- + \bar{\nu}_e$), the energy of the electrons is a continuous spectrum with a maximal energy limit given by the Q value of the process minus the rest mass of the electron anti-neutrino produced. The induced β-decay ($^3H + \nu_e \rightarrow {}^3He + e^-$) on the other hand produces an energy spectrum with a minimum energy at the Q value of the β-decay plus the rest mass of the absorbed electron neutrino. Given that the width of this spectrum is equivalent to the kinetic energy of the involved neutrino, this results in a rather narrow peak in the energy spectrum about two neutrino rest masses above the "normal" spectrum. A major challenge in such an experiment besides the energy resolution is the rare occurrence of such neutrino-induced events as with current estimates of the local relic neutrino-overdensity, the half-life of tritium and the cross-section for such an event, only about 9.5×10^2 event/(year × gram Tritium) are expected to occur. But if successful, this experi-

ment would not only allow us to determine the (electron) neutrino mass (cf. Section 2.1.1), but would also confirm the predicted presence of such a low-energy relic neutrino background for the first time. Unfortunately even with the proposed energy resolution, the experiment would not allow us to study the momentum dispersion of the relic neutrinos involved in the induced decays and thus can not tell us anything further about the properties and history of the CνB.

6.3.2 Astrophysics/Cosmology

With even proposed next-generation particle experiments not being able to measure the properties of the CνB, the interest of neutrino physicists turned towards the largest experiment available, the observable Universe itself. While the neutrino relic density, mass and interaction cross section may be small compared to those of many other particles making up the Universe, the huge time and length scales involved here allow us to study the impact these particles have on the traceable matter. In Section 6.2 we discussed how to predict the matter distribution in the Universe based on linear perturbation theory. These predictions have been compared to observation of actual density perturbations in the early Universe (Bennett et al., 2003; Tauber, 2005) that are imprinted in the CMB as well as at late times where galaxy and galaxy clusters (Weinberg, 1992; Tegmark et al., 2004) or lensing (Simon, 2012) can be used to trace the large-scale density perturbations in the linear regime. In the standard 6-parameter ΛCDM model, neutrinos are treated as thermal fermionic relic with a mass fixed to the lower bound given by oscillation experiments, i.e. $\sum m_\nu = 0.06$eV for the normal hierarchy. Also their temperature is fixed relative to the CMB temperature (Eq.6.8). In a minimal extension as used e.g. in (Planck Collaboration et al., 2015d), the neutrino mass is included as a free parameter. Fig.6.5 compares the total matter (angular) power spectra in the predicted with linear theory for a sum of the masses of the neutrino eigenstates $\sum m_\nu = 0.2$eV with a model containing the same amount of matter, but without massive neutrinos. As the neutrinos stream out of small primordial perturbations, growth on these scales is suppressed. This can be seen as a suppression below the maximum free-streaming length in the matter power spectrum at around $k = 10^{-2}$h/Mpc. As the free-streaming neutrinos cause a larger decay in the gravitational potential on scales below the free-streaming scale, this drives acoustic oscillation in the baryon-photon fluid more strongly and results in the slightly higher amplitudes of the second and higher peaks in the angular power spectrum in the middle panel. Additionally, a delay in the matter-radiation equality enhances the *early integrated Sachs-*
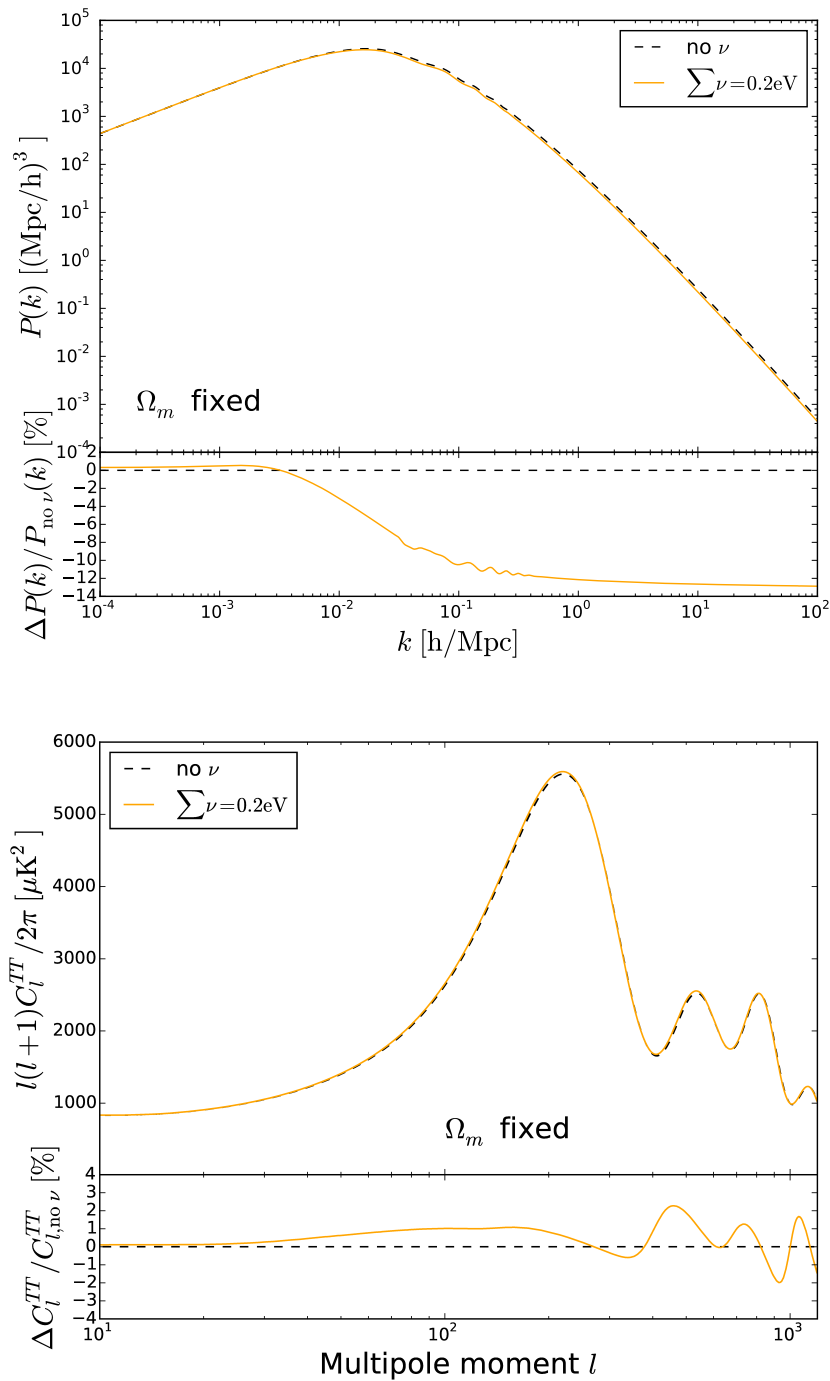
FIGURE 6.5: Impact of the neutrino mass on the early Universe: The (left panel) matter power spectrum and (right panel) angular power spectrum for a Λ-CDM universe with (orange/solid line) and without massive neutrinos (black/dashed line).

Wolfe effect which boosts the power on scales larger than the first acoustic peak and thus shifts the resulting peak further to larger scales. The overall shift in all the

peaks can be additionally explained by the change in the non-relativistic matter density at late times that occurs when the neutrinos become fully non-relativistic after decoupling. This has an impact on the angular diameter distance to the last scattering surface and thus the position of the features in the spectrum (cf. Ichikawa et al. (2005); Lesgourgues and Pastor (2014)).
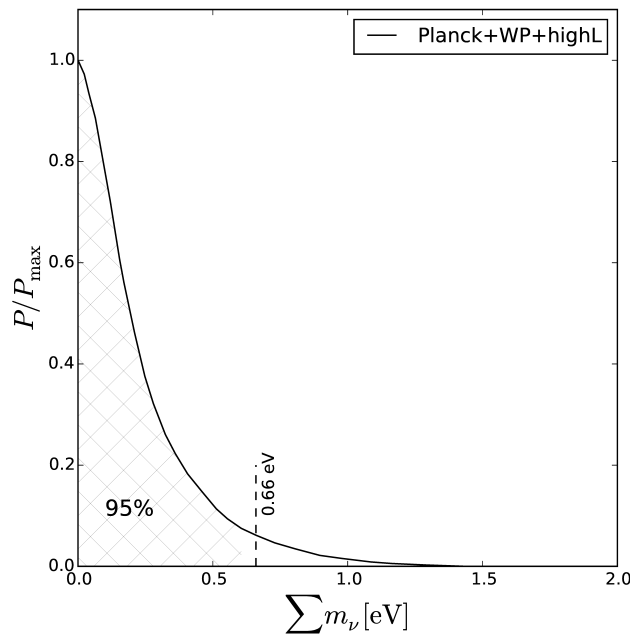
FIGURE 6.6: CMB constraints on the sum of neutrino masses $\sum m_\nu$ using the combined Planck, WMAP polarization and high-resolution data.

Fig. 6.6 shows the relative likelihood for the sum of the neutrino masses, $\sum m_\nu$, using this method with the first-year Planck data together with WMAP polarization and CMB-high resolution data (Ade et al., 2014). While there is no signal for a specific non-zero neutrino mass in these results, at least an upper bound of 0.66eV can be determined with 95% confidence. Including BAO, external H_0 as well as full Planck polarization and lensing data, these constraints can be tightened further to $\sum m_\nu \leq 0.23$eV (2σCL) (Planck Collaboration et al., 2015c) within this extended ΛCDM framework. Alternatively, we can also try to determine other properties like the neutrino temperature that way by allowing for more free parameters.

In Chapter 7 and 8, we also discuss how to predict the non-linear evolution of the cosmic neutrino content using very different techniques and the resulting impact on late-time structure formation using simulations. This becomes very important when we have to take non-linear contributions into account for the very

accurate predictions needed for future galaxy surveys (e.g. Tereno et al. (2015)) which will provide us with much more sensitivity at the measurements of the neutrino mass (Hamann et al., 2012).

CHAPTER 7

Neutrinos in structure formation

As discussed in Chapter 6, it is rather easy to solve the Boltzmann equations for neutrinos in linear order, but very challenging to obtain a solution beyond that. In this chapter, it is discussed how linear solutions can be used to study the non-linear evolution of the other components in the Universe. Neutrinos may play an important role in the evolution of the Universe at late times and therefore must not be neglected in numerical cosmological simulations in order to accurately predict the formation of the structures found in the Universe today. In this Chapter I present two techniques that have been introduced before and used in the research I was involved in, in particular in Shanks et al. (2014), which is presented as an example in the final section.

7.1 Simulation techniques & implementation

Linear Background technique The simplest approach to include massive neutrinos in numerical simulations it to treat them as a background that follows a strictly linear evolution of the primordial matter perturbations. This has been first proposed in Brandbyge and Hannestad (2009) and also been used by us as a simple approach to study the contributions of free-streaming neutrinos on the structure formation in the Universe. For the implementation of the neutrinos as a linear background in the GADGET Springel (2005) N-body simulation code, we use a very similar approach to what has been previously done in Brandbyge and Hannestad (2009). First we calculate the transfer function in linear theory with a numerical Boltzmann solver (Lewis and Challinor, 2011) for a set of redshifts between our initial conditions and today with a sufficiently fine redshift spacing to accurately interpolate the solutions for the redshifts in-between. We use a logarithmic spacing in redshift in order to get equal spacing in time in the simulation. With this knowledge, we can interpolate the neutrino transfer function/power spectrum for every redshift in-between. As a next step, we now have to (re)construct a realization

of the Universe with exactly these 2-point statistics. As for our initial conditions, we need to determine the phases and amplitudes of the Gaussian perturbation in the neutrino density for each of the discrete grid points $\vec{k} = \{2\pi\vec{j}/L_{\text{Box}}\|j \in N_{\text{grid}} \times N_{\text{grid}} \times N_{\text{grid}}\}$ in Fourier space. To obtain the observable configuration-space distribution, we would then have to Fourier-transform these results back. Fortunately, due to the way Gadget's Poisson solver is designed, this last step is not necessary. In the code, the DM/baryon density field is reconstructed from the N-body tracers, before being Fourier-transformed itself to solve the Poisson PDE much more conveniently in Fourier-space. Thus, we can simply add the contribution of the neutrinos directly to the complex Fourier-transformed DM/baryon density field:

$$
\begin{aligned}
\hat{\delta}(\vec{k},t) &= \frac{1}{(2\pi)^3} \int \delta(\vec{x},t)\exp(i(\vec{k}\cdot\vec{x}))\mathrm{d}^3x \\
&\quad + C \cdot \sqrt{-\ln(A_\nu(\vec{k}))} P_\nu(\|k\|,t)(\cos(\phi(\vec{k})) + i\cdot\sin(\phi(\vec{k})))
\end{aligned}
\tag{7.1}
$$

where $C = \sqrt{2\pi L_{\text{Box}})^3}\Omega_\nu\rho_{\text{crit}}$ is a global constant, $P_\nu(k,t)$ is the power spectrum at time t and A and ϕ are the amplitudes and phases. For each realization A and ϕ have to be randomly picked for each of our grid points in Fourier space. Fortunately we can avoid storing these two scalar fields by exploiting the fact that the pseudo-random number generator we used for them is completely deterministic for a given seed. Thus, by ensuring that these pseudo-random variables are picked by the same random generator (algorithm) in the same order for both the initial conditions and the realizations for each time step, we can reduce the storage requirements to a single number while ensuring that both DM and neutrinos start off with the same adiabatic initial fluctuations.

Neutrinos as N-body particles   The linear neutrino background provides the means to include their behaviour according to linear perturbation theory, but misses completely the possibility of neutrinos interacting freely with the forming collapsed structures in the non-linear regime. As an alternative, we introduce here most common numerical technique to predict the non-linear evolution of the matter distribution in the late Universe, Lagrangian N-body simulations and discuss the possibility and challenges of representing neutrinos as particle tracers in such N-body simulations. In the Lagrangian approach, the continuous phase-space fluids that make up the Universe are represented by a finite number of phase-space tracers with their own discrete position and velocities. These tracers are then used to reconstruct

the local density field, to calculate the gravitational interactions and propagation of the matter content governed by Newtonian mechanics and the Poisson equation.

Here, we use the GADGET-2 (Springel, 2005) N-body code with the following optimizations based on the proposals made in Viel et al. (2010):

1. As we are expecting to encounter high velocities for the neutrino fluid tracers due to the assigned thermal velocities, we keep the neutrinos off the tree in the TreePM method that GADGET uses to calculate gravitational short-range interactions. This should not introduce a significant error since we do not expect any neutrino clustering on scales smaller than the overlying mesh, on which we calculate their long-range gravitational interactions. This has the advantage that it avoids significant computational costs as the tree-calculation for fast neutrinos would force a small time step and a lot of expensive tree-reconstruction as the tracers quickly traverse the simulation box.

2. Another way to reduce the costs of the simulation at the cost of minor inaccuracies is to modify the rules that determine the step size in the simulation. There are certain rules that limit the step size of the time integration also based on the drift velocity of the particles. If applied to neutrinos, they lead to very small time steps and therefore much higher computational costs. For neutrinos we therefore relax these rules to avoid these costs in exchange for a reduced accuracy.

The detailed benchmarks for these modifications of the code are discussed in Sec. 7.1.3. They allow us to obtain results with almost the same accuracy as the vanilla version for the total matter distribution.

7.1.1 Initial conditions

The first step in every numerical cosmological simulation is to set up the initial conditions (IC). These have to represent the state of the Universe at the starting redshift z_i in a discrete way that can be handled by the numerical code, i.e. by assigning the right properties to a set of particles whose evolution is then calculated numerically from that point in time onwards. The choice of z_i depends on the subject of the study. In Section 7.1.2 a way to calculate non-linear effects on the neutrino velocity distribution starting as early as $z_i \sim 10^9$ is discussed, but, in general, simulations for cosmological structure formation usually start at a redshift much later than the era of recombination and just before non-linear effects in structure

formation become relevant. Thus, z_i can range from redshifts of about 100 down to redshifts as late as 5-7.

Zel'dovic Approximation / Individual transfer functions

A standard way to obtain the initial discrete phase-space positions for the particles of a simulation is to use the Zel'dovich approximation (Zel'dovich, 1970) based on linear perturbation theory. It gives a prescription to assign displacements and velocities to the particles that are initially distributed unperturbed on some regular grid- or glass-like pattern (cf. e.g. L'Huillier et al. (2014)). An initial Gaussian density field $\delta(x)$ is generated in Fourier space and convoluted with a linear power spectrum that is obtained from a given transfer function. This provides the displacements $S(q)$ in position space for the particles according to

$$x = q + D(a)S(q) \,, \tag{7.2}$$

where q is the initial, unperturbed Lagrangian position, $D(z)$ the linear growth factor at redshift z and x the resulting Eulerian position of the particle at z. The comoving initial velocities are obtained by using

$$v_{com} = \dot{D}(z)S(q) \,. \tag{7.3}$$

There is a problem with this approach when it comes to neutrinos when using the N-body technique for them. First of all, it assumes that the growth factor is scale-independent. For neutrinos, this is obviously not the case since the damping due to free-streaming is both scale- and redshift-dependent. The displacements can still be obtained by simply using the transfer function at the redshift of the IC instead of using those at $z = 0$. But for the velocities, we cannot use that trick as we are facing the time derivative of the growth factor. To overcome this I followed an approximation that has been also already used by other groups in this situation (Brandbyge et al., 2008). Instead of using Eq. 7.3, I modified the publicly available `2LPTic` (Crocce et al., 2012) code to create the initial conditions such that it calculates displacements at redshifts close to z_i and uses the difference in the displacements for a small time step around z_i to determine the velocities. This way, initial conditions for arbitrary cosmologies and particle types can be obtained as long as the transfer functions around the initial redshift are provided by a Boltzmann solver.

7.1.2   Thermal velocity distribution

An important problem in N-body simulations is to model free streaming properly. In the case of CDM this is negligible as the total velocity of a particle is by far dominated by the velocity of the gravitational flows and not by the thermal velocity of the individual particles. But the latter may be sub-dominant and even dominant in case of gas, warm dark matter (WDM) and hot dark matter (HDM) like the light standard neutrinos. While particles of CDM effectively sample only the three-dimensional positions space as their initial velocity is uniquely determined by the flow defined in Eq. 7.3, gas, WDM and HDM particles not only have to represent a finite mass element and (bounded) three-dimensional part of position space, but additionally the unbounded continuum of thermal velocities within each of these mass elements.

There are two ways to tackle this problem - the thermal velocities can be represented *implicitly* or *explicitly*. In the first case, each mass element comes with an additional set of parameters that describe the velocity distribution. In the case of thermalized bosons and fermions, their energy and therefore thermal velocities are distributed according to the *Maxwell-Boltzmann* or *Fermi-Dirac* statistics (cf. Section 6.1.1) which is completely determined by the temperature (if we neglect the chemical potential). This information is attached to each particle and can then be used to calculate additional interactions besides the pure gravitation that account for the effect of free-streaming. This was used e.g. in the νSPH approach (Hannestad et al., 2012).

The other possibility is to model the thermal velocities explicitly by initially assigning one to each N-body particle of the simulation by drawing it from the correct velocity distribution. It is essential to notice that we do not identify these N-body particles with discrete mass or volume elements, but simply as tracers of random points in phase-space, which we follow along their trajectories at each step in the simulation. By choosing an initial sampling of these tracers that reflects the local phase-space densities of the neutrino fluid, we can then reconstruct the density field as before by counting the particles in a given spatial volume and normalize the result to obtain the correct total mass.

Naively, one would assume that the neutrino momenta would simply follow the Fermi-Dirac statistics (cf. Eq. 6.11) with a globally uniform neutrino temperature T_ν (cf. Eq. 6.8). But Ma and Bertschinger (1994b) have shown that non-linear contributions to the evolution of the neutrinos between their early decoupling and the time of usual initial conditions seem to result in a globally non-constant thermal

velocity distribution. By evolving neutrinos from redshift $z \sim 10^9$ as tracer particles along their geodesics in the perturbed cosmological background, they could compare the resulting local thermal velocities at $z \sim 13.55$ to those obtained by simply assuming a global velocity distribution (see Fig. 7.1).

FIGURE 7.1: (left) rms neutrino velocities vs. the neutrino density perturbation at $z = 13.55$. The solid line is the result of the geodesic equation integration, the dashed line for a set of ZA initial conditions with thermal velocities sampled from a global Fermi-Dirac distribution (Ma and Bertschinger, 1994b, Fig.6). (right) Contour plot of constant particle number in the neutrino velocity component-overdensity plane with contour lines for $10, 100, 1000, 10^4$ and 10^5 neutrinos per bin of height $\Delta(\frac{\mathrm{d}x}{\mathrm{d}t}) = 40 km/s$ and width $\Delta\delta_{HDM} = 0.02$ ((Ma and Bertschinger, 1994b, Fig.9)).

By ruling out gravitational flows as a simple explanation for the observed higher rms neutrino velocities in denser regions, Ma and Bertschinger (1994b) concluded that there is a local increase in the thermal velocities that depends on the local over-density of the neutrino content and that thus, the assumption of a global Fermi-Dirac distribution is not accurate. While there was a comparison in Ma and Bertschinger (1994b), subsequent publications did not address this any more. In order to verify whether the approximation made using ICs obtained from a global Fermi-Dirac distribution follow instead the geodesic equation integration, we studied whether a similar effect can be observed within the redshift range usually used for ICs. We therefore created initial conditions at a high redshift ($z \sim 49$) assuming a global Fermi-Dirac distribution and evolved them in a N-body simulation until $z \sim 7$ where we compared the results with ICs created at this redshift, again assuming a Fermi-Dirac distribution that is only perturbed by the local gravitational flows. The final redshift was chosen well within the regime, where the DM background is still close to linear with only minor higher-order non-linear contributions. The neutrino over-density for each particle was calculated using a grid with a CIC assignment scheme. For this work we used a "vanilla" GADGET-2 ver-

sion without any optimizations (cf. Sec. 7.1.3) that could cause the loss of those small non-linear contributions. The results of this run are shown in Fig. 7.2 in form of plots similar to those of Ma and Bertschinger (1994b).

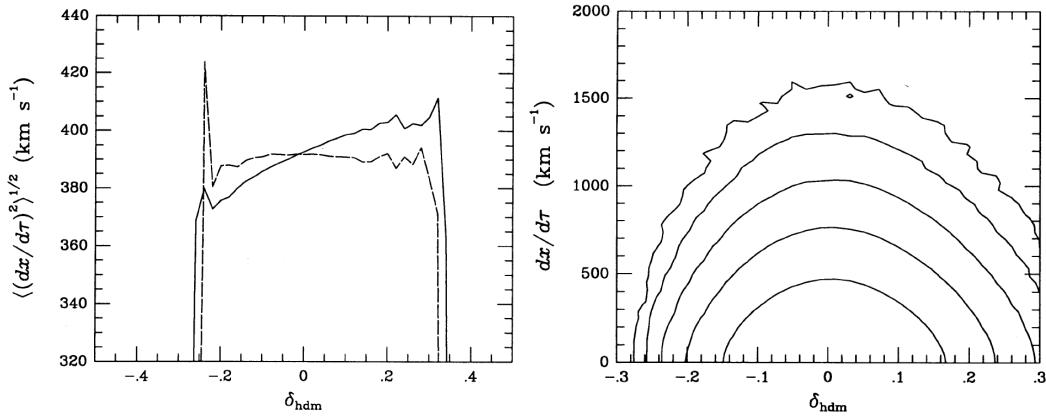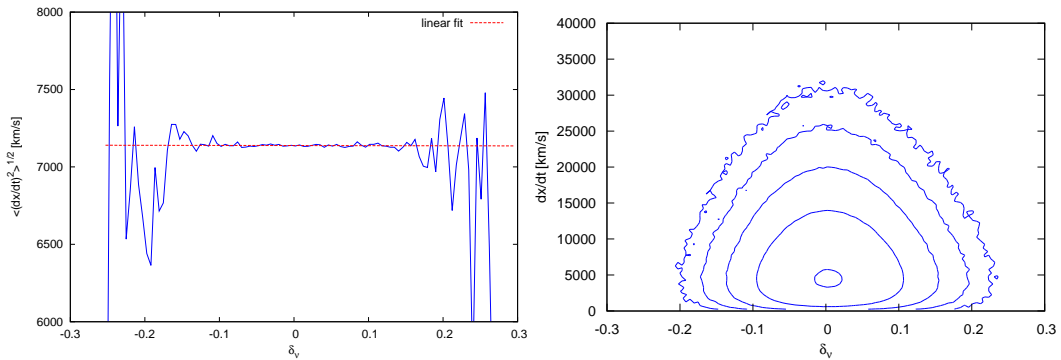FIGURE 7.2: (left) rms neutrino velocities vs. the neutrino density perturbation at $z = 7$. The solid line is the result of the N-body simulation, the dashed line for a linear fit of this data. (right) Contour plot of constant particle number in the neutrino velocity component-overdensity plane for evolution of neutrinos from redshift $zi = 49$ to $z = 7$ with contour lines for $10, 100, 1000, 10^4$ and 10^5 neutrinos per bin of height $\Delta(\frac{\mathrm{d}x}{\mathrm{d}t}) = 100 km/s$ and width $\Delta\delta_{HDM} = 0.0055$.

In these results, we could not observe a non-linear contribution that is similar to what was observed in Ma and Bertschinger (1994b). The linear fit in the left plot did not reveal any statically significant non-vanishing slope and the only visible asymmetry in the contour plot is most probably caused by the particle counts which are by construction higher in over-densities leading to the observable stretching along this axis, but no correlation between the over-density and the velocities. It has to be noted that Ma and Bertschinger (1994b) used a rather high mass for the active neutrinos of 7 eV which resulted in much smaller thermal velocities which could lead to stronger non-linear effects. For all of our studies we ignore the possibility of such early non-linear contributions and use in all of our initial conditions a simple Fermi-Dirac distribution on top of the gravitational flows.

Sampling of phase space

While Sec. 7.1.2 dealt with the distribution of thermal velocities, another valid concern arises from the sparse sampling of the phase-space by the finite amount of N-body particles in the simulation. As particles represent a macroscopic sample set for the underlying phase-space distribution, it is not obvious how to represent the microscopic property of thermal motion properly. Explicitly assigning thermal velocities to each single mass elements in a simulation would imply huge local flows

of neutrinos at the resolution scale that do no exist for natural thermal velocities as the thermal motion is already averaged out on any macroscopic scale. To address this concern, we performed and analysed a series of pure N-body simulation runs with initial conditions that were especially designed for this purpose as follows. Starting with 128^3 perturbed grid for both the CDM and the neutrinos in a 128 Mpc/h box, we refined the phase-space sampling by doubling the grid size in each dimension while re-sampling the momentum/velocity-space in the following three different ways (cf. Fig. 7.3 (left)):
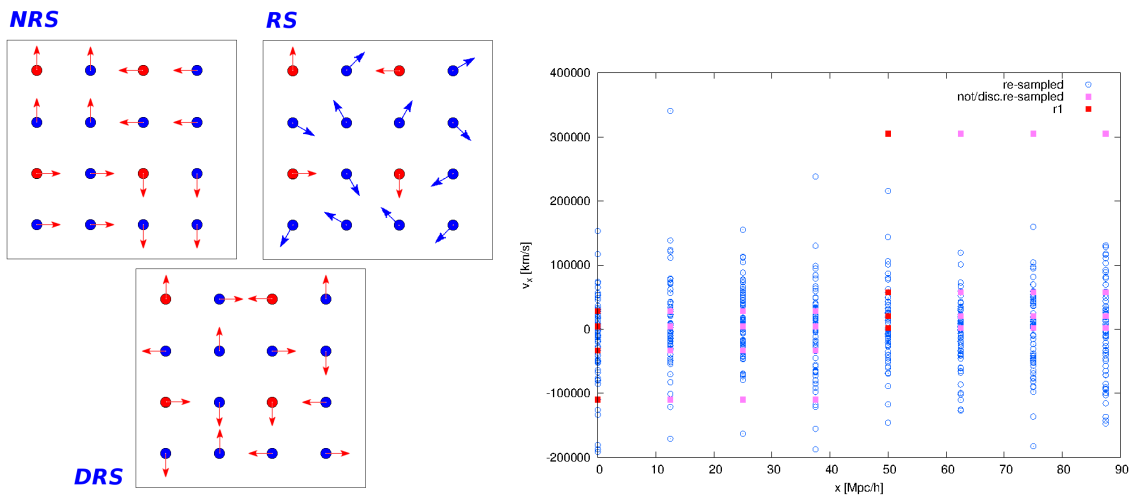
FIGURE 7.3: (Left) Illustration of resolution refinement schemes at first level of refinement (r2) in two dimensions. (Right) 2d-projection of the space-space onto one position and one momentum axis for the second refinement level (r4).

re-sampling (RS) For this refinement of the resolution in position space, the mass elements of the original particles are now represented by 2^3 smaller particles. While the new particle at the original position keeps the same thermal velocity, the others obtain new ones drawn again from the corresponding velocity distribution.

non re-sampling (NRS) Each of the 8 new "refined" particles keeps the same thermal velocity of the original "parent" particle.

discrete re-sampling (DRS) Similar to the first method, but the new thermal velocities are only drawn from the set of already existing samples.

alternative sampling (AS) Similar to the first method, but all thermal velocities are drawn anew.

Hence, we obtain 256^3 N-body particles sampling the neutrino fluid for the first refinement level (r2) and 512^3 for the second refinement (r4).

It is obvious that even the global velocity distribution in the NRS and DRS case is no longer the original one since the probability for obtaining identical velocities in so many cases is very low. The NRS refinement is used to study the impact of changes in position-space resolution while keeping the local velocities the same. This ensures that the refined particles are still close neighbours in the phase-space as seen in Fig.7.3(right). The DRS results are used to probe the effect of using this altered global velocity distribution, that is on a global level identical to that of NRS. This is needed to quantify contributions arising from this altered distribution for comparing the NRS and RS schemes. Finally, the AS scheme allows us to study how much the results vary by choosing an alternative realization of the phase-space sampling.

We tested these different refinements using GADGET-2 with the discussed optimizations for the neutrino N-body particles. Especially with the higher numbers of neutrinos at the higher refinement levels (i.e. higher resolutions), the advantage of the modifications made to the GADGET code pay off as they save valuable computation time and make these simulation runs feasible. The induced error in the neutrino spectrum is thereby only a minor concern as we compare relative differences in results obtained by the same code and we are mostly interested in the accuracy of the total matter power spectra.

Each setup was run from an early starting redshift($z_i = 49$)[20]. Fig. 7.4 shows the results for each scheme at $z = 0$.

It can be seen that the deviation in the neutrino power spectrum introduced by the DRS scheme are in fact very small for all refinement levels and stays within the marked 1% error bounds with only a few exception going out as far as 1.5-2%. The power spectrum coincides with that of the more accurate (RS) scheme and differs from one refinement level to another only in the decrease of the shot-noise level at small scales that results from the increased number of particles. This small error could be explained by the fact that the 128^3 samples of thermal velocities drawn before the refinement (r1) already represent the underlying distribution quite well. In contrast, the results of the NRS scheme show a totally different behaviour. While they still more or less coincide on large scales with those of the other schemes, their

---

[20]Additionally, we also ran simulations with a late starting redshift ($z_i = 7$). Those produced similar results with only minor differences between the power spectra at early redshifts, that are probably due to early shot-noise. Due to this agreement, we will only present the results for $z_i = 49$ here.
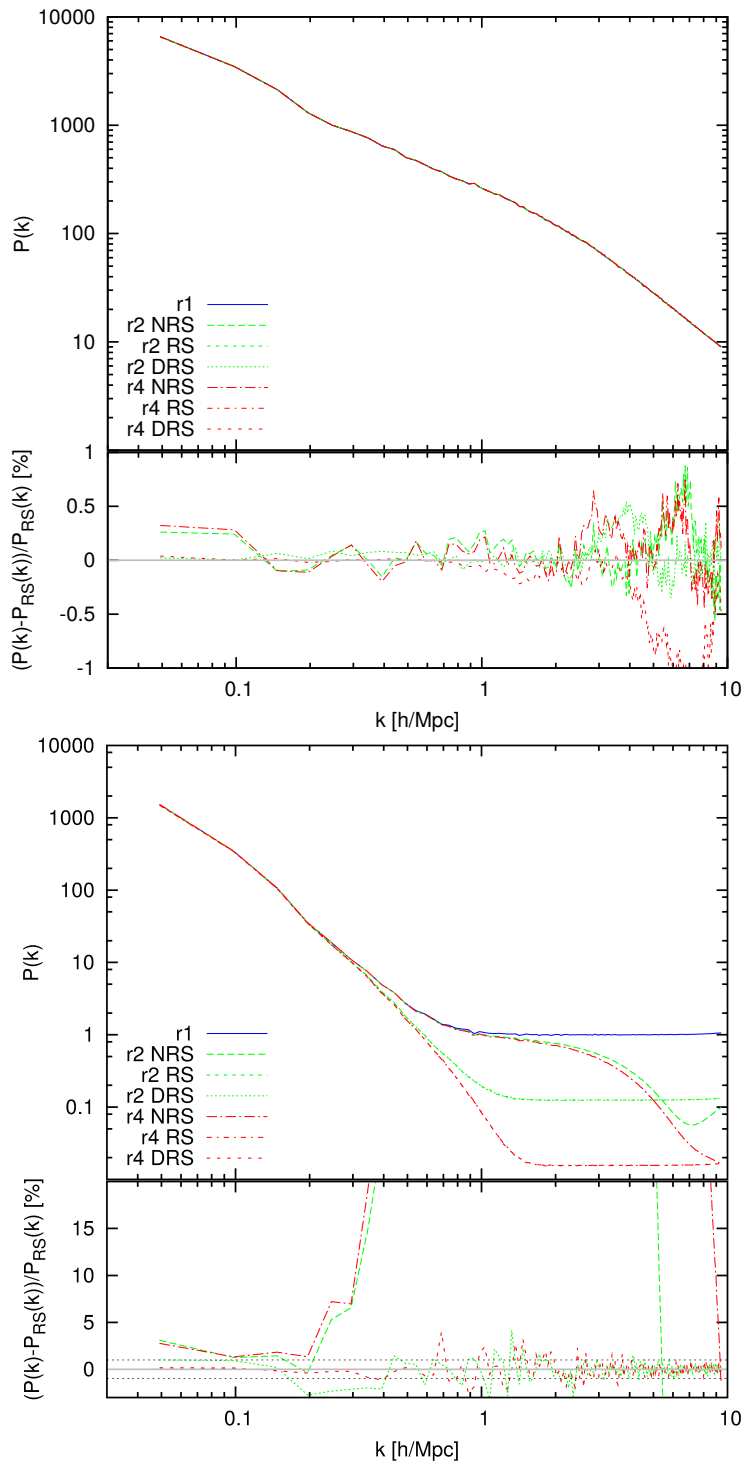
FIGURE 7.4: Power spectra at $z = 0$ obtained from ICs created at $z_i = 49$ with the different refinement schemes. The bottom part in each panel shows the relative difference with respect to the RS scheme: (Top panel) all matter content (Bottom panel) neutrinos only

power spectra seem to trace that with no refinement and only start to approach the

lower shot-noise levels that correspond to their particle numbers on very small scales. This is indeed the effect that was intended by construction. As refined particles that are obtained from the same parent remain close neighbours in the initial phase-space in the NRS scheme and only interact weakly with the environment, they experience very similar evolutions. Those, despite refining the position space sampling, mass elements of the size of the unrefined mass elements stay together and behave like the parent. Only on smallest scales one could see signals of a break up as the power spectra start to decrease towards the shot-noise levels of the other refinement schemes with the same number of particles. But despite these differences, the discrepancies between the corresponding total matter power spectrum at $z = 0$ as shown in the left plot of Fig. 7.4 are smaller than 1.2% over all scales.

In order to study whether these small errors are only limited to late redshifts where non-linear structure growth may have already eradicated differences between the schemes, We also compared the results for RS and NRS obtained at earlier redshifts in Fig. 7.5 for the second refinement level (r4).

While the NRS scheme does indeed result in significant errors at very early times and on scales where its neutrino power spectrum traces the one for the unrefined ICs, this could be explained by the fact that the total matter spectrum at $z = 24$ is still very sensitive to the high level of shot-noise in the neutrinos for NRS. Thus, the error of several percent can simply be caused by the difference in the shot-noise levels in the neutrino power spectra and their contributions to the total matter spectrum. Beside this outlier, the errors stay well below 1 % for all redshifts lower than $z = 7$ studied here.

Finally, we also tried to examine the effect of choosing an alternative sample set for the thermal velocities drawn from the velocity distribution. This is useful to quantify the dependency of the final results on the random selection of the initial velocities. In Fig. 7.6, the results for ICs with both the original (RS) and the alternative velocity samples (AS) at lowest and highest refinement level are shown and compared.

The refinement for both have been obtained using the same RS scheme but with different random seeds. The difference in the total power spectra is again within the 1% boundaries being slightly smaller at $z = 2$ than at $z = 0$ and at r4 compared to the r1 level. While both these results could indicate that there is indeed an error induced by assigning macroscopic thermal velocities besides that one caused by early shot-noise, it is well within the accuracy of 1% in the total matter power spectrum. For the neutrino content, choosing an alternative sampling does
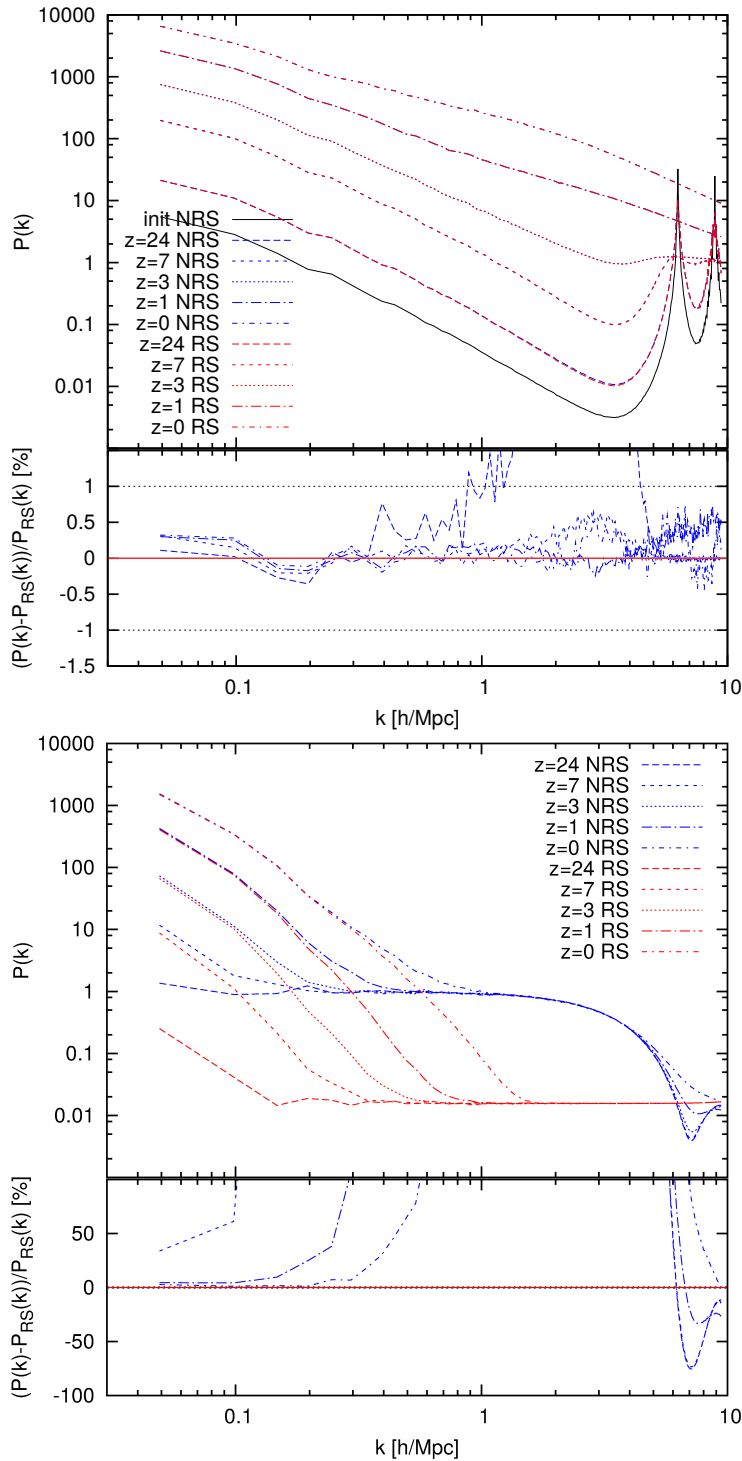
FIGURE 7.5: Power spectra at various redshifts obtained from ICs created at $z_i = 49$ with the RS and NRS refinement schemes at the second refinement level. The lower part of each panel shows the relative difference in respect to the RS scheme: (Top panel) all matter content (Bottom panel) neutrinos only
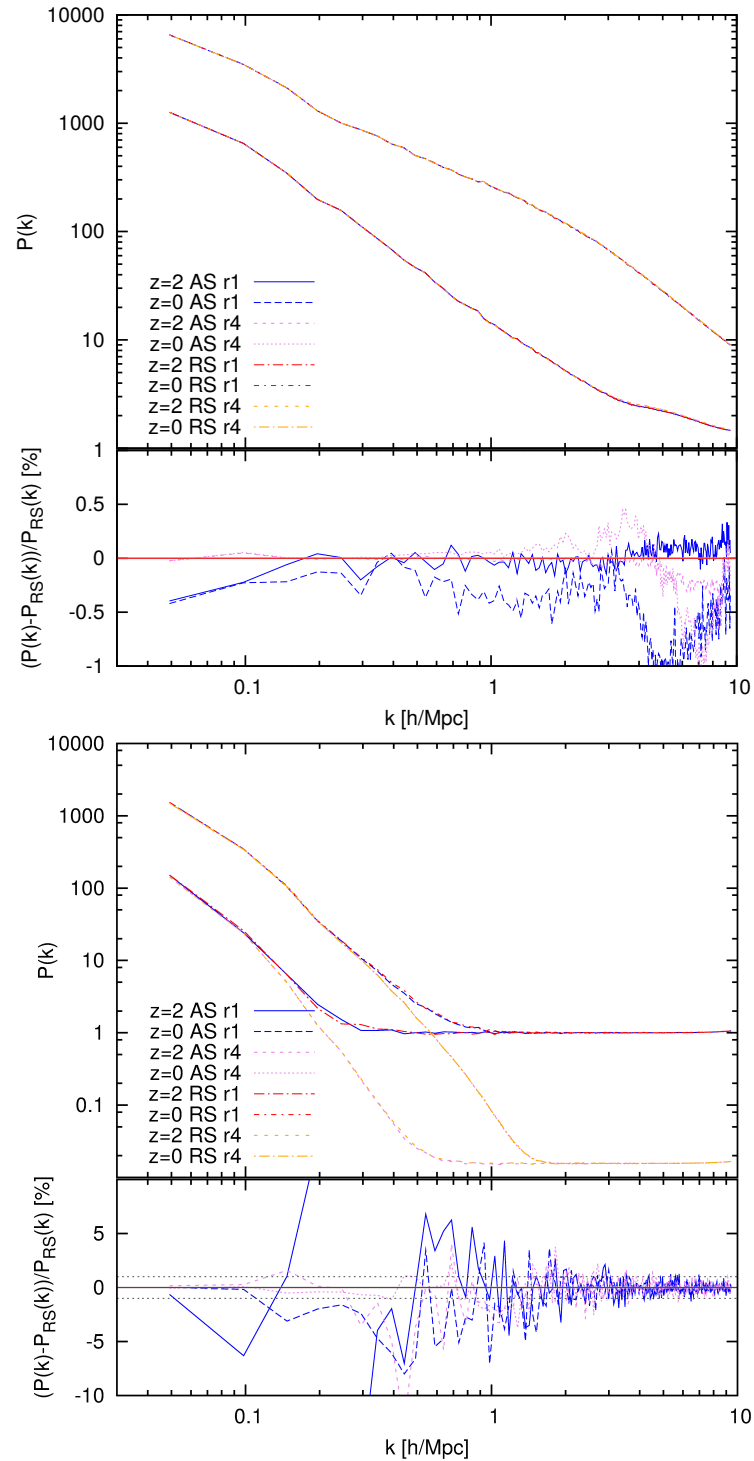
FIGURE 7.6: Power spectra at various redshifts obtained from ICs created at $z_i = 49$ with the RS refinement scheme using two different velocity sample sets (RS/AS). The bottom part of each panel shows the relative difference in respect to the RS scheme: (Top panel) all matter content (Bottom panel) neutrinos only

result in a power spectrum that "scatters" around the original one. The amplitude of these relative deviations are hereby surprisingly large at large scales while it converge towards 1% at smaller scales.

7.1.3 Optimization of neutrino N-body code

In the "explicit" approach with explicit thermal velocities, neutrinos are simply treated in the N-body simulation as an additional particle species that interact only via gravitation with the CDM and, if present, gas and stellar matter. The thermal velocities are added to the peculiar gravitational flow of each particle in the ICs. For the simulations we use the *GADGET-2* Springel (2005) N-body code, where the original code has been modified based on the two optimization listed above.

The first optimization is motivated by the observation that the free-streaming scale of neutrinos (Eq.6.12) is rather large compared to the resolution of the PM grid that is usually used in cosmological simulation with GADGET to calculate the long-distance forces. To be more precise, this scale is larger than the spatial scale r_s of the force split and the tree-force cut-off distance r_{cut} in the TreePM calculations in GADGET (cf. Fig. 7.7).
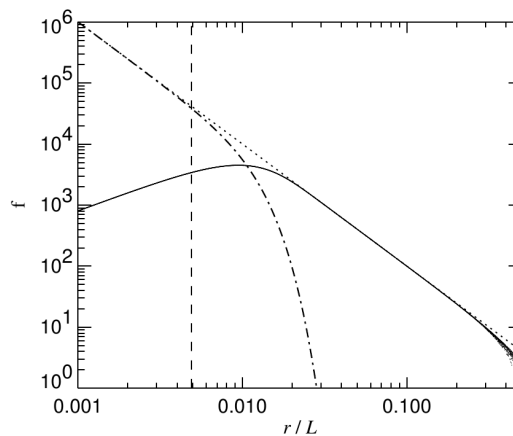
FIGURE 7.7: Force decomposition and force error of the TreePM scheme. The plot illustrates the size of the short-range (dot- dashed) and long-range force (solid) as a function of distance in a periodic box. The spatial scale r_s of the split is marked with a vertical dashed line (Springel, 2005, Fig.2).

Both lengths are defined by a constant parameter times the size of the PM grid resulting in $r_s = 1.25 \, \text{Mpc}/h$ and $r_{cut} = 4.5 \, \text{Mpc}/h$ for the 128 Mpc Box size and 128^3 grid points used in most of the test simulations here. Thus, to a very good approximation, it is possible to neglect the neutrinos in the tree-based short-range force calculations and let them only contribute to the long-range PM forces.

This is achieved by omitting all neutrino particles each time the force-tree is constructed. Additionally it would be possible to additionally decrease r_s for this particle species to compensate for the missing short-range forces close to that scale. I checked the impact of such a modification and, as expected from the fact that the free-streaming stays mostly even above r_{cut}, and thus error due to this cut-off should be negligible. Furthermore by skipping the force calculations in the leafs of the tree, we avoid any undesired artificial two-body relaxation that may lead to artificial large-angle scattering caused by close encounters of particles[21]. This first modification improved the performance of the code significantly for larger numbers of neutrinos as it gets rid of the costly $\mathcal{O}(n \log n)$ tree force calculations for these particles and uses only the much less expensive grid-based Fast Fourier transform (FFT) force calculations instead ($\mathcal{O}(n)$+costs depending only on PM grid size). This can be seen in Fig. 7.8 as a decrease of the computational costs by at factor of 4 with nearly the same number of time steps.

Our second improvement of the code is to modify the rules that determine the step size in the simulation. `GADGET-2` uses a leap-frog integration scheme with an adaptive timestep set according to $\Delta t \propto 1/\sqrt{|a|}$ with a being the acceleration of the last time step and uses separates short- and long-range time stepping. Additionally, it usually limits the maximal step size such that each particle does not drift further per step than a predefined distance within the simulation box. While this restriction ensures that particles do not "accidentally" drift through locally concentrated inhomogeneities in the case of one large time step obtained by the first rule, the large velocities of neutrino particles significantly lower the maximally allowed step size. This leads to an enormous increase in computation time as seen in Fig. 7.8 by comparing simulations runs with and without neutrino thermal velocities. It also reveals that most of this computational costs are spent at high redshift ($z > 7$) due to the higher neutrino velocities at these times where not many large-scale structures have formed yet. By ignoring the maximal drift criterion, the number of steps and therefore the computation times are extremely reduced by a factor of 10. In combinations, both optimizations almost bring the computational costs down to the level where they would be without thermal velocities.

To check if my modifications do not compromise the accuracy of `GADGET-2`, I ran a set of simulations with 256^3 N-body particles for each DM and neutrinos and a starting redshift of $z_i = 49$. Fig. 7.9 compares the results obtained for each

---

[21] Alternatively, we would have to use large softening for neutrinos to smooth out these artificial effects.
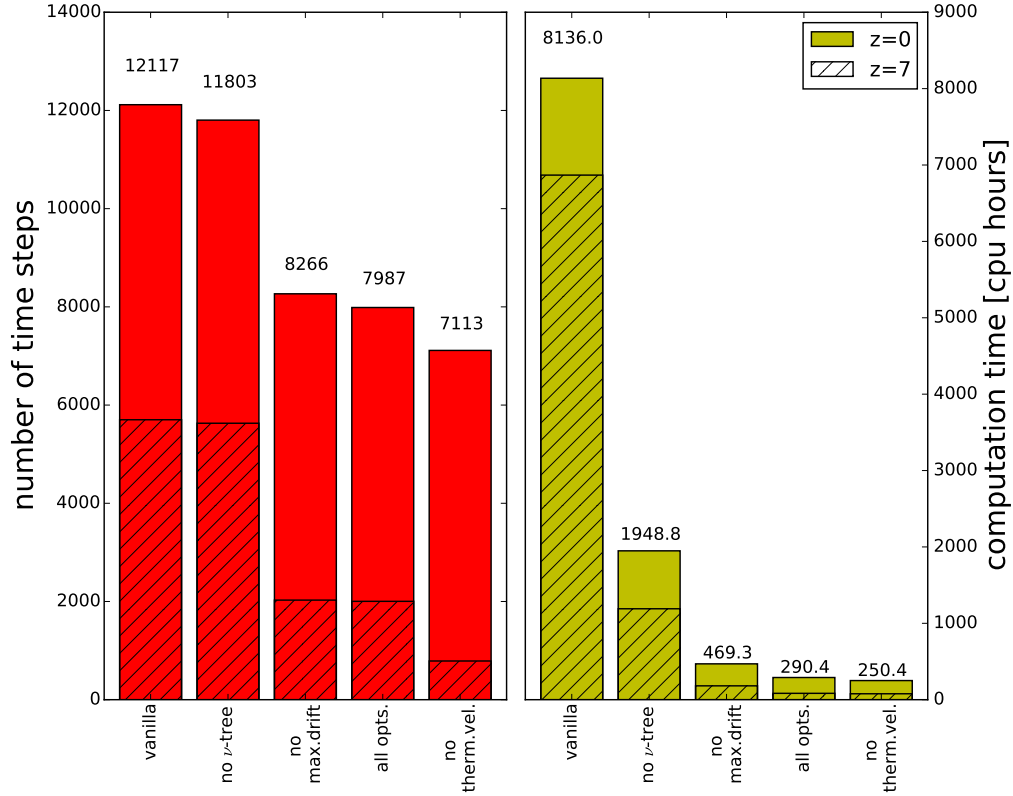
FIGURE 7.8: Computational costs to run neutrino simulations with and without optimization: (left) number of time steps (right) computation time. The results for a simulation without thermal velocities has been added for comparison. The coloured bars show the costs to run the simulation from the starting redshift of $z_i = 49$ to $z_f = 0$ while the hatched bars refer to the costs until $z = 7$ is reached.

modification and their combination.

The variation in the total power spectrum does not exceed 0.5% here. The errors induced by each modification are thereby not cumulative. At some scales and times, the tree modification, for example, results in a larger relative error than both optimizations combined. The tree modification, on the other hand, has a significant impact on the neutrino distribution, in particular around around the resolution of the PM. The observed loss in power may result from missed non-linear feed-back from the CDM in the simulation as it tends to become larger at later times. This could become a problem for studies of neutrino distributions at smaller scales. The best way to minimize this error is to ensure that the spatial resolution on PM grid is always smaller than the largest structures most neutrinos can still free-stream out off. Otherwise the results for the neutrino power spectrum with the optimization would highly underestimate the structure formation on those scales.
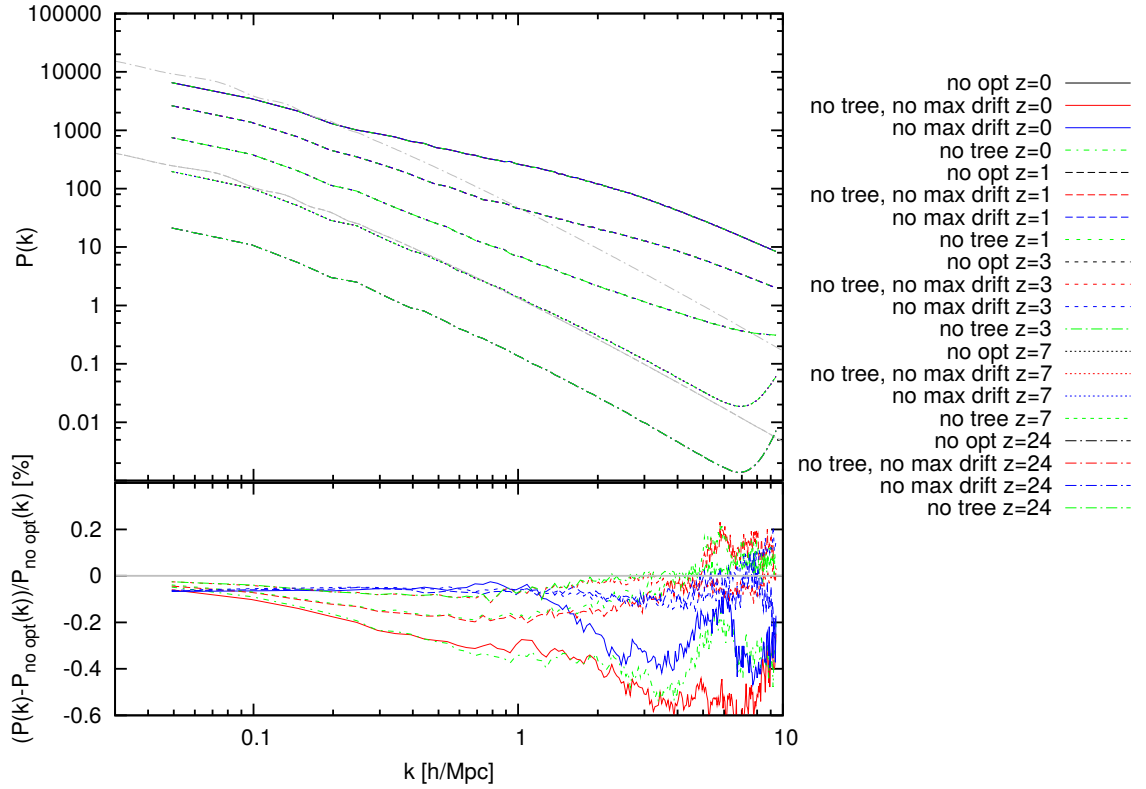
FIGURE 7.9: Power spectra at various redshifts obtained from the same ICs by using the `GADGET-2` code with varying combinations of optimizations for the neutrino component. The bottom plot shows the relative difference in respect to the results obtained when no optimizations are used.

7.2   Comparison & Application in current research

7.2.1   Massive neutrinos in ΛCDM

To compare the two described techniques described in Sec. 7.1, we tested them in a standard ΛCDM model (Planck1 cosmology) with massive neutrinos ($\sum m_\nu = 0.5$eV) in a simulation box with a size of 512 Mpc/h and starting at a redshift of $z_i = 49$. Softening was chosen at 2% of the mean separation of the 256^3 N-body tracer particles of CDM and in case of the N-body technique for neutrinos as well. The transfer functions for the CDM and neutrino components in the initial conditions as well as for the 128 explicitly calculated neutrino backgrounds have been calculated by the `CAMB` Boltzmann solver. The redshifts for the pre-calculated neutrinos backgrounds are equally spaced in time and are used for interpolation of the background for intermediate redshifts. We additionally performed a third simulation where we use a single cold collision-less fluid with the identical total matter

power spectrum at z_i for comparison[22]. In Fig. 7.10, we show the absolute projected DM density and difference in neutrino densities found in the simulation volume for the two techniques, while in Fig. 7.11 the total, DM and neutrino matter power spectrum are plotted.
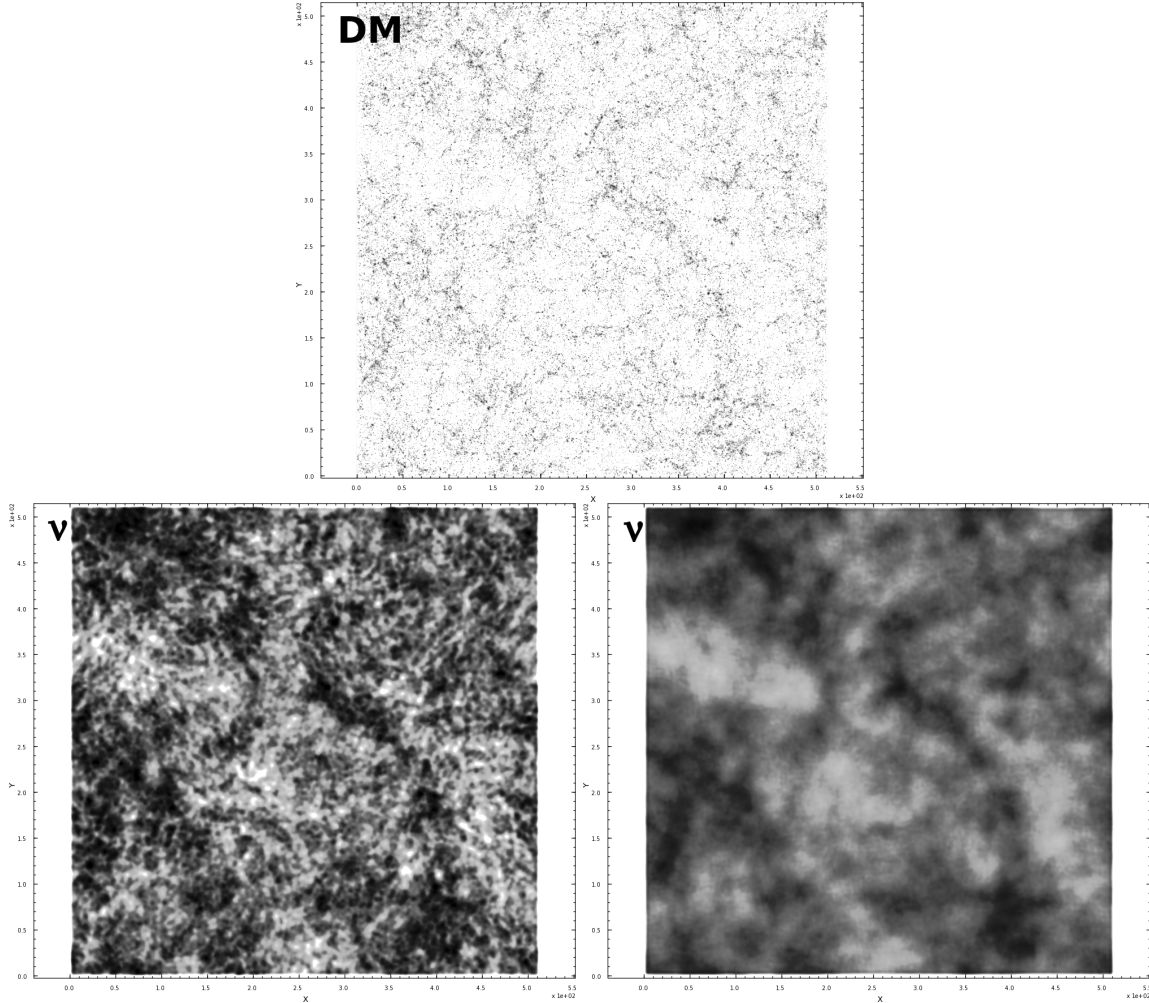
FIGURE 7.10: Projected matter density of DM and massive neutrinos in simulation box at $z = 0$: (top panel) DM matter density from using N-body technique for neutrinos with a logarithmic density scale with darker regions marking a higher density; (bottom panels) massive neutrino distribution in N-body (left) and linear background technique (right) with a logarithmic density scale with darker regions marking a higher density.

First, the obvious difference in the distribution of the neutrino fluid can be noticed. The neutrino power spectrum for the particle approach shows a significant excess with respect to that for the linear neutrino background on small scales. In results shown in Fig. 7.11 we can distinguish between two between two regimes each

---

[22]This should not be confused with the scenario of massless neutrinos, i.e. $\sum m_\nu = 0$.
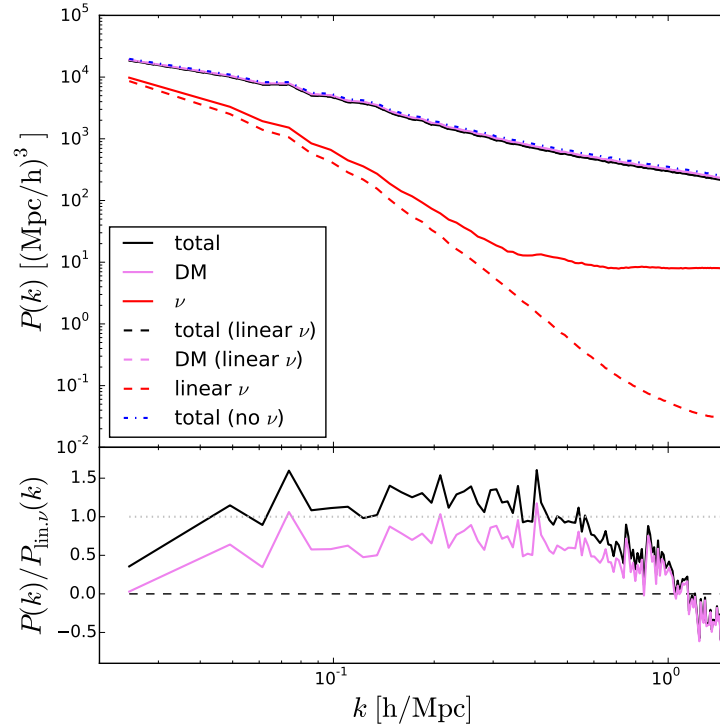
FIGURE 7.11: Matter power spectra for N-body simulation of ΛCDM with massive neutrino background ($\sum m_\nu = 0.5\text{eV}$) as either linear background (dashed lines) or N-body particles (solid lines). All results shown are at $z = 0$ and distinguish between power spectra for only DM (violet), the neutrinos (red) and both combined (black). Additionally, the results for a simulation with identical IC but with only a single cold component ('no ν', blue dashed-dotted line) is included for comparison. The bottom part of the panel shows the relative differences between the power spectra with respect to the results for a linear neutrino background. The dotted line marks the 1%.

dominated by a different cause for this excess. On scales larger than $k = 0.4\,h/\text{Mpc}$, the power of the perturbations in the neutrino component still decreases with increasing wave-number k, but shows an increasing excess towards the linear neutrino power spectrum. Below this threshold, the non-linear neutrino power spectrum obtained from the simulation levels out leading to an even sharper rise of the excess towards smaller scales. The excess in the first case can be explained by non-linear corrections to the neutrino distribution which stem from neutrinos being able to "feel" the collapsed CDM structures, i.e. galaxy and galaxy cluster halos that formed on these scales where those neutrinos with lower momenta may be accreted and further boost the growth of those structures. This can be seen in Fig. 7.10 where the neutrino density is visibly higher around the clusters. Below the threshold, the so-called shot-noise becomes the dominant contribution to the mea-

sured non-linear power spectrum. This is a purely numerical error resulting from finite number of neutrinos available to reconstruct the neutrino density field. We already encountered this effect when discussing the sampling of the neutrinos by the discrete tracer particles in Sec. 7.1.2. By starting of a grid or glass in the initial conditions, this shot-noise may be avoided initially, but as the neutrinos stream freely through the simulation volume, this "randomness" propagates to larger scales as well until we get the constant shot-noise "floor" that can be seen in Fig. 7.11. At late times, this shot-noise in the neutrino component is no concern since it contributes only little to the total matter perturbations on those scales which are by far dominated by the grown DM structures. But at high redshift, these DM structures are still relatively small and the shot-noise can have a larger contribution to the total power spectrum and these random fluctuations in the density field can dominate genuine perturbations in the DM distribution and thus slow down growth.

Like previous publications (Brandbyge and Hannestad, 2009; Villaescusa-Navarro et al., 2013), we also observed a difference in power when comparing the N-body approach with the linear background technique, which peaks around $k = 0.1 - 1$ h/Mpc with a maximum excess in power for the N-body technique of about 1%. By comparing the DM power spectra in Fig. 7.11, one can see that these non-linear corrections to total matter power spectrum not only stem from the neutrinos interacting with the non-linear CDM structures, which are missed in linear theory, but also from a boost in the growth of DM structures due to the non-linear treatment of the neutrinos. The corrections to the total matter spectrum are of similar size to what is expected by the relation $(\sum m_\nu / 0.54 eV)^2$ reported in Brandbyge and Hannestad (2009). This shows that for light neutrinos with $\sum m_\nu < 0.5 eV$, one may use the computationally less expensive linear background technique if the interest is only on the overall matter distribution and not in particular on that of the neutrinos, which is obviously incorrect, and still remains within a sub-percentage difference relative to the full non-linear treatment with neutrino N-body tracers. For cosmologies with more massive neutrinos as presented in Sec. 7.2.2, not only becomes the neutrino component a larger share of the total matter and thus the differences in the neutrino distribution contributes more to the total matter power spectrum, but additionally the free-streaming velocities are smaller for heavier neutrinos, thus allowing a greater share of the neutrinos to cluster on smaller structures and boost the structure growth there. The combination of both effects leads to the relation of the corrections shown above and thus to error due to missing non-linear contributions that exceed the often desired 1% accuracy for the total matter power spectrum

by far.

Finally, the simulation without no free-streaming component ('no ν') possesses significantly more power on small scales, which is expected as all matter is cold and contributes to the perturbation growth on those scales unlike in the two techniques that include the free-streaming. The excess for our choice of neutrino masses amounts to about 15% excess in the total matter power spectrum at $k = 1\,\text{h/Mpc}$. This simply emphasizes how significant the impact of free-streaming of neutrinos is on the structure formation process in the simulations and must not be ignored.

7.2.2   Neutrinos to rescue Einstein-de Sitter

One example of how neutrinos can play a vital role in a cosmological model was recently explored in Shanks et al. (2014). This work was motivated by the lack of any successful detection of both dark matter and dark energy which form the core of ΛCDM. The only exception is the massive neutrino, which accounts at least for a fraction of the DM present in the Universe.

Originally, Shanks (1985) argued that an Einstein-de Sitter model with a low H_0 would address several problems with a baryon-only model. Unfortunately, the low Hubble constant combined with $\Omega_b = 1$ predicts a first acoustic peak in the CMB angular power spectrum at significantly smaller scales than observed. Two proposals have been made to move the first peak by smoothing it. Shanks (2007) attempted to attribute this to lensing by foreground galaxy groups and clusters which might smooth the peak enough to shift and damp the peaks in the baryonic model to fit the peaks seen in the CMB data on slightly larger scale and with lower amplitudes, but found that the amplitude of foreground clustering had to be 10 larger than expected from observations Sawangwit and Shanks (2010) took another approach by arguing that the WMAP beam for the CMB measurements could have a significant smoothing effect on the peaks in the spectrum which seemed to be supported by studies of radio sources suggesting a wider WMAP beam than previously expected. All these attempts profited from the fact that the power spectrum in the WMAP era was only measured accurately up to the first peaks and beyond that became less constraint. In the era of the more accurate Planck CMB survey, it becomes impossible to fit such a $\Omega_b = 1$ model to the available data.

In Section 6.3.2, we discussed how the presence of neutrinos affects the observable CMB spectra. Their inclusion in the model introduces another degree of freedom that allows for more accurate fits to the CMB. Shanks et al. (2014) studied this possibility and came up with a best-fit for an Einstein-de Sitter cosmology

($\Omega_0 = 1$), where neutrinos not only make up a fraction of the energy density in the Universe today like in ΛCDM, but contain very high masses at the very upper bound of what is not ruled out by particle experiments (cf. Sec. 2.1.1) that result for thermal neutrino relics in a energy density that dominates the baryons even today, i.e. $\Omega_{\nu,0} \gg \Omega_{b,0}$.

In Fig. 7.12, we present the results for the simulations, we ran for the publication. We used `GADGET-2` with a very simply hydrodynamics model (no feedback or star formation) for the 256^3 baryons SPH particles in the periodic simulation box with a side length of $150 Mpc/h$. $\sum m_\nu = 15$eV. The neutrinos with a sum of masses of $\sum m_\nu = 15$ eV have been represented by 256^3 N-body tracers with the thermal velocities according to their particle mass. As we discussed in Sec. 7.2.1, using the linear background would lead to huge missed non-linear corrections for such high neutrino masses and thus disqualifies it for being used here. To avoid the impact of the neutrino shot-noise, which could significantly affect the structure growth in the baryonic component on small scales, as much as possible, we decided to start at a rather low redshift of $z = 7$. The results may not look very encouraging for the best-fitting reference model with a normalization of $\sigma_8 = 0.2$. The initial strong cut-off in the total matter power spectrum due to the free-streaming of the neutrinos, leaves next to no perturbations on small scales to support an hierarchical growth of the baryonic structures. Shot-noise is still an issue on smaller scales at early times in the simulation, but propagates much slower towards larger scales due to the much smaller free-streaming scale of the numerical tracers compared to the simulations discussed for the ΛCDM model in Sec. 7.2.1. Without the supporting DM fluctuations or collapsed DM structures on small scales, the gas in the simulations collapses very late and at far too small numbers. This is why the it has been argued that alternative seeds for galaxy formation such as *primordial magnetic fields* (PMF) (Peebles, 1980) may exist and compensate for that shortcoming.

7.3 Conclusion

In our studies of the N-body technique with explicit thermal velocities, it can be concluded that the errors made by assigning microscopic thermal motion explicitly on a macroscopic level as described in this section seem to be limited to the desired accuracy of about 1% in the total power spectrum.

We have further tested in the two examples how to include neutrinos as a linear background for N-body simulation of DM and a simplified SPH approach
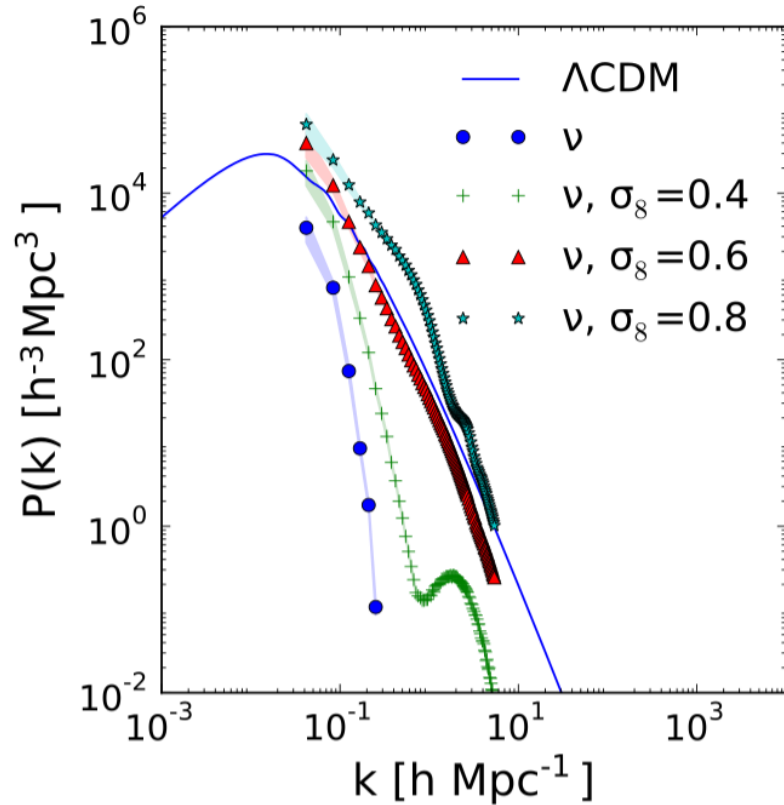
FIGURE 7.12: Results of hydrodynamics simulation of Shanks2014 model ($\sum m_\nu = 15\text{eV}$): Matter power spectrum with errors (shaded regions) for simulation with reference normalisation of $\sigma_8 = 0.2$ (blue) and the alternative normalisations of $\sigma_8 = 0.4$ (green), $\sigma_8 = 0.6$ (red) and $\sigma_8 = 0.8$ (light blue). The linear matter power spectrum for the ΛCDM model is shown for comparison (solid line) (Shanks et al., 2014).

with baryons.

The study of the ΛCDM model with massive neutrinos has confirmed previous results by other groups that for low mass neutrinos, the linear neutrino background provides an inexpensive way to predict the total matter distribution with only a sub-percentage deviation from the results obtained by giving the neutrinos the more expensive full non-linear treatment with the N-body technique. The results are more accurate for neutrinos with a very low mass, which stay mostly linear. On the other hand, the linear neutrino background fails to predict the neutrino distribution correctly, as it not only neglects any potential non-linear collapse in the neutrino component, but even misses any boost in linear growth neutrino perturbations may get from the collapse of DM structures and the resulting deeper potential wells. In Section 6.2.1 we discussed how to counter this analytically by using higher-order theories for CDM which then couple to the linear theory for

neutrinos. Ali-Haïmoud and Bird (2013) came up with a similar approach where the linear growth of neutrinos is calculated in the non-linear background of CDM obtained on-the-fly from an N-body simulation rather than the linear predictions for CDM used to pre-calculate the neutrino evolution in our calculation in advance. The result serves then in return as a background for the next time step in the N-body simulation of DM. For the mass neutrino masses that are currently favoured by cosmological observations, this semi-linear method seems to improve the results significantly at very low additional computational costs.

For models as presented in our second example however, that contain more massive neutrinos and do not have a dominant non-linear background as in the case of ΛCDM, the error due to missed non-linear growth in the neutrino sector is larger while the correction in the feedback from the non-linear background have far less impact on the gravitationally dominating neutrino fluid. In models like this, even the improved approach in Ali-Haïmoud and Bird (2013) would most likely fail as it misses the non-linear growth in the neutrino component, which could help to form neutrino halos above the free-streaming scale for the baryons to be accreted upon to form galaxies. This leaves us with the N-body technique, which we used to produced the results shown here.

There was also a proposal in Brandbyge and Hannestad (2010) to combine the linear and particle method by splitting the neutrino fluid into different components based on their absolute momenta, where each of those components was treated linearly on the grid until its average momentum was redshifted below a certain threshold. At that point, this component was converted into particle tracers. While this method was a major improvement over both the pure linear and particle method, it was much more complicated to implement and to use and additionally faces problems with mass conservation along the split between the linear and non-linear neutrino components.

In conclusion, we have seen that each of the techniques discussed in this chapter has its shortcomings when trying predict the evolution of the distribution of the neutrino content accurately. This motivated the development of our new grid-based approach that we present in Chapter 8.

CHAPTER 8

SEPARA - a way to treat neutrinos correctly

In the previous chapter we pointed out the difficulties faced when representing neutrinos as tracer particles or a background in our numerical simulations. In this chapter we introduce as an alternative an Eulerian 6D phase-space approach. We briefly discuss the technique used and its implementation, called `SEPARA`. We then compare the efficiency of the code and results with those obtained using the alternative methods.

8.1 Eulerian method

One major drawback of the N-body technique is the sparse sampling of the 6-dimensional phase-space with the finite number of tracers. There is the problem of reconstructing the three-dimensional matter density field to calculate the correct gravitational force-field or the neutrino velocity field which are subject to the intrinsic shot noise due to the sparse, random sampling. But additionally, two-body relaxation at close encounters of two tracers may lead to erroneous results for interactions on smaller scales. The latter was only avoided in our simulations with neutrino particles by limiting the force calculations for neutrinos to the PM grid (see Sec. 7.1.3). This grid is static and we have to find a trade-off for each simulation we run to make it small enough to avoid neutrinos missing interactions with smaller structures while at the same time keeping it as large as possible in order to not lose the advantages of the tree for the force-calculations of the CDM in the simulation.

We have already seen that the issue with shot noise was not present for the linear background technique, where we reconstructed the local density from the integration of the linearised Boltzmann equation and the stored initial perturbations (phases and amplitudes). In order to get the same advantage for a full nonlinear treatment of the evolution of the neutrino distribution, we have to switch from the *Lagrangian paradigm*, where we track the trajectories of a sample set of

tracers to a *Eulerian method*, where the neutrino fluid is treated as a continuum that is parametrized by values at fixed position in (phase-)space. Usually regular grids such as cartesian grids are used to store this parametrisation of the fluid properties. This unfortunately breaks the Galilean invariance as it has certain preferred directions. In the case of collisionless, free-streaming matter such as neutrinos, the only property we need to keep track of is the phase-space density field. At each fixed position, we can determine the evolution of the local phase-space density by solving the Boltzmann equation (Eq. 2.27), that is known in its collision-less form as the *Vlasov equation*[23]:

$$\frac{\partial f}{\partial \vec{x}} \frac{\mathrm{d}\vec{x}}{\mathrm{d}t} + \frac{\partial f}{\partial \vec{v}} \nabla \rho = 0 \, , \tag{8.1}$$

We used here, that the only momentum transfer that changes the velocities of the particles originates from the local gravitational forces. These are given by the local gradient of the gravitational potential ϕ, which itself can be determined by solving *Poisson's equation*

$$\nabla^2 \phi = 4\pi G \delta \rho(x, t) \tag{8.2}$$

where G is the gravitational constant and $\delta\rho(x,t) = (\rho(x,t) - \bar{\rho})/\rho$ is the local overdensity in the spatial density fluctuations $\rho(x,t) = \int f(x,v,t)dv$.

There have been attempts before to solve these coupled *Vlasov-Poisson equations* on a discrete Eulerian grid rather than with Lagrangian particles. Yoshikawa et al. (2013) presented a first test for a six-dimensional phase-space code on a regular grid that aimed at simulating a neutrino fluid. These authors adopted numerical techniques that have been previously used in numerical simulations of plasma physics (Filbet et al., 2001). A major problem of their approach was however, that their grid had a globally fixed resolution. While this allows for very simple and efficient data structures to store the necessary information about the neutrino fluid, there is no way to increase the resolution in regions of interest without doing so on the whole grid. As we show in Sec. 8.2, the high dimensionality of phase-space makes such increases of the resolution computationally highly expensive as the costs scale to the sixth power. So the maximal resolution that would be achievable with such a technique for such box sizes as used in e.g. Sec. 7.2, could well be larger than e.g. Milky Way-sized galaxies or even small clusters which we are interested in studying. This is why we eventually had to come up with an improved technique that addresses this issue and which is presented in the following sections.

---

[23]We reduced the four vectors by the respective three-vectors by applying the same identities as in Sec. 2.2.6

8.2 Numerical Methods / Implementation

Our implementation is based on the RAMSES AMR code (Teyssier, 2002) and is called SEPARA[24]. It is designed as a patch to make use of CDM and baryonic physics solvers that already implemented in the RAMSES framework[25].

The techniques used to implement our neutrino solver can be split up into 4 categories: Discretization of the neutrino phase-space fluid, solving the Boltzmann-Vlasov equation, initial conditions and the cosmological setup. But before we dive into the discussion of those topics, we want to establish a certain nomenclature. First of all, without loss of generality, we will limit most of the following discussions to the case with one dimension in both spatial and velocity coordinates (1+1D). This allows for a much simpler visualization, but can easily generalized to the 3+3D case we are aiming to solve. The *spatial* coordinates with be denoted by x and the velocity coordinates with v. When discussing dimensionality dependent issues, we denote as $n_{\dim} = \{1, 2, 3\}$ the dimensionality of the position space, hence the full phase-space has $2n_{\dim}$ dimensions according to this definition.

8.2.1 Discretization

Mesh / Approximation of phase-space distribution

As a discrete representation of the six-dimensional phase-space fluid, we chose a *finite volume* approximation approach, where we store the *volume averaged* value of the phase-space density field $f(\vec{x}, \vec{v}, t)$ on a Cartesian mesh of cells, i.e.

$$f_{i,j}(t) = \frac{1}{\Delta x \Delta v} \int_{x_{i-\frac{1}{2}}}^{x_{i+\frac{1}{2}}} \int_{v_{j-\frac{1}{2}}}^{v_{j+\frac{1}{2}}} f(x, v, t) \mathrm{d}x \mathrm{d}v \,, \tag{8.3}$$

where $x_{i\pm\frac{1}{2}}$ and $x_{i\pm\frac{1}{2}}$ are the coordinates at the cell boundaries in the respective dimensions with $\Delta x = x_{i+\frac{1}{2}} - x_{i-\frac{1}{2}}$, $\Delta v = v_{j+\frac{1}{2}} - v_{j-\frac{1}{2}}$ being the cell size and thus defining the resolution of our mesh. By convention, the first index of our mesh points will numerate the mesh points in position space and the second one in velocity.

The phase-density for points within the cells i.e. at coordinates $(x, v) = [x_{i-\frac{1}{2}}, x_{i+\frac{1}{2}}] \times$

---

[24]Acronym for **S**imulations d'**E**space des **P**hases **A**vec un **R**éseau **A**daptatif (French; "phase-space simulations with an adaptive mesh")

[25]SEPARA can also be used in parallel with a huge variety of additional patches that add additional physics so long as they do not modify certain key parts of the source code. For more details refer to the README file in the patch folder of the source code.

$[v_{j-\frac{1}{2}}, v_{j+\frac{1}{2}}]$ is approximated by interpolating between our stored cell-centred values $f_{i,j}$ with slope-limited *Lagrange polynomials* in each dimension, i.e.

$$\tilde{f}(x,v,t) = P^{(m)}(\{f_{k,j}\}, x, v, t) P^{(n)}(\{f_{i,k}\}, x, v, t) , \qquad (8.4)$$

where *n,m* is the order of those polynomials based on the stencils $\{f_{i,k}\}$ and $\{f_{k,j}\}$ respectively. The symmetry of the Lagrange polynomials preserves the cell average identified with the cell-centred values $f_{i,j}$. In the current implementation, we use a simple second-order-accurate approximation, thus obtaining a piecewise linear reconstruction of the phase-space density.

The slope limiters that are available for the reconstruction/interpolation of the phase-space density are the same as those used by the hydro solver in RAMSES, i.e. a simple MinMod scheme, a Monotonized Central slope scheme and an unlimited Central slope scheme.

Adaptive Mesh Refinement

So far, our discussion has only considered a regular mesh with a given resolution of Δx and Δv in position and velocity space respectively. Implementations of such regular phase-space mesh exist (Yoshikawa et al., 2013), but are riddled with the infeasible costs that come with a fully refined six-dimensional mesh as for each increase of the overall resolution by a factor of two, the computational costs rise by a factor of $2^6 = 64$. This becomes a concern mostly with respect to the amount of memory needed to store the data. Even if only a single double-precision float per cell is stored, even rather low-resolution meshes dividing each dimension into only 128 equally spaced divisions already result in a memory requirement of about 32 TB[26]. Fig. 8.1 illustrates this problem by plotting the memory requirements depending on the dimensionality and level of refinement as solid lines. The grey horizontal dashed line marks the feasibility limit on the local COSMA-5 supercomputer with respect to the memory requirements. The mere two orders of magnitude in resolution possible are hardly sufficient in the context of cosmological simulations which have to cover both velocity and spatial scales stretching over a much wider dynamic range. On the other hand, if we look at the density plot shown in Fig. 8.2 for a typical phase-space distribution of neutrinos, we can see that many regions do not reveal any complex structures and so do not require a highly-resolved mesh

---

[26]For comparison, the total amount of memory (RAM) of the COSMA-4 and COSMA-5 supercomputers in Durham are 14 TB and 52 TB respectively.
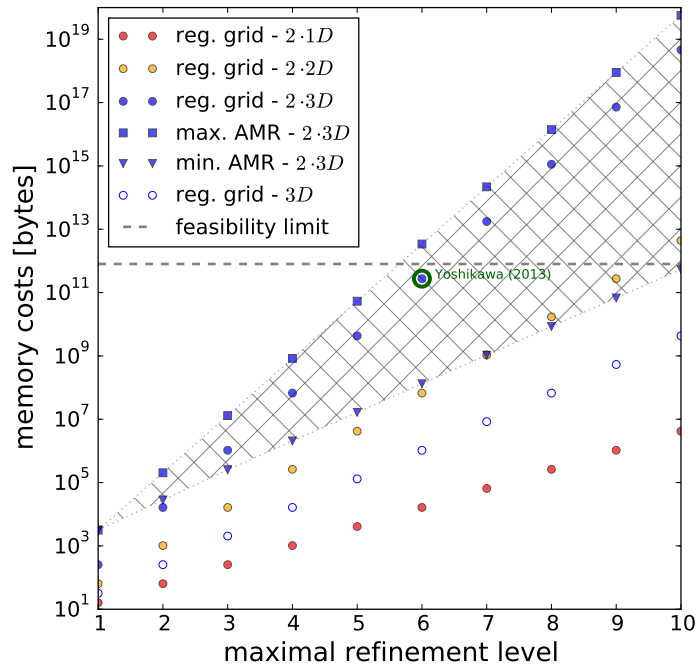
FIGURE 8.1: Estimates for the memory requirement for a fully-refined mesh (circles) and best- and worst-case AMR scenarios (squares). For the fully refined mesh, these estimates only include the actual costs per cell to store the local value f_i as one double-precision float, while for the AMR case they already more accurately include the total costs including temporary buffers and overheads from the AMR tree structure. The hatched region marks the range between the best- and worst-case scenario, while the dashed line marks approximately the feasibility limit. The biggest simulation run in Yoshikawa et al. (2013) is highlighted in green for comparison.

for a good approximation. These are in particular the regions that have a low matter density in position space without any strong gradients, but also the regions of high-velocity in which the low-density phase-space fluid streams freely through even the largest non-linear structures. Forcing these regions into a high resolution mesh wastes precious resources that could be better spent on the high-density regions of interest where high resolution is crucial to follow the highly non-linear flows. Thus, to overcome the strict limitations, we apply an *Adaptive Mesh Refinement* where we start with a regular minimally-resolved coarse mesh and then only refine those cells further that meet certain *user-defined* refinement criteria. Like in RAMSES, we use a *dyadic* refinement strategy, i.e. upon refinement each cell is split into cells of half the original side length in each dimension. This group of $2^{2n_{\dim}}$ siblings of the refined father cell (or so-called *split-cell*) is organized in a so-called *grid* as the fundamental data structure. Thus, we obtain a *Fully Threaded Tree* (FTT)
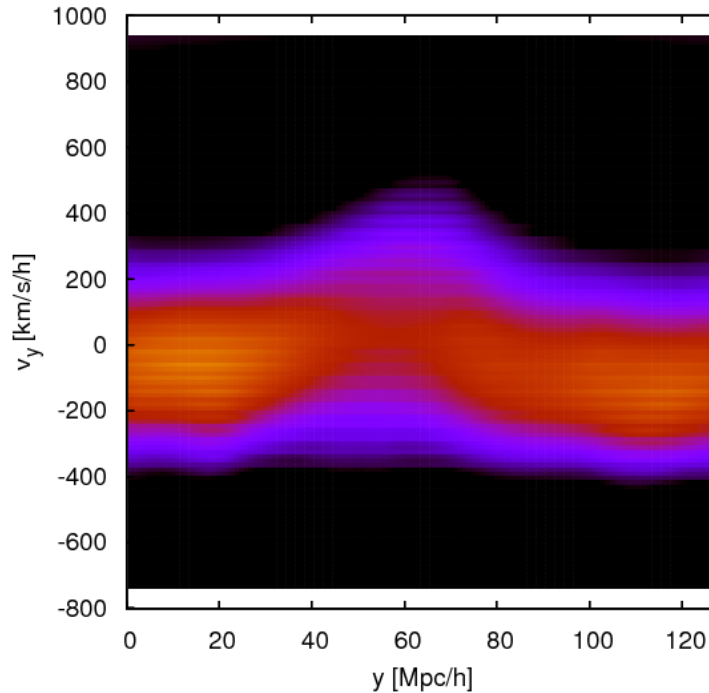
FIGURE 8.2: 2D Phase-space density around a simulated large-scale dark matter structure.

structure as shown in Fig. 8.3 where defined relations between those grids and its group of sub-cells, their associated father cells and their neighbour cell as well as a double-linked list structure on all grids allow an efficient organization and access to the cells at the different levels of refinement. Traversing the tree from split-cells to their grids and sibling cells, we eventually reach a level of a locally maximal refinement. The cells on this level are not associated with grids any more and mark the leafs of the $2^{2\text{ndim}}$-tree and hence are called *leaf cells*. Our phase-space tree exists
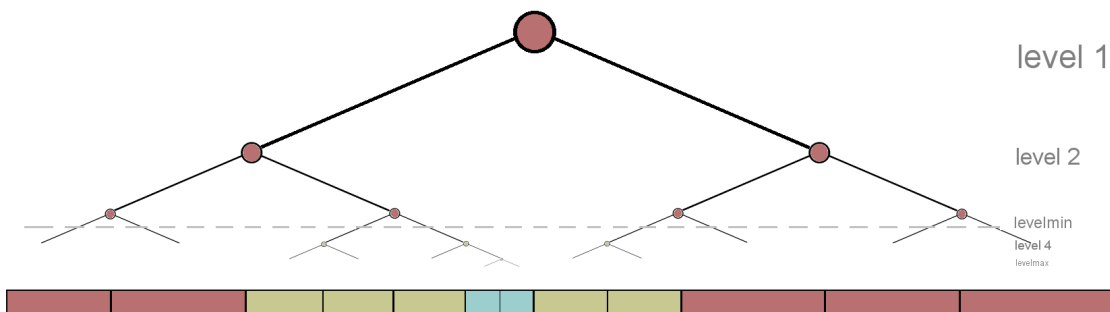
FIGURE 8.3: Illustration of a 1D Fully Threaded Tree (FFT) data structure used in RAMSES/SEPARA.

alongside the n_{dim}-dimensional tree of the original RAMSES code which is used for the hydrodynamics and Particle-Mesh solver. The only interaction between our collisionless phase-space fluid and the "standard" components is via gravity, which itself only depends on the gradients of the spatial matter density of all components combined. Modifications of the phase-space tree structure are done in the same, efficient way as in RAMSES using using the same double-linked list to navigate and modify the tree.

Besides adapting the relations between phase-space grids/cells to the $2n_{\text{dim}}$ dimensions of the full phase-space, we also introduce a new relation between each phase-space cell and its so-called *shadow cell* in the PM/Hydro tree, i.e. the cells covering the identical volume in position space. If no such cell exists, a refinement is forced in the PM/Hydro tree until the requirement is satisfied. These *pure shadow cells* are masked and thus invisible to the PM/Hydro solvers, but are essential to calculate the correct local gravitational accelerations.

In total, the organization in the AMR trees requires 80 pointers per grid, or equivalently 1.25 per cell. Additionally, each grid stores the values for the local averaged phase-space density f_i as well as certain buffers for flagging and the phase-space solvers.

Computing the density field / Solving Poisson Equation

The existence of a defined relation between each phase-space cell and its *shadow cell*, simplifies the calculation of the resulting gravitational forces within the simulation. In the original RAMSES code, the matter density field on each refinement level is reconstructed using a multipole-*cloud-in-cell* (CIC) or -*triangular-shaped cloud* (TSC) assignment scheme within each PM/Hydro cell. We use an identical approach where we calculate the multipoles in $2n_{\text{dim}}$ dimensions and then add them to the density field stored in the *shadow cells* using the same assignment scheme. In the case of either pure shadow cells or PM/Hydro cells that are not shadow cells themselves, we interpolate the respective missing contributions from the coarser father cells down to the finest leafs.

The Poisson equation (Eq. 8.2) is then solved on each level in the "standard" RAMSES fashion using either a *multi-grid* or *conjugate-gradient* method with a modification to also consider the pure shadow cells in the calculations. The resulting forces are stored within each shadow to be used in the time integration.

8.2.2 Time Integration

Upon advection schemes for the neutrino fluid, we would like to impose the desirable requirement of strict mass conservation. As this is a fundamental property, we want to preserve it as well as possible when calculating the advections through phase-space. In its integral and unsplit form, this conservation law is written as

$$\int_{x_{i-\frac{1}{2}}}^{x_{i+\frac{1}{2}}} \int_{v_{j-\frac{1}{2}}}^{v_{j+\frac{1}{2}}} \int_{t^{(n)}}^{t^{(n+1)}} (\partial_t f + v \partial_x f + a \partial_v f) \mathrm{d}x \mathrm{d}v \mathrm{d}t = 0 \,. \tag{8.5}$$

As in RAMSES, an important requirement in our coupled N-body and phase-space grid code is the possibility to deal with variable time steps and the stability conditions for the time step size is given by the Courant Friedrich Levy (CFL) condition, which can vary over time. For the time integration of Eq. 8.1, a second-order mid-point scheme is used, which reduces exactly to the standard second-order leapfrog scheme (Hockney and Eastwood, 1981) for constant time steps, i.e. the advection equations (Eq. 8.1) are split up into separate updates along the velocity direction ("kick")

$$\frac{\partial f}{\partial \tau} - \sum_{i=1}^{n_{\mathrm{dim}}} \nabla \phi \frac{\partial f}{\partial v_i} = 0 \tag{8.6}$$

and along spatial dimensions ("drift")

$$\frac{\partial f}{\partial \tau} - \sum_{i=1}^{n_{\mathrm{dim}}} v_i \frac{\partial f}{\partial x_i} = 0 \,. \tag{8.7}$$

We use the *kick-drift-kick* (KDK) leapfrog scheme with a predictor "kick" half-step followed by a full "drift" step and a corrector "kick" half-step that uses the new forces obtained by solving the Poisson equation for the updated spatial matter distribution.

Drift - Single-Mesh Godunov solver   To solve the advection in spatial directions ("drifts", Eq. 8.7), we decided to use a similar solver as RAMSES uses in its hydrodynamics solver, namely a conservative, second-order, unsplit MUSCL-HANCOCK scheme. This scheme offers us certain advantages, while the inherent limitations in this scheme are already accounted for in the design of our AMR approach copied from RAMSES.

For our volume-averaged phase-space density, Eq.8.7 for a finite time step Δt

reads

$$\frac{f_{i,j}^{(n+1)} - f_{i,j}^{(n)}}{\Delta t} + v_i \bar{f}_{i+\frac{1}{2},j}^{(n+\frac{1}{2})} - \bar{f}_{(i-\frac{1}{2}),j}^{(n+\frac{1}{2})} \Delta x = 0 \tag{8.8}$$

where

$$\bar{f}_{i\pm\frac{1}{2},j}^{n+\frac{1}{2}} = \frac{1}{\Delta}t \int_{t^n}^{t^{n+1}} \tilde{f}(x_{i\pm\frac{1}{2}}, t) \tag{8.9}$$

is the time-averaged phase-space density at the spatial cell borders, where $\tilde{f}(\cdot)$ is the reconstruction of the phase-space density using the cells in the upwind direction of the advection[27]. This method is an unsplit *corner transport upwind* (CTU) method for simulations in more than one dimension which allows us to perform the whole advection in position space in one cell update, thus avoiding the numerical diffusion we would get from performing the advection for each dimension separately.

Starting with leaf cells on the highest level of refinement, the resulting fluxes within refined boundaries are then propagated using constriction operations to the coarser father cells. Fluxes at refinement boundaries are computed on the finer level. This scheme is very memory-efficient as we only have to store the resulting total flux per cell. Everything else is only relevant within the $6^{n_{\dim}}$ stencil, i.e. the grid containing the cells and 2 ghost cells on each side for our second-order solver, used to calculate the fluxes and only has to be stored for the time each grid is processed. Thus, this approach has a complexity of $\mathcal{O}(N)$ in both time and memory, but comes at the cost of a strict maximal time step limit given by the necessary *Courant-Friedrichs-Levy* (CFL) condition for such CTU-like schemes under which the scheme becomes stable:

$$\Delta t_{\mathrm{CFL}} = \max(C^i, i \in \{1, n_{\dim}\}) < C_{\mathrm{CFL}}, \tag{8.10}$$

where C_i in our case with vanishing sound speed is given simply by $C^i = \max_{j \in \mathrm{cells}} \left(\frac{\Delta x_j^i}{\|\Delta v_j^i\|} \right)$ for each of the $n_{\dim}$ dimensions.

Kick - Semi-Lagrangian PCF solver   The second half-kick in our second-order symplectic "leap-frog" integrator requires knowledge about the gravitational accelerations resulting from the density field at the end of this time step. For N-body methods and the usual single-stream solvers, this is not a problem as the local

---

[27]We do not have to average the orthogonal velocity-dependence of $\tilde{f}$ since we average over the full size of the cell and our symmetric reconstruction scheme with Lagrange Polynomials ensures that we can simply use $\tilde{f}$ interpolated in spatial direction alone.

velocity/momentum is just a quantity and the gravitational interaction a simple source term that can be easily added and subtracted as used for the correction of the second half-kick for both the particles and the baryonic matter and impose no direct limitation on the time-stepping. For our phase-space mesh approach, this is no longer the case. First of all, kicks are here advections of phase-space fluid in the velocity hyperplanes orthogonal to the spatial dimensions in which the forces are calculated. Such density updates cannot be reverted to be corrected due to the numerical diffusion of such operations. Secondly, the stability of certain advection solvers such as the scheme used for the spatial advection depends on time-stepping conditions that themselves require the knowledge of the advection velocity. But, as mentioned, we do not have any knowledge about the advection speed for the second half-kick without performing the first half-kick and the drift, which we cannot perform without knowing the maximal allowed time-step size. A way to avoid this dilemma is to use a scheme that does not depend on such a strict time-stepping condition. Thus, in SEPARA, the kicks are performed using the *semi-lagrangian* (SL) *positive,flux-conservative* (PCF) scheme as introduced in Filbet et al. (2001) which is conservative by construction. The difference between such SL techniques and the Eulerian methods to numerically solve PDEs on a mesh is that they use the characteristics of the advection equations along with an interpolation method to calculate the updates for cells even in the case that the source cells are not adjacent to the target cell. Fig. 8.4 (left) illustrates this for an advection in 2D where the new value for the target cell at timestep $n + 1$ is constructed from the content of the volume covered by the cell i at the previous time-step if traced back in time along the characteristics $X(t, t^{(n+1)}, v_i)$ using the fact that the content of such a volume is conserved along characteristics.

For one dimension, this can be written as:

$$f_{i,j}^{(n+1)} = \int_{v_{j-\frac{1}{2}}}^{v_{j+\frac{1}{2}}} \tilde{f}(x_i, v, t^{(n+1)}) \mathrm{d}v = \int_{X(t^{(n)},t^{(n+1)},v_{j-\frac{1}{2}})}^{X(t^{(n)},t^{(n+1)},v_{j+\frac{1}{2}})} \tilde{f}(x_i, v, t^{(n)}) \mathrm{d}v \,. \tag{8.11}$$

We can rewrite this equation by setting

$$\Phi_{i,j+\frac{1}{2}}(t^{(n)}) = \int_{X(t^{(n)},t^{(n+1)},v_{j-\frac{1}{2}})}^{v_{j+\frac{1}{2}}} \tilde{f}(x_i, v, t^{(n)}) \mathrm{d}v \,, \tag{8.12}$$

to obtain the conservative scheme

$$f_{i,j}^{(n+1)} = f_{i,j}^{(n)} + \Phi_{i,j-\frac{1}{2}}(t^{(n)}) - \Phi_{i,j+\frac{1}{2}}(t^{(n)}) \,. \tag{8.13}$$
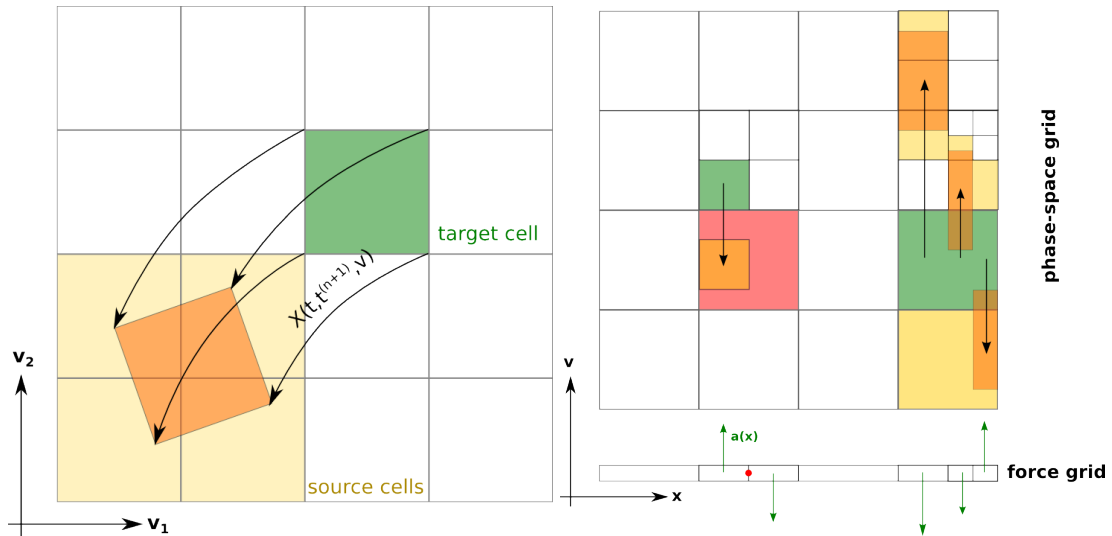
FIGURE 8.4: Illustration of the semi-lagrangian advection scheme. (left panel) Trajectories with arrow heads pointing backward in time and identification of source cells for a 2D advection in the velocity plane. (right panel) In AMR, mass conservation may be violated if the same advection velocity is not used for all refinement levels. The net force on the refinement level of the big red cell is zero while it is non-zero for the small green cell at the same location but on a higher refinement level. Thus, the part of the content of the red cells marked in orange is used more than once as a source in the advection. As a solution, coarser target cells (big green cell) have to be "sliced up" along the spatial dimensions to match the finest local refinement level.

This form looks very similar to our Godunov scheme, but instead of the fluxes from adjacent source cells, we calculate the fluxes through the cell boundaries based on the phase-space fluid that flows through our target cell during the time-step. The calculation of the characteristics becomes trivial as our advection field does not depend on the local velocity and trajectories in each time step are therefore simply straight lines defined by their point of origin at the cell corner of the target cell and the local advection velocity vector $\vec{a}(\vec{x})$, i.e.

$$X(t, t^{(n+1)}, v) = v - \Delta t \cdot a(t^{(n+\frac{1}{2})}) \tag{8.14}$$

and perform the following steps:

(1) Backtrack the corners of target cell along the characteristics and identify the source cells that lie within the backtracked volume, V.

(2) Reconstruction of the phase-space density, $\tilde{f}$, in the source cells.

(3) Calculate the new cell average at the target cell by integrating $\tilde{f}$ over V in all the source cells.

Before we discuss our adaptation of this scheme for AMR, we use, for the sake of simplicity, a piecewise constant reconstruction of the advection field $\vec{a}(\vec{x})$ based on the cell-centred value found by our Poisson solver for each cell. This results in discontinuities in the advection flow as the cell corners now have different characteristics for each adjacent cell, but it also reduces the calculation costs significantly as we only have to consider $2^{n_{\dim}}$ corners instead of the $2^{2n_{\dim}}$.

We now want to adapt this SL scheme for our non-regular mesh. Fig. 8.4 (right) illustrates we would violate mass conservation by simply using the advection velocity for each cell at its refinement level. While the net acceleration in the red cell is assumed to be zero and thus the content of the cell consists of the old content, there may be a non-zero gravitational acceleration at finer levels, which can lead to cells at those levels (green) to also source their new content from the red cell and thus duplicate the content of that (orange) intersection and as a result breaking the mass conservation. A solution to this problem is to slice up each target cell along the spatial dimension until it matches the finest local resolution for the forces. The fluxes are then calculated based on the source volumes for each of these slices using the same advection velocity for local contributions to target cells over all refinement levels. Unfortunately, this forces us to use a single time step scheme for our refinement levels instead of the potentially cheaper alternative adaptive time step scheme with sub-steps on finer levels that `RAMSES` offers.

8.2.3 Parallelisation

Most problems in modern numerical cosmology are by far too big to be treated by a single processing core/node, either due to time or memory limits. Thus, the simulation code has to provide parallelisation techniques to allow to split up the workload on multiple processing nodes. In `SEPARA` code, we use the existing framework found in `RAMSES` which we modified to suit our requirements. `RAMSES` in its current version uses a purely MPI-based parallelisation, where each CPU works on its own process/memory and communicates through the MPI framework with the other processes involved in the simulation. The workload is divided among these processes by splitting up the cells in the simulation into domains. Their boundaries are determined by a geometrical algorithm that decomposes the position space while trying to balance the workload among those domains. `RAMSES` provides two strategies to do this: linearisation of the position space with a *Peano-Hilbert* curve to reduce the higher-dimensional decomposition problem into a one-dimensional one, or, *bisection* splitting, where the domains are cuboidal partitions

obtained by orthogonal recursive bisection[28]. The computational costs are predicted by a weighted counting of both the N-Body particles and the leaf cells in the cell-tree in each domain to balance out the processing time as well as the memory requirement between the processes. Each domain then contains both its own cells/grids as well as so-called virtual grids. The latter are those grids adjacent to the domain that belong to other processes, but whose properties are needed in the calculations (e.g. for restriction operations or flows across domain boundaries). They usually consist of the grid siblings of each domain cell and its father grid/cell and their stored values are updated to those on their host process via MPI communication when needed.

In RAMSES, this decomposition is limited to the n_{dim} space the code is working on. For SEPARA, we have to generalize this for our $2n_{\mathrm{dim}}$ phase-space. Due to our choice of integration schemes, we are very limited on how to decompose phase-space if we want to minimize the amount cross-domain communication and buffer cells (=virtual grids). Thanks to our second-order reconstruction scheme and Upwind method used for advection in position space, drift calculations only require knowledge about the immediate neighbourhood of each cell ($\rightarrow 6^{n_{\mathrm{dim}}}$ stencil). On the other hand, our Semi-Lagrangian advection scheme for the "kicks" may require knowledge about source cells at distances that are pre-determined in velocity space. Thus, the only way to save the very efficient and simple way of using virtual grids as cross-domain communication buffers, is either to ensure that either the source cells are known to the process hosting the target cell or that all source cell reside on the host of the target cell by construction. Sharing all possible source cells between processes would be highly inefficient as it would force us to limit the decomposition along the cell borders at our finest, still fully refined level, which would be in the worst-case levelmin. Hence, in SEPARA we have chosen to go for the second, very simple option and we end up with a domain decomposition $\{D_i\}$ that operates on the n_{dim} spatial sub-manifold of the phase-space and trivially extends it into the the velocity space as illustrated in Fig. 8.5:

$$D_i = D_i^{\mathrm{pos}} \times [v_{\mathrm{min}}, v_{\mathrm{max}}]^{n_{\mathrm{dim}}} . \tag{8.15}$$

---

[28]While this methods is very cheap to perform, it may result in long, thin domains with large surfaces with a resulting large amount of inter-process communication and virtual buffer grids. Since this method is part of the original RAMSES code, we decided to adapt and include it in SEPARA as well, but we are not actually using it in any of the test cases so far due to these potential shortcomings.
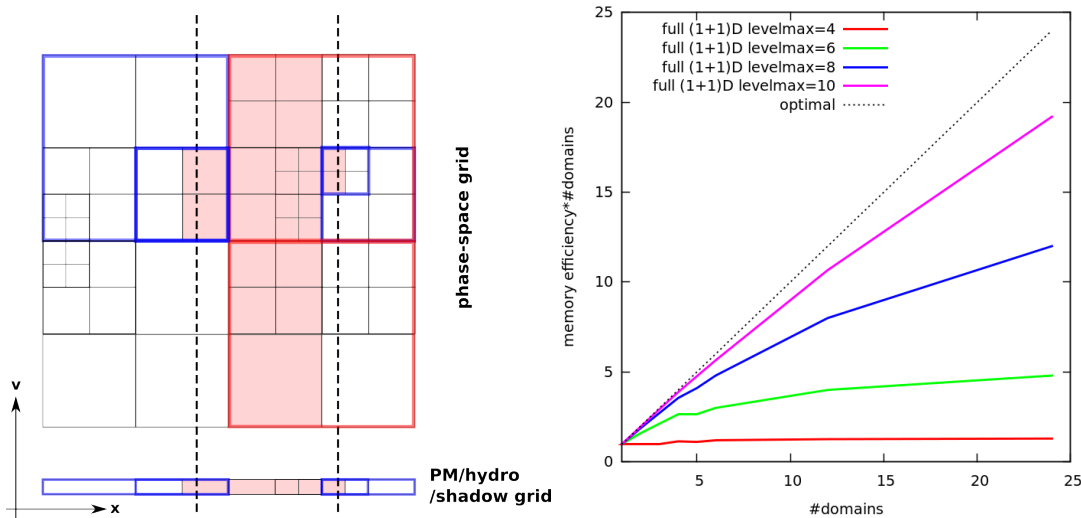
FIGURE 8.5: Domain decomposition in SEPARA: (left) Illustration of (1+1)D domain decomposition. Red borders mark the "active" grids that belong to the central domain while grids with blue borders are "virtual" grids that are needed to communicate inter-domain flows (right) Memory efficiency vs the number of domains/nodes measured in SEPARA (using fully refined meshes). The efficiency per domain is given by the ratio between the number of grids belonging to each process and the total number of grids (i.e. including virtual buffer grids). Ideally, i.e. without the need of any virtual grids for communication, the efficiency in each domain would be 1. This case is marked by the dotted line.

This choice comes, of course, with certain potential disadvantages. First of all, load-balancing may be suboptimal in cases where a lot of work in phase-space is spatially localized as this kind of decomposition does not allow for splitting up the velocity "stacks". In reality, this scenario is not very likely as the different spatial advection speeds in the same stack naturally disperse such alignments quickly. Secondly, these velocity "stacks" come with very large surface covering the whole of velocity space between bordering domains. Thus, in general, each process has to share a large amount of virtual cells along these boundaries with the processes owning the neighbouring domains.

The right panel in Fig. 8.5 illustrates this problem by plotting the memory efficiency, which we define as the ratio between the number of "active" grids belonging to the domains and the total numbers of grids including the shared "virtual" grids, against the number of domains. This shows that for a worst-case scenario with a fully-refined mesh, our parallelisation strategy eventually lead to a very inefficient use of memory for a large amount of domains. This could become a serious issue for planning simulations with a very high resolution which naturally require the use of more nodes and thus, more domains. Assuming that we double the number of domains, then the number of "active" grids decreases by the same

factor while the number of grids on the $2^{2\,\mathrm{dim}\,-1}$ dimensional domain surface only decreases by approximately a factor of $2^{2/3}$. This means that in the likely case, that we run our nodes at maximum memory capacity, we may reach the point where we waste most of the memory that we gain by adding new nodes on the communication buffers instead of spending it on an actual improvement in the simulation.

For the HDM scenarios we want to study, high refinement levels are mainly located in low-velocity bins. Because of that, large boundary surfaces are far less problematic as they are mostly only populated by very few coarse grids. If we assume e.g. a typical refinement found for a Fermi-Dirac distribution in velocity space, we end up with domain surface whose number of grids now scale roughly as $2^{lvl\cdot(n_{\mathrm{dim}}-1)}\log(2^{lvl\cdot n_{\mathrm{dim}}})$ instead of $2^{lvl\cdot(2n_{\mathrm{dim}}-1)}$ in the worst-case scenario described above, where lvl denotes the maximum level of refinement. This minimizes the penalty we receive from our choice of domain decomposition strategy significantly.

When it comes to estimating of the computational costs for the optimal domain decomposition, we have to note that due to the way we advect the neutrino phase-space density in velocity space where we "slice" target cells, the computation time does not simply depend on the number of phase-space cells, but also on the maximal local spatial refinement which determines the resolution of the force-field. At the moment we ignore this when determining the optimal domain decomposition since it is not trivial to predict these costs in advance. We instead rely on a weighted counting of the leaf cells which not only provides a decent estimate of the memory load, but also of the work load needed for the spatial advection with the Godunov solver in the "drift" step.

8.2.4 Cosmological Settings

For our studies of neutrinos, we are interested in performing our simulations in a cosmological context, i.e. in an expanding space-time environment. To take this into account we have to solve the Vlasov-Poisson equations (Eq.8.1) for a expanding Universe. Following the implementation of the N-body and hydrodynamics solver in RAMSES, we use the same *supercomoving coordinate* scheme (Martel and

Shapiro, 1998) with the following substitutions:

$$d\tilde{t} = H_0 \frac{dt}{a^2} \quad \text{(conformal time)} \tag{8.16}$$

$$\tilde{x} = \frac{x}{aL} \quad \text{and} \quad \tilde{v} = \frac{a(v - Hr)}{H_0 L} \tag{8.17}$$

$$\tilde{f} = \frac{H_0^3 L^3}{\Omega_0 \rho_{c,0}} f \Rightarrow \tilde{\rho} = \int \tilde{f} \mathrm{d}\tilde{v} = \frac{a^3}{\Omega_0 \rho_{c,0}} \rho \tag{8.18}$$

$$\tilde{\phi} = \frac{a^2}{L^2 H_0^2} \Phi - \frac{a \Omega_0 \tilde{x}^2}{4} \tag{8.19}$$

where H_0 is the Hubble constant. Ω_0 and $\rho_{c,0}$ are the total matter density parameter and critical matter density today. The length units are normalized to the side length L of the simulation volume, while the densities are normalized to the average matter density. $\tilde{\phi}$ is the supercomoving equivalent of the peculiar gravitational potential ϕ, which we obtain by subtracting the contributions from the homogeneous background cosmic matter distribution. Note that under these substitutions, the Vlasov equation (Eq.8.1) remains invariant, while the Poisson equation becomes:

$$\nabla_{\tilde{x}} \tilde{\phi} = \frac{3}{2} a \Omega_0 \left[\left(\int \tilde{f} \mathrm{d}^3 \tilde{v} + \tilde{\rho}_{CDM} + \tilde{\rho}_b \right) - 1 \right] . \tag{8.20}$$

With this set of units, we do not have to worry about the expansion of the Universe at all. Both the spatial expansion and the redshifting of velocities are intrinsically taken care of.

While this is ideal for neutrinos at high redshifts, since they start off at significantly high velocities, this choice of coordinate system may become an issue once we reach low redshifts where the maximum physical velocities allowed within the boundaries of the phase-space volume have been redshifted to the point where non-linear flows no longer fit within the boundaries. Yoshikawa et al. (2013) avoided this scenario by choosing instead to use peculiar velocities to provide a fixed physical velocity range over all redshifts. This suits cold phase-space fluids well, but forces an additional advection in the velocity dimensions even in the case of a completely homogeneous Universe. We have chosen to avoid this and the numerical diffusion that comes along with it and keep the mesh in comoving coordinates. To address the issue with the shrinking physical velocity range, we introduce a new parameter v_minmax to set the minimal maximal peculiar velocity. This should be chosen to be smaller than the maximal velocity dispersion in the expected struc-

tures in the simulation, which scales with

$$\sigma \sim \sqrt{\frac{GM_{\mathrm{vir}}}{R_{\mathrm{vir}}}} \, , \tag{8.21}$$

for virialized structures of radius R_{vir} and mass M_{vir}. Once the velocity boundaries of our mesh redshift enough to cross this threshold, we immediately decrease the coarse velocity resolution by a factor of 2 before the next coarse time step. This particular scale factor allows us to embed the existing grid easily into the new bigger one as illustrated in Fig. 8.6 by simply interpolating along the spatial direction. This would greatly increase the number of grids. But many of the cells such as the
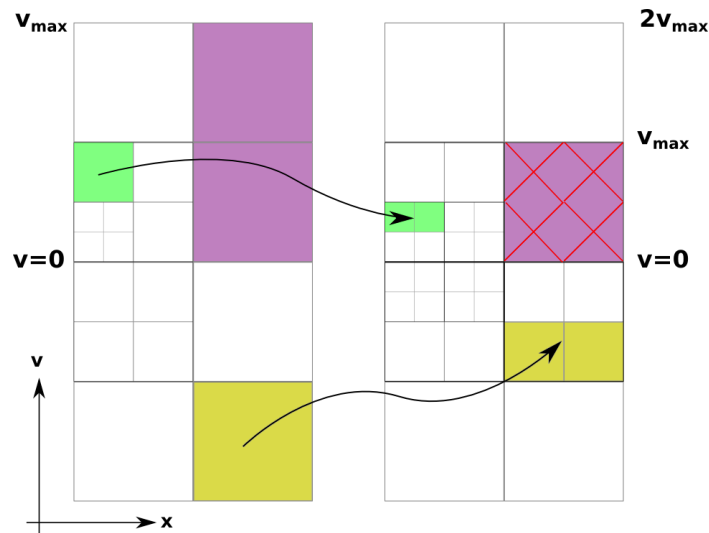
FIGURE 8.6: Scheme to double the velocity boundaries of the phase-space grid. The green and yellow cell are copied into the $2^{n_{\mathrm{dim}}}$ target cell on the new grid, where the density for each cell is determined by interpolation in the spatial dimensions. The purple cells both end up in the single big hatched cell as this target cell does not meet the criteria to justify a further refinement.

purple one in Fig. 8.6 do not actually need to be refined at the higher level. So by performing this transformation on a grid by grid basis and applying our refinement criterion right away like we do for our velocity convection, the amount of additional grids can be reduced to a minimum while the numerical diffusion in this step in the velocity direction is limited in low density regions.

8.2.5 Initial Conditions

While SEPARA has the ability to read in fully $2n_{\mathrm{dim}}$-dimensional initial conditions created in the grafic format (Bertschinger, 2001), the main focus in the

development of the code was on cosmological simulations where the initial velocity distribution is known and thus the full phase-space density distribution can be reconstructed from the n_{dim} projected matter density map. In order to obtain initial conditions for our cosmological runs, we first compute the spatial distribution of our phase-space components (e.g. neutrinos) using the already available tools like MUSIC (Hahn and Abel, 2013) used for the dark and baryonic matter, rename the outputs accordingly and then use the internal mechanisms within SEPARA the extrapolate the distribution in full phase-space as described below. Besides using pre-calculated initial spatial matter distributions, SEPARA allows the user to choose an initial simple spatially homogeneous distribution for a given matter energy density (rhomean_ps).
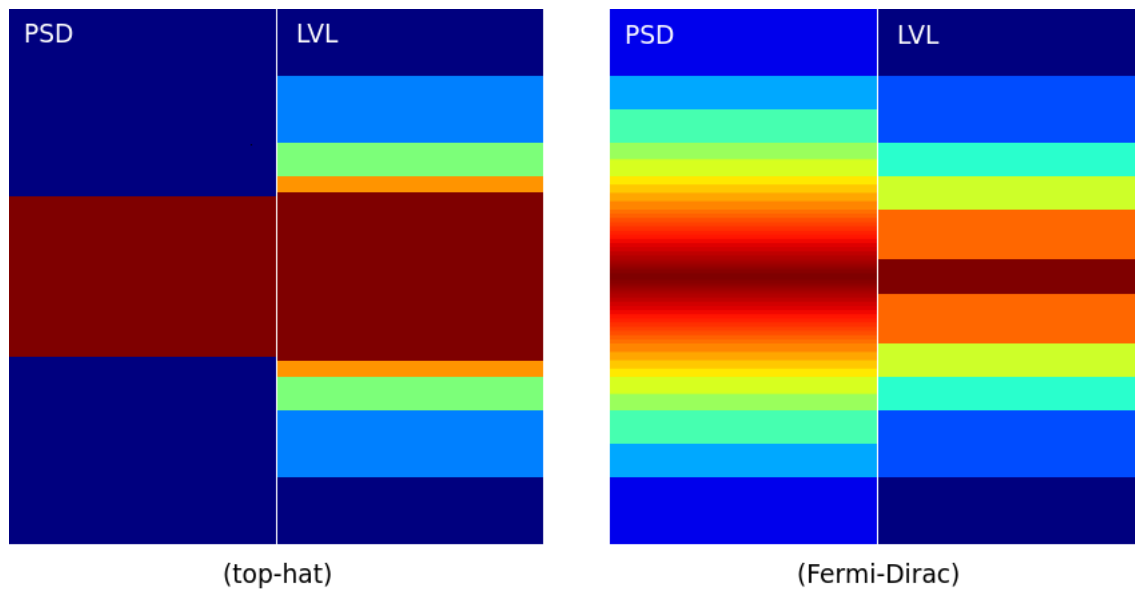
(top-hat)   (Fermi-Dirac)

FIGURE 8.7: 2D ICs generated with a top-hat (left) and Fermi-Dirac (right) velocity distribution. For the phase-space density (PSD) we use a logarithmic color scale running from blue to red for the highest density. For the refinement plot (LVL), the different colours encode the refinement level for each cell (dark blue=2, red=7).

Initial Velocity Dispersion   If no full $2n_{dim}$-dimensional IC conditions are provided, SEPARA let the user choose between pre-defined analytical profiles for the initial velocity distribution (vel_profile_ps) for which a set of parameters (vel_profile_param) has to be provided. At the moment, there are two kinds of such profiles defined: *Spherical top-hat* ('TH') with a single parameter specifying the maximal velocity and a *Fermi-Dirac* ('FD') profile with another parameter for

the average velocity. The latter is used for all simulations with neutrinos. Examples for both of those initial conditions can be found in Fig. 8.7.

8.2.6 Distribution

SEPARA is distributed as open source software under the CeCILL license[29]. The latest version of the source code can be downloaded from our git repository using the following command[30]:

```
1   $ git clone https://bitbucket.org/jschewts/separa
```

In order to obtain the binaries, simply adapt the special SEPARA Makefiles[31] according to your computation environment and compile the code using the provided scripts:

```
1   $ cd bin
    $ ./compile_separa.sh
    $ ./compile_separa_MPI.sh
```

For further information on how to compile and run SEPARA, check the README file in the phspace/ folder.

8.3 Conclusions

In this chapter, we have presented a new method that allows us to predict the fully non-linear evolution of the cosmic neutrino distribution while avoiding the problems that beset the N-body particle technique.This comes at the price of a more complex code. Where the N-body particle technique discussed in Chapter 7 only demanded that we modify the code used to create the initial conditions, so that it assigns thermal velocities to the neutrino tracers and to optimize the N-body simulation code slightly to improve the computational costs, this AMR approach required the implementation of an extended data structure together with the new Vlasov solvers on top of the existing RAMSES framework. The reward is a highly flexible code, which can be used for light neutrinos as well as for heavier ones without any loss of accuracy. Despite the improvements we made by adopting this

---

[29]see http://www.cecill.info for more details

[30]All instructions are given for a bash shell environment with all necessary libraries assumed to be installed.

[31]bin/Makefile.separa for single process or bin/Makefile.separa.MPI for the parallelised version

AMR technique, the computational costs, however, still represent a disadvantage. While future benchmarks still have to show how the code performs in a full cosmological setup, the code is still demanding compared to the two other techniques used in this thesis, especially when it comes to memory requirements.

A proper cosmological simulation also provides a much more representative scenario to test our memory efficiency and scaling properties for the parallelisation. We also still lack the proper convergence test that prove that our code meets the second-order accuracy in both phase-space and time that it should have by our choice of solvers. This all will be part of the future publication about our code (Schewtschenko et al., 2016), that is still in preparation.
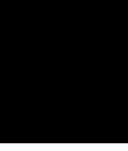
EPILOGUE

CHAPTER 9

Final discussion / Outlook

In this final chapter, we want to have a final look at the two main topics discussed in the thesis, i.e. interacting DM and neutrinos in simulations, and how the results may be used or open questions that may motivate future work.

We have seen how DM interactions with photons and neutrinos in the early Universe may affect the formation of the DM structures that originate from primordial perturbations. Even for cross-sections as small as the weak cross-section and below, the sensitivity of the formation process and resulting DM halo properties to alterations in these initial fluctuations in the matter distribution allowed us to show how these models can be potentially distinguished from CDM as well as alternative DM models such as WDM. Finally, we have shown how observations of substructures in our local cosmic neighbourhood can be used to rule out cross-section in this models that lie above a certain threshold.

All the work on dark matter interactions in this thesis was based on simulations that ignored the impact of baryons and their feedback. With modern models for baryonic physics in GADGET such as those developed for the EAGLE project (Schaye et al. (2015)), the next step could be to include this vital component into the numerical predictions. Due to the observed degeneracy between the impact of baryonic physics and of DM interactions on the observables, this could significantly improve the constraints on the physical parameters of the DM model. Additionally it would eliminate the need for certain assumptions we had to make to translate our predictions for the dark matter to the observables based on the gas and stars that visible in surveys. First, it would be interesting to see if the predicted changes of e.g. the DM halo spin could be also observed somehow in the angular momentum of the stars or gas that populate the halos. Equally interesting would be to use simulations with baryons to obtain the luminosity of the galaxies that form in the halos. This would not only allow us translate the limitations of our galaxy survey like limits to the apparent magnitude of observable satellite galaxies to the predictions in our simulations in a direct way, but could also avoid all the

problems we had with the reconstruction of Andromeda's SHVF by comparing the stellar mass functions instead. This would most likely lead to tighter constraints on the cross section for two reasons. First, the number of predicted galaxies is lower than the number of DM halos since especially many smaller halos fail to form stars and remain below the threshold of the brightness filter. Secondly, the stellar mass function for Andromeda is much higher than expected from the reconstructed sub-halo mass function and comparison with the Milky Way. Combining these two effects could move the current upper bound on the interaction cross section to significantly smaller values.

With all these possible advantages that the inclusion of baryons in the simulations may provide, there is one **big caveat** here that needs to be addressed. The subgrid models for all the baryonic physics (e.g. SN and AGN feedback) in the simulations contain a lot of parameters that are not fixed by astrophysical measurements, but rather are fine-tuned such that the simulation results are in agreement with selected observations in the Universe (Schaye et al., 2015). Therefore, claims that baryons already solve all previously observed tensions between CDM simulations and observations (cf. Sawala et al. (2016a)) and thus strongly support standard collision-less CDM as the favourite model for DM have to be taken with more than just a grain of salt. We have to remind ourselves, that this is only true under the belief that the fine-tuned model truly reproduces the actual baryonic physics in the Universe.

Thus, after taking the naive approach of constraining the interacting DM model parameters in simulations with such a baryonic physics model tuned to standard CDM, it would be of immense interest to see to what extent it would be possible to retune the model for alternative DM models. It has to be checked whether we can reproduce similarly good agreement with observations that way which would debunk the aforementioned claims and at what point we eventually break the degeneracy between the impact of baryons and non-standard DM. By failing to find a tuning for a specific kind of non-standard DM, it would then allow for the first time to determine constraints on DM properties that are based on completely consistent simulations with both CDM and baryons, yet remain independent of any arbitrary calibration of fudge factor therein.

With regard to our work on neutrinos, there also remains a lot to be done. With the SEPARA code finished, a lot more tests need to be performed in the near future to confirm the accuracy and convergence, that the code should have by construction. This includes simple tests such as the collapse of over-densities into

Zel'dovich Pancakes and test of neutrinos clustering on galactic halos. Once these tests are done, we can finally run the first full cosmological simulations. This will allow us to compare our new adaptive 6D mesh approach with the other techniques mentioned in the thesis.

Since SEPARA was explicitly designed to work along side the state-of-the-art hydrodynamics and other physics solvers implemented in the RAMSES itself or extensions such as e.g. ECOSMOG (Li et al., 2012) for modified gravity, the next step will be to run simulations with DM, neutrinos and baryons. Like in the case of IDM, the inclusion of baryons is essential to the correct prediction of structure formation of neutrinos as well as for the matter in general. While small structures are less interesting for studies of neutrino clustering as their free-streaming allows most of them to escape any halo smaller than the mass of about the Milky Way, studies like Schaller et al. (2015) have shown that the presence of baryons in the simulation reduces the mass and affects the density profiles of halos that are even orders of magnitude bigger than this threshold. Thus, if we are interested to predict e.g. the local CνB density in MW-like halos correctly, we need these kind of corrections. Furthermore, like in the case of interacting DM, baryons provide us with predictions that are directly comparable to observables found in astronomical and cosmological observations without the need to trust fitted semi-analytical techniques to derive these results from DM-only data.

There are two very interesting future neutrino studies where the flexibility of SEPARA can be used. In Sec. 6.3, we discussed how future terrestrial experiments are potentially able to detect the CνB. To estimate the expected signal rate for such an experiment, we need to know the local non-linear relic neutrino density. The ability to simulate the neutrino distribution accurately even down to smaller scales is essential for such predictions and can be performed by our new code.

Another subject for future studies is the temperature of the relic neutrinos. We have seen in Sec. 6.1.1, that in the standard model of Cosmology, neutrinos are a thermal relic and their temperature differs from that of the CMB by a constant factor due to the reheating by positron-electron annihilation, the latter went through after neutrinos thermally decoupled from the cosmic thermal bath. Studies like Steigman (2013) proposed that annihilation of BSM particles in the dark sector may lead to an additional reheating of either the CMB or CνB which would result in a different relation between those two components than commonly used. This is important because cosmological observations are mostly sensitive to the offset in the power spectrum, i.e. to the neutrino energy density and not to the neutrino
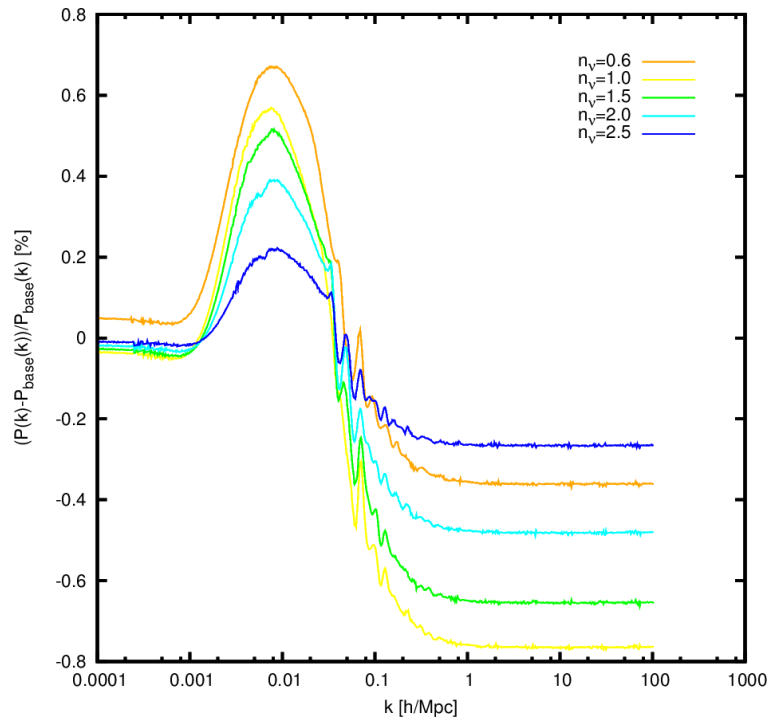
FIGURE 9.1: Relative total matter power spectra for neutrinos with $\sum m_\nu = 0.2$ eV and different neutrino temperatures with constant N_{eff} compared to reference models with standard temperature and same Ω_ν ($\Rightarrow \sum m_\nu$ varies).

mass directly as the published mass bounds may suggest. Thus, it would be very interesting to see if we can break the degeneracy between Ω_ν and $\sum m_\nu$ in our predictions, which would not only allow us to provide less model-dependent bounds on the neutrino mass, but also would let us probe the early Universe for such BSM physics.

Fig. 9.1 shows a comparison of linear power spectra for such a BSM scenario with the power spectra for reference models with a SM temperature. In the BSM case, we deal here with three massive neutrino species that are cooler than expected by the SM, i.e. their contribution to the effective number of relativistic degrees of freedom n_ν is smaller at around recombination as a larger share of neutrinos already turned non-relativistic. As recent BBN and CMB measurements tend to favour an effective number of relativistic degrees of freedom $N_{\text{eff}} \approx 3$, we keep it fixed by assuming the presence of additional dark radiation as e.g. expected from DM candidates like light sterile neutrinos. We can note in this comparison, that the degeneracy between Ω_ν, which is kept constant here, and $\sum m_\nu$ and the neutrino temperature T_ν can be broken. The signal in the linear power spectrum may be very small, but one may hope for an amplification of such differences in the non-

linear structure formation where the reduced free-streaming scale results in growth boosts at the galaxy cluster-sized scales of the peak in Fig. 9.1.

Finally, as a combination of all aforementioned proposals here, we could use the new, more accurate constraints on the BSM nature of DM and on the neutrino temperature obtained that way to revise previous constrains on the neutrino masses[32] to obtain results that truly take into account how much we still do not know (yet) about dark matter and the Universe.

---

[32]In the case of neutrinos, the tightest bounds on their energy density/mass have been obtained by comparing the predicted and observed distribution of intergalactic gas (Palanque-Delabrouille et al., 2015).

Bibliography

G. Aad, T. Abajyan, B. Abbott, J. Abdallah, S. Abdel Khalek, A. A. Abdelalim, O. Abdinov, R. Aben, B. Abi, M. Abolins, and et al. Observation of a new particle in the search for the Standard Model Higgs boson with the ATLAS detector at the LHC. *Physics Letters B*, 716:1–29, September 2012. doi: 10.1016/j.physletb.2012. 08.020.

C. V. Achar, M. G. K. Menon, V. S. Narasimhan, P. V. Ramana Murthy, B. V. Sreekantan, K. Hinotani, S. Miyake, D. R. Creed, J. L. Osborne, J. B. M. Pattison, and A. W. Wolfendale. The Kolar Gold Field neutrino experiment. *International Cosmic Ray Conference*, 2:1012, 1965.

M. Ackermann et al. Dark matter constraints from observations of 25 Milky Way satellite galaxies with the Fermi Large Area Telescope. *Phys.Rev.*, D89(4):042001, 2014. doi: 10.1103/PhysRevD.89.042001.

P.A.R. Ade et al. Planck 2013 results. XVI. Cosmological parameters. *Astron.Astrophys.*, 571:A16, 2014. doi: 10.1051/0004-6361/201321591.

S. Agarwal, P.-S. Corasaniti, S. Das, and Y. Rasera. Small scale clustering of late forming dark matter. *Phys.Rev.D*, 92(6):063502, September 2015. doi: 10.1103/ PhysRevD.92.063502.

D.S. Akerib et al. First results from the LUX dark matter experiment at the Sanford Underground Research Facility. *Phys.Rev.Lett.*, 112(9):091303, 2014a. doi: 10.1103/PhysRevLett.112.091303.

D.S. Akerib et al. First results from the LUX dark matter experiment at the Sanford Underground Research Facility. *Phys.Rev.Lett.*, 112(9):091303, 2014b. doi: 10.1103/PhysRevLett.112.091303.

S. Alam, F. D. Albareti, C. Allende Prieto, F. Anders, S. F. Anderson, T. Anderton, B. H. Andrews, E. Armengaud, É. Aubourg, S. Bailey, and et al. The Eleventh and Twelfth Data Releases of the Sloan Digital Sky Survey: Final Data from SDSS-III. *ApJS*, 219:12, July 2015. doi: 10.1088/0067-0049/219/1/12.

Y. Ali-Haïmoud and S. Bird. An efficient implementation of massive neutrinos in non-linear structure formation simulations. *MNRAS*, 428:3375–3389, February 2013. doi: 10.1093/mnras/sts286.

F. P. An, J. Z. Bai, A. B. Balantekin, H. R. Band, D. Beavis, W. Beriguete, M. Bishai, S. Blyth, K. Boddy, R. L. Brown, and et al. Observation of Electron-Antineutrino Disappearance at Daya Bay. *Physical Review Letters*, 108(17):171803, April 2012. doi: 10.1103/PhysRevLett.108.171803.

R.E. Angulo, C.M. Baugh, and C.G. Lacey. The assembly bias of dark matter haloes to higher orders. *MNRAS*, 387:921, 2008. doi: 10.1111/j.1365-2966.2008.13304.x.

M. Archidiacono and S. Hannestad. Efficient calculation of cosmological neutrino clustering with both linear and non-linear gravity. *ArXiv e-prints*, October 2015. arXiv:1510.02907.

T. Asaka, S. Blanchet, and M. Shaposhnikov. The νMSM, dark matter and neutrino masses [rapid communication]. *Physics Letters B*, 631:151–156, December 2005. doi: 10.1016/j.physletb.2005.09.070.

B. Audren. Monte python - the monte carlo code for class in python, 2014. URL <http://baudren.github.io/montepython.html>.

H. W. Babcock. The rotation of the Andromeda Nebula. *Lick Observatory Bulletin*, 19:41–51, 1939. doi: 10.5479/ADS/bib/1939LicOB.19.41B.

Jacob D. Bekenstein. The Modified Newtonian Dynamics: MOND and its implications for new physics. *Contemp.Phys.*, 47:387, 2006. doi: 10.1080/00107510701244055.

C. L. Bennett, M. Bay, M. Halpern, G. Hinshaw, C. Jackson, N. Jarosik, A. Kogut, M. Limon, S. S. Meyer, L. Page, D. N. Spergel, G. S. Tucker, D. T. Wilkinson, E. Wollack, and E. L. Wright. The Microwave Anisotropy Probe Mission. *ApJ*, 583: 1–23, January 2003. doi: 10.1086/345346.

A. J. Benson, A. Farahi, S. Cole, L. A. Moustakas, A. Jenkins, M. Lovell, R. Kennedy, J. Helly, and C. Frenk. Dark matter halo merger histories beyond cold dark matter - I. Methods and application to warm dark matter. *MNRAS*, 428:1774–1789, January 2013. doi: 10.1093/mnras/sts159.

Andrew J. Benson, C.G. Lacey, C.M. Baugh, S. Cole, and C.S. Frenk. The Effects of photoionization on galaxy formation. 1. Model and results at z = 0. *MNRAS*, 333: 156, 2002. doi: 10.1046/j.1365-8711.2002.05387.x.

J. Bergström, M. C. Gonzalez-Garcia, M. Maltoni, and T. Schwetz. Bayesian global analysis of neutrino oscillation data. *Journal of High Energy Physics*, 9:200, September 2015. doi: 10.1007/JHEP09(2015)200.

B. Bertoni, S. Ipek, D. McKeen, and A. E. Nelson. Reducing cosmological small scale structure via a large dark matter-neutrino interaction: constraints and consequences. *ArXiv e-prints*, December 2014. arXiv:1412.3113.

E. Bertschinger. Multiscale Gaussian Random Fields and Their Application to Cosmological Simulations. *ApJS*, 137:1–20, November 2001. doi: 10.1086/322526.

S. Betts, W. R. Blanchard, R. H. Carnevale, C. Chang, C. Chen, S. Chidzik, L. Ciebiera, P. Cloessner, A. Cocco, A. Cohen, J. Dong, R. Klemmer, M. Komor, C. Gentile, B. Harrop, A. Hopkins, N. Jarosik, G. Mangano, M. Messina, B. Osherson, Y. Raitses, W. Sands, M. Schaefer, J. Taylor, C. G. Tully, R. Woolley, and A. Zwicker. Development of a Relic Neutrino Detection Experiment at PTOLEMY: Princeton Tritium Observatory for Light, Early-Universe, Massive-Neutrino Yield. *ArXiv e-prints*, July 2013. arXiv:1307.4738.

Paul Bode, Jeremiah P. Ostriker, and Neil Turok. Halo formation in warm dark matter models. *Astrophys.J.*, 556:93–107, 2001. doi: 10.1086/321541.

C. Boehm and Pierre Fayet. Scalar dark matter candidates. *Nucl.Phys.*, B683:219–263, 2004. doi: 10.1016/j.nuclphysb.2004.01.015.

C. Boehm, Pierre Fayet, and R. Schaeffer. Constraining dark matter candidates from structure formation. *Phys.Lett.*, B518:8–14, 2001a. doi: 10.1016/S0370-2693(01)01060-7.

C. Boehm, Pierre Fayet, and R. Schaeffer. Constraining dark matter candidates from structure formation. *Phys.Lett.*, B518:8–14, 2001b. doi: 10.1016/S0370-2693(01)01060-7.

C. Boehm, H. Mathis, J. Devriendt, and J. Silk. Non-linear evolution of suppressed dark matter primordial power spectra. *MNRAS*, 360:282–287, 2005. doi: 10.1111/j.1365-2966.2005.09032.x.

C. Boehm, J.A. Schewtschenko, R.J. Wilkinson, C.M. Baugh, and S. Pascoli. Using the Milky Way satellites to study interactions between cold dark matter and radiation. *MNRAS*, 445:L31–L35, 2014. doi: 10.1093/mnrasl/slu115.

Celine Boehm and Richard Schaeffer. Constraints on dark matter interactions from structure formation: Damping lengths. *Astron.Astrophys.*, 438:419–442, 2005. doi: 10.1051/0004-6361:20042238.

Celine Boehm, Alain Riazuelo, Steen H. Hansen, and Richard Schaeffer. Interacting dark matter disguised as warm dark matter. *Phys.Rev.*, D66:083505, 2002. doi: 10.1103/PhysRevD.66.083505.

Celine Boehm, Yasaman Farzan, Thomas Hambye, Sergio Palomares-Ruiz, and Silvia Pascoli. Is it possible to explain neutrino masses with scalar dark matter? *Phys.Rev.*, D77:043516, 2008. doi: 10.1103/PhysRevD.77.043516.

A. Bonaca, M. Geha, A. H. W. Küpper, J. Diemand, K. V. Johnston, and D. W. Hogg. Milky Way Mass and Potential Recovery Using Tidal Streams in a Realistic Halo. *ApJ*, 795:94, November 2014. doi: 10.1088/0004-637X/795/1/94.

F. Bournaud. Tidal Dwarf Galaxies and Missing Baryons. *Advances in Astronomy*, 2010:735284, 2010. doi: 10.1155/2010/735284.

Daniel Boyanovsky and Jun Wu. Small scale aspects of warm dark matter : power spectra and acoustic oscillations. *Phys.Rev.*, D83:043524, 2011. doi: 10.1103/PhysRevD.83.043524.

Michael Boylan-Kolchin, James S. Bullock, and Manoj Kaplinghat. Too big to fail? The puzzling darkness of massive Milky Way subhaloes. *MNRAS*, 415:L40, 2011.

Michael Boylan-Kolchin, James S. Bullock, Sangmo Tony Sohn, Gurtina Besla, and Roeland P. van der Marel. The Space Motion of Leo I: The Mass of the Milky Way's Dark Matter Halo. *Astrophys.J.*, 768:140, 2013. doi: 10.1088/0004-637X/768/2/140.

J. Brandbyge and S. Hannestad. Grid based linear neutrino perturbations in cosmological N-body simulations. *JCAP*, 5:002, May 2009. doi: 10.1088/1475-7516/2009/05/002.

J. Brandbyge and S. Hannestad. Resolving cosmic neutrino structure: a hybrid neutrino N-body scheme. *JCAP*, 1:021, January 2010. doi: 10.1088/1475-7516/2010/01/021.

J. Brandbyge, S. Hannestad, T. Haugbølle, and B. Thomsen. The effect of thermal neutrino motion on the non-linear cosmological matter power spectrum. *JCAP*, 8:020, August 2008. doi: 10.1088/1475-7516/2008/08/020.

L. M. Brown. The idea of the neutrino. *Physics Today*, 31:23–28, September 1978.

S.E. Bryan, S.T. Kay, A.R. Duffy, J. Schaye, C. Dalla Vecchia, et al. The impact of baryons on the spins and shapes of dark matter haloes. *MNRAS*, 429:3316–3329, March 2013. doi: 10.1093/mnras/sts587.

Matthew R. Buckley, Jesús Zavala, Francis-Yan Cyr-Racine, Kris Sigurdson, and Mark Vogelsberger. Scattering, Damping, and Acoustic Oscillations: Simulating the Structure of Dark Matter Halos with Relativistic Force Carriers. *Phys.Rev.*, D90:043524, 2014. doi: 10.1103/PhysRevD.90.043524.

J. S. Bullock. Notes on the Missing Satellites Problem. *ArXiv e-prints*, September 2010. arXiv:1009.4505.

James S. Bullock, Andrey V. Kravtsov, and David H. Weinberg. Reionization and the abundance of galactic satellites. *Astrophys.J.*, 539:517, 2000. doi: 10.1086/309279.

M. Cautun, S. Bose, C. S. Frenk, Q. Guo, J. Han, W. A. Hellwing, T. Sawala, and W. Wang. Planes of satellite galaxies: when exceptions are the rule. *MNRAS*, 452: 3838–3852, October 2015. doi: 10.1093/mnras/stv1557.

Marius Cautun, Carlos S. Frenk, Rien van de Weygaert, Wojciech A. Hellwing, and Bernard J. T. Jones. Milky Way mass constraints from the Galactic satellite gap. *MNRAS*, 445:2049, 2014. doi: 10.1093/mnras/stu1849.

Xue-lei Chen, Steen Hannestad, and Robert J. Scherrer. Cosmic microwave background and large scale structure limits on the interaction between dark matter and baryons. *Phys.Rev.*, D65:123515, 2002. doi: 10.1103/PhysRevD.65.123515.

Xiaoyong Chu and Basudeb Dasgupta. Dark Radiation Alleviates Problems with Dark Matter Halos. *Phys.Rev.Lett.*, 113(16):161301, 2014. doi: 10.1103/PhysRevLett.113.161301.

D. J. H. Chung, L. L. Everett, G. L. Kane, S. F. King, J. Lykken, and L.-T. Wang. The soft supersymmetry-breaking Lagrangian: theory and applications. *PhR*, 407: 1–203, February 2005. doi: 10.1016/j.physrep.2004.08.032.

Marco Cirelli. Indirect Searches for Dark Matter: a status review. *Pramana*, 79: 1021–1043, 2012. doi: 10.1007/s12043-012-0419-x.

Douglas Clowe, Marusa Bradac, Anthony H. Gonzalez, Maxim Markevitch, Scott W. Randall, et al. A direct empirical proof of the existence of dark matter. *Astrophys.J.*, 648:L109–L113, 2006. doi: 10.1086/508162.

A. Coc, E. Vangioni-Flam, P. Descouvemont, A. Adahchour, and C. Angulo. Updated Big Bang Nucleosynthesis Compared with Wilkinson Microwave Anisotropy Probe Observations and the Abundance of Light Elements. *ApJ*, 600: 544–552, January 2004. doi: 10.1086/380121.

S. Cole, W. J. Percival, J. A. Peacock, P. Norberg, C. M. Baugh, C. S. Frenk, I. Baldry, J. Bland-Hawthorn, T. Bridges, R. Cannon, M. Colless, C. Collins, W. Couch, N. J. G. Cross, G. Dalton, V. R. Eke, R. De Propris, S. P. Driver, G. Efstathiou, R. S. Ellis, K. Glazebrook, C. Jackson, A. Jenkins, O. Lahav, I. Lewis, S. Lumsden, S. Maddox, D. Madgwick, B. A. Peterson, W. Sutherland, and K. Taylor. The 2dF Galaxy Redshift Survey: power-spectrum analysis of the final data set and cosmological implications. *MNRAS*, 362:505–534, September 2005. doi: 10.1111/j.1365-2966.2005.09318.x.

P. Colin, O. Valenzuela, and V. Avila-Reese. On the Structure of Dark Matter Halos at the Damping Scale of the Power Spectrum with and without Relict Velocities. *Astrophys.J.*, 673:203–214, 2008. doi: 10.1086/524030.

J. Conrad. Indirect Detection of WIMP Dark Matter: a compact review. *ArXiv e-prints*, November 2014. arXiv:1411.1925.

Asantha Cooray and Ravi K. Sheth. Halo models of large scale structure. *Phys.Rept.*, 372:1–129, 2002. doi: 10.1016/S0370-1573(02)00276-4.

Helene M. Courtois, Daniel Pomarede, R. Brent Tully, and Denis Courtois. Cosmography of the Local Universe. *Astron.J.*, 146:69, 2013. doi: 10.1088/0004-6256/146/3/69.

M. Crocce, S. Pueblas, and R. Scoccimarro. 2lpt initial conditions parallel code. 2012. URL <http://cosmo.nyu.edu/roman/2LPT/>.

Francis-Yan Cyr-Racine and Kris Sigurdson. Cosmology of atomic dark matter. *Phys.Rev.*, D87(10):103515, 2013. doi: 10.1103/PhysRevD.87.103515.

Marc Davis, George Efstathiou, Carlos S. Frenk, and Simon D.M. White. The Evolution of Large Scale Structure in a Universe Dominated by Cold Dark Matter. *Astrophys.J.*, 292:371–394, 1985. doi: 10.1086/163168.

R. Davis, D. S. Harmer, and K. C. Hoffman. Search for Neutrinos from the Sun. *Physical Review Letters*, 20:1205–1209, May 1968. doi: 10.1103/PhysRevLett.20. 1205.

J. Diemand, B. Moore, and J. Stadel. Earth-mass dark-matter haloes as the first structures in the early Universe. *Nature*, 433:389–391, January 2005. doi: 10.1038/ nature03270.

S. Dodelson. *Modern Cosmology*. Elsevier Science, 2003. ISBN 9780080511979.

A. D. Dolgov. Neutrinos in cosmology. *Physics Reports*, 370:333–535, November 2002. doi: 10.1016/S0370-1573(02)00139-4.

A.D. Dolgov, S.L. Dubovsky, G.I. Rubtsov, and I.I. Tkachev. Constraints on millicharged particles from Planck data. *Phys.Rev.*, D88(11):117701, 2013. doi: 10.1103/PhysRevD.88.117701.

Elena D'Onghia and Julio F. Navarro. Do Mergers Spin up Dark Matter Halos? *MNRAS*, 380:58, 2007. doi: 10.1111/j.1745-3933.2007.00348.x.

John Dubinski and R.G. Carlberg. The Structure of cold dark matter halos. *Astrophys.J.*, 378:496, 1991. doi: 10.1086/170451.

H. Dupuy and F. Bernardeau. Describing massive neutrinos in cosmology as a collection of independent flows. *JCAP*, 1:030, January 2014. doi: 10.1088/1475-7516/ 2014/01/030.

Cora Dvorkin, Kfir Blum, and Marc Kamionkowski. Constraining Dark Matter-Baryon Scattering with Linear Cosmology. *Phys.Rev.*, D89:023519, 2014. doi: 10.1103/PhysRevD.89.023519.

M. A. Fardal, M. D. Weinberg, A. Babul, M. J. Irwin, P. Guhathakurta, K. M. Gilbert, A. M. N. Ferguson, R. A. Ibata, G. F. Lewis, N. R. Tanvir, and A. P. Huxor. Inferring the Andromeda Galaxy's mass from its giant southern stream with Bayesian simulation sampling. *MNRAS*, 434:2779–2802, October 2013. doi: 10.1093/mnras/stt1121.

Yasaman Farzan, Silvia Pascoli, and Michael A. Schmidt. AMEND: A model explaining neutrino masses and dark matter testable at the LHC and MEG. *JHEP*, 1010:111, 2010. doi: 10.1007/JHEP10(2010)111.

A. Fattahi, J. F. Navarro, T. Sawala, C. S. Frenk, K. A. Oman, R. A. Crain, M. Furlong, M. Schaller, J. Schaye, T. Theuns, and A. Jenkins. The APOSTLE project: Local Group kinematic mass constraints and simulation candidate selection. *MNRAS*, 457:844–856, March 2016. doi: 10.1093/mnras/stv2970.

F. Filbet, E. Sonnendrücker, and P. Bertrand. Conservative Numerical Schemes for the Vlasov Equation. *Journal of Computational Physics*, 172:166–187, September 2001. doi: 10.1006/jcph.2001.6818.

G. L. Fogli, E. Lisi, A. Marrone, A. Melchiorri, A. Palazzo, A. M. Rotunno, P. Serra, J. Silk, and A. Slosar. Observables sensitive to absolute neutrino masses. II. *Phy.Rev.D*, 78(3):033010, August 2008. doi: 10.1103/PhysRevD.78.033010.

A. S. Font, A. J. Benson, R. G. Bower, C. S. Frenk, A. Cooper, G. De Lucia, J. C. Helly, A. Helmi, Y.-S. Li, I. G. McCarthy, J. F. Navarro, V. Springel, E. Starkenburg, J. Wang, and S. D. M. White. The population of Milky Way satellites in the Λ cold dark matter cosmology. *MNRAS*, 417:1260–1279, October 2011. doi: 10.1111/j. 1365-2966.2011.19339.x.

C.S. Frenk and Simon D.M. White. Dark matter and cosmic structure. *Annalen Phys.*, 524:507–534, 2012. doi: 10.1002/andp.201200212.

S. Garrison-Kimmel, M. Boylan-Kolchin, J. S. Bullock, and E. N. Kirby. Too big to fail in the Local Group. *MNRAS*, 444:222–236, October 2014. doi: 10.1093/ mnras/stu1477.

C. Giocoli, M. Meneghetti, R. B. Metcalf, S. Ettori, and L. Moscardini. Mass and concentration estimates from weak and strong gravitational lensing: a systematic study. *MNRAS*, 440:1899–1915, May 2014. doi: 10.1093/mnras/stu303.

Carlo Giocoli, Matthias Bartelmann, Ravi K. Sheth, and Marcello Cacciato. Halo model description of the non-linear dark matter power spectrum at $k \gg 1$ Mpc^{-1}. *MNRAS*, 408:300, 2010. doi: 10.1111/j.1365-2966.2010.17108.x.

P. Gnacinski and M. Krogulec. Composition of the Interstellar Medium. Acta Astron., 56:373–384, December 2006.

J. E. Gunn and B. A. Peterson. On the Density of Neutral Hydrogen in Intergalactic Space. *ApJ*, 142:1633–1641, November 1965. doi: 10.1086/148444.

O. Hahn and T. Abel. MUSIC: MUlti-Scale Initial Conditions. Astrophysics Source Code Library, November 2013.

J. Hamann, S. Hannestad, and Y. Y. Y. Wong. Measuring neutrino masses with a future galaxy survey. *JCAP*, 11:052, November 2012. doi: 10.1088/1475-7516/2012/11/052.

W. Hampel. GALLEX and Gno. In J. Bahcall, W. Haxton, P. Langacker, H. Robertson, and Y. Totsuka, editors, *KITP Conference: Solar Neutrinos: News About SNUs*, page 14, December 1997.

S. Hannestad. Neutrino physics from precision cosmology. *Progress in Particle and Nuclear Physics*, 65:185–208, October 2010. doi: 10.1016/j.ppnp.2010.07.001.

S. Hannestad, T. Haugbølle, and C. Schultz. Neutrinos in non-linear structure formation – a simple SPH approach. *JCAP*, 2:045, February 2012. doi: 10.1088/1475-7516/2012/02/045.

R. W. Hockney and J. W. Eastwood. *Computer Simulation Using Particles*. 1981.

H. Hoekstra, M. Bartelmann, H. Dahle, H. Israel, M. Limousin, and M. Meneghetti. Masses of Galaxy Clusters from Gravitational Lensing. *SSRv*, 177:75–118, August 2013. doi: 10.1007/s11214-013-9978-5.

J. Hubisz and P. Meade. Phenomenology of the littlest Higgs model with T-parity. *Phy.Rev.D*, 71(3):035016, February 2005. doi: 10.1103/PhysRevD.71.035016.

R. A. Ibata, G. F. Lewis, A. R. Conn, M. J. Irwin, A. W. McConnachie, S. C. Chapman, M. L. Collins, M. Fardal, A. M. N. Ferguson, N. G. Ibata, A. D. Mackey, N. F. Martin, J. Navarro, R. M. Rich, D. Valls-Gabaud, and L. M. Widrow. A vast, thin plane of corotating dwarf galaxies orbiting the Andromeda galaxy. *Nature*, 493: 62–65, January 2013. doi: 10.1038/nature11717.

IceCube Collaboration, A. Achterberg, M. Ackermann, J. Adams, J. Ahrens, K. Andeen, D. W. Atlee, J. Baccus, J. N. Bahcall, X. Bai, and et al. First year performance of the IceCube neutrino telescope. *Astroparticle Physics*, 26:155–173, October 2006. doi: 10.1016/j.astropartphys.2006.06.007.

K. Ichikawa, M. Fukugita, and M. Kawasaki. Constraining neutrino masses by CMB experiments alone. *PhRvD*, 71(4):043001, February 2005. doi: 10.1103/PhysRevD.71.043001.

K. Inoue. Kamland Results. In Y. Suzuki, M. Nakahata, Y. Itow, M. Shiozawa, and Y. Obayashi, editors, *Neutrino Oscillations and their Origin*, pages 3–12, April 2004. doi: 10.1142/9789812703101_0001.

A. Jenkins. Second-order Lagrangian perturbation theory initial conditions for re-simulations. *MNRAS*, 403:1859–1872, April 2010. doi: 10.1111/j.1365-2966.2010.16259.x.

A. Jenkins, C.S. Frenk, Simon D.M. White, J.M. Colberg, S. Cole, et al. The Mass function of dark matter halos. *MNRAS*, 321:372, 2001. doi: 10.1046/j.1365-8711.2001.04029.x.

T. Kajita. Atmospheric neutrino results from Super-Kamiokande and Kamiokande - Evidence for ν_μ oscillations. *Nuclear Physics B Proceedings Supplements*, 77:123–132, May 1999. doi: 10.1016/S0920-5632(99)00407-7.

J. S. Kalirai, R. L. Beaton, M. C. Geha, K. M. Gilbert, P. Guhathakurta, E. N. Kirby, S. R. Majewski, J. C. Ostheimer, R. J. Patterson, and J. Wolf. The SPLASH Survey: Internal Kinematics, Chemical Abundances, and Masses of the Andromeda I, II, III, VII, X, and XIV Dwarf Spheroidal Galaxies. *ApJ*, 711:671–692, March 2010. doi: 10.1088/0004-637X/711/2/671.

Anatoly A. Klypin, Andrey V. Kravtsov, Octavio Valenzuela, and Francisco Prada. Where are the missing Galactic satellites? *Astrophys.J.*, 522:82–92, 1999. doi: 10.1086/307643.

Steffen R. Knollmann and Alexander Knebe. Ahf: Amiga's Halo Finder. *Astrophys.J.Suppl.*, 182:608–624, 2009. doi: 10.1088/0067-0049/182/2/608.

S. Koposov and V. Belokurov. *Observational Constraints on the "Missing Satellite" Problem from SDSS*, page 195. NA, 2008. doi: 10.1007/978-1-4020-6933-8_42.

Andrey V. Kravtsov, Oleg Y. Gnedin, and Anatoly A. Klypin. The Tumultuous lives of Galactic dwarfs and the missing satellites problem. *Astrophys.J.*, 609:482–497, 2004. doi: 10.1086/421322.

F. Lacasa. Non-Gaussianity and extragalactic foregrounds to the Cosmic Microwave Background. *ArXiv e-prints*, June 2014. arXiv:1406.0441.

Cedric G. Lacey and Shaun Cole. Merger rates in hierarchical models of galaxy formation. *MNRAS*, 262:627–649, 1993.

Sandy S.C. Law and Kristian L. McDonald. A Class of Inert N-tuplet Models with Radiative Neutrino Mass and Dark Matter. *JHEP*, 1309:092, 2013. doi: 10.1007/ JHEP09(2013)092.

J. Lesgourgues. The Cosmic Linear Anisotropy Solving System (CLASS) I: Overview. *ArXiv e-prints*, April 2011. arXiv:1104.2932.

J. Lesgourgues and S. Pastor. Neutrino cosmology and Planck. *New Journal of Physics*, 16(6):065002, June 2014. doi: 10.1088/1367-2630/16/6/065002.

Julien Lesgourgues. The Cosmic Linear Anisotropy Solving System (CLASS) I: Overview. 2011.

A. Lewis and A. Challinor. CAMB: Code for Anisotropies in the Microwave Background. Astrophysics Source Code Library, February 2011. ascl:1102.026.

B. L'Huillier, C. Park, and J. Kim. Effects of the initial conditions on cosmological N-body simulations. *New Astronomy*, 30:79–88, July 2014. doi: 10.1016/j.newast. 2014.01.007.

B. Li, G.-B. Zhao, R. Teyssier, and K. Koyama. ECOSMOG: an Efficient COde for Simulating MOdified Gravity. J. Cosmology Astropart. Phys., 1:051, January 2012. doi: 10.1088/1475-7516/2012/01/051.

Manfred Lindner, Daniel Schmidt, and Thomas Schwetz. Dark Matter and Neutrino Masses from Global $U(1)_{B-L}$ Symmetry Breaking. *Phys.Lett.*, B705:324–330, 2011. doi: 10.1016/j.physletb.2011.10.022.

Mark R. Lovell, Vincent Eke, Carlos S. Frenk, Liang Gao, Adrian Jenkins, et al. The Haloes of Bright Satellite Galaxies in a Warm Dark Matter Universe. *MNRAS*, 420:2318–2324, 2012. doi: 10.1111/j.1365-2966.2011.20200.x.

Mark R. Lovell, Carlos S. Frenk, Vincent R. Eke, Adrian Jenkins, Liang Gao, et al. The properties of warm dark matter haloes. *MNRAS*, 439:300–317, 2014. doi: 10.1093/mnras/stt2431.

R. Lynds. The Absorption-Line Spectrum of 4c 05.34. *ApJL*, 164:L73, March 1971. doi: 10.1086/180695.

C.-P. Ma and E. Bertschinger. Cosmological Perturbation Theory in the Synchronous vs. Conformal Newtonian Gauge. *ArXiv Astrophysics e-prints*, January 1994a. arXiv:astro-ph/9401007.

C.-P. Ma and E. Bertschinger. A calculation of the full neutrino phase space in cold + hot dark matter models. *ApJ*, 429:22–28, July 1994b. doi: 10.1086/174298.

Andrea V. Maccio', Aaron A. Dutton, Frank C. van den Bosch, Ben Moore, Doug Potter, et al. Concentration, Spin and Shape of Dark Matter Haloes: Scatter and the Dependence on Mass and Environment. *MNRAS*, 378:55–71, 2007. doi: 10.1111/j.1365-2966.2007.11720.x.

Ariyeh H. Maller, Avishai Dekel, and Rachel S. Somerville. Modeling angular-momentum history in dark-matter halos. *MNRAS*, 329:423, 2002. doi: 10.1046/j.1365-8711.2002.04983.x.

Gianpiero Mangano, Alessandro Melchiorri, Paolo Serra, Asantha Cooray, and Marc Kamionkowski. Cosmological bounds on dark matter-neutrino interactions. *Phys.Rev.*, D74:043517, 2006. doi: 10.1103/PhysRevD.74.043517.

T. Marrodán Undagoitia and L. Rauch. Dark matter direct-detection experiments. *Journal of Physics G Nuclear Physics*, 43(1):013001, January 2016. doi: 10.1088/0954-3899/43/1/013001.

H. Martel and P. R. Shapiro. A convenient set of comoving cosmological variables and their application. *MNRAS*, 297:467–485, June 1998. doi: 10.1046/j.1365-8711.1998.01497.x.

S. P. Martin. a Supersymmetry Primer. *Perspectives On Supersymmetry. Series: Advanced Series on Directions in High Energy Physics, ISBN: <ISBN>978-981-02-3553-6</ISBN>. WORLD SCIENTIFIC, Edited by Gordon L Kane, vol. 18, pp. 1-98*, 18: 1–98, July 1998. doi: 10.1142/9789812839657_0001.

A. W. McConnachie. The Observed Properties of Dwarf Galaxies in and around the Local Group. *AJ*, 144:4, July 2012. doi: 10.1088/0004-6256/144/1/4.

A. B. McDonald and SNO Collaboration. The Sudbury Neutrino Observatory. In *American Astronomical Society Meeting Abstracts*, volume 31 of *Bulletin of the American Astronomical Society*, page 1412, December 1999.

A. L. Melott. The formation of galactic haloes in the neutrino-adiabatic theory. *Nature*, 296:721–723, April 1982. doi: 10.1038/296721a0.

M. Milgrom. A modification of the Newtonian dynamics as a possible alternative to the hidden mass hypothesis. *ApJ*, 270:365–370, July 1983. doi: 10.1086/161130.

Á. Moliné, J. A. Schewtschenko, S. Palomares-Ruiz, C. Boehm, and C. M. Baugh. Isotropic extragalactic flux from dark matter annihilations: lessons from interacting dark matter scenarios. *ArXiv e-prints*, February 2016. arXiv:1602.07282.

B. Moore, S. Ghigna, F. Governato, G. Lake, Thomas R. Quinn, et al. Dark matter substructure within galactic halos. *Astrophys.J.*, 524:L19–L22, 1999. doi: 10.1086/312287.

Julio F. Navarro, Carlos S. Frenk, and Simon D.M. White. A Universal density profile from hierarchical clustering. *Astrophys.J.*, 490:493–508, 1997. doi: 10.1086/304888.

Angelo F. Neto, Liang Gao, Philip Bett, Shaun Cole, Julio F. Navarro, et al. The statistics of lambda CDM Halo Concentrations. *MNRAS*, 381:1450–1462, 2007. doi: 10.1111/j.1365-2966.2007.12381.x.

N. Palanque-Delabrouille, C. Yèche, J. Baur, C. Magneville, G. Rossi, J. Lesgourgues, A. Borde, E. Burtin, J.-M. LeGoff, J. Rich, M. Viel, and D. Weinberg. Neutrino masses and cosmology with Lyman-alpha forest power spectrum. *JCAP*, 11:011, November 2015. doi: 10.1088/1475-7516/2015/11/011.

W. Pauli. Offener Brief an die Gruppe der Radioaktiven bei der Gauvereins-Tagung zu Tübingen. 1930.

P. J. E. Peebles. *The large-scale structure of the universe*. Princeton University Press, 1980. ISBN 9780691082400.

P. J. E. Peebles. *Principles of Physical Cosmology*. Princeton University Press, 1993. ISBN 9780691019338.

P.J.E. Peebles. Origin of the Angular Momentum of Galaxies. *Astrophys.J.*, 155:393, 1969. doi: 10.1086/149876.

Til Piffl, Cecilia Scannapieco, James Binney, Matthias Steinmetz, Ralf-Dieter Scholz, et al. The RAVE survey: the Galactic escape speed and the mass of the Milky Way. *Astron.Astrophys.*, 562:A91, 2014. doi: 10.1051/0004-6361/201322531.

Planck Collaboration, R. Adam, P. A. R. Ade, N. Aghanim, Y. Akrami, M. I. R. Alves, M. Arnaud, F. Arroja, J. Aumont, C. Baccigalupi, and et al. Planck 2015 results. I. Overview of products and scientific results. *ArXiv e-prints*, February 2015a. arXiv:1502.01582.

Planck Collaboration, P. A. R. Ade, N. Aghanim, M. Arnaud, F. Arroja, M. Ashdown, J. Aumont, C. Baccigalupi, M. Ballardini, A. J. Banday, and et al. Planck 2015 results. XX. Constraints on inflation. *ArXiv e-prints*, February 2015b. arXiv:1502.02114.

Planck Collaboration, P. A. R. Ade, N. Aghanim, M. Arnaud, M. Ashdown, J. Aumont, C. Baccigalupi, A. J. Banday, R. B. Barreiro, J. G. Bartlett, and et al. Planck 2015 results. XIII. Cosmological parameters. *ArXiv e-prints*, February 2015c. arXiv:1502.01589.

Planck Collaboration, P. A. R. Ade, N. Aghanim, M. Arnaud, M. Ashdown, J. Aumont, C. Baccigalupi, A. J. Banday, R. B. Barreiro, J. G. Bartlett, and et al. Planck 2015 results. XIII. Cosmological parameters. *ArXiv e-prints*, February 2015d. arXiv:1502.01589.

Planck Collaboration, N. Aghanim, M. Arnaud, M. Ashdown, J. Aumont, C. Baccigalupi, A. J. Banday, R. B. Barreiro, J. G. Bartlett, N. Bartolo, and et al. Planck 2015 results. XI. CMB power spectra, likelihoods, and robustness of parameters. *ArXiv e-prints*, July 2015e. arXiv:1507.02704.

Cristiano Porciani, Avishai Dekel, and Yehuda Hoffman. Testing tidal-torque theory. 2. Alignment of inertia and shear and the characteristics of proto-haloes. *MNRAS*, 332:339, 2002. doi: 10.1046/j.1365-8711.2002.05306.x.

Chris Power, J.F. Navarro, A. Jenkins, C.S. Frenk, Simon D.M. White, et al. The Inner structure of Lambda CDM halos. 1. A Numerical convergence study. *MNRAS*, 338:14–34, 2003. doi: 10.1046/j.1365-8711.2003.05925.x.

Francisco Prada, Anatoly A. Klypin, Antonio J. Cuesta, Juan E. Betancort-Rijo, and Joel Primack. Halo concentrations in the standard LCDM cosmology. *MNRAS*, 428:3018–3030, 2012. doi: 10.1111/j.1365-2966.2012.21007.x.

William H. Press and Paul Schechter. Formation of galaxies and clusters of galaxies by selfsimilar gravitational condensation. *Astrophys.J.*, 187:425–438, 1974. doi: 10.1086/152650.

F. Reines and C. L. Cowan. The Neutrino. *Nature*, 178:446–449, September 1956. doi: 10.1038/178446a0.

Miguel Rocha, Annika H.G. Peter, James S. Bullock, Manoj Kaplinghat, Shea Garrison-Kimmel, et al. Cosmological Simulations with Self-Interacting Dark Matter I: Constant Density Cores and Substructure. *MNRAS*, 430:81–104, 2013a. doi: 10.1093/mnras/sts514.

Miguel Rocha, Annika H.G. Peter, James S. Bullock, Manoj Kaplinghat, Shea Garrison-Kimmel, et al. Cosmological Simulations with Self-Interacting Dark Matter I: Constant Density Cores and Substructure. *MNRAS*, 430:81–104, 2013b. doi: 10.1093/mnras/sts514.

V. C. Rubin and W. K. Ford, Jr. Rotation of the Andromeda Nebula from a Spectroscopic Survey of Emission Regions. *ApJ*, 159:379, February 1970. doi: 10.1086/150317.

S. Saito, M. Takada, and A. Taruya. Nonlinear power spectrum in the presence of massive neutrinos: Perturbation theory approach, galaxy bias, and parameter forecasts. *PhRvD*, 80(8):083528, October 2009. doi: 10.1103/PhysRevD.80.083528.

T. Sawala, C. S. Frenk, A. Fattahi, J. F. Navarro, R. G. Bower, R. A. Crain, C. Dalla Vecchia, M. Furlong, J. C. Helly, A. Jenkins, K. A. Oman, M. Schaller, J. Schaye, T. Theuns, J. Trayford, and S. D. M. White. Local Group galaxies emerge from the dark. *ArXiv e-prints*, December 2014. arXiv:1412.2748.

T. Sawala, C. S. Frenk, A. Fattahi, J. F. Navarro, R. G. Bower, R. A. Crain, C. Dalla Vecchia, M. Furlong, A. Jenkins, I. G. McCarthy, Y. Qu, M. Schaller, J. Schaye, and T. Theuns. Bent by baryons: the low-mass galaxy-halo relation. *MNRAS*, 448:2941–2947, April 2015. doi: 10.1093/mnras/stu2753.

T. Sawala, C. S. Frenk, A. Fattahi, J. F. Navarro, R. G. Bower, R. A. Crain, C. Dalla Vecchia, M. Furlong, J. C. Helly, A. Jenkins, K. A. Oman, M. Schaller, J. Schaye, T. Theuns, J. Trayford, and S. D. M. White. The APOSTLE simulations: solutions to the Local Group's cosmic puzzles. *MNRAS*, 457:1931–1943, April 2016a. doi: 10.1093/mnras/stw145.

T. Sawala, C. S. Frenk, A. Fattahi, J. F. Navarro, T. Theuns, R. G. Bower, R. A. Crain, M. Furlong, A. Jenkins, M. Schaller, and J. Schaye. The chosen few: the low-mass haloes that host faint galaxies. *MNRAS*, 456:85–97, February 2016b. doi: 10.1093/mnras/stv2597.

U. Sawangwit and T. Shanks. Beam profile sensitivity of the WMAP CMB power spectrum. *MNRAS*, 407:L16–L20, September 2010. doi: 10.1111/j.1745-3933.2010. 00894.x.

R. Schaeffer and J. Silk. Cold, warm, or hot dark matter - Biased galaxy formation and pancakes. *Astrophys.J.*, 332:1–16, September 1988. doi: 10.1086/166624.

M. Schaller, C. S. Frenk, R. G. Bower, T. Theuns, A. Jenkins, J. Schaye, R. A. Crain, M. Furlong, C. Dalla Vecchia, and I. G. McCarthy. Baryon effects on the internal structure of ΛCDM haloes in the EAGLE simulations. *MNRAS*, 451:1247–1267, August 2015. doi: 10.1093/mnras/stv1067.

J. Schaye, R. A. Crain, R. G. Bower, M. Furlong, M. Schaller, T. Theuns, C. Dalla Vecchia, C. S. Frenk, I. G. McCarthy, J. C. Helly, A. Jenkins, Y. M. Rosas-Guevara, S. D. M. White, M. Baes, C. M. Booth, P. Camps, J. F. Navarro, Y. Qu, A. Rahmati, T. Sawala, P. A. Thomas, and J. Trayford. The EAGLE project: simulating the evolution and assembly of galaxies and their environments. *MNRAS*, 446:521–554, January 2015. doi: 10.1093/mnras/stu2058.

J. A. Schewtschenko. DM-radiation interaction cross-section constraints revisited with Andromeda data. in prep., 2016.

J. A. Schewtschenko, C. M. Baugh, R. J. Wilkinson, C. Boehm, S. Pascoli, and T. Sawala. Dark matter-radiation interactions: the structure of Milky Way satellite galaxies. *ArXiv e-prints*, December 2015a. arXiv:1512.06774.

J. A. Schewtschenko, R. J. Wilkinson, C. M. Baugh, C. Bœhm, and S. Pascoli. Dark matter-radiation interactions: the impact on dark matter haloes. *MNRAS*, 449: 3587–3596, June 2015b. doi: 10.1093/mnras/stv431.

J. A. Schewtschenko, C. M. Baugh, and S. Pascoli. SEPARA: an adaptive cosmological phase-space code. in prep., 2016.

A. Schneider. Structure formation with suppressed small-scale perturbations. *MNRAS*, 451:3117–3130, August 2015. doi: 10.1093/mnras/stv1169.

A. Schneider, R. E. Smith, A. V. Macciò, and B. Moore. Non-linear evolution of cosmological structures in warm dark matter models. *MNRAS*, 424:684–698, July 2012. doi: 10.1111/j.1365-2966.2012.21252.x.

A. Schneider, D. Anderhalden, A. V. Macciò, and J. Diemand. Warm dark matter does not do better than cold dark matter in solving small-scale inconsistencies. *MNRAS*, 441:L6–L10, June 2014. doi: 10.1093/mnrasl/slu034.

Aurel Schneider, Robert E. Smith, and Darren Reed. Halo Mass Function and the Free Streaming Scale. *MNRAS*, 433:1573–1587, August 2013. doi: 10.1093/mnras/stt829.

T. Schwetz, M. Tórtola, and J. W. F. Valle. Global neutrino data and recent reactor fluxes: the status of three-flavour oscillation parameters. *New Journal of Physics*, 13(6):063004, June 2011. doi: 10.1088/1367-2630/13/6/063004.

Paolo Serra, Federico Zalamea, Asantha Cooray, Gianpiero Mangano, and Alessandro Melchiorri. Constraints on neutrino – dark matter interactions from cosmic microwave background and large scale structure data. *Phys.Rev.*, D81:043507, 2010. doi: 10.1103/PhysRevD.81.043507.

G. Servant and T. M. P. Tait. Is the lightest Kaluza-Klein particle a viable dark matter candidate? *Nuclear Physics B*, 650:391–419, February 2003. doi: 10.1016/S0550-3213(02)01012-X.

T. Shanks. Arguments for an Omega = 1, low H0 baryon dominated universe. *Vistas in Astronomy*, 28:595–609, 1985. doi: 10.1016/0083-6656(85)90062-5.

T. Shanks. The effect of lensing on the large-scale cosmic microwave background anisotropy. *MNRAS*, 376:173–179, March 2007. doi: 10.1111/j.1365-2966.2007.11391.x.

T. Shanks, R. W. F. Johnson, J. A. Schewtschenko, and J. R. Whitbourn. A neutrino model fit to the CMB power spectrum. *MNRAS*, 445:2836–2841, December 2014. doi: 10.1093/mnras/stu1956.

Ravi K. Sheth and Giuseppe Tormen. Large scale bias and the peak background split. *MNRAS*, 308:119, 1999. doi: 10.1046/j.1365-8711.1999.02692.x.

Ravi K. Sheth, H.J. Mo, and Giuseppe Tormen. Ellipsoidal collapse and an improved model for the number and spatial distribution of dark matter haloes. *MNRAS*, 323:1, 2001. doi: 10.1046/j.1365-8711.2001.04006.x.

K. Shi, Y.-F. Huang, and T. Lu. The effects of parametrization of the dark energy equation of state. *Research in Astronomy and Astrophysics*, 11:1403–1412, December 2011. doi: 10.1088/1674-4527/11/12/003.

M. Shoji and E. Komatsu. Massive neutrinos in cosmology: Analytic solutions and fluid approximation. *Phys. Rev. D*, 82(8):089901, October 2010. doi: 10.1103/PhysRevD.82.089901.

Kris Sigurdson, Michael Doran, Andriy Kurylov, Robert R. Caldwell, and Marc Kamionkowski. Dark-matter electric and magnetic dipole moments. *Phys.Rev.*, D70:083501, 2004. doi: 10.1103/PhysRevD.70.083501,10.1103/PhysRevD.70.08350110.1103/PhysRevD.73.089903,10.1103/PhysRevD.73.089903.

Joshua D. Simon and Marla Geha. The Kinematics of the Ultra-Faint Milky Way Satellites: Solving the Missing Satellite Problem. *Astrophys.J.*, 670:313–331, 2007. doi: 10.1086/521816.

P. Simon. Retrieving the three-dimensional matter power spectrum and galaxy biasing parameters from lensing tomography. *AAP*, 543:A2, July 2012. doi: 10.1051/0004-6361/201118224.

Constantinos Skordis, D.F. Mota, P.G. Ferreira, and C. Boehm. Large Scale Structure in Bekenstein's theory of relativistic Modified Newtonian Dynamics. *Phys.Rev.Lett.*, 96:011301, 2006. doi: 10.1103/PhysRevLett.96.011301.

R.E. Smith et al. Stable clustering, the halo model and nonlinear cosmological power spectra. *MNRAS*, 341:1311, 2003. doi: 10.1046/j.1365-8711.2003.06503.x.

Robert E. Smith and Katarina Markovic. Testing the Warm Dark Matter paradigm with large-scale structures. *Phys.Rev.*, D84:063507, 2011. doi: 10.1103/PhysRevD.84.063507.

Y. Sofue. Dark halos of M 31 and the Milky Way. *PASJ*, 67:75, August 2015. doi: 10.1093/pasj/psv042.

Rachel S. Somerville. Can photoionization squelching resolve the sub-structure crisis? *Astrophys.J.*, 572:L23–L26, 2002. doi: 10.1086/341444.

Volker Springel. The Cosmological simulation code GADGET-2. *MNRAS*, 364:1105–1134, 2005. doi: 10.1111/j.1365-2966.2005.09655.x.

Volker Springel, Naoki Yoshida, and Simon D.M. White. GADGET: A Code for collisionless and gasdynamical cosmological simulations. *New Astron.*, 6:79, 2001. doi: 10.1016/S1384-1076(01)00042-2.

Volker Springel, Jie Wang, Mark Vogelsberger, Aaron Ludlow, Adrian Jenkins, Amina Helmi, Julio F. Navarro, Carlos S. Frenk, and Simon D. M. White. The Aquarius Project: the subhalos of galactic halos. *Mon. Not. Roy. Astron. Soc.*, 391:1685–1711, 2008. doi: 10.1111/j.1365-2966.2008.14066.x.

G. Steigman. Equivalent neutrinos, light WIMPs, and the chimera of dark radiation. *PhRvD*, 87(10):103517, May 2013. doi: 10.1103/PhysRevD.87.103517.

N. Straumann. From primordial quantum fluctuations to the anisotropies of the cosmic microwave background radiation. *Annalen der Physik*, 518:701–847, October 2006. doi: 10.1002/andp.200610212.

J. A. Tauber. The Planck Mission. In A. N. Lasenby and A. Wilkinson, editors, *New Cosmological Data and the Values of the Fundamental Parameters*, volume 201 of *IAU Symposium*, page 86, 2005.

M. Tegmark, M. R. Blanton, M. A. Strauss, F. Hoyle, D. Schlegel, R. Scoccimarro, M. S. Vogeley, D. H. Weinberg, I. Zehavi, A. Berlind, T. Budavari, A. Connolly, D. J. Eisenstein, D. Finkbeiner, J. A. Frieman, J. E. Gunn, A. J. S. Hamilton, L. Hui, B. Jain, D. Johnston, S. Kent, H. Lin, R. Nakajima, R. C. Nichol, J. P. Ostriker, A. Pope, R. Scranton, U. Seljak, R. K. Sheth, A. Stebbins, A. S. Szalay, I. Szapudi, L. Verde, Y. Xu, J. Annis, N. A. Bahcall, J. Brinkmann, S. Burles, F. J. Castander, I. Csabai, J. Loveday, M. Doi, M. Fukugita, J. R. Gott, III, G. Hennessy, D. W. Hogg, Z. Ivezić, G. R. Knapp, D. Q. Lamb, B. C. Lee, R. H. Lupton, T. A. McKay, P. Kunszt, J. A. Munn, L. O'Connell, J. Peoples, J. R. Pier, M. Richmond, C. Rockosi, D. P. Schneider, C. Stoughton, D. L. Tucker, D. E. Vanden Berk, B. Yanny, D. G. York, and SDSS Collaboration. The Three-Dimensional Power Spectrum of Galaxies from the Sloan Digital Sky Survey. *ApJ*, 606:702–740, May 2004. doi: 10.1086/382125.

I. Tereno, C. S. Carvalho, J. Dinis, R. Scaramella, J. Amiaux, C. Burigana, J. C. Cuillandre, A. da Silva, A. Derosa, E. Maiorano, M. Maris, D. Oliveira, P. Franzetti, B. Garilli, P. Gomez-Alvarez, M. Meneghetti, S. Wachter, and the Euclid Collaboration. Euclid Space Mission: building the sky survey. *ArXiv e-prints*, January 2015. arXiv:1502.00903.

R. Teyssier. Cosmological hydrodynamics with adaptive mesh refinement. A new high resolution code called RAMSES. *AAP*, 385:337–364, April 2002. doi: 10.1051/0004-6361:20011817.

Erik J. Tollerud, James S. Bullock, Louis E. Strigari, and Beth Willman. Hundreds of Milky Way Satellites? Luminosity Bias in the Satellite Luminosity Function. *Astrophys.J.*, 688:277–289, 2008. doi: 10.1086/592102.

T. S. van Albada, J. N. Bahcall, K. Begeman, and R. Sancisi. Distribution of dark matter in the spiral galaxy NGC 3198. *ApJ*, 295:305–313, August 1985. doi: 10. 1086/163375.

Laura G. van den Aarssen, Torsten Bringmann, and Christoph Pfrommer. Is dark matter with long-range interactions a solution to all small-scale problems of Λ CDM cosmology? *Phys.Rev.Lett.*, 109:231301, 2012. doi: 10.1103/PhysRevLett. 109.231301.

M. Viel, M. G. Haehnelt, and V. Springel. The effect of neutrinos on the matter distribution as probed by the intergalactic medium. J. Cosmology Astropart. Phys., 6:015, June 2010. doi: 10.1088/1475-7516/2010/06/015.

M. Viel, K. Markovic, M. Baldi, and J. Weller. The non-linear matter power spectrum in warm dark matter cosmologies. *MNRAS*, 421:50–62, March 2012. doi: 10.1111/j.1365-2966.2011.19910.x.

Matteo Viel, Julien Lesgourgues, Martin G. Haehnelt, Sabino Matarrese, and Antonio Riotto. Constraining warm dark matter candidates including sterile neutrinos and light gravitinos with WMAP and the Lyman-alpha forest. *Phys.Rev.*, D71:063534, 2005. doi: 10.1103/PhysRevD.71.063534.

Matteo Viel, George D. Becker, James S. Bolton, and Martin G. Haehnelt. Warm dark matter as a solution to the small scale crisis: New constraints from high redshift Lyman-α forest data. *Phys.Rev.*, D88:043502, 2013. doi: 10.1103/PhysRevD.88. 043502.

F. Villaescusa-Navarro, S. Bird, C. Peña-Garay, and M. Viel. Non-linear evolution of the cosmic neutrino background. J. Cosmology Astropart. Phys., 3:019, March 2013. doi: 10.1088/1475-7516/2013/03/019.

Mark Vogelsberger, Jesus Zavala, Christine Simpson, and Adrian Jenkins. Dwarf galaxies in CDM and SIDM with baryons: observational probes of the nature of dark matter. *MNRAS*, 444:3684, 2014. doi: 10.1093/mnras/stu1713.

J. Wang, C. S. Frenk, and A. P. Cooper. The spatial distribution of galactic satellites in the Λ cold dark matter cosmology. *MNRAS*, 429:1502–1513, February 2013. doi: 10.1093/mnras/sts442.

Jie Wang and Simon D.M. White. Discreteness effects in simulations of Hot/Warm dark matter. *MNRAS*, 380:93–103, 2007. doi: 10.1111/j.1365-2966.2007.12053.x.

Jie Wang, Carlos S. Frenk, Julio F. Navarro, and Liang Gao. The Missing Massive Satellites of the Milky Way. *MNRAS*, 424:2715–2721, 2012. doi: 10.1111/j.1365-2966.2012.21357.x.

Mei-Yu Wang, Annika H. G. Peter, Louis E. Strigari, Andrew R. Zentner, Bryan Arant, et al. Cosmological Simulations of Decaying Dark Matter: Implications for Small-scale Structure of Dark Matter Halos. *MNRAS*, 445:614, 2014. doi: 10.1093/mnras/stu1747.

D. H. Weinberg. Reconstructing primordial density fluctuations. I - Method. *MNRAS*, 254:315–342, January 1992. doi: 10.1093/mnras/254.2.315.

D. H. Weinberg, J. S. Bullock, F. Governato, R. Kuzio de Naray, and A. H. G. Peter. Cold dark matter: controversies on small scales. *ArXiv e-prints*, June 2013. arXiv:1306.0913.

S. Weinberg. Universal Neutrino Degeneracy. *Physical Review*, 128:1457–1473, November 1962. doi: 10.1103/PhysRev.128.1457.

S.D.M. White. Angular momentum growth in protogalaxies. *Astrophys.J.*, 286:38–41, 1984. doi: 10.1086/162573.

Ryan J. Wilkinson, Celine Boehm, and Julien Lesgourgues. *JCAP*, 1404:026, 2014a. doi: 10.1088/1475-7516/2014/04/026.

Ryan J. Wilkinson, Celine Boehm, and Julien Lesgourgues. *JCAP*, 1405:011, 2014b. doi: 10.1088/1475-7516/2014/05/011.

Beth Willman. In Pursuit of the Least Luminous Galaxies. *Adv.Astron.*, 2010:285454, 2010. doi: 10.1155/2010/285454.

J. Wolf, G. D. Martinez, J. S. Bullock, M. Kaplinghat, M. Geha, R. R. Muñoz, J. D. Simon, and F. F. Avedo. Accurate masses for dispersion-supported galaxies. *MNRAS*, 406:1220–1237, August 2010a. doi: 10.1111/j.1365-2966.2010.16753.x.

J. Wolf, G. D. Martinez, J. S. Bullock, M. Kaplinghat, M. Geha, R. R. Muñoz, J. D. Simon, and F. F. Avedo. Accurate masses for dispersion-supported galaxies. *MNRAS*, 406:1220–1237, August 2010b. doi: 10.1111/j.1365-2966.2010.16753.x.

Y. Y. Y. Wong. Higher order corrections to the large scale matter power spectrum in the presence of massive neutrinos. *JCAP*, 10:035, October 2008. doi: 10.1088/1475-7516/2008/10/035.

X.X. Xue et al. The Milky Way's Circular Velocity Curve to 60 kpc and an Estimate of the Dark Matter Halo Mass from Kinematics of 2400 SDSS Blue Horizontal Branch Stars. *Astrophys.J.*, 684:1143–1158, 2008. doi: 10.1086/589500.

K. Yoshikawa, N. Yoshida, and M. Umemura. Direct Integration of the Collisionless Boltzmann Equation in Six-dimensional Phase Space: Self-gravitating Systems. *ApJ*, 762:116, January 2013. doi: 10.1088/0004-637X/762/2/116.

Y. B. Zel'dovich. Gravitational instability: An approximate theory for large density perturbations. *AAP*, 5:84–89, March 1970.

F. Zwicky. On the Masses of Nebulae and of Clusters of Nebulae. *ApJ*, 86:217, October 1937. doi: 10.1086/143864.